# Alkali Rydberg States in Electromagnetic Fields: Computational Physics Meets Experiment

Dissertation
an der Fakultät für Physik
der Ludwig-Maximilians-Universität München

vorgelegt von Andreas Krug
aus München

München, den 29. August 2001

# Alkali Rydberg States in Electromagnetic Fields: Computational Physics Meets Experiment

Dissertation
an der Fakultät für Physik
der Ludwig-Maximilians-Universität München

vorgelegt von Andreas Krug
aus München

München, den 29. August 2001

1. Gutachter: Priv. Doz. Dr. A. Buchleitner
2. Gutachter: Prof. Dr. K. T. Taylor
Tag der mündlichen Prüfung: 9. November 2001

Though this be madness,
yet there is method in it.
W. Shakespeare, *Hamlet*

# Zusammenfassung

Wir untersuchen hochangeregte Wasserstoff- und Alkaliatome („Rydbergatome“) unter dem Einfluß eines starken Mikrowellenfeldes. Das äußere Feld, dessen Frequenz von der Größenordnung der klassischen Keplerfrequenz des Valenzelektrons ist, bewirkt eine starke Kopplung vieler verschiedener quantenmechanischer Energieniveaus und führt schließlich zur Ionisation des äußeren Elektrons. Während periodisch getriebene Wasserstoffatome als ein Paradebeispiel quantenchaotischen Verhaltens in einem offenen (zerfallenden) System angesehen werden können, bringt ein nicht-wasserstoffartiger Atomrumpf, der als ein rein quantenmechanisches Objekt zu betrachten ist, einige Komplikationen mit sich. Tatsächlich zeigen Experimente an verschiedenen Elementen deutliche Unterschiede im Ionisationsverhalten von Wasserstoff- und Alkaliatomen im Mikrowellenfeld.

Im ersten Teil dieser Arbeit wird ein theoretisch-numerischer Apparat entwickelt, der es ermöglicht, numerische Experimente sowohl an Wasserstoff als auch an Alkaliatomen unter *exakt den gleichen* Laborbedingungen durchzuführen. Aufgrund der hohen Niveaudichte der periodisch getriebenen, dreidimensionalen Atome im Bereich typischer experimenteller Parameter sind solche Simulationen nur mit Hilfe modernster Parallelrechner in Verbindung mit einer effizienten parallelen Implementierung unseres numerischen Verfahrens möglich.

Im zweiten Teil der Arbeit werden die Ergebnisse des numerischen Experiments vorgestellt und diskutiert. Wir finden ebenso deutliche Unterschiede wie überraschende Gemeinsamkeiten im Ionisationsverhalten von Wasserstoff- und Alkaliatomen und können jene Frequenzbereiche identifizieren, in welchen Alkaliatome wasserstoff- bzw. nicht-wasserstoffartiges Ionisationsverhalten zeigen. Unsere Resultate erzwingen die Neuinterpretation eines großen Teils der vorhandenen experimentellen Daten und erlauben es insbesondere, das seit ca. einem Jahrzehnt ungelöste Problem des deutlich unterschiedlichen Ionisationsverhaltens verschiedener atomarer Spezies unter dem Einfluß eines elektromagnetischen Feldes zu lösen.

Schließlich betrachten wir periodisch getriebene Rydbergatome als ein typisches offenes, komplexes Quantensystem, das einen komplizierten zeitlichen Zerfall zeigt. Insbesondere finden wir im Zerfall dieses realen atomaren Systems qualitative wie quantitative Unterschiede zu Vorhersagen, die auf Untersuchungen quantenmechanischer Abbildungen mit gemischt regulär-chaotischem klassischen Analogon beruhen.

# Abstract

We study highly excited hydrogen and alkali atoms (’Rydberg states’) under the influence of a strong microwave field. As the external frequency is comparable to the highly excited electron’s classical Kepler frequency, the external field induces a strong coupling of many different quantum mechanical energy levels and finally leads to the ionization of the outer electron. While periodically driven atomic hydrogen can be seen as a paradigm of quantum chaotic motion in an open (decaying) quantum system, the presence of the non-hydrogenic atomic core – which unavoidably has to be treated quantum mechanically – entails some complications. Indeed, laboratory experiments show clear differences in the ionization dynamics of microwave driven hydrogen and non-hydrogenic Rydberg states.

In the first part of this thesis, a machinery is developed that allows for numerical experiments on alkali and hydrogen atoms under precisely identical laboratory conditions. Due to the high density of states in the parameter regime typically explored in laboratory experiments, such simulations are only possible with the most advanced parallel computing facilities, in combination with an efficient parallel implementation of the numerical approach.

The second part of the thesis is devoted to the results of the numerical experiment. We identify and describe significant differences and surprising similarities in the ionization dynamics of atomic hydrogen as compared to alkali atoms, and give account of the relevant frequency scales that distinguish hydrogenic from non-hydrogenic ionization behavior. Our results necessitate a reinterpretation of the experimental results so far available, and solve the puzzle of a distinct ionization behavior of periodically driven hydrogen and non-hydrogenic Rydberg atoms – an unresolved question for about one decade.

Finally, microwave-driven Rydberg states will be considered as prototypes of open, complex quantum systems that exhibit a complicated temporal decay. However, we find considerable differences in the decay of such real and experimentally accessible atomic systems, as opposed to predictions based on the study of quantum maps or other toy models with mixed regular-chaotic classical counterparts.

# Contents

**1 Introduction** **1**
- 1.1 History of the problem . . . 2
  - 1.1.1 Microwave driven hydrogen atoms . . . 2
  - 1.1.2 Microwave driven alkali atoms . . . 6
- 1.2 Microwave driven Rydberg states as an open quantum system . . . 11
- 1.3 Structure of the thesis . . . 12

**I The Set-Up** **15**

**2 Description of the system** **17**
- 2.1 Atomic Rydberg states in a microwave field . . . 17
  - 2.1.1 Atoms in electromagnetic fields . . . 17
  - 2.1.2 Floquet theorem . . . 18
  - 2.1.3 Complex dilation . . . 20
- 2.2 Atomic hydrogen . . . 22
- 2.3 Alkali atoms . . . 24
  - 2.3.1 Quantum defect theory . . . 24
  - 2.3.2 Alkali atoms in an external field . . . 27
  - 2.3.3 Periodically driven alkali atoms . . . 29
- 2.4 Representation in a Sturmian basis set . . . 30
- 2.5 Physical quantities . . . 33
  - 2.5.1 Ionization probability . . . 33
  - 2.5.2 Shannon width . . . 34

**3 Numerical treatment of the system** **37**
- 3.1 The Lanczos algorithm . . . 37
- 3.2 Numerical implementation . . . 39
  - 3.2.1 Some basic ideas of parallel computing . . . 39
  - 3.2.2 Storage of the matrices . . . 42
  - 3.2.3 Implementation of the Lanczos algorithm . . . 45

3.2.4 Performance of the parallel code . . . . . . . . . . . . . . . 50
3.3 Application . . . . . . . . . . . . . . . . . . . . . . . . . . . . . 52
3.3.1 The parameters . . . . . . . . . . . . . . . . . . . . . . . . 55

**II The Results 67**

**4 Microwave Ionization of lithium Rydberg atoms 71**
4.1 Fixed field amplitude – various initial states . . . . . . . . . . . . . 71
4.2 Fixed initial states – changing the field amplitude . . . . . . . . . . 75
4.2.1 Comparison with the single Floquet state approximation . . 77
4.2.2 Shannon width . . . . . . . . . . . . . . . . . . . . . . . . . 79
4.3 Time dependence of the ionization signal . . . . . . . . . . . . . 81

**5 (Scaled) Frequency dependence of the ionization threshold 87**
5.1 Atomic hydrogen . . . . . . . . . . . . . . . . . . . . . . . . . . . 87
5.2 Alkali atoms . . . . . . . . . . . . . . . . . . . . . . . . . . . . . . 90
5.2.1 Lithium vs. hydrogen – three frequency regimes in the ionization dynamics . . . . . . . . . . . . . . . . . . . . . . . . 90
5.2.2 The Shannon width . . . . . . . . . . . . . . . . . . . . . . . 97
5.2.3 Rubidium . . . . . . . . . . . . . . . . . . . . . . . . . . . . . 98
5.3 Does the alkali ionization dynamics obey scaling rules? . . . . . . . 104
5.4 Laboratory experiments . . . . . . . . . . . . . . . . . . . . . . . . 106
5.4.1 The Virginia experiments on lithium and sodium . . . . . . 108
5.4.2 The Munich experiments on rubidium . . . . . . . . . . . . 108
5.5 Time dependence of the 10% ionization threshold . . . . . . . . . . 111
5.5.1 Time dependence of $n_0^4 \cdot F_{10\%}(t)$ vs. $n_0^3 \cdot \omega$ . . . . . . . . . 111
5.5.2 Algebraic time dependence of the ionization threshold . . . 114

**6 Time dependence of the ionization yield 117**
6.1 Algebraic decay of the survival probability . . . . . . . . . . . . . . 118
6.2 Microwave driven Rydberg states as an open quantum system . . . . 120
6.2.1 Lithium . . . . . . . . . . . . . . . . . . . . . . . . . . . . . . 120
6.2.2 Rubidium . . . . . . . . . . . . . . . . . . . . . . . . . . . . . 133
6.2.3 Atomic hydrogen . . . . . . . . . . . . . . . . . . . . . . . . . 134
6.3 Outlook . . . . . . . . . . . . . . . . . . . . . . . . . . . . . . . . . 136

**7 Summary and perspectives 139**
7.1 Summary . . . . . . . . . . . . . . . . . . . . . . . . . . . . . . . . 139
7.2 Perspectives . . . . . . . . . . . . . . . . . . . . . . . . . . . . . . 141

**Bibliography 145**

# Chapter 1

# Introduction

The interaction of matter with radiation is one of the primary experimental means to test theoretical ideas and to develop or search for novel physical phenomena. An important example is the famous photoelectric effect [1] in which the critical dependence of the ionization yield on the frequency rather than on the intensity of the incoming radiation was observed. This led to the hypothesis of the quantum nature of light and was crucial for the fast development of quantum theory in the beginning of the last century.

In the second half of the last century, with the availability of quantum sources of intense and coherent radiation – the laser and the maser – many highly sophisticated experiments became possible, such as slowing down and cooling particles to extremely low temperatures [2, 3, 4], high resolution spectroscopic or quantum optics experiments to provide a rigorous verification of quantum-electro-dynamics and quantum mechanics [5], or the control of chemical reactions by the transfer of population with the help of an optimally shaped laser pulse [6, 7]. At even higher intensities, these light sources also open new fields regarding the dissociation and ionization process of molecules and atoms, with a crucial role played by multiphoton processes. Among such strong field phenomena, experiments on the microwave ionization of highly excited hydrogen atoms were of particular conceptual interest [8]. In contrast to the above mentioned photoelectric effect, the ionization yield in these experiments strongly depends on the field amplitude, and only weakly on the frequency. Furthermore, the microwave field induces a relatively large ionization probability, inexplicable at that time. Subsequent theoretical investigation of the process stressed the importance of the system's classical counterpart, and the transition from classically regular to classically chaotic motion taking place at a given field amplitude. Thus, microwave driven Rydberg atoms can nowadays be seen as a key phenomenon that stimulated the search for fingerprints of classical chaos in quantum systems. The ongoing study on this system for nearly three decades now has produced an enormous richness of results and has spurred research in the field of quantum chaos.

Microwave driven hydrogen atoms have now been studied by many groups in a more or less exact fashion. Despite their apparent similarity, little understanding has been gained on microwave driven, singly excited multi-electron atoms. In fact, laboratory experiments on alkali atoms have shown dramatic differences in their ionization behavior as compared to that observed with atomic hydrogen [9].

All the theoretical work on microwave ionization so far has only tackled the simpler atomic system of atomic hydrogen. Experimentally established differences [9] in the ionization dynamics of alkali atoms have remained an open question. One reason for the complications experienced with non-hydrogenic atomic cores is the fact that such systems are indubitable three-dimensional objects. Hence, any theoretical approach has to deal with an extremely high density of bound states strongly coupled to the continuum.

The aim of this work is to develop an algorithmic apparatus for the exact description of this system in its full complexity. Any such program requires the combination of an accurate description of the atom coupled to the continuum and of state-of-the-art high-performance parallel computing techniques to execute the underlying model. Our numerical experiment will provide the first results on microwave driven Rydberg states both on alkali atoms and of atomic hydrogen, in the regime of typical laboratory parameters, *without the need for any adjustable parameters*. As a result, we will develop a thorough understanding of the ionization process in both atomic species.

## 1.1 History of the problem

### 1.1.1 Microwave driven hydrogen atoms

First experiments on the ionization of microwave driven Rydberg states of atomic hydrogen were already performed in the nineteen seventies [8, 10]. Although microwave ionization requires the absorption of a large number of photons (in [8, 10] the energy difference between the atomic initial state and the atomic continuum exceeds 80 times the photon energy), these experiments showed a relatively efficient ionization, what was inconsistent with the quantum mechanical theories on multi-photon ionization available at that time. Classical (Monte Carlo) calculations [11], on the other hand, were able to reproduce the experimental results [8] rather well. This gave clear evidence of the relevance of the underlying classical dynamics, i.e. of the dynamics of the periodically driven Kepler problem. Investigations of the stability properties of the classical dynamics indicated that the ionization process can be ascribed to a diffusion mechanism [12]. More precisely, it was shown that at sufficiently large field amplitudes – at the classical “chaos border” – non-linear resonances in the classical phase space begin to overlap [13, 14, 15], leading to diffusive energy gain of the electron, and finally to its ionization. The quantum mechanical, experimentally measured 10% ionization threshold (i.e. the amplitude of the external field which induces 10 % ionization probability at given atom-field interaction time) was identified with the onset of classically chaotic motion. Both, quantum mechanical calculations [16, 17, 18] and experiments covering a broad range of microwave frequencies and principal quantum numbers of the atomic initial state [19] confirmed these predictions for driving frequencies below the Kepler frequency of the unperturbed highly excited electron.

For larger frequencies, however, quantum mechanics starts to deviate from the classical predictions [20, 21], and the real (quantum mechanical) atom appears more stable against ionization than its classical (chaotic) counterpart. To understand this apparent violation of the correspondence principle, the dynamics of microwave driven atomic hydrogen was linearized and approximated by the Kepler map [22, 23, 24], similar to the dynamics of a kicked rotor [24]. For the latter system, it had been shown already before that classically diffusive motion is suppressed by quantum interference effects, a process essentially equivalent to Anderson localization [25] in disordered solid state samples, labeled 'dynamical localization' [26], to stress the explicit time dependence of the underlying, perfectly deterministic Hamiltonian dynamics. According to the statistical description of the electronic transport (along the energy axis) from the initial atomic state to the atomic continuum in terms of a diffusion process, the real atom initially follows the classical model which predicts an onset of ionization at the classical chaos border, with the initial wave-packet starting to spread diffusively over the bound-state spectrum. Since, in contrast to the continuous spectrum which describes the classical dynamics, the bound-space quantum spectrum is pure point,(1) the spreading of the quantum mechanical electronic population must stop after some time, leading to a quasi-stationary distribution of the initial wave-packet, as opposed to an unbounded diffusion in the classical system. While Anderson localization explains the localization of the electronic density in configuration space, and hence – in a certain parameter regime – the transition from a metal to an insulator in disordered solids [25, 27], the time-dependent (dynamical) counterpart predicts the localization of the electronic wave-function in energy space, for frequencies larger than the Kepler frequency. This localization effect leads to a freezing of the electronic distribution over a number of eigenstates, which is measured by the localization length [24]. However, the theory of dynamical localization does not imply that ionization is not possible for frequencies larger than the Kepler frequency of the electron. Here, an increasing field amplitude leads to an increase of the localization length, and finally to a localization length comparable to or larger than the energy difference between the initial atomic state and the continuum.(2) This defines a delocalization border, above which the electron ionizes even in the presence of (Anderson respectively dynamical) localization.

---

(1) We will see that, in a periodically driven atom, the bound pure point part actually turns into a set of decaying states (see section 2.1.3). However, the widths of these resonance states are in general much smaller than the average level spacing, and the spectrum can be considered as quasi-discrete, on the appropriate time scales, since the Heisenberg time (see section 6.2.1.2) remains well-defined.

(2) This is in analogy to disordered solids, where a localization length larger than the sample size – the equivalence of the energy difference between the initial state and the atomic continuum in dynamical localization – leads to a finite conductance.

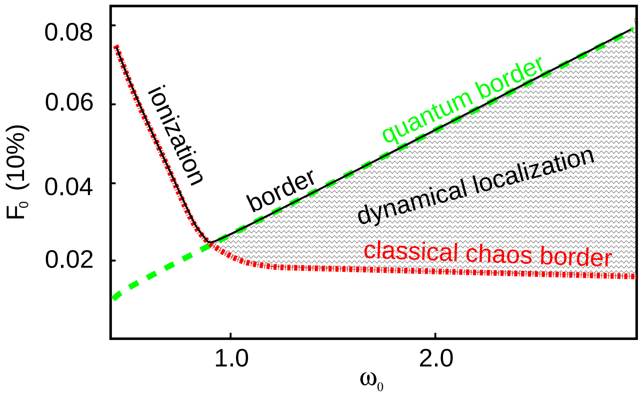

Figure 1.1: Sketch of the ionization dynamics of microwave driven Rydberg states of atomic hydrogen: For low scaled frequencies $\omega_0$, the quantum ionization border, displayed by the scaled 10% ionization threshold $F_0(10\%)$, follows the classical chaos border; for larger scaled frequencies, the classically chaotic motion is suppressed ('dynamical localization'), and the quantum system is more stable than its classical counterpart. The driving frequency and the field amplitude are scaled with respect to the Kepler frequency of the unperturbed, highly excited electron, and of the Coulomb field between the highly excited electron and the nucleus, respectively.

To understand the relevance of classical dynamics for the driven atom as the quantum analogue of the periodically driven Kepler problem, one can take advantage of the scale invariance of the classical equations of motion [28, 29]: As the electron and the nucleus interact through Coulomb forces, the potential energy of the system is a homogeneous function of the coordinates. Thus the equations of motion obey a scaling rule, i.e. by measuring the frequency $\omega$ of the driving field in units of the Kepler frequency of the electron, and the amplitude $F$ in units of the Coulomb field between the electron and the nucleus, it is possible to keep the phase space structure fixed while probing different initial conditions (e. g. principal actions and this is principal quantum numbers of the atom). Apart from the finite size of Planck's constant $\hbar$, these scaling rules also hold for the (quantum mechanical) periodically driven hydrogen atom, and different atomic initial states can therefore be identified with a well-defined classical dynamics which we fixed by the scaled frequency $\omega_0$ and the scaled field strength $F_0$ [24, 30, 31].

Figure 1.1 summarizes the global trend of the ionization border of microwave driven atomic hydrogen as predicted by the sketched theory of dynamical localization [24]: For scaled frequencies $\omega_0 < 1$ (where the frequency is smaller than the electronic Kepler frequency) the (quantum) dynamics essentially follows the classical prediction and the 10% threshold – displayed by the ionization border – decreases with increasing scaled frequency. Chaotic ionization is suppressed for larger (scaled) frequencies by the aforementioned dynamical localization, hence the real atom is more stable than the classical atom, and the ionization border increases with increasing (scaled) frequency for $\omega_0 > 1$.(3)

Quantum calculations on simplified models like the quantum Kepler map [24] or one-dimensional hydrogen atoms [18], and equally fully three-dimensional calculations on moderately excited microwave driven hydrogen atoms [32, 33, 34], as well as experimental results [20, 21, 31] confirmed the global trend of the scenario described above.

Yet, on top of the ionization border in figure 1.1, the 10% ionization threshold observed in the laboratory and in quantum calculations shows also local maxima, when the frequency reaches an integer multiple (for $\omega_0 > 1$) or a low order rational fraction (for $\omega_0 < 1$) of the electron's Kepler frequency [31]. Since both, the description of the ionization process in terms of classical diffusion and the theory of dynamical localization, are statistical descriptions of the ionization dynamics and do not take into account classical nonlinear resonances, they obviously cannot provide for an interpretation of local structures in the ionization border.

As a matter of fact, (classically) diffusive energy gain is only possible once the classical resonance islands overlap, or if the phase space is purely chaotic. In the generic case of microwave driven Rydberg atoms, however, and also for driving frequencies larger than the Kepler frequency, the classical phase space structure is not fully chaotic but mixed, and regular and chaotic regions coexist. This intricate (hierarchical) phase space structure prevents a fast, diffusive energy gain of the electron, since the electron's trajectory gets trapped in the vicinity of regular islands that are embedded in the 'chaotic sea'. These regular islands are induced by non-linear resonances when the driving frequency is an integer multiple or a low order fractional of the Kepler frequency [35]. Quantum mechanical simulations on the dynamics of the driven atom showed that these classical stability islands cause also the quantum mechanical atom to be locally (in $\omega_0$) more stable against ionization, provided the atomic initial state has some nonvanishing overlap with the island. Note that these quantum non-linear resonances [36, 37] locally dominate the quantum dynamics not only for frequencies below the electron's Kepler frequency ($\omega_0 < 1$), where the ionization process is well described by the classical dynamics, but also in the (non-classical) regime of dynamical localization [33].

The above description summarizes the essential characteristics of the ionization process of microwave-driven atomic hydrogen. Most of these characteristics have been observed in the laboratory and found consistent explanations based on theoretical model calculations. While the latter, so far, always had to rely on some approximations, due to the tremendous complexity of the real atomic excitation and ionization process, the more serious of them nonetheless were founded on well-controlled approximations, with a well-defined range of applicability (such as reduced dimensionality of the model [38, 34, 33, 39], reduced principal quantum numbers combined with the above mentioned scaling rules [32, 34, 33]). What remains to be accomplished, and what will be accomplished in the present thesis, is an ab initio treatment of the hydrogen problem, without any essential approximations, nor adjustable parameters. This is the final conclusive step in the comparison of theory and experiment, and provides a 'standard' to which we will compare our results on alkali Rydberg states.

---

(3) Here, it has to be noted that figure 1.1 displays the situation in scaled variables, $F_0$, and $\omega_0$ (for fixed laboratory frequency and a given interaction time). The quantum ionization border, however, depends not only on the scaled, but also on the laboratory frequency, and it decreases for decreasing laboratory frequency (and fixed scaled frequency, what can be achieved by doing both, employing a smaller frequency and using higher excited states). This explains the aforementioned apparent violation of the correspondence principle in the dynamically localized regime, since the quantum ionization border tends to the classical chaos border for increasing principal quantum numbers $n_0$ and fixed scaled frequency $\omega_0$. Note that increasing $n_0$ is tantamount to increasing the typical classical actions in the system and to decreasing the effective Planck's constant (i.e. Planck's constant scaled by the typical action describing the motion of the electron). Thus, in the semiclassical limit (for $\hbar_{\mathrm{effective}} \to 0$), the gap between the quantum and the classical ionization border (see figure 1.1) vanishes.

### 1.1.2 Microwave driven alkali atoms

While nearly all of the theoretical work on microwave driven Rydberg states deals with atomic hydrogen, arguably the larger part of the laboratory experiments are performed on multi-electron atoms. From the experimental point of view, the use of alkali rather than of hydrogen atoms entails some advantages:

Firstly, due to the absence of the angular momentum degeneracy in non-hydrogenic atoms, the preparation of a well defined initial atomic state $|n_0, m_0, \ell_0\rangle$ is easier. Secondly, as alkali atoms are heavier elements than atomic hydrogen, a thermal beam of alkali atoms is slower than a beam of atomic hydrogen with the same temperature. Since the size of the atom-field interaction region is determined by the microwave frequency, using a slower beam of atoms enables the experimentalist to vary the atom-field interaction time over a broader range.

Apart from a few experiments on helium atoms [40, 41], in which the ionization probability was not studied very systematically, there are two experimental groups working on microwave ionization of Rydberg atoms different from hydrogen. At the University of Munich [42, 43, 44, 9], the ionization of rubidium Rydberg states is studied, and at the University of Virginia various alkali atoms [45, 46, 47, 48, 49, 50] and alkaline earths [51] are being investigated. The two groups not only employ different atomic species, but also probe different parameter regimes of the ionization process, and hence they have produced results that until now have not led to a clear understanding of the microwave ionization of alkali Rydberg states as compared to the one of atomic hydrogen.

#### 1.1.2.1 The Munich experiments

Before entering into a detailed discussion of the differences between the experimental observations of the Munich and the Virginia group and the results of the hydrogen experiments, we briefly sketch a typical experimental set-up, as used by the Munich group (see also figure 1.2):

A thermal beam of rubidium atoms enters the apparatus. After the beam is collimated in (A), the atoms are excited from the ground state to Rydberg states with

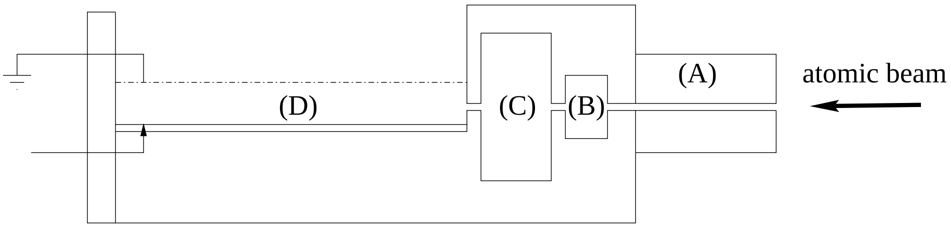

Figure 1.2: Typical experimental set-up [9] for the microwave ionization of rubidium Rydberg atoms.

principal quantum numbers in the range $n_0 = 50, \ldots, 95$, angular momentum $\ell_0 = 1$,(4) and angular momentum projection on the field axis $m_0 = 0$, by a pulsed laser in region (B). The beam of Rydberg atoms then enters the interaction region (C), where they are irradiated by a microwave pulse of frequency $\omega$ and well-defined duration $t$. After leaving the interaction region, the non-ionized atoms are field-ionized by a static electric field in region (D), and the electrons are recorded. By iteratively repeating the experiment with and without microwave field, it is thus possible to determine the ionization probability as a function of the principal quantum number $n_0$ of the initial atomic state, of the microwave field amplitude $F$, of the frequency $\omega$, and of the atom-field interaction time $t$ (for fixed $\ell_0 = 1$ and angular momentum projection $m_0 = 0$).

At first glance, the experiments on rubidium showed qualitatively similar results as those on atomic hydrogen in the regime of dynamical localization: starting from a certain value of the principal quantum number the 'scaled' ionization threshold increases with an increasing quantum number $n_0$. As explained above, keeping the frequency constant and increasing the principal quantum number corresponds to an increase of the scaled frequency in the case of atomic hydrogen. To interpret the experimental results [42, 44, 9] in equal terms as the hydrogen results of [20, 21], heuristic scaling rules were employed which consist in scaling the laboratory frequency with respect to the energy difference between the initial state and the nearest atomic state accessible by an energy gaining dipole transition. However, it has to be noted here that, in contrast to the pure Coulomb potential, there is no justification in terms of the classical equations of motion or of the quantum mechanical Schrödinger equation for the existence of scaling rules for the alkali dynamics. On the contrary, the existence of a non-hydrogenic atomic core introduces a finite length scale that a priori prohibits the use of scaled variables. With the help of the aforementioned semi-empirical scaling rules, qualitative agreement of the experimental results on rubidium atoms with the ionization dynamics of atomic hydrogen in the presence of dynamical localization could be achieved. However, apart from this resemblance to the hydrogen results (i.e. the emergence of dynamical localization for both atomic species), these experiments raised some questions that hitherto have not found a satisfactory answer:

---

(4) Highly excited electrons with a low angular momentum have a finite probability to stay in the region of the atomic core, consisting of the nucleus and the inner electrons. Therefore, these low angular momentum states exhibit a non-hydrogenic phase shift ('quantum defect'), and the unperturbed energy of these 'non-hydrogenic' states is separated from the 'hydrogenic' part – i.e. from the high angular momentum part – of the same $n_0$ manifold. A more detailed discussion of the difference between alkali and hydrogen atoms will be provided in section 2.3.

- The experimental results showed a strongly enhanced ionization probability for rubidium atoms as compared to the hydrogen experiments (i.e. the 'scaled' 10% threshold measured in the rubidium experiments are only 1/10 of those observed for microwave driven atomic hydrogen). What causes alkali atoms to be less stable under periodic driving than atomic hydrogen?
- Given the qualitative agreement of the $\omega$- and $n_0$- dependence of the ionization threshold for atomic hydrogen and alkali species, does some sort of classical scaling prevail in this manifestly quantum mechanical problem?

#### 1.1.2.2 The Virginia experiments

While the results of the rubidium experiments do not quantitatively match with those of the hydrogen experiments, they do at least find qualitatively similar results as experiments on atomic hydrogen, since also in these experiments the signature of dynamical localization was observed, for non-hydrogenic atomic initial states. Thus the Munich experiments suggest an alkali ionization process similar to atomic hydrogen which, however, appears for some unexplained reason more efficient than in the case of atomic hydrogen. The experiments at the University of Virginia, on the other hand, seem to tell a different story. These experiments were mainly performed using relatively low microwave frequencies, and with the atoms initially prepared in hydrogen-like (high angular momentum) states with nearly hydrogenic energies, as well as in low angular momentum, non-hydrogenic states.

The low-frequency experiments on 'hydrogen-like' initial states [46, 50, 48] produced qualitatively and quantitatively similar results as experiments on atomic hydrogen. They found a dependence of the ionization threshold on the principal quantum number $n_0$ following $F_{10\%} \simeq 1/9n_0^4$, in rough agreement with the experiments on atomic hydrogen [52] in the low-frequency regime (far below the regime of dynamical localization), for $\omega_0 < 0.05$. In addition, the same functional dependence of the ionization threshold on $n_0$ is expected in the limit of a static field. Experimental results on non-hydrogenic initial states, however, differed dramatically. In the same frequency regime, and for the same range of principal quantum numbers $n_0$, a dependence $F_{10\%} \simeq 1/3n_0^5$ [53, 47, 48] was found, resulting in alkali thresholds of 1/10 of the hydrogenic ones, qualitatively matching the results of the rubidium experiments (which, however showed a different functional dependence of $F_{10\%}(n_0)$ on $n_0$).

To understand the $1/n_0^5$ scaling law of the ionization threshold – that is valid for low frequencies – the Virginia group proposed the following mechanism: It is known that the atomic energy levels with principal quantum number $n_0$ and $n_0 + 1$ start to cross at field amplitudes equal to $1/3n_0^5$ [54], in a static electric field. While the Hamiltonian of hydrogen atoms exposed to a static electric field is separable [55, 56] due to the high ('dynamical') symmetry of the Coulomb potential and thus the (hydrogen) energy levels of adjacent $n_0$ manifolds really cross at this field amplitude, the Hamiltonian for an atom with a non-Coulombic potential is non-separable. As a consequence, the same manifolds actually undergo an avoided crossing at this field amplitude. The non-hydrogenic (low angular momentum) state itself, which is detached from the hydrogenic part of the manifold, exhibits an avoided crossing with the rest of the manifold at an even lower field, namely at $F_{\rm ac} \simeq 2\delta/3n_0^5$ (where $0 \leq \delta \leq 1$ is the 'quantum defect' of the low angular momentum state) [57]. For a very small external frequency, it is expected that adjacent $n_0$ manifolds of a periodically driven alkali atom perform an anti-crossing at the same field strength ($F \simeq 1/3n_0^5$) as in the static field. Hence this also describes the field at which the electronic population can perform a Landau-Zener transition from the $n_0$ to the $n_0 + 1$ manifold. Once the transition from a non-hydrogenic initial state via the $n_0$ to the $n_0 + 1$ manifold is initiated, a fast 'ladder climbing' in the Rydberg energy progression is started, as the higher lying $n$ manifolds perform avoided crossings already at weaker field amplitudes (due to the inequality $1/3(n_0 + 1)^5 < 1/3n_0^5$). Consequently, the field $1/3n_0^5$ defines the 'rate limiting step' for electronic transport to higher energies, and is expected to define the threshold for the onset of the ionization process, approximately confirmed by the experiments [53, 47, 48].

However, the Virginia experiments with non-hydrogenic alkali initial states were never performed over a broad range of frequencies, nor over a broad range of principal quantum numbers $n_0$, and therefore the range of validity of this low-frequency picture remained unclear (it is obviously only applicable for 'low' frequencies, but the notion of 'low' frequencies remains to be quantified for alkali atoms).

Only in a recent series of new experiments by the same group on microwave driven, hydrogenic initial states of lithium [49], with a frequency comparable to that used in [31], a large range of principal quantum numbers $n_0 = 47, \ldots, 95$ was scanned, and, both, a qualitatively and a quantitatively good match was observed with the hydrogen experiments [31] in the scaled frequency range $\omega_0 = 0.2, \ldots, 1.5$.

#### 1.1.2.3 Theoretical description of microwave driven alkali states – a challenge for more than one decade

While the laboratory experiments are easier realized using alkali instead of hydrogen atoms, the situation is exactly the opposite in a theoretical attempt to describe the dynamics:

Firstly, due to the scattering of the highly excited electron off the multi-particle core consisting of the nucleus and the inner electrons [58, 59], alkali atoms are intrinsically quantum mechanical objects. Therefore, the notion of a classical counterpart is at least questionable and the discussion in terms of some classical dynamics by far less straightforward than in the hydrogen case. Furthermore, already unperturbed alkali atoms are indubitable three-dimensional objects, what is manifest in the loss of the angular momentum degeneracy in the unperturbed atom. Therefore, we cannot expect that calculations on one-dimensional model atoms can reasonably mimic or even reproduce the (three-dimensional) reality – only fully three-dimensional quantum calculations can provide reliable results. In addition, as already mentioned and as we will see in chapter 2.2, due to the finite size of the atomic core the alkali dynamics cannot be scale invariant. Thus, in contrast to atomic hydrogen, it is a priori illegitimate for alkali atoms to perform quantum calculations for moderate excitations, and to re-scale the obtained results to higher, typical experimental values of the principal quantum number. Therefore, a thorough investigation of the observed differences in the ionization of alkali and hydrogen atoms imperatively requires the description of the alkali dynamics for the experimental values of $n_0 \simeq 60$. There, the density of states (which scales roughly as $n_0^5$) is extremely large, and hence the computational demands are much higher than in the range of only moderately excited states.

Apart from the low-frequency approach of the Virginia group and a refined version of the Kepler map that is advertised to describe alkali atoms exposed to a microwave plus a static electric field [60], without, however, any quantitative comparison to the available experimental data, there is – to the best of our knowledge – so far no serious theoretical attempt to describe the ionization of microwave driven alkali atoms.(5) In particular, there is no treatment of the problem where a broad range of principal quantum numbers is probed. Thus, a connection of the two scenarios described by the two experimental groups – dynamical localization as in driven hydrogen atoms, together with a strong enhancement of the ionization probability, and an ionization threshold following $F \simeq 1/3n^5$ for low frequencies – has not been established so far.

In this thesis, we will present the first *exact* treatment of microwave driven hydrogen and alkali atoms, without any adjustable parameter. With our theoretical and numerical apparatus it is possible to perform a (numerical) experiment on alkali atoms as well as on atomic hydrogen, employing precisely the same parameters as in laboratory experiments. In this way, we provide for the missing link between the Munich and the Virginia experiments, and we will also address the puzzle of the experimentally observed discrepancies between the ionization thresholds of non-hydrogenic alkali states and those of atomic hydrogen. In this context, we will elucidate the question whether the classical Kepler frequency (which plays a crucial role for the understanding of microwave driven hydrogen) plays any role in the dynamics of microwave driven alkali atoms, and hence the question whether or under which conditions there exist any scaling rules for the ionization dynamics in the presence of a non-hydrogenic core. Furthermore, this program also bears consequences for the emergence of dynamical localization in alkali atoms, and consequently for the emergence of chaotic dynamics and its suppression in a pure quantum object.

---

(5) Apart from the mentioned approaches recently another study of microwave-driven alkali atoms was performed [61]. These studies, however, concentrated on the transition probabilities between moderately excited Rydberg states exposed to a slowly varying field, and did not take into account ionization – which is appropriate in the parameter regime employed by this group.

## 1.2 Microwave driven Rydberg states as an open quantum system

While research in the field of quantum chaos concentrated on the dynamics of closed, bound systems in the beginning, later on many groups became also interested in the dynamics of open systems. In non-integrable systems, chaotic scattering processes lead to fluctuations of scattering matrix elements and of the cross section, a phenomenon known from nuclear physics as Ericson fluctuations [62, 63]. Such fluctuations have been theoretically observed also in atomic physics, in the cross section of hydrogen atoms exposed to crossed (static) magnetic and electric fields [64]. In systems exhibiting Anderson localization (i.e. in systems where the classically chaotic dynamics is suppressed by quantum effects), in both, the localized and the metallic regime, similar fluctuations were observed in the conductance [27, 65] across the sample. Using a suitable generalization of the concept of conductance for a periodically driven atomic system and a one-dimensional model of the hydrogen atom, similar fluctuations have recently been found for microwave driven hydrogen atoms in the dynamically localized regime [66, 67].

In this thesis, we will not concentrate on this kind of fluctuations, but rather on a related theme, which is subject to ongoing vivid discussion in the literature since at least one decade, namely the temporal decay of the system. For classical systems, it is known that a chaotic phase space structure results in a fast decay of correlation functions. A typical function to measure this decay is the survival probability $P_{\mathrm{surv}}^{\mathrm{class}}(t)$, which measures the probability that a particle's trajectory can be found in a given region of phase space after time $t$. In a completely chaotic system, this function behaves like $P_{\mathrm{surv}}^{\mathrm{class}}(t) \sim \mathrm{e}^{-\alpha t}$ [68], where $\alpha$ is determined by parameters that describe the system's phase space structure, such as the largest Lyapunov exponent. However, typical Hamiltonian systems do exhibit neither completely integrable nor completely chaotic structure, but exhibit a mixed regular-chaotic dynamics. The corresponding phase space consists of regular islands, surrounded by so-called 'KAM' tori, that break up for an increasing strength of the perturbation (i.e. at an enhanced 'chaoticity') of the system, and are surrounded by chaotic regions. The existence of regular islands causes the trajectories to remain trapped inside a given phase space region for longer times, due to the hierarchical phase space structure in the immediate vicinity of the islands [69, 70, 71, 72]. Thus it is found that the survival probability does not decay exponentially, but algebraically $P_{\mathrm{surv}}^{\mathrm{class}}(t) \sim t^{-\alpha}$ [71, 73, 68]. While the general behavior – an algebraic decay of the survival probability – is nowadays common sense, the actual value of the positive decay constant $\alpha$ for classical, mixed regular-chaotic systems is still under active debate [74, 75, 76, 77].

The situation obviously gets even more complicated for a quantum mechanical system: According to the correspondence principle, the quantum system should follow the classical prediction. However, for long times – after the Heisenberg time, which is given by the inverse of the mean level spacing – the system can resolve the quantum nature of the spectrum, and the quantum motion deviates from the classical prediction [78]. Furthermore, pure quantum effects can lead to interference effects, leading to a different decay of the system on longer time scales, as compared to the classical system. And indeed, there are proposals of decay constants $z$ for the decay $P_{\mathrm{surv}}(t) \sim t^{-z}$ of quantum mechanical systems with mixed regular-chaotic classical counterpart, that deviate from the corresponding proposals of decay constants of classical systems [78]. However, many groups studying the decay of quantum systems found different exponents [79, 80, 81, 82] in various systems, and the proposals of decay constants range from $z = 2/3$ [83], to $z = 1$ [78], and $z = 3/2$ [82].

Most of the systems that have been studied in this context are model systems, like billiard systems [79], driven square potentials [84], or the kicked rotator [78, 85] without a clear, straightforward experimental implementation. Furthermore, the fact that the system is a decaying system is often modeled by the introduction of absorbing boundary conditions [78, 85, 81], instead of an exact account of the continuum-coupling.

In contrast to such toy models, microwave driven Rydberg atoms are also studied experimentally, and an algebraic decay of the survival probability was already experimentally measured [86] and found in more (one-dimensional) [87] or less (three-dimensional, amended by classical scaling rules) [86] simplified calculations on atomic hydrogen. With our work on alkali Rydberg atoms exposed to a microwave field, we develop a powerful tool to investigate the decay of a time-dependent, open quantum system: As mentioned in the previous section, we employ fully three-dimensional simulations, and, as we will see in section 2.1.3, our framework really presents an open system with decaying states, where the interaction with the continuum (leading to the decay) is described exactly. Furthermore, we are dealing with a pure quantum mechanical system which exhibits effects like dynamical localization – as we will see in the progress of this thesis. As a result, our work enables us to study the decay of a typical quantum system while our approach is designed to simulate the parameters used in laboratory experiments exactly. Therefore, our results can be immediately verified in state-of-the-art experiments [49, 9].

## 1.3 Structure of the thesis

The present thesis is separated in two parts: **Part I** describes the 'set-up' of our numerical experiment on microwave driven Rydberg states. Here we describe the theoretical/numerical counterpart of the laboratory set-up, described in the above introductory section.

In **chapter 2**, we provide the theoretical tools to describe our system. Due to time-periodicity, we employ the Floquet theorem and, as our system is a decaying system, we use the method of complex dilation. The non-hydrogenic core potential will be taken into account with a combination of quantum defect theory and R-matrix theory, and the resulting Hamiltonian will be represented in an appropriate basis set.

In **chapter 3**, we show how we are handling the generalized eigenvalue problem obtained in chapter 2. We briefly explain the diagonalization routine we are using, and its implementation on a parallel computer. We further give account of the numerical parameters we employ to achieve converged results.

In **part II**, the previously explained apparatus will be applied to microwave driven lithium and rubidium atoms, as well as to atomic hydrogen.

**Chapter 4** presents first results, the ionization probability of driven lithium atoms. We show typical ionization curves, similar to those observed in laboratory experiments and in simplified simulations on microwave driven atomic hydrogen.

**Chapter 5** concentrates on the difference between the ionization process of alkali and hydrogen atoms. For this purpose we employ exactly the same laboratory parameters (frequency, field amplitude, interaction time, principal quantum number of the atomic initial state) as used in experiments on atomic hydrogen, with the only difference of a finite quantum defect of low-angular-momentum states. We will explain the experimentally observed differences between the alkali and the hydrogen thresholds, and identify regimes of hydrogenic and non-hydrogenic ionization behavior for alkali atoms. In this way we can establish a connection between the experimental observations of the Virginia and the Munich group.

**Chapter 6** is devoted to the time dependence of the ionization dynamics. We will study the survival probability of microwave driven Rydberg atoms under different conditions, and find an algebraic decay of the system. The decay exponent of our system, however, is *not* a fixed, universal constant.

In **chapter 7** we shortly summarize our results, and give an outlook on future perspectives.

# Part I

# The Set-Up

# Chapter 2

# Description of the system

## 2.1 Atomic Rydberg states in a microwave field

### 2.1.1 Atoms in electromagnetic fields

In this thesis, we are interested in Rydberg atoms with principal quantum numbers of the valence electron between $n_0 \simeq 30$ and $80$, exposed to a microwave field. As we are dealing with singly excited states, correlation effects between the electrons, that are of importance, e.g., in the dynamics of doubly excited helium atoms [88, 89], can be neglected, and the atomic dynamics is determined by a spherically symmetric, effective one-electron potential $V_{\rm atom}$. Furthermore, the fine structure splitting is negligible as compared to the mean level spacing.

For atomic hydrogen, the atomic potential $V_{\rm atom}$ is given by the attractive Coulomb potential $-1/r$, and for alkali atoms we will specify $V_{\rm atom}$ in section 2.3. Hence, the non-relativistic Hamilton operator of the atom interacting with the external field reads, in atomic units ($m_{\rm e} = |q_{\rm e}| = \hbar = 4\pi\varepsilon_0 = 1$):(1)

$$H = \frac{1}{2}(\mathbf{p} - \mathbf{A}(\mathbf{r}, t))^2 + V_{\rm atom}(r) + \Phi(\mathrm{r}, t). \qquad (2.1)$$

Here $\mathbf{A}(\mathbf{r}, t)$ and $\Phi(\mathrm{r}, t)$ denote the vector and the scalar potential of the external electromagnetic field, respectively. Since the frequency $\omega$ of the microwave fields we are interested in is typically of the order of $10^{-6}$ a.u., its wave-length $\lambda = 2\pi \mathrm{c}/\omega \simeq 2\pi \cdot 137/\omega$ is much larger than the approximate radius of the electron orbit (which is of the order of $n^2$ a.u.). Therefore we can employ the dipole approximation [56], which leads to the following Hamiltonian, written in the length and in the velocity gauge, respectively:

$$H = \frac{\mathbf{p}^2}{2} + V_{\rm atom}(r) + \mathbf{r} \cdot \mathbf{F} \cdot \cos(\omega t) \ \ (\text{length gauge}), \qquad (2.2)$$

$$H = \frac{\mathbf{p}^2}{2} + V_{\rm atom}\,(r) - \frac{\mathbf{F}}{\omega} \cdot \mathbf{p} \sin(\omega t) \ \ (\text{velocity gauge}). \qquad (2.3)$$

---

(1) Throughout this thesis we will use atomic units. Only the microwave frequency will mostly be specified in Hz (with $1$ a.u. $= 4.1341 \cdot 10^{16}$ Hz [90]) to ease the comparison to experimental data.

In both representations, $\mathbf{F}$ expresses the amplitude and orientation of the external field. The transition from the Hamiltonian in length gauge (2.2) to the one in velocity gauge (2.3) is achieved via a gauge transformation ('Göppert-Mayer-transformation' [91]). Of course, both Hamiltonians (2.2) and (2.3) describe the same physical situation. However, in a numerical treatment, depending on the particular physical situation at hand, the appropriate representation of the Hamiltonian can lead to a faster convergence of the results [92, 93]. For this reason we will employ (2.3) to describe microwave driven atomic hydrogen. In order to specify the atomic potential $V_{\mathrm{atom}}$ of alkali atoms, however, we will explicitly make use of configuration space – therefore, in this case, the length gauge is the appropriate choice. The following discussion will thus start from the representation (2.2) of the Hamilton operator.

### 2.1.2 Floquet theorem

As the external field in (2.2) and (2.3) is periodic in time, with period $T = 2\pi/\omega$, we can use the Floquet theorem [94] to solve the time-dependent Schrödinger equation

$$\mathrm{i}\partial_t|\Phi(\mathbf{r},t)\rangle = H|\Phi(\mathbf{r},t)\rangle, \text{ with } H(t+T) = H(t). \tag{2.4}$$

Following this theorem, each solution of (2.4) can be written as a product of a phase factor $\exp(-\mathrm{i}\varepsilon_j t)$ and of a time-periodic function $|\Psi(\mathbf{r},t)\rangle$ [95, 96]. Thus, any solution of (2.4) is given by a linear combination

$$|\Phi(\mathbf{r},t)\rangle = \sum_j c_j e^{-\mathrm{i}\varepsilon_j t}|\Psi_{\varepsilon_j}(\mathbf{r},t)\rangle, \tag{2.5}$$

$$\text{with } |\Psi_{\varepsilon_j}(\mathbf{r},t)\rangle = |\Psi_{\varepsilon_j}(\mathbf{r},t+T)\rangle. \tag{2.6}$$

The 'Floquet eigenstates' $|\Psi_{\varepsilon_j}(\mathbf{r},t)\rangle$ and the quasi-energies $\varepsilon_j$ [96] are given by the eigenfunctions and the eigenvalues of the Floquet Hamilton operator $\mathcal{H} = H - \mathrm{i}\partial_t$. This operator acts on the extended Hilbert space of square integrable, time-periodic functions $\mathcal{L}^2(\mathbb{R}^3) \otimes \mathcal{L}^2(T)$. The Floquet eigenvalue problem has the structure of the stationary Schrödinger equation:

$$\mathcal{H}|\Psi_{\varepsilon_j}(\mathbf{r},t)\rangle = \varepsilon_j|\Psi_{\varepsilon_j}(\mathbf{r},t)\rangle, \ j \in \mathbb{Z}. \tag{2.7}$$

Each solution of (2.7), i.e. each Floquet eigenstate $|\Psi_{\varepsilon_j}(\mathbf{r},t)\rangle$, defines a whole class of solutions $\exp(\mathrm{i}k\omega t)|\Psi_{\varepsilon_j}(\mathbf{r},t)\rangle$ (with $k \in \mathbb{Z}$) with corresponding quasi-energies $\varepsilon_j + k\omega$. Each member of this class represents the same physical state, since the function

$$e^{-\mathrm{i}(\varepsilon_j+k\omega)t}|\Psi_{\varepsilon_j+k\omega}(\mathbf{r},t)\rangle = e^{-\mathrm{i}(\varepsilon_j+k\omega)t}e^{\mathrm{i}k\omega t}|\Psi_{\varepsilon_j}(\mathbf{r},t)\rangle = e^{-\mathrm{i}\varepsilon_j t}|\Psi_{\varepsilon_j}(\mathbf{r},t)\rangle \tag{2.8}$$

is independent of $k$. Hence, the spectrum of $\mathcal{H}$ is periodic with period $\omega$, and we can restrict ourselves to a single Floquet zone of width $\omega$ to find the solutions of (2.7).(2)

---

(2) The discussion is in analogy to solid state physics, where the potential is *spatially* periodic [97]. There, the Bloch waves play the role of the Floquet states, and the well known Brillouin zone cor-

Since the whole spectrum is folded into a single Floquet zone of width $\omega$, the choice of the Floquet zone is – in principle – arbitrary.

With the help of the Floquet Hamiltonian and employing the length gauge (2.2), the time-dependent Schrödinger equation for the microwave driven Rydberg atom turns into

$$\left(\frac{\mathbf{p}^2}{2} + V_{\text{atom}}(r) + \frac{\mathbf{F}\cdot\mathbf{r}}{2}\left(e^{\mathrm{i}\omega t} + e^{-\mathrm{i}\omega t}\right) - \mathrm{i}\partial_t\right)|\Psi_{\varepsilon_j}(\mathbf{r},t)\rangle = \varepsilon_j|\Psi_{\varepsilon_j}(\mathbf{r},t)\rangle,\ j\in\mathbb{Z}. \tag{2.9}$$

Due to the time-periodicity of the Floquet states $|\Psi_{\varepsilon_j}(\mathbf{r},t)\rangle$, it is convenient to expand them in a Fourier series:

$$|\Psi_{\varepsilon_j}(\mathbf{r},t)\rangle = \sum_k e^{-\mathrm{i}k\omega t}|\Psi^k_{\varepsilon_j}\rangle. \tag{2.10}$$

Inserting the Fourier expansion (2.10) in the Floquet eigenvalue problem (2.9) leads to the following set of coupled, time-independent differential equations:

$$\left(\frac{\mathbf{p}^2}{2} + V_{\text{atom}}(r)\right)|\Psi^k_{\varepsilon_j}\rangle + \frac{\mathbf{F}\cdot\mathbf{r}}{2}\left(|\Psi^{k+1}_{\varepsilon_j}\rangle + |\Psi^{k-1}_{\varepsilon_j}\rangle\right) = (\varepsilon_j + k\omega)\,|\Psi^k_{\varepsilon_j}\rangle,\ k\in\mathbb{Z}. \tag{2.11}$$

The price for the transformation of the time-dependent eigenvalue problem into a time-independent set of differential equations has to be paid by keeping track of the additional quantum number $k$, which counts the number of photons exchanged between the atom and the field. The notion of an exchange of photons can be used in this context, although we employed a classical field in (2.2) and (2.3). In this 'semiclassical description' the atom-field interaction is described by $\mathbf{r}\cdot\mathbf{F}\cdot\cos(\omega t)$, instead of $\mathbf{g}(\mathbf{a}^\dagger + \mathbf{a})$ (with $\mathbf{a}^\dagger$ and $\mathbf{a}$ the creation and the annihilation operator, respectively, of the photon field) in a fully quantized treatment of an atom interacting with a single mode coherent state of the photon field. In the fully quantized version, the expectation value of $\mathbf{a}^\dagger\mathbf{a}$ expresses the average number $\overline{N}$ of photons in the field, i.e. the field intensity. If $\overline{N}$ is large, the difference between $\sqrt{\overline{N}}$ and $\sqrt{\overline{N}+1}$ is small, and it can be shown [95, 98] that the Hamilton operator in the fully quantized, dressed state approach [91] is equivalent to the Floquet Hamiltonian $\mathcal{H}$, provided the quantum number $k$ is identified with $N-\overline{N}$ (where $N$ is the occupation number of the mode), and $F$ is identified with $\sqrt{\overline{N}}$, independently of $k$.

As is generally known, the spectrum of unperturbed atoms not only consists of a discrete, but also of a continuous part. An external oscillating field induces a coupling of all atomic states dressed with $k$ photons to states dressed with $k-1$

---

responds to the Floquet zone. However - due to the explicit time dependence - the Floquet problem for a three-dimensional, atom with one active electron, leads to a $3+1$ dimensional problem – the extra dimension given by the time axis – whereas the spatially periodic problem in general leads to a time-independent eigenvalue problem, without increase of the dimensionality.

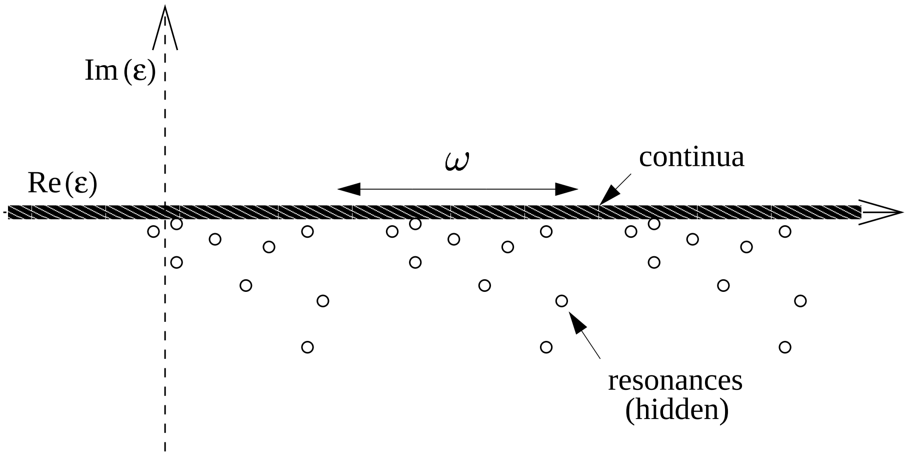

Figure 2.1: Poles of the resolvent operator of the Floquet Hamiltonian of a periodically driven atom. The resonances that are embedded in the continuum without the analytic continuation, can be uncovered only by analytic continuation of the resolvent operator.

and $k+1$ photons, as apparent from (2.11). Consequently, all bound states are coupled to the continuum, and thus each bound state can decay via a multi-photon transition. Therefore, the spectrum of (2.9) consists of resonances with finite lifetimes embedded in the continuum. An elegant way to extract the quasi-energies $\varepsilon_j$ and the corresponding life times is provided by …

### 2.1.3 Complex dilation

Since all Floquet eigenstates of the driven atom are decaying states [99, 100], all these states are represented by outgoing waves after a sufficiently long atom-field interaction time. The situation can be described as a half scattering process. Consequently, the eigenstates can be identified with the poles of the resolvent operator $G(E) = (E-H)^{-1}$ of the Hamilton operator $H$ [101]. The spectrum of the analytic continuation of $G(E)$ in the complex plane is sketched in figure 2.1, it consists of:

- Poles in the negative complex plane (more accurately, on the second Riemann sheet). They correspond to the scattering resonances at complex energies $\varepsilon = E - \mathrm{i}\Gamma/2,\ \Gamma > 0$.

- The eigenvalues of the continuum states which are situated on the real energy axis.

- Finally, if there are any bound states (due to accidental destructive interference of continuum transition amplitudes), they correspond to discrete eigenvalues on the real axis, embedded in the continuum.

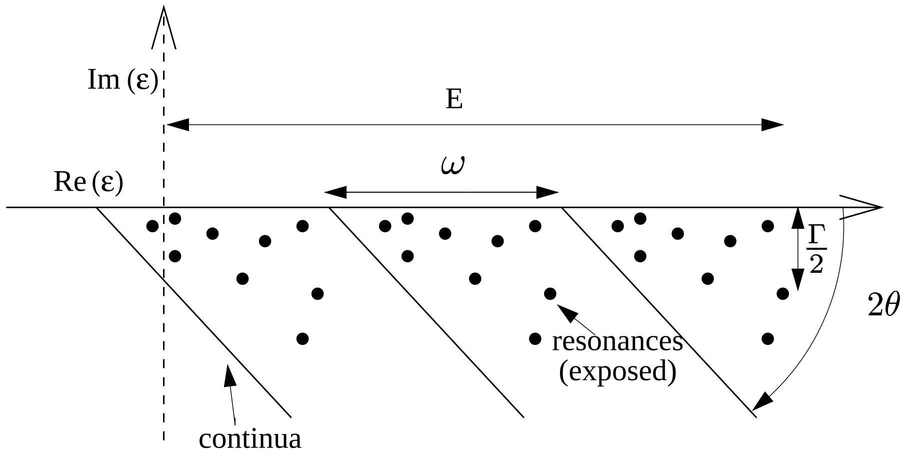

Figure 2.2: Spectrum of the complex dilated Floquet Hamiltonian. For sufficiently large rotation angle $\Theta$ the resonances $\varepsilon = E - \mathrm{i}\Gamma/2$ are exposed and independent of $\Theta$.

To separate the quasi-energies $\varepsilon_j$ with the corresponding life times (given by the inverse of the ionization rates $\Gamma_j$) of the resonances from the continuum, we do not explicitly use the resolvent operator in the following, but the method of complex dilation. This method is based on theorems of functional and operator analysis [102], its applicability for the Coulomb potential is demonstrated in [100]. The method consists in the complexification of the position and momentum operators, according to:

$$\begin{gathered} \mathbf{r} \to \mathbf{r}\mathrm{e}^{\mathrm{i}\Theta},\ \mathbf{p} \to \mathbf{p}\mathrm{e}^{-\mathrm{i}\Theta}, \\ \text{with: } 0 < \Theta < \frac{\pi}{4}. \end{gathered} \tag{2.12}$$

Note that the dilation (2.12) of the position and momentum operators leaves the value of the commutator invariant, i.e $[\mathbf{r}, \mathbf{p}] = [\mathbf{r}\mathrm{e}^{\mathrm{i}\Theta}, \mathbf{p}\mathrm{e}^{-\mathrm{i}\Theta}]$. The transformation (2.12) is accomplished by the non-unitary complex dilation operator

$$R(\Theta) = \exp\left(-\frac{\Theta}{2}\left(\mathbf{r}\cdot\mathbf{p} + \mathbf{p}\cdot\mathbf{r}\right)\right). \tag{2.13}$$

The spectrum of the dilated Floquet Hamiltonian is sketched in figure 2.2, it consists of the following components:

a) The continuum part of the spectrum. The continuum states are situated on half lines rotated by an angle $-2\Theta$ from the real axis, branching at the multiphoton ionization threshold energies $K\omega$ ($K$ an integer).

b) Complex eigenvalues $\varepsilon_j = E_j - \mathrm{i}\Gamma_j/2$ with positive ionization rates $\Gamma_j$. These resonance poles of the analytic continuation of the resolvent operator are $\Theta$-independent, provided the rotation angle is large enough to separate them from the continuum states (see a) above), i.e. for $\Theta > -\arg(\varepsilon_j - \mathrm{i}\Gamma/2)/2$. The corresponding wave-functions are square integrable functions [103] (in contrast to the eigenfunctions of the unrotated Hamiltonian, which are outgoing waves [104], as mentioned above).

c) Apart from exceptional values of $F$ and $\omega$, there are no real eigenvalues, as under periodic driving all bound states of an atom turn into resonances with finite ionization rates [99], and thus all eigenvalues exhibit non-vanishing imaginary parts.

If the complex dilated Hamiltonian

$$\mathcal{H}_\Theta := R(\Theta)\mathcal{H}R(-\Theta) \tag{2.14}$$

is represented in a real basis, such as the Sturmian basis set we will employ in section 2.4, the resulting matrix is a complex symmetric instead of a hermitian matrix. Hence, the left eigenvectors of the complex dilated Hamiltonian are the transpose and not the hermitian conjugate of the right eigenvectors. To express this, we will use the notation $\langle\overline{\Psi^k_{\varepsilon_j,\Theta}}|$ for the left eigenvectors corresponding to $|\Psi^k_{\varepsilon_j,\Theta}\rangle$. However, since the time-dependent part of a solution of the Floquet eigenvalue problem is unchanged under the transformation (2.13), only the spatial part of the eigenvectors has to be transposed, while the time-dependent part also has to be complex conjugated. The left eigenfunctions corresponding to the eigenvalues $\varepsilon_j$ of the complex dilated Hamiltonian are thus given by

$$\langle\overline{\Psi_{\varepsilon_j,\Theta}(\mathbf{r},t)}|\mathcal{H}_\Theta = \varepsilon_j\langle\overline{\Psi_{\varepsilon_j,\Theta}(\mathbf{r},t)}|,\quad \langle\overline{\Psi_{\varepsilon_j,\Theta}(\mathbf{r},t)}| = \sum_k e^{\mathrm{i}k\omega t}\langle\overline{\psi^k_{\varepsilon_j,\Theta}}|. \tag{2.15}$$

For the spatial part, we consequently have the following scalar product:

$$\langle\overline{\psi^k_{\varepsilon_j,\Theta}}|\phi^k_{\varepsilon_j,\Theta}\rangle = \int d^3r\,\psi^k_{\varepsilon_j,\Theta}(\mathbf{r})\phi^k_{\varepsilon_j,\Theta}(\mathbf{r}). \tag{2.16}$$

In the following chapters we will be interested in the ionization probability of a given initial state. Therefore, we will implicitly make use of the time evolution operator $U(t_2,t_1)$, which propagates the wave-function from $t_1$ to $t_2$. A representation of this operator for a complex dilated Floquet Hamiltonian was derived in [33, 34]. For the sake of completeness, we quote the result:

$$U(t_2,t_1) = \sum_{j,k_1,k_2} e^{-\mathrm{i}\varepsilon_j(t_2-t_1)}e^{\mathrm{i}k_1\omega t_1}e^{-\mathrm{i}k_2\omega t_2}R(-\Theta)|\psi^{k_2}_{\varepsilon_j,\Theta}\rangle\langle\overline{\psi^{k_1}_{\varepsilon_j,\Theta}}|R(\Theta). \tag{2.17}$$

## 2.2 Atomic hydrogen

So far, our discussion was not specific for any particular atomic species – we simply assumed a single electron Rydberg state, bound by an effective one-electron potential $V_{\text{atom}}$. For atomic hydrogen, this potential is given by the attractive Coulomb potential $-1/r$. In this case, all operators in the Hamiltonian (2.2) (which also describes the classical Hamilton function, provided the operators $\mathbf{r}$ and $\mathbf{p}$ are replaced by the position and momentum variables) are power functions of the position and momentum operator, more generally, they are homogeneous functions in $\mathbf{r}$ and $\mathbf{p}$ [28]. This suggests to take advantage of the scale invariance of the *classical* dynamics of the driven Kepler problem [28, 29] in our description of the quantum excitation and ionization process. The classical equations of motion are invariant under the following transformations,

$$\begin{aligned} H_0 &= \lambda H, & t_0 &= \lambda^{-\frac{3}{2}} t \\ r_0 &= \lambda^{-1} r, & p_0 &= \lambda^{\frac{1}{2}} p \\ \mathbf{F}_0 &= \lambda^2 \mathbf{F}, & \omega_0 &= \lambda^{\frac{3}{2}} \omega, \end{aligned} \tag{2.18}$$

with a real, positive scaling parameter $\lambda$. An appropriate choice is $\lambda = n_0^2$ (with $n_0$ the principal action, which corresponds to the principal quantum number in quantum mechanics), since in this way the scaled, unperturbed energy can be kept constant ($E_0 = n_0^2 E = -1/2$). We already mentioned in the introduction that it is thus possible to keep the (classical) phase space structure fixed while changing the actual energy of the atomic initial state, i.e. the energy $-1/n_0^2$ of an electron moving on the $n_0$-th Bohr orbit. As easily deduced from (2.18), the relevant scaled quantities describing the external field are

$$\omega_0 = \omega \cdot n_0^3, \tag{2.19}$$

and

$$\mathbf{F}_0 = \mathbf{F} \cdot n_0^4. \tag{2.20}$$

$\omega_0$ and $\mathbf{F}_0$ measure frequency and field amplitude in units of the Kepler frequency of the classical electron and of the Coulomb force between electron and nucleus on the $n_0$-th Bohr orbit, as already noted in section 1.1.1. Furthermore, due to Bohr's correspondence principle (applicable for large $n_0$), the Kepler frequency also approximates the local energy spacing in the Rydberg progression of the quantum spectrum. Thus measuring $\omega$ in units of the Kepler frequency is tantamount to scaling $\omega$ with respect to the difference between the quantum mechanical (unperturbed) hydrogenic energy levels $E_n$ and $E_{n+1}$, and provides a direct link between the characteristic time scale of the driving force and the local energy splitting of the unperturbed quantum spectrum. Note, however, that the local energy splitting lends itself as a natural measure of the driving frequency, even in the absence of a classical analogue of the atomic dynamics.

Applying the scaling rules (2.18) to the quantum mechanical operators also affects the commutator of the scaled position operator $r_0$ with the scaled momentum operator $p_0$, according to

$$[r_0, p_0] = \mathrm{i}\lambda^{-\frac{1}{2}}\hbar = \mathrm{i}\frac{1}{n_0}\hbar. \tag{2.21}$$

Thus, the use of scaled variables seems to introduce an effective value $\hbar/n_0$ of Planck's constant. This highlights the fact that the so-called 'semiclassical limit $\hbar \rightarrow 0$' [105] is reached for highly excited states. (Of course, also in this case the actual Planck constant is constant. However, as $n_0$ is increased, $\hbar$ is small compared to the typical actions which characterize the dynamics of the system).

With this caveat in mind, the above scaling rules remain very instructive for the interpretation of the actual quantum dynamics. The use of scaled rather than laboratory parameters facilitates the understanding of the quantum dynamics of driven atomic hydrogen considerably, and allows to identify highly relevant and robust signatures of the underlying non-linear classical dynamics in the quantum spectrum [106, 107, 108], which cannot be fully appreciated on the basis of a purely quantum mechanical description.

Furthermore, the approximate validity of classical scaling for the quantum dynamics has an important practical consequence: Since the number of photons that separate the atomic initial state from the continuum scales as $1/2n_0^2\omega = n_0/2\omega_0$, and the density of states scales as $n_0^5$, fully three-dimensional quantum calculations using typical experimental parameters ($\omega_0 = 1$ for $n_0 \simeq 60$) were not feasible up to now. Therefore, in the only three-dimensional quantum calculations on microwave driven atomic hydrogen [32, 34, 86] reported up to now, the scaling rules (2.20) were employed to map the results of exact calculations for $n_0 \simeq 23$ on experimentally used parameters. These simulations led to a qualitatively satisfactory comparison with the experimental results, amended by a systematic difference between the numerical ($n_0 = 23$) and the experimental ($n_0 \simeq 60$) ionization thresholds of up to a factor two. This latter discrepancy illustrates that the classical scaling rules hold only approximately in the real quantum system, as a consequence of (2.21) [34] (see also the footnote on page 5). Only now, as we shall illustrate further down in this thesis, can we treat the fully three-dimensional problem with $n_0 \simeq 60$, without additional reference to classical scaling rules.

For alkali atoms, on the other hand, the situation changes significantly. The difference between highly excited alkali atoms and Rydberg states of atomic hydrogen consists in the presence of an atomic core, made of the nucleus and a multi-electron cloud which screens the nuclear charge. In contrast to hydrogen, where the nucleus is given by a single proton, with a radius of the order of $10^{-5}$ $\mathrm{a.u.}$ [109], the atomic core of alkali atoms has a size of some atomic units. Since the use of scaled parameters also includes the scaling of radii, the existence of such a finite-size radius – which obviously does not scale as suggested by (2.18) – makes the use of the scaling rules introduced above a priori *impossible*.

## 2.3 Alkali atoms

### 2.3.1 Quantum defect theory

The effect of the atomic core on the dynamics of the highly excited outer electron of an alkali atom is twofold. Firstly, it causes a scattering of the wave-function of the outer electron, which consequently accumulates a phase shift relative to the hydrogenic wave-function. Secondly, for large distances $r > r_{\mathrm{core}}$ (where $r_{\mathrm{core}}$ defines the size of the atomic core), the inner electrons screen the nuclear charge, and the Rydberg electron moves in an attractive Coulomb potential with charge $+1$, as in the case of atomic hydrogen. Thus, the radial part of the bound electronic wave-function $F_{\ell,E_{\mathrm{alk}}}$ has to fulfill the following equation:

$$\left(-\frac{1}{2}\left(\frac{\mathrm{d}^2}{\mathrm{d}r^2}-\frac{\ell\left(\ell+1\right)}{r^2}\right)+V_{\mathrm{atom}}\left(r\right)-E_{\mathrm{alk}}\right)F_{\ell,E_{\mathrm{alk}}}(r)=0, \tag{2.22}$$
$$\text{with } E_{\mathrm{alk}}<0, \text{ and } V_{\mathrm{atom}}=-1/r, \text{ for } r>r_{\mathrm{core}}>0.$$

Equation (2.22) is a second order differential equation and therefore has two linearly independent solutions, the 'regular' $f(E,\ell,r)$ and the 'irregular' $g(E,\ell,r)$ Coulomb function [110, 111, 112]. The notion regular and irregular indicates the behavior of these functions at the origin:

$$f(E,\ell,r)\rightarrow r^{\ell+1}, \tag{2.23}$$
$$g(E,\ell,r)\rightarrow r^{-\ell}. \tag{2.24}$$

Because of the boundary condition of a vanishing wave-function at the origin, the hydrogenic wave-function is given by (2.23). For alkali atoms on the other hand, the origin is excluded from the domain of equation (2.22), and hence also an irregular contribution to the wave-function is possible. Thus, the hydrogenic boundary condition at $r=0$ has to be replaced by the requirement that the wave-function acquires a phase shift $\tau$ with respect to the hydrogenic function (for $r>r_{\mathrm{core}}$). A solution of (2.22) is given by [110, 111, 112]:

$$F_{\ell,E_{\mathrm{alk}}}\left(r\right)=\mathcal{N}\left(E_{\mathrm{alk}}\right)\left(f\left(E_{\mathrm{alk}},\ell,r\right)\cos\left(\tau\right)-g\left(E_{\mathrm{alk}},\ell,r\right)\sin\left(\tau\right)\right), \tag{2.25}$$

where $\mathcal{N}(E_{\mathrm{alk}})$ is a suitably chosen, energy-dependent normalization constant. As we consider bound states here, the function $F_{\ell,E_{\mathrm{alk}}}(r)$ has to vanish for $r\rightarrow\infty$. Therefore, we need to know the behavior of the Coulomb functions for large $r$. Asymptotically they tend to:

$$f(E,\ell,r)\rightarrow \quad u(m,\ell,r)\sin(\pi m)-\nu(m,\ell,r)e^{\mathrm{i}\pi m}, \tag{2.26}$$
$$g(E,\ell,r)\rightarrow \quad -u(m,\ell,r)\cos(\pi m)+\nu(m,\ell,r)e^{\mathrm{i}\pi m+\frac{1}{2}}, \tag{2.27}$$
$$\text{with } m=\sqrt{-\frac{1}{2E}} \tag{2.28}$$

where $u(m,\ell,r)$ and $\nu(m,\ell,r)$ are exponentially increasing and exponentially decreasing functions, respectively [110, 111, 112]. To obtain an asymptotically decreasing function, the prefactors of $u(m,\ell,r)$ in (2.25) have to vanish. This leads to the following condition:

$$\sin(\tau+\pi m)=\sin(\tau+\pi\sqrt{-\frac{1}{2E_{\mathrm{alk}}}})=0. \tag{2.29}$$

Ergo, the energy $E_{\text{alk}}$ of unperturbed, bound alkali states has to fulfill the equation:

$$E_{\text{alk}} = -\frac{1}{2n_{\text{eff}}^2} = -\frac{1}{2(n-\delta_\ell)^2},\ n \in \mathbb{N}, \tag{2.30}$$

where $\delta_\ell$ is connected with the phase shift of the alkali wave-function by $\tau = \delta_\ell \cdot \pi$, and denotes the angular momentum dependent quantum defect. To emphasize the correspondence with the hydrogen atom, the non-integer quantity $n_{\text{eff}}$ is often called the 'effective principal quantum number'.

The quantum defects only weakly depend on the energy, and can be obtained from experimental, high-resolution spectroscopic data [113, 114]. As we see in table 2.3.1, they take non-vanishing values only for small angular momenta ($\ell < 3$).

| | $\delta_{\ell=0}$ | $\delta_{\ell=1}$ | $\delta_{\ell=2}$ | $\delta_{\ell=3}$ | $\delta_{\ell>3}$ |
|---|---|---|---|---|---|
| Li | 0.399468 | 0.047263 | 0.002129 | $-7.7 \cdot 10^{-5}$ | 0.0 |
| Na | 1.347964 | 0.855 | 0.015543 | 0.001453 | 0.0 |
| K | 2.180199 | 1.71 | 0.277 | 0.010098 | 0.0 |
| Rb | 3.1309 | 2.6515 | 1.3472 | 0.016312 | 0.0 |

Table 2.3.1: Quantum defects of lithium, sodium, potassium, and rubidium [113]. For sodium, potassium and rubidium the quantum defects of the $\ell = 1$ states (and of the $\ell = 2$ states in the case of K) are the average values of the quantum defects of states with total (spin and orbital) angular momenta $1/2$ and $3/2$.

Finally, for bound states, the properly normalized solution of (2.22) is given by:

$$F_{\ell,E_{\text{alk}}}(r) = \cos(\pi\delta_\ell) s_\ell(E_{\text{alk}}, r) + \sin(\pi\delta_\ell) c_\ell(E_{\text{alk}}, r). \tag{2.31}$$

Here, the functions $s_\ell(E_{\text{alk}}, r)$ and $c_\ell(E_{\text{alk}}, r)$ are the energy-normalized regular and irregular Coulomb functions $f(E, \ell, r)$ and $g(E, \ell, r)$, respectively [115, 110].

As the external driving field induces a coupling of all bound states to the continuum (see section 2.1.3), we also need to know the representation of the continuum states. A relation between the quantum defects and the asymptotic phase shift of the alkali continuum wave-function relative to the hydrogenic wave-function is given by Seaton's theorem [115, 110]:

$$\lim_{n\to\infty} \delta_\ell = \frac{1}{\pi} \lim_{E\to 0^+} \delta(E). \tag{2.32}$$

For $E > 0$, the solution of (2.22) can be written as:

$$F(E, r) \simeq \frac{1}{\sqrt{2\pi E}} (s(\xi)\cos(\delta(E)) + c(\xi)\sin(\delta(E))), \tag{2.33}$$

$$\xi = \sqrt{2E} - \frac{\ell}{2}\ln(2\sqrt{2E}r) + \arg\Gamma(\ell + 1 - \frac{\mathrm{i}}{\sqrt{2E}}),$$

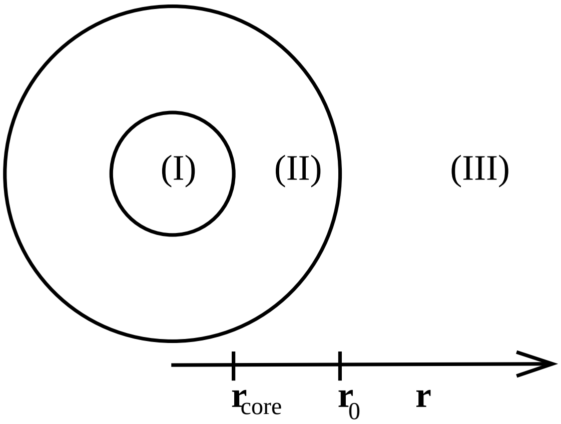

Figure 2.3: For alkali atoms exposed to an external field, configuration space can be divided in three regions: the inner region (I), the intermediate region (II), and the external region (III). In all three regions the dynamics has to be described differently.

with $\Gamma$ the well-known Gamma function [116]. The regular and irregular Coulomb functions both for $E < 0$ and $E > 0$ can be expressed in terms of Whittaker functions and expanded in power series, as described in [117, 110, 118, 119, 115]. The continuation of the Coulomb functions, analytic in energy, for complex radii and energies was developed in [120, 121, 122].

### 2.3.2 Alkali atoms in an external field

As already pointed out, we cannot specify an effective one-electron potential for alkali atoms valid for all $r \in \mathbb{R}^+$, without the use of free, adjustable parameters. However, knowing an expression for the wave-function of the valence electron outside the atomic core, we can treat the interaction of alkali Rydberg states with an external field without the use of free parameters. The only parameters that will be used are the quantum defects introduced above – obtained by highly accurate spectroscopic experiments.

For our approach we split configuration space in three regions (see figure 2.3) distinguished by the relative relevance of the external field and the multi-particle atomic fields:

(I) Inner region, $0 < r < r_{\rm core}$: Inside the atomic core the dynamics is dominated by complicated multi-particle effects. Here, it is impossible to describe the dynamics in terms of a one-particle picture.

(II) Intermediate region $r_{\rm core} < r < r_0$: Outside the atomic core, but not far away from the origin, the external field is small compared with the field between atomic core and electron. In this region, the wave-function of the outer electron is given by (2.31) for bound states and by (2.33) for continuum states, respectively.

(III) External region, $r \geq r_0$: For large distances $r$, the electron is subject to the potential $-1/r + V_{\text{ext}}$, i.e. the radial part of the wave-function has to obey the following differential equation:

$$\left(-\frac{1}{2}\frac{\mathrm{d}^2}{\mathrm{d}r^2} + \frac{\ell\,(\ell+1)}{2r^2} - \frac{1}{r} + V_{\text{ext}}\,(r)\right) F_{\ell,E}\,(r) = EF_{\ell,E}(r),\ r \geq r_0. \tag{2.34}$$

At $r = r_0$, the solution of (2.34) has to be matched smoothly to the wave-function in region (II). This determines the phase shift of $F_{\ell,E}(r)$ relative to the hydrogenic solution of (2.34).

To find the eigenfunctions of the problem, we thus have to find a solution of (2.34). However, in the restricted range $r \geq r_0$ of this equation, the operator $\mathrm{d}^2/\mathrm{d}r^2$ is no more hermitian.(3) To enforce the hermiticity of the second derivative also in the reduced range, we have to add a surface term [123]

$$\mathcal{L} = -\frac{1}{2}\delta(r - r_0)(\frac{\partial}{\partial r} - C) \tag{2.35}$$

to the left hand side of (2.34), where $\delta(r)$ denotes the Dirac delta function. The constant $C$ in $\mathcal{L}$ – which is in principle arbitrary – helps to match the solution in region (III) to that in (II) [124]. Therefore, we define $C$ as the logarithmic derivative of the wave-function in (II), at the position $r_0$:

$$C = C_{\ell,E} = \frac{1}{F_{\ell,E}(r_0)}\left(\frac{\mathrm{d}}{\mathrm{d}r}F_{\ell,E}\,(r)\right)\Bigg|_{r=r_0}. \tag{2.36}$$

The eigenfunctions of our problem are thus given by the solutions of equation (2.34), amended by (2.36). The described approach was baptized a variant of R-matrix in [124, 120]. In the following, we briefly sketch the conventional R-matrix method as used in [125, 126, 127], and show the relation to our present approach.

The starting point for standard R-matrix methods is the same division of configuration space as in figure 2.3, with the differential equation (2.34) for the radial wave-function $F_{\ell,E}(r)$ in region (III). Again, a surface term $\mathcal{L}$ is added, but now the constant $C$ is set to zero. This leads to the following differential equation:

$$(H + \mathcal{L}_\ell)\xi_{\ell,q}(r) = E_q\xi_{\ell,q}(r),\ r \geq r_0 \tag{2.37}$$

where $H$ denotes the operator on the left hand side of (2.34). The radial eigenfunctions $\xi_{\ell,q}(r)$ to the eigenvalues $E_q$ of (2.37) satisfy arbitrary boundary conditions at

---

(3) Note that here the loss of hermiticity is not related to the complex dilation of position and momentum operators introduced in section 2.1.3. It is just a simple example that hermiticity of an operator can only be stated if its domain is defined.

$r = r_0$. These normalized functions form a complete set over $[r_0, \infty)$, hence we can represent $F_{\ell,E}(r)$ in this set:

$$F_{\ell,E}(r) = \sum_q \int_{r_0}^{\infty} \xi^*_{\ell,q}(r') F_{\ell,E}(r') \mathrm{d}r' \xi_{\ell,q}(r). \tag{2.38}$$

The wave-function in region (III), $F_{\ell,E}(r)$, has to satisfy (2.34). Adding the surface term $\mathcal{L}$ to this equation we obtain:

$$(H + \mathcal{L} - E) F_{\ell,E}(r) = \mathcal{L} F_{\ell,E}(r),\ r \geq r_0. \tag{2.39}$$

Multiplying (2.39) with $\xi^*_{\ell,q}(r)$ from the left, and integrating over $[r_0, \infty)$, we obtain:

$$(E_q - E) \int_{r_0}^{\infty} \xi^*_{\ell,q}(r) F_{\ell,E}(r) \mathrm{d}r = -\frac{1}{2} \xi^*_{\ell,q}(r_0) \frac{\mathrm{d}F_{\ell,E}(r)}{\mathrm{d}r}\bigg|_{r=r_0}. \tag{2.40}$$

With (2.40) and (2.38) we thus obtain an expression for $F_{\ell,E}(r)$ at the boundary $r = r_0$:

$$\begin{aligned} F_{\ell,E}(r_0) =& \frac{1}{2} \sum_q \frac{\xi^*_{\ell,q}(r_0) \xi_{\ell,q}(r_0)}{E - E_q} \frac{\mathrm{d}F_{\ell,E}(r)}{\mathrm{d}r}\bigg|_{r=r_0} \\ =& R(r_0, E) \frac{\mathrm{d}F_{\ell,E}(r)}{\mathrm{d}r}\bigg|_{r=r_0}, \end{aligned} \tag{2.41}$$

with the R-matrix $R(r_0, E)$. The typical procedure in this approach is to compute the function $\xi_{\ell,q}(r)$ in region (III) according to (2.37), and to extract the eigenvalue $E$ subsequently with the help of (2.41), where $F_{\ell,E}(r_0)$ and $\mathrm{d}F_{\ell,E}/\mathrm{d}r\big|_{r=r_0}$ are determined by the wave-function and its derivative at the boundary of region (II). The eigenfunction $F_{\ell,E}(r)$ valid for all $r \in [r_0, \infty)$ is then given by (2.38).

The disadvantage of this approach for our problem is that the eigenfunctions and eigenvalues from the region (III) are needed to form the R-matrix. *After* this matrix is formed it is matched to the region (II) wave-function known from quantum defect theory. The method we are using instead uses this information already *before* the diagonalization.

### 2.3.3 Periodically driven alkali atoms

To solve the Floquet problem (2.11), the method explained in the preceding section has to be slightly modified. As shown in section 2.1.2, the spectrum of (2.11) is $\omega$-periodic, and thus for each quasi-energy $\varepsilon_j$ also $\varepsilon_j + k\omega$ ($k \in \mathbb{Z}$) is an eigenvalue of the problem. Thus, we have to adapt the surface term for the Floquet problem, by redefining the constant $C$, (2.36), in the following way:

$$C = C_{\ell,\varepsilon_j,k} = \frac{1}{F_{\ell,\varepsilon_j,k}(r_0)} \left( \frac{\mathrm{d}}{\mathrm{d}r} F_{\ell,\varepsilon_j,k}(r) \right)\bigg|_{r=r_0}. \tag{2.42}$$

Hence, the function $F_{\ell,E}(r) = F_{\ell,\varepsilon_j,k}(r)$ has to be evaluated at the quasi-energy $\varepsilon_j + k\omega$:

$$F_{\ell,\varepsilon_j,k}(r) = \cos(\pi\delta_\ell) \cdot s_\ell(\varepsilon_j + k\omega, r) + \sin(\pi\delta_\ell) \cdot c_\ell(\varepsilon_j + k\omega, r), \text{ at } r = r_0. \tag{2.43}$$

To compute $c_\ell$ and $s_\ell$ at (quasi-) energies different from the unperturbed alkali levels $-1/(2(n-\delta_\ell)^2)$, we make in particular use of the representation of the Coulomb functions as analytic functions of energy. Furthermore, since $k$ covers all integer numbers, we also need the Coulomb functions in the continuum, i.e. Seaton's theorem (2.32).

From the definitions (2.36) and (2.42), it is clear that $C_{\ell,\varepsilon_j,k}$ has to be evaluated exactly at the (quasi-) energy $\varepsilon_{\text{match}} = \varepsilon_j + k\omega$, which is an eigenvalue of the Floquet problem. As $\varepsilon_j$ is not known beforehand, this requires in principle an iterative procedure. Consequently, the diagonalization of the resulting eigenvalue problem only yields a single converged eigenvalue, which is obtained after some iterations in a self consistent way. To overcome this problem and to obtain more than just one converged eigenvalue per diagonalization, we use an improvement that was also used to describe alkali atoms in the presence of static fields [121]. The idea is to expand (2.42), which is a smooth function of energy, as a power series in energy:

$$C_{\ell,\varepsilon_j,k} = C^0_{\ell,\varepsilon_j,k} + (\varepsilon + k\omega)C^1_{\ell,\varepsilon_j,k} + \ldots, \tag{2.44}$$

Instead of the exact term $C_{\ell,\varepsilon_j,k}$, we employ only the constant and the linear term, $C^0_{\ell,\varepsilon_j,k}$ and $C^1_{\ell,\varepsilon_j,k}$. They are found by computing the Coulomb functions at the position $r_0$ over a suitable energy grid, and fitting the logarithmic derivative to a linear function. This approach ('approximation of the linear energy dependence of the surface term', ALEDST) allows to obtain some hundred converged eigenvalues within a single diagonalization. We will briefly account for the quality of this approximation in section 3.3.1.

## 2.4 Representation in a Sturmian basis set

The complex dilated set of coupled differential equations (2.11), amended by the core induced surface term (2.42), is now represented in a suitable basis set. An appropriate choice are the real Sturmian basis functions [128, 129, 130] $|S^{(\alpha)}_{n,\ell,m}\rangle$. In spherical coordinates, the Sturmian functions are given by the expression:

$$\langle r,\theta,\phi|S^{(\alpha)}_{n,\ell,m}\rangle = \mathcal{D}(n,\ell)\exp\left(\frac{-r}{\alpha}\right)\left(\frac{2r}{\alpha}\right)^\ell L^{(2\ell+1)}_{n-\ell-1}\left(\frac{2r}{\alpha}\right)Y_{\ell,m}(\theta,\phi), \tag{2.45}$$

$$\text{with } \mathcal{D}(n,\ell) = \sqrt{\frac{(n-\ell-1)!}{(n+\ell)!}}, \text{ and } |m| \le \ell < n,$$

where $Y_{\ell,m}(\theta,\phi)$ denote the usual spherical harmonics [131, 132], and $L_q^{(k)}(r)$ the associated Laguerre polynomials [132, 116].(4) The ideal suitability of this set of functions for hydrogen (-like) problems consists in the fact that they perfectly match the internal SO(4) symmetry of the Coulomb problem [134]. The $n$-th Sturmian function with $n = \alpha$, for instance, coincides exactly with the eigenfunction of the unperturbed hydrogen atom with energy $-1/(2n^2)$, angular momentum $\ell$, and $m$ the projection of the angular momentum on the quantization axis. Furthermore, the Sturmian functions are a discrete (though non-orthogonal) basis set representing both the discrete and the continuum part of the spectrum.

The real scaling parameter $\alpha$ in (2.45) determines the scale of the oscillations of the functions $|S_{n,\ell,m}^{(\alpha)}\rangle$. Comparing the definition (2.45) to the analytical form of hydrogen wave-functions, we note that (up to normalization constants) the $n$th bound hydrogen wave-function is represented by the $n$th Sturmian function, given that $r_{\text{hydro}} = (n/\alpha) r_{\text{sturm}}$. A suitable choice of $\alpha$ enables us thus to define the region where an optimal 'resolution' of the wave-function is achieved, even for not too large a basis size. In a numerical simulation we obviously have to introduce a cutoff $n_{\text{sup}}$ of the Sturmian basis. This also introduces a shift of the continuum threshold to a lower value: Since the expectation value of the position operator $\langle r_{\text{hydro}}\rangle$ scales as $n^2$ [131], using Sturmian functions the expectation value $\langle r_{\text{sturm}}\rangle$ scales as $n\cdot\alpha$. The expectation value of the position of the $n_{\text{sup}}$th Sturmian function thus scales as $n_{\text{sup}}\cdot\alpha$, hence the effective continuum thresholds $n_{\text{max}}^{\text{eff}}$ is given by:

$$n_{\text{max}}^{\text{eff}} = \sqrt{n_{\text{sup}}\cdot\alpha}, \text{ and } E_{\text{cont}}^{\text{eff}} = -\frac{1}{2n_{\text{sup}}\alpha}. \tag{2.46}$$

Note that also in laboratory experiments an effective cutoff quantum number $n_{\text{max}}^{\text{eff}}$ is introduced, i.e. highly excited bound states with $n > n_{\text{max}}^{\text{eff}}$ cannot be distinguished from continuum states. There, the existence of an effective continuum threshold is caused by unavoidable stray electric fields created by contact potentials [20, 42].

The Sturmian functions are only orthogonal for a scalar product involving a factor $1/r$, instead of the usual scalar product. Hence, our eigenvalue problem (2.11), which is of the form $\mathcal{A}\mathbf{x} = \lambda\mathbf{x}$, turns into a generalized eigenvalue problem of the form:

$$\mathcal{A}\mathbf{x} = \lambda\mathcal{B}\mathbf{x}. \tag{2.47}$$

The matrix $\mathcal{A}$ is given by the matrix elements (evaluated as radial integrals in the range $[r_0,\infty)$):

$$\mathcal{A} = \left(S_{n',\ell',m',k'}^{(\alpha)}\middle|2\mathcal{H}_\Theta\middle|S_{n,\ell,m,k}^{(\alpha)}\right), \tag{2.48}$$

where the symbol $\mathcal{H}_\Theta$ in (2.48) denotes the complex dilated operator on the left hand side of equation (2.11), amended by the (complex dilated) surface term $(\delta(r -$

---

(4) Note that there are different definitions of the associated Laguerre polynomials. The definition we are using here differs from that used in [133] by a factor $(-1)^k$ and from that used in [131] by a factor $(q+k)!$.

$r_0)(\frac{\partial}{\partial r} + C_{\ell,\varepsilon_j,k}))_\Theta$ that was derived in section 2.3. Yet, if we follow (2.44) and approximate the surface term $C_{\ell,\varepsilon_j,k}$ by $C^0_{\ell,\varepsilon_j,k} + (\varepsilon + k\omega)C^1_{\ell,\varepsilon_j,k}$, it is convenient to split the function $C_{\ell,\varepsilon_j,k}$ between the matrices $\mathcal{A}$ and $\mathcal{B}$: The constant term $C^0_{\ell,\varepsilon_j,k}$ is added to $\mathcal{A}$, while the linear term $C^1_{\ell,\varepsilon_j,k}$ is absorbed in $\mathcal{B}$, which is then given by:

$$\mathcal{B} = \left(S^{(\alpha)}_{n',\ell',m',k'}\middle|2-\left(\delta\left(r-r_0\right)\left(C^1_{\ell,\varepsilon_j,k}\right)\right)_\Theta\middle|S^{(\alpha)}_{n,\ell,m,k}\right). \tag{2.49}$$

The notation $(\cdot|\cdot|\cdot)$ in (2.48) and (2.49) instead of the usual brackets $\langle\cdot|\cdot|\cdot\rangle$ shall illustrate that the radial part of the integral is not evaluated for all $r \in \mathbb{R}$, but only for $r_0 \leq r < \infty$, due to the division of configuration space. Furthermore, the additional subscript $k$ in $|S^{(\alpha)}_{n,\ell,m,k})$ denotes the Sturmian function $|S^{(\alpha)}_{n,\ell,m})$ dressed by $k$ photons.

From now on we will specify the polarization of the microwave field, and in the following we employ a linearly polarized external field $\mathbf{F}$, along the $z$-axis. With this choice, the spatial part of the atom-field interaction operator reduces to $\mathbf{F}\cdot\mathbf{r} = Fz = Fr\cos\theta$. After integrating $\mathcal{H}_\Theta$ and $(2-(\delta(r-r_0)(C^1_{\ell,\varepsilon_j,k}))_\Theta)$ over the solid angle $\mathrm{d}\Omega$, we finally obtain the following expressions for the matrices defining our generalized eigenvalue problem (2.47)

$$\begin{aligned}
\mathcal{A} = \;& \left(S^{(\alpha)}_{n',\ell',k'}\middle|\left[\frac{e^{-\mathrm{i}\Theta}}{r}\left[e^{-\mathrm{i}\Theta}2\frac{n}{\alpha}-2\right]\right]\delta_{k,k'}\delta_{\ell,\ell'}\middle|S^{(\alpha)}_{n,\ell,k}\right)\\
+\;& \left(S^{(\alpha)}_{n',\ell',k'}\middle|\left[-e^{-2\mathrm{i}\Theta}\frac{1}{\alpha^2}-2k\omega\right]\delta_{k,k'}\delta_{\ell,\ell'}\middle|S^{(\alpha)}_{n,\ell,k}\right)\\
+\;& \left(S^{(\alpha)}_{n',\ell',k'}\middle|\left[-e^{-\mathrm{i}\Theta}\delta(r-r_0)\left[e^{-\mathrm{i}\Theta}\frac{d}{dr}-\left(C^0_{\varepsilon_j,\ell,k}\right)_\Theta\right]\right]\delta_{k,k'}\delta_{\ell,\ell'}\middle|S^{(\alpha)}_{n,\ell,k}\right)\\
+\;& \left(S^{(\alpha)}_{n',\ell',k'}\middle|\left[Fe^{\mathrm{i}\Theta}rA_{\ell+1}\left[\delta_{k-1,k'}+\delta_{k+1,k'}\right]\right]\delta_{\ell+1,\ell'}\middle|S^{(\alpha)}_{n,\ell,k}\right)\\
+\;& \left(S^{(\alpha)}_{n',\ell',k'}\middle|\left[Fe^{\mathrm{i}\Theta}rA_{\ell}\left[\delta_{k-1,k'}+\delta_{k+1,k'}\right]\right]\delta_{\ell-1,\ell'}\middle|S^{(\alpha)}_{n,\ell,k}\right),
\end{aligned} \tag{2.50}$$

with

$$A_\ell = \sqrt{\frac{\ell^2-m^2}{4\ell^2-1}}, \tag{2.51}$$

and

$$\mathcal{B} = \left(S^{(\alpha)}_{n',\ell',k'}\middle|(2-e^{-\mathrm{i}\Theta}\delta\left(r-r_0\right)\left(C^1_{\ell,\varepsilon_j,k}\right)_\Theta)\delta_{k,k'}\delta_{\ell,\ell'}\middle|S^{(\alpha)}_{n,\ell,k}\right). \tag{2.52}$$

In (2.50) and (2.52) we used the notation $\left|S^{(\alpha)}_{n,\ell,k}\right)$ instead of $\left|S^{(\alpha)}_{n,\ell,m,k}\right)$. Omission of the $m$-quantum number indicates that, after integration over the solid angle – apart from $k$ counting the 'photons' – only the $\ell$ and the $n$ quantum numbers are left. Since – in the dipole approximation – the external field conserves the $z$-projection of the angular momentum, $m$ is a good quantum number and is not changed by the external field. Apart from this selection rule $\Delta m = 0$, there are also selection rules in the photon number $k$ and the angular momentum quantum number $\ell$, as immediately apparent from (2.50) and (2.52): $\mathcal{A}$ can be split into two parts, the first three lines of (2.50) describe the unperturbed atom, for which the angular momentum is conserved. Consequently, for this part we have the selection rules

$$\Delta\ell = 0,\ \Delta k = 0, \tag{2.53}$$

equally valid for $\mathcal{B}$. The last two lines of (2.50) represent the interaction with the field, which induces the following selection rules:

$$\Delta k = \pm 1,\ \Delta\ell = \pm 1. \tag{2.54}$$

The selection rules for $\mathcal{A}$ are an expression of the fact that the external (dipole) field couples only neighboring angular momenta. A change of the angular momentum by one quantum is connected with the absorption or emission of a photon (which carries away one quantum). Therefore we can define a generalized parity

$$\Pi = (-1)^{\Delta\ell + \Delta k}, \tag{2.55}$$

which is conserved by the external field. This means that we have to solve (2.47) separately in the two subspaces with parity $\Pi = +1$ and $\Pi = -1$. In practice, the separation into these two subspaces entails the advantage that the matrix $\mathcal{A}$ (the same as $\mathcal{B}$) is split in two (uncoupled) matrices, and thus only half the memory is needed to store each of them for numerical diagonalization.

If the integrals in (2.50) and (2.52) are evaluated for all $r \in \mathbb{R}^+$, as it is the case for atomic hydrogen and for the large angular momentum states of alkali atoms, there are further strict selection rules for the principal quantum number $n$ [34]. These, however, are invalidated in the presence of a non-hydrogenic core which restricts the range of the integrals to $r \in [r_0, \infty)$.

## 2.5 Physical quantities

### 2.5.1 Ionization probability

The theoretical apparatus explained so far will be applied to determine the ionization probability of microwave driven Rydberg atoms, with the results presented in part II of this thesis. Much the same as in the (laboratory) experiments on alkali atoms, in our calculations the atoms are initially prepared in a well defined state $|n_0, \ell_0, m_0\rangle$. For a situation like this, the survival probability $P_{\text{surv}}$, i.e. the probability to find the atom in a bound state after an atom-field interaction time $t = t_2 - t_1$, writes:

$$P_{\text{surv}}(t_2 - t_1) = \sum_{\text{bound states } |\xi_m\rangle} \left|\langle \xi_m | U(t_2, t_1) | n_0, \ell_0, m_0\rangle\right|^2, \tag{2.56}$$

where $U(t_2, t_1)$ is the time evolution operator (2.17). Following the derivation in [33, 34], this leads to the expression:

$$P_{\rm surv}(t) = \sum_{\Pi,k,j} \overline{\langle\psi^k_{\varepsilon_j,\Theta}|R(\Theta)|n_0,\ell_0,m_0\rangle^2} \exp(-\Gamma_j t), \tag{2.57}$$

and, consequently, the ionization probability $P_{\rm ion}(t) = 1 - P_{\rm surv}(t)$ is given by:

$$P_{\rm ion}(t) = 1 - \sum_{\Pi,k,j} \overline{\langle\psi^k_{\varepsilon_j,\Theta}|R(\Theta)|n_0,\ell_0,m_0\rangle^2} \exp(-\Gamma_j t). \tag{2.58}$$

In (2.57) and (2.58) we averaged the phase of the driving field over one field cycle $T$, as it is also done in typical experiments, where only the interaction time $t = t_2 - t_1$ is well defined, while the times $t_1$ and $t_2$ when the atom enters or leaves the interaction zone are averaged over $T$.(5) Furthermore, the sum in (2.57) and (2.58) runs over all Fourier components of all atom-field eigenstates $|\psi_{\varepsilon_j}\rangle$ in one Floquet zone of width $\omega$, in both subspaces with parity $\Pi = +1$ and $\Pi = -1$. The projection of the atomic initial state on all atom-field eigenstates in (2.58) is equivalent to assuming a flat pulse of duration $t$ in the (laboratory) experiment. Of course, this so called 'sudden approximation' [136] is not completely correct if the microwave field is switched on 'slowly'. For a sufficiently long switching time of the field, it might even be that only one Floquet state is populated. In this case, the single Floquet state approximation (SFSA) [137, 138] can be employed, in which the ionization probability writes

$$P^{\rm SFSA}_{\rm ion}(t) = 1 - \overline{\langle\psi^k_{\varepsilon_j,\Theta}|R(\Theta)|n_0,\ell_0,m_0\rangle^2} \exp(-\Gamma_j t). \tag{2.59}$$

Here, $|\psi^k_{\varepsilon_j,\Theta}\rangle$ denotes the Floquet state which is adiabatically connected to the field-free atomic initial state. To apply the SFSA, it is crucial that the evolution of the initial atomic state follows the change of the external field slowly enough that only one state is populated, what is usually not the case in typical microwave experiments. Therefore, we will in general employ the sudden approximation. Only in section 4.2.1 will we draw a comparison between results of the sudden approximation and of the SFSA.

### 2.5.2 Shannon width

As we will see, the initial atomic state gets strongly distorted under periodic driving, and spreads over many atom-field eigenstates. To quantify the number of atom-field eigenstates contributing to the representation of the atomic initial state in the external field, we follow [16, 139] and borrow a concept of information theory. In [16, 139] the Shannon width [140] was used as a measure for the localization properties of an atomic initial state. The Shannon entropy $S(n_0, F, \omega)$ and the Shannon width $W(n_0, F, \omega)$ [140] are defined as:

---

(5) Only in a very recent experiment of the Virginia group, $t_1$ and $t_2$ were well-defined. In this experiment, a Rydberg wave packet was excited at a well-defined phase of the microwave field, and the dependence of the ionization yield of the wave packet on the relative phase between the motion of the wave packet and the oscillations of the field was investigated [135].

$$S(n_0, F, \omega) = -\sum_j w_j \ln w_j, \text{ with } w_j = \sum_k \langle\overline{\psi^k_{\varepsilon_j,\Theta}}|R(\Theta)|n_0, \ell_0, m_0\rangle^2, \quad (2.60)$$

$$W(n_0, F, \omega) = \exp S(n_0, F, \omega). \quad (2.61)$$

The Shannon width expresses the average number of atom-field eigenstates needed to represent the initial state $|n_0, \ell_0, m_0\rangle$ in the Floquet basis at a given field amplitude $F$ and frequency $\omega$. Obviously, $W(n_0, F, \omega) = 1$ if and only if the initial atomic state is represented by a single atom-field eigenstate.

However, since all eigenstates of microwave driven atoms are decaying states, the above definition of $W(n_0, F, \omega)$ is only valid at time $t = 0$, and the exponential functions $\exp(-\Gamma_j t)$ of (2.58) do not appear in (2.61). With the description of the atom-field eigenstates as decaying states, investigations of the change of the Shannon width with the interaction time require a modified definition, taking into account the finite ionization rates of the atom-field eigenstates [141, 142]. However, for our present purposes, the definition (2.61) will be sufficient.

# Chapter 3

# Numerical treatment of the system

In the preceding chapter we provided the theoretical description of microwave driven alkali Rydberg states, and obtained the generalized eigenvalue problem (2.47). As the quantum numbers $k \in \mathbb{Z}$, $n \in \mathbb{N}$, and $\ell = 0, \ldots, n-1$ in (2.50) and (2.52) have an infinite domain, the matrices $\mathcal{A}$ and $\mathcal{B}$ are in principle infinite matrices. Obviously, the range of these quantum numbers has to be truncated in practice. The cutoff values are specified by the condition that the results have to be converged. The way we determine these cutoff values will be explained in section 3.3.1. However, though the truncated matrices are finite, they are still rather huge. For the numerical treatment – i.e. the diagonalization of the generalized eigenvalue problem, as it will be described in section 3.1 – we thus need a large main memory of the computing system, which is only available on parallel architectures. We therefore need, in addition, an efficient, intelligent parallel implementation of the diagonalization routine, which is explained in section 3.2.

## 3.1 The Lanczos algorithm

To compute the ionization probability (2.58), we need the eigenvalues and eigenvectors of the generalized eigenvalue problem (2.47). While – employing suitably chosen cutoff values of the quantum numbers – the dimension of the problem becomes rather large (up to $10^6$), we do not need to know all eigenvalues (and eigenvectors), but only those within a single Floquet zone of width $\omega$ around an arbitrary energy $E_0$. This means that typically less than $10^4$ eigenvalues (of all the $10^6$ eigenvalues) are required. A suitable routine to find only a ’few’ eigenvalues (with the corresponding eigenvectors) of a huge matrix is the Lanczos routine [143, 144], which enables us to find the largest eigenvalues of a given eigenvalue problem. To apply the Lanczos algorithm to our generalized eigenvalue problem (2.47), we shift $\mathcal{A}$ by $E_0$, i.e., by the energy that defines the position of the chosen Floquet zone:

$$\mathbf{A} = \mathcal{A} - E_0\mathcal{B} \tag{3.1}$$

and are looking now for the smallest eigenvalues of the shifted generalized eigenvalue problem

$$\mathbf{A} \cdot \mathbf{x} = \lambda \mathcal{B} \cdot \mathbf{x}. \tag{3.2}$$

Multiplying (3.2) by $\mathbf{A}^{-1}$ we obtain the eigenvalue problem:

$$\mathbf{A}^{-1} \cdot \mathcal{B} \cdot \mathbf{x} = \mu \cdot \mathbf{x}. \tag{3.3}$$

The largest eigenvalues $\mu_i$ in the eigenvalue problem (3.3) are the inverse of the smallest eigenvalues $\lambda_i$, i.e. the inverse of the eigenvalues in the Floquet zone around $E_0$. In this way we transformed the original generalized eigenvalue problem to equation (3.3), which can be solved with the help of the Lanczos routine.

The idea of the Lanczos algorithm is to construct iteratively a $n_{\text{lancz}}$-dimensional subspace spanned by $\mathbf{s}_1, (\mathbf{A}^{-1} \cdot \mathcal{B}) \cdot \mathbf{s}_1, (\mathbf{A}^{-1} \cdot \mathcal{B})^2 \cdot \mathbf{s}_1, (\mathbf{A}^{-1} \cdot \mathcal{B})^3 \cdot \mathbf{s}_1, \ldots, (\mathbf{A}^{-1} \cdot \mathcal{B})^{n_{\text{lancz}}-1} \cdot \mathbf{s}_1$ (with an arbitrary, normalized starting vector $\mathbf{s}_1$), in which the best approximations of the eigenvalues $\mu_i$ are found. The construction of this subspace is achieved by building an orthonormalized basis $\mathbf{s}_1, \mathbf{s}_2, \ldots, \mathbf{s}_{n_{\text{lancz}}}$ (in our case the Lanczos vectors $\mathbf{s}_i$ are orthonormalized with respect to $\mathcal{B}$, since the Sturmian functions are not orthogonal with respect to the usual scalar product) of the subspace, where in general a good approximation is reached already for $n_{\text{lancz}} << \dim \mathcal{A}$. The matrix of the basis vectors $\mathbf{S} = \mathbf{s}_1, \mathbf{s}_2, \ldots, \mathbf{s}_{n_{\text{lancz}}}$ transforms $\mathbf{A}^{-1} \cdot \mathcal{B}$ into a tridiagonal, complex symmetric matrix:

$$\mathbf{S}^{-1} \cdot (\mathbf{A^{-1}} \cdot \mathcal{B}) \cdot \mathbf{S} = \begin{pmatrix} \alpha_1 & \beta_1 & 0 & \ldots & 0 \\ \beta_1 & \alpha_2 & \beta_2 & 0 & \ldots \\ 0 & \beta_2 & \alpha_3 & \beta_3 & \ddots \\ 0 & \ddots & \ddots & \ddots & \ddots \\ 0 & \ldots & 0 & \beta_{n_{\text{lancz}}-1} & \alpha_{n_{\text{lancz}}} \end{pmatrix}. \tag{3.4}$$

The tridiagonal matrix obtained in this way can then be diagonalized with standard diagonalization routines like the QR-decomposition [145].

To understand the construction of the Lanczos vectors, we have a look at the $j$th column of the product $\mathbf{A}^{-1} \cdot \mathcal{B} \cdot \mathbf{S}$:

$$\mathbf{A}^{-1} \cdot \mathcal{B} \cdot \mathbf{s}_j = \alpha_j \mathbf{s}_j + \beta_{j-1} \mathbf{s}_{j-1} + \beta_j \mathbf{s}_{j+1}. \tag{3.5}$$

Since the vectors $\mathbf{s}_j$ are orthonormal, we obtain the following relations for the coefficients $\alpha_j$ and $\beta_j$:

$$\alpha_j = \mathbf{s}_j^T \cdot \mathcal{B} \cdot \mathbf{A}^{-1} \cdot \mathcal{B} \cdot \mathbf{s}_j, \tag{3.6}$$

$$\beta_j = \sqrt{\mathbf{t}_{j+1}^T \cdot \mathcal{B} \cdot \mathbf{t}_{j+1}}, \text{ with } \mathbf{t}_{j+1} = \mathbf{A}^{-1} \cdot \mathcal{B} \cdot \mathbf{s}_j - \alpha_j \mathbf{s}_j - \beta_{j-1} \mathbf{s}_{j-1}, \tag{3.7}$$

and the recurrence relation for the Lanczos vectors:

$$\mathbf{s}_{j+1} = \frac{1}{\beta_j} \mathbf{t}_{j+1}, \ (j \geq 1). \tag{3.8}$$

The first Lanczos vector $\mathbf{s}_1$ is chosen as an arbitrary unit vector, and $\beta_0 = \alpha_0 = 0$. With these settings and (3.8), it is clear (by induction) that the $\mathbf{s}_j$ are orthogonal.

The implementation of the sketched algorithm, and how, in particular, this is accomplished on a parallel computing architecture, will be described in section 3.2.3, but before we will mention some basic ideas of parallel computing.

## 3.2 Numerical implementation

### 3.2.1 Some basic ideas of parallel computing

Many problems in physics can be solved faster on a parallel instead of a scalar or vector computer, or (as it is the case with our problem) they can only be solved with the help of a parallel computer, due to the bare size of the problem, for instance. The idea of parallel computing is that all processing elements work on different parts of the problem simultaneously. Thus, on the one hand it is in principle possible to speed-up the numerical routine by a factor up to the number of processing elements working in parallel, if the work is equally distributed ('balanced') and if the whole routine can be done in parallel. On the other hand, the main memory is multiplied by the number of processing elements involved in the problem (given that the memory of the machine is distributed over the processing elements, see below). In our specific case, the concept is to split the huge matrices $\mathbf{A}$ and $\mathcal{B}$ into smaller matrices, which are treated locally on each processing element. Therefore it is important to know how the main memory can be accessed in the computer.

In principle, there are two concepts handling the memory: Shared memory machines, where each processing element has access to the whole memory, and distributed memory machines, where the main memory is physically distributed over the different processing elements. If large memory is needed, so far most machines (e.g., the CRAY T3E [146]) are organized in the latter way, and the parallel machine consists of many processing elements having access to not too large memory each. Recently, another concept of the organization of the memory emerged, which is a mixture of the two aforementioned ones, the hybrid architecture, where subgroups of processing elements (e.g. eight in the case of the HITACHI SR8000-F1 [147]) share the same memory, to form a shared memory node. Several of these nodes are organized as a distributed memory machine.

To design an efficient parallel program, one not only has to take into account an efficient sequential computation on the single processing elements, but also the interaction of the processing elements for the exchange of data. The required communication between the processing elements needed for this can be achieved by the use of special message passing software, like MPI [148, 149] (Message Passing Interface), or PVM (Parallel Virtual Machine). In addition, there are special 'data-parallel' programming languages like HPF (High Performance Fortran), message passing libraries for shared memory architectures like OpenMP (Open Message Passing), or vendor specific libraries like the CRAY specific SHMEM (Shared

Memory access library, which simulates the direct access of a processing element to the memory of the other processing elements, although the machine physically has a distributed memory). Apart from OpenMP, which requires a shared memory architecture, and the CRAY specific SHMEM, the mentioned examples are claimed to be portable between different machines and there exist implementations on most of the modern parallel computing facilities, but MPI appears to become the standard [150, 151] and is widely used. Thus, to optimize the portability, this was also our choice for the implementation of our code.

In MPI there are several modes of communication between the processing elements of a given computing architecture:

- point-to-point communication (a single processing element sends or receives a message, which is received or was sent by another processing element),
- collective communication (a single processing element sends or receives a message to or from all the other processing elements, each processing element broadcasts data to all other elements, or the processing elements have to be synchronized at a certain point in the code),
- global reduction operations (evaluation of the maximum, the sum, logical operations,..., of a data set distributed over all processing elements).

With the help of calls to this communication interface it is thus in principle possible to transform an existing sequential code ’with a minimum effort’ into a parallel code (where ’minimum’ does not mean that the effort is really small, but that the structure of the parallel code can be similar to that of the sequential code), which typically will be executed by the various processing elements in parallel. One only has to know at which places in the code communication (i.e. exchange of relevant information) with individual or all involved processing elements is necessary, and how this communication is accomplished to achieve an efficient code producing correct results. In particular, appropriate timing of the communication is crucial for optimal synchronization.

An efficient code should allow a considerable speedup if the problem is solved on $p > 1$ processing elements, instead of execution on a single processing element. The speedup $S(p)$ is defined as [152, 153]

$$S(p) = \frac{T(1)}{T(p)}, \tag{3.9}$$

where $T(p)$ is the execution time on $p$ processing elements. With (3.9), the efficiency $E(p)$ of a code running on $p$ processing elements is defined as

$$E(p) = \frac{S(p)}{p} = \frac{T(1)}{pT(p)}. \tag{3.10}$$

High efficiency $E(p) \to 1$ is reached if the time required for communication in the parallel code does not produce too much overhead, i.e. if the communication time is short compared to the time spent for purely local operations, and if the non-parallel part of the algorithm (that has to be done in a sequential fashion) can be minimized. Therefore, it is in general worthwhile to restructure the sequential code when implementing it on a parallel architecture, with particular care for the synchronization of the processing elements. This is often achieved by dividing the work (i.e. the loops) into smaller tasks to be distributed over the different processing elements, to end up with a balanced code. However, it is in general impossible to achieve the optimal efficiency $E(p) = 1$, since in generic cases there is always a portion $f$ of the problem, which has to be solved sequentially. An estimate for the possible speedup that can be reached is given by the well-known Amdahl's law [154, 153, 152]

$$S_{\mathrm{A}}(p) = \frac{p}{pf + (1 - f)}. \tag{3.11}$$

Thus, the optimal speedup is limited by $1/f$, no matter how many processing elements are employed. Note that the estimate (3.11) characterizes only a simplified situation. Also other estimates [155, 152] introduce an upper bound of $S(p)$, due to the sequential part of the code, and therefore $E(p) = 1$ cannot be reached.(1)

Appropriate synchronization of the processing elements is also crucial to obtain correct results. A typical problem occurring with a badly synchronized code is that a processing element starts a computation without having received yet the value of some variable necessary on input but calculated by some other processing element. If no synchronization mechanism prevents the processing element from executing the local computation before receipt of the relevant data, the result of this computation will be uncontrolled, typically without generation of any error message. Another relevant problem is the occurrence of 'deadlocks'. A deadlock describes a situation when two or more processing elements are waiting for an event or a communication call from one of the other processing elements, but this event never occurs (because, e.g., the waiting processing element is the last one to finish a loop in which the event should take place).

The first implementation of our code [156] was done on a CRAY T3E of the Rechenzentrum of the Max-Planck Society [146], using mainly MPI. Since the point-to-point communications in MPI are implemented as double-sided communication routines,(2) i.e. they consist of a message from the sending together with a message from the receiving processing element, for some of the point-to-point communications needed in our code we employed calls to (one-sided) communication routines from the CRAY specific SHMEM library. Since the SHMEM library simulates the direct access of all processing elements to the memory of the other processing elements (although the CRAY T3E is a distributed memory machine), it allows a point-to-point communications employing only a single processing element to send or receive the data. Therefore the SHMEM routines are typically faster than the MPI routines where both processing elements, i.e., the sending and the receiving processing element are involved in the communication process.

---

(1) Another notion to specify the efficiency of a parallel code is the scalability of the code. In contrast to the estimate for the optimal speedup given by (3.11), it is assumed that on a larger parallel computer typically a larger problem is solved than on a scalar computer, and thus the fraction $f$ that has to be solved sequentially is not constant. A code is called scalable if its performance is approximately constant when the size of the problem (i.e. the number of elementary operations) and the number of processing elements are increased by the same factor.

(2) So far we referred to MPI-1. The more recent, extended version MPI-2 provides also one-sided communication calls, however, this extension is only rarely implemented up to now. In particular, there was at least no stable implementation on the CRAY T3E nor on the HITACHI SR8000-F1, at least at the time when the code was implemented on these machines.

In a second step, to describe multi-photon ionization processes starting at low principal quantum numbers of the atomic initial state $n_0 \simeq 28, \ldots, 40$, and demanding the absorption of $112, \ldots, 50$ photons to access the atomic continuum, a larger amount of available main memory (approximately 100 GByte) was needed, and we ported the code to the HITACHI SR8000-F1 of the Leibniz-Rechenzentrum (LRZ) at Munich. For the migration from the CRAY T3E to the HITACHI SR8000-F1 the CRAY specific SHMEM calls had to be replaced by (two-sided) communication calls to MPI. In addition, some of the point-to-point MPI communication routines are implemented in a different way on the different architectures, what led occasionally to deadlocks on the HITACHI SR8000-F1. For this purpose we replaced pairs of separate calls to sending and receiving routines (MPI_SEND and MPI_RECV) by single calls (MPI_SENDRECV or MPI_SENDRECV_REPLACE), which perform sending and receiving of the data in one call. (However, though only one call to MPI is employed to transfer data from one processing element to another in this way, both the sending and the receiving processing element are involved in the communication process, and the communication routine is still a double-sided communication routine).

Hitherto we do not use the new features of the HITACHI SR8000-F1, i.e. the hybrid architecture which allows for the use of intra-node shared memory programming and the use of MPI only between the nodes, but we use a massively parallel code, which does not distinguish between inter- and intra-node communication. This is justified, as we obtained a satisfactory performance of our code, even by using the HITACHI SR8000-F1 in a massively parallel way, if the physical problem has suitable dimensions (we will account for the efficiency of our code in section 3.2.4). A refinement of the code for the hybrid architecture will probably provide a further speed up of the program, and will be completed soon.

### 3.2.2 Storage of the matrices

Before presenting the structure of our code, we briefly sketch the structure of the matrices $\mathbf{A}$ and $\mathcal{B}$ and the way they are stored.

As we have seen in section 2.4, the external field couples only Floquet-states with the quantum numbers $\Delta\ell = \pm 1$ and $\Delta k = \pm 1$. With this selection rules it is possible to build up $\mathbf{A}$ as a banded, complex matrix with block structure. Each of the blocks in the matrix consists of matrix elements defined by integrals between the states with angular momentum $\ell$ and photon number $k$, according to the aforementioned rules. For microwave driven atomic hydrogen, or for the blocks containing the large angular momentum alkali states (i.e. when the integrals are evaluated between states with vanishing quantum defect) the integrals are evaluated for all $r \in \mathbb{R}^+$, and there are also restrictive selection rules for the principal quantum number (i.e. $\Delta n = 0, \pm 1, \pm 2$). Therefore, these block are essentially empty. However, in the general case of alkali states with non-vanishing angular momentum $\delta_\ell$, there are no more selection rules in $n$. Yet, in both cases – for alkali or hydrogenic states – the banded matrix $\mathbf{A}$ (with dimension $n_{\mathrm{tot}}$, and bandwidth $n_{\mathrm{larg}}$) is symmetric.

Consequently, all the relevant information is contained in the lower triangular band, which we store as an array of size $n_{\mathrm{larg}} \times n_{\mathrm{tot}}$, and distribute it over $n_{\mathrm{procs}}$ processing elements. This number depends on the effective size of $\mathbf{A}$ (which is given in GByte by $n_{\mathrm{larg}} \cdot n_{\mathrm{tot}} \cdot 16/2^{30}$, since individual elements are complex numbers represented in double precision arithmetics), and on the accessible memory $M$ per processing element (for the HITACHI SR8000-F1 $M$ is approximately given by $6.5\ \mathrm{GByte}/\mathrm{PE}$ with $\mathrm{PE} = 1, \ldots, 8$, the number of processing elements employed per node):

$$n_{\mathrm{procs}} = \frac{n_{\mathrm{tot}} \cdot n_{\mathrm{larg}}}{M}. \tag{3.12}$$

For the sake of efficiency and portability of the code, we perform most of the calculations locally on each processing element, using BLAS-2 and BLAS-3 (Basic Linear Algebra Subprograms [157, 158, 152]), for matrix-vector (level 2) and matrix-matrix (level 3) operations. These subroutines are standardized and optimized for most machines. Therefore, the matrix is divided in $n_{\mathrm{sizg}} \times n_{\mathrm{sizg}}$ blocks that are stored in the memory of the processing elements, and on which the BLAS operations can be performed. The way we partition the matrix is sketched in figure 3.1. The connection between the size $n_{\mathrm{sizg}}$ of the blocks and the bandwidth $n_{\mathrm{larg}}$ of the matrix is given by

$$n_{\mathrm{larg}} = n_{\mathrm{r}} \cdot n_{\mathrm{procs}} \cdot n_{\mathrm{sizg}}. \tag{3.13}$$

Here $n_{\mathrm{r}}$ is the number of $n_{\mathrm{sizg}} \times n_{\mathrm{sizg}}$ block lines of the $n_{\mathrm{larg}} \times n_{\mathrm{larg}}$ blocks, that are stored in the memory of each processing element, where in practice the choice $n_{\mathrm{r}} = 2$ leads to the best performance.(3) Thus, until a $n_{\mathrm{larg}} \times n_{\mathrm{larg}}$ block of $\mathbf{A}$ is completed in a certain matrix calculation, each processing element has to process $n_{\mathrm{r}}$ lines, each of them containing $n_{\mathrm{band}}$ of the $n_{\mathrm{sizg}} \times n_{\mathrm{sizg}}$ blocks, where $n_{\mathrm{band}}$ is given by

$$n_{\mathrm{band}} = n_{\mathrm{r}} \cdot n_{\mathrm{procs}}. \tag{3.14}$$

---

(3) If $n_{\mathrm{tot}}$ gets very large, the block-size $n_{\mathrm{sizg}}$ gets too small, and hence the BLAS performance – which shows an optimal performance for a specific block-size depending on the available cache (high speed buffers between the processing element and the main memory that capture those portions of the memory currently in use [152]) of the specific machine – decreases. In this case the choice $n_{\mathrm{r}} = 1$ may become more appropriate.

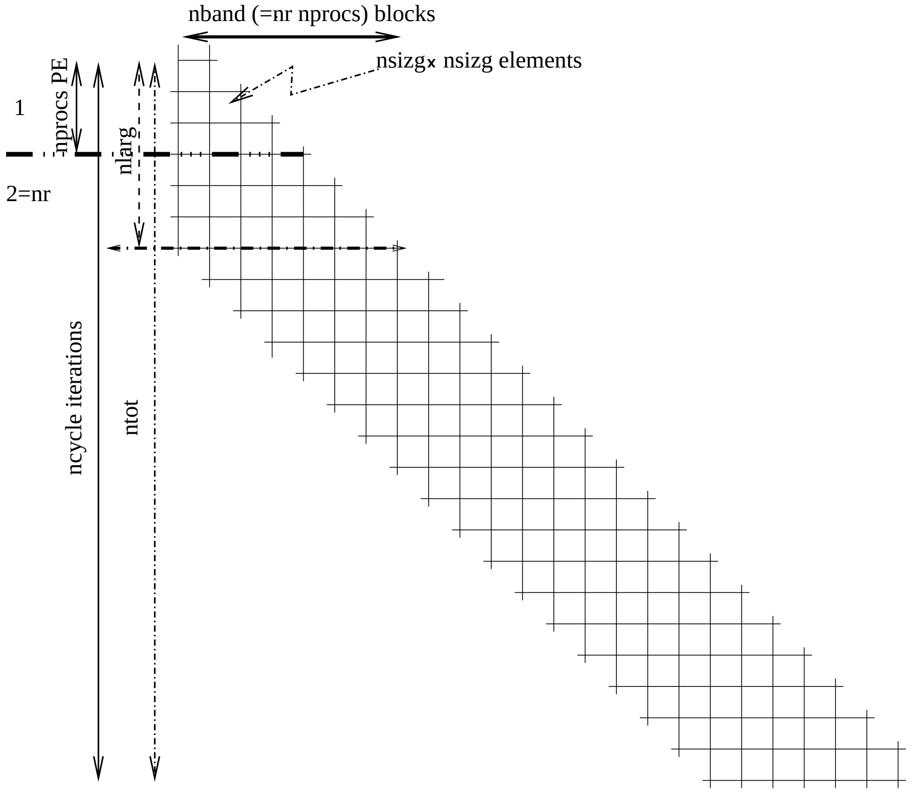

Figure 3.1: Partitioning of the matrices: $n_{\rm tot}$ is the total dimension, $n_{\rm larg}$ its bandwidth; $n_{\rm band}$ denotes the number of $n_{\rm sizg} \times n_{\rm sizg}$ blocks in a line, and $n_{\rm r}$ the number of such lines stored in the memory of each of the $n_{\rm procs}$ processing elements.

All processing elements will be working on one of these lines simultaneously. Therefore, working through the total matrix requires to process $n_{\rm cycle}$ lines, with

$$n_{\rm cycle} = \frac{n_{\rm tot}}{n_{\rm sizg} \cdot n_{\rm procs}}. \tag{3.15}$$

In the memory of each processing element, the matrices are stored as $n_{\rm band} \times n_{\rm cycle}$ arrays, whose entries are given by the $n_{\rm sizg} \times n_{\rm sizg}$ matrices, which are exactly the same sub-matrices that appear also in the (physical) matrix $\mathbf{A}$.

Due to the selection rules $\Delta k = \Delta \ell = 0$ for the matrix $\mathcal{B}$, the only non-vanishing matrix elements of $\mathcal{B}$ are the diagonal blocks. Hence, the bandwidth $n_{\rm larg}$ of $\mathcal{B}$ is much smaller as compared to $\mathbf{A}$. However, the organization and storage of $\mathcal{B}$ is done in the same way as explained above, with a smaller $n_{\rm larg}$ and a smaller $n_{\rm band}$.

In a similar way each vector that is needed (e.g. eigenvectors, or the Lanczos vectors) is distributed over all processing elements: As a vector can be seen as the equivalent of a banded matrix with the bandwidth 1, the storage of a vector reduces to the storage of a two-dimensional array of size $n_{\mathrm{sizg}} \times n_{\mathrm{cycle}}$, in the memory of each processing element.

### 3.2.3 Implementation of the Lanczos algorithm

After filling the matrices $\mathbf{A}$ and $\mathcal{B}$, and storing them in the memory of the $n_{\mathrm{procs}}$ processing elements as described above, the generalized eigenvalue problem has to be diagonalized. For that purpose we use a parallel implementation of the Lanczos algorithm. In section 3.1 we have seen that the Lanczos algorithm is defined by the equations (3.6), (3.7), and the recurrence relation for the Lanczos vectors (3.8). Thus an implementation of the algorithm requires the following operations:

1. several scalar products $\mathbf{x}^{\mathrm{T}} \cdot \mathbf{y}$,
2. a matrix-vector product $\mathcal{B} \cdot \mathbf{x}$,
3. and a routine that allows to compute $\mathbf{A}^{-1} \cdot \mathcal{B} \cdot \mathbf{x}$.

Having provided routines to perform these three operations, it is possible to implement the algorithm. However, in a parallel routine, the three operations are less 'trivial' than in a sequential routine. Before we sketch the implementation of the Lanczos routine itself, we therefore explain the parallel implementation of these routines.

#### 3.2.3.1 $\mathbf{x}^{\mathrm{T}} \cdot \mathbf{y}$

Using BLAS, each of the $n_{\mathrm{procs}}$ processing elements performs a scalar product locally, on the part of the vectors $\mathbf{x}$ and $\mathbf{y}$ stored on the processing element's memory. Afterwards, the local results of all processing elements are added up by means of a MPI global reduction operation (MPI_REDUCE). The result is broadcasted (MPI_BCAST) to all processing elements.

#### 3.2.3.2 $\mathcal{B} \cdot \mathbf{x}$

The product of $\mathcal{B}$ with a vector $\mathbf{x}$

$$\begin{pmatrix} \ddots & & & & \\ \mathcal{B}_{i-2,i-2} & & & & \\ \mathcal{B}_{i-1,i-2} & \mathcal{B}_{i-1,i-1} & & & \\ \mathcal{B}_{i\ ,i-2} & \mathcal{B}_{i\ ,i-1} & \mathcal{B}_{i\ ,i} & & \\ \mathcal{B}_{i+1,i-2} & \mathcal{B}_{i+1,i-1} & \mathcal{B}_{i+1,i} & \mathcal{B}_{i+1,i+1} & \\ & & & & \ddots \end{pmatrix} \cdot \begin{pmatrix} \vdots \\ x_{i-2} \\ x_{i-1} \\ x_i \\ x_{i+1} \\ \vdots \end{pmatrix} \tag{3.16}$$

is reduced to multiplications of the $n_{\mathrm{sizg}} \times n_{\mathrm{sizg}}$ matrices (labeled by $B_{i,j}$ in (3.16)) and the $n_{\mathrm{sizg}}$ vectors (labeled by $x_i$ in (3.16)) that are stored locally on each processing element. These matrix-vector multiplications are performed with the help of BLAS.

The routine starts with the products along the diagonal, i.e. each processing element computes a product $\mathcal{B}_{i,i} \cdot x_i$.

Afterwards the sub-diagonal is processed: For this purpose, each processing element sends its part of the input vector (the part used for the product along the diagonal) to the next processing element (we define the order of the processing elements as ascending along the block diagonal) and receives a part of the input vector from the previous processing element. With this new part of the input vector the processing element computes the product with the sub-diagonal block, i.e. each processing element performs the calculation $\mathcal{B}_{i,i-1} \cdot x_{i-1}$. The result is added to the output vector at position $i$, and the part of the vector used for the calculation (i.e. $x_{i-1}$) is sent to the subsequent processing element.

The previous step is repeated (with the matrix $\mathcal{B}_{i,i-2}$), in this way the processing elements work through all the blocks in one line of $\mathcal{B}$, and so on, until the bandwidth of the matrix is reached. As requested, the entry in the output vector at position $i$ is now

$$\mathcal{B}_{i,i} \cdot x_i \; + \; \mathcal{B}_{i,i-1} \cdot x_{i-1} \; + \; \mathcal{B}_{i,i-2} \cdot x_{i-2} \; + \; \ldots . \tag{3.17}$$

Having finished one block line, the processing element proceeds with the next line which is stored in the processing element's memory, i.e. with the line $i + n_{\mathrm{procs}}$ in $\mathcal{B}$, and starts again with the product of the diagonal block, now $\mathcal{B}_{i+n_{\mathrm{procs}},i+n_{\mathrm{procs}}} \cdot x_{i+n_{\mathrm{procs}}}$.

#### 3.2.3.3 $\mathbf{A}^{-1} \cdot \mathcal{B} \cdot \mathbf{x}$

Before computing the product $\mathbf{A}^{-1} \cdot \mathcal{B} \cdot \mathbf{x}$ we note that the matrix $\mathbf{A}^{-1}$ is never used, but only the product $\mathbf{A}^{-1} \cdot \mathcal{B} \cdot \mathbf{x}$. Consequently, we do not invert the matrix $\mathbf{A}$, since a matrix inversion is hard to parallelize, but solve the system

$$\mathbf{A} \cdot \mathbf{x} = \mathcal{B} \cdot \mathbf{y} \tag{3.18}$$

for $\mathbf{x} = \mathbf{A}^{-1} \cdot \mathcal{B} \cdot \mathbf{y}$. The solution of (3.18) is obtained in two steps: First, $\mathbf{A}$ is decomposed in a product of a lower triangular matrix $\mathbf{L}$, a diagonal matrix $\mathbf{D}$, and an upper triangular matrix $\mathbf{L}^T$ (with unity as the diagonal elements of $\mathbf{L}$ and $\mathbf{L}^T$):

$$\mathbf{A} = \mathbf{L} \cdot \mathbf{D} \cdot \mathbf{L}^T . \tag{3.19}$$

This allows to solve equation (3.18) by backward substitution [145].

The decomposition of $\mathbf{A}$ is achieved with the help of a parallel block $\mathrm{LDL^T}$-decomposition, which is performed similarly to a conventional, sequential $\mathrm{LDL^T}$-decomposition [145]. To save memory, the decomposition is done 'in place', and the matrix $\mathbf{A}$ – which is not used anymore afterwards – is overwritten by the matrix $\mathbf{L}$ and $\mathbf{D}$, while the matrix elements of the latter are written on the diagonal elements of $\mathbf{L}$ (which are unity). In the following we sketch the routine we are using. To illustrate our notation, we rewrite (3.19) in matrix form:

$$\begin{pmatrix} A_{11} & & & \\ A_{21} & A_{22} & & \\ A_{31} & A_{32} & A_{33} & \\ \vdots & \vdots & \vdots & \ddots \end{pmatrix} = \tag{3.20}$$

$$\begin{pmatrix} L_{11} & & & \\ L_{21} & L_{22} & & \\ L_{31} & L_{32} & L_{33} & \\ \vdots & \vdots & \vdots & \ddots \end{pmatrix} \cdot \begin{pmatrix} D_{11} & & & \\ & D_{22} & & \\ & & D_{33} & \\ & & & \ddots \end{pmatrix} \cdot \begin{pmatrix} L_{11}^T & L_{21}^T & L_{31}^T & \dots \\ & L_{22}^T & L_{32}^T & \dots \\ & & L_{33}^T & \dots \\ & & & \ddots \end{pmatrix} .$$

The entries of the matrices in (3.20) are $n_{\text{sizg}} \times n_{\text{sizg}}$ blocks as they are stored in the memory of the processing elements, where each processing element has access to $n_{\text{cycle}}$ lines of these blocks, as explained in section 3.2.2.

Alike a sequential LDL$^{\text{T}}$-decomposition of a complex symmetric matrix, the diagonal block $A_{11}$ is decomposed at first, according to

$$A_{11} = L_{11} \cdot D_1 \cdot L_{11}^T. \tag{3.21}$$

The result (i.e., the triangular matrix $L_{11}$ with the elements of the diagonal matrix $D_1$ on the diagonal) is stored in place of the block $A_{11}$, and also sent to the other processing elements.

Afterwards, the succeeding processing elements decompose the rest of the blocks in the first row, by solving the equation

$$A_{j1} = L_{j1} \cdot (D_1 \cdot L_{11}^T). \tag{3.22}$$

After this calculation, $L_{j1}$ is stored in place of $A_{j1}$, and sent to the other processing elements.

With the received block, the processing elements update their blocks of $\mathbf{A}$ in line $j$: $A_{ji} \rightarrow A_{ji} - L_{j1} \cdot D_1 \cdot L_{i1}^T,\ (i \leq j)$ and the second row will be processed: The diagonal element – belonging to the second processing element – is decomposed as

$$A_{22} = L_{22} \cdot D_2 \cdot L_{22}^T, \tag{3.23}$$

where $A_{22}$ is the new, updated block (using the old block the equation that has to be solved reads $A_{22}^{\text{old}} = L_{21} \cdot D_1 \cdot L_{21}^T + L_{22} \cdot D_2 \cdot L_{22}^T$). Again, $L_{22}$ and $D_2$ are stored in place of the old diagonal block, and sent to the other processing elements. With this block, the other processing elements can decompose the rest of the second row, by solving the equation

$$A_{j2} = L_{j2} \cdot (D_2 \cdot L_{22}^T). \tag{3.24}$$

Again, $L_{j2}$ is stored in place of $A_{j2}$ and sent to the other processing elements, that update their blocks in a line by replacing $A_{ji} \rightarrow A_{ji} - L_{j2} \cdot D_2 \cdot L_{i2}^T$.

Thereafter the third row is processed, the diagonal block (which belongs now to the third processing element) has to be decomposed as

$$A_{33} = L_{33} \cdot D_3 \cdot L_{33}^T. \tag{3.25}$$

After $L_{33}$ and $D_3$ are stored and sent to the other processing elements, the processing elements proceed in decomposing the third row in an analogous way as already for the first two rows. The procedure continues until the LDL$^\mathrm{T}$ decomposition is completed.

In this decomposition, all operations on single blocks (decomposing $A_{ji}$) are done locally on a single processing element. The decomposition of the diagonal blocks ($A_{ii} = L_{ii} D_i L_{ii}^T$) is performed with a usual LDL$^\mathrm{T}$- decomposition, as described in [145], and the solution of the non-diagonal matrix equations ($A_{ji} = L_{ji} \cdot D_i \cdot L_{ii}^T$) is achieved by a call to BLAS-3.

After the decomposition (3.19), the solution of (3.18) requires two steps: In the first step we solve the equation

$$\begin{aligned} \mathbf{L} \cdot \mathbf{a} \quad &= \mathbf{b}, \\ \text{with:} \quad \mathbf{a} = \quad &\mathbf{D} \cdot \mathbf{L}^T \cdot \mathbf{x}, \text{ and } \mathbf{b} = \mathcal{B} \cdot \mathbf{y}, \end{aligned} \tag{3.26}$$

by backward substitution. Therefore, we rewrite (3.26):

$$\sum_{j=j_\mathrm{min}}^{i} L_{ij} a_j = b_i, \tag{3.27}$$

where $L_{ij}$ are $n_\mathrm{sizg} \times n_\mathrm{sizg}$ blocks, and $a_j$, $b_i$ are vectors of length $n_\mathrm{sizg}$. As the original matrix $\mathbf{A}$ was a banded matrix, also the triangular matrix $\mathbf{L}$ is a banded matrix, with the same bandwidth. Therefore, the sum in (3.27) starts from $j_\mathrm{min}$ instead of one. Solving (3.27) is done in the spirit of a usual (sequential, not blocked) backward substitution [145], and we solve the equation

$$a_i = L_{ii}^{-1} \left[ b_i - \sum_{j=j_\mathrm{min}}^{i-1} L_{ij} a_j \right]. \tag{3.28}$$

The procedure is similar to the LDL$^\mathrm{T}$-decomposition, i.e., at first the diagonal problem $y_1 = L_{11}^{-1} b_1$ is solved by the first processing element, and $y_1$ is sent to the next processing elements. These update their right hand sides of (3.27), according to $b_i \to b_i - L_{ij} a_j$ (for $j < i$). Afterwards the second row is processed, starting with the diagonal block $a_2 = L_{22}^{-1} b_2$ (of course this is done with the updated block $b_2$), and the result is sent to the next processing elements. This procedure is continued until equation (3.26) is solved. As in the LDL$^\mathrm{T}$-decomposition explained above, all operations on the blocks (solution of the diagonal problems, or updating the right-hand sides) are performed with calls to BLAS.

After solution of (3.26) equation (3.18) can be solved. This is achieved by another backward substitution, to solve the system

$$\mathbf{L}^T \cdot \mathbf{x} = \mathbf{D}^{-1} \cdot \mathbf{a}, \tag{3.29}$$

where $\mathbf{a}$ is the solution of the previous backward substitution, and $\mathbf{D}$ is the diagonal matrix, whose entries are stored on the diagonal of the (decomposed) matrix $\mathbf{A}$. The solution of (3.29) is obtained in the same way as solving (3.26).

#### 3.2.3.4 Lanczos algorithm

With 3.2.3.1, 3.2.3.2, and 3.2.3.3, we have provided parallel implementations of the routines needed in the Lanczos algorithm. Here we briefly sketch the parallel version of the Lanczos routine:

Before starting the actual Lanczos iteration, we define the first Lanczos vector (which is in principle arbitrary) as $\tilde{\mathbf{s}}_1 = (1, 1, \ldots, 1)^T$, and normalize it with respect to the correct scalar product: $\mathbf{s}_1 = \tilde{\mathbf{s}}_1 / (\tilde{\mathbf{s}}_1^T \cdot \mathcal{B} \cdot \tilde{\mathbf{s}}_1)$. In addition, we set $\alpha_0 = \beta_0 = 0$. Subsequently, the Lanczos steps can be performed:

1. Evaluate $\mathbf{A}^{-1} \cdot \mathcal{B} \cdot \mathbf{s}_j$ with the help of the LDL$^\mathrm{T}$-decomposition and of the subsequent backward substitution.
2. Calculate $\alpha_j = \mathbf{s}_j^T \cdot \mathbf{A}^{-1} \cdot \mathcal{B} \cdot \mathbf{s}_j$, according to (3.6).
3. Calculate the vector $\mathbf{t}_{j+1} = \mathbf{A}^{-1} \cdot \mathcal{B} \cdot \mathbf{s}_j - \alpha_j \mathbf{s}_j - \beta_{j-1} \mathbf{s}_{j-1}$, according to (3.7).
4. Calculate $\beta_j = \sqrt{\mathbf{t}_{j+1}^T \cdot \mathcal{B} \cdot \mathbf{t}_{j+1}}$, according to (3.7).
5. According to (3.8), the next Lanczos-vector is given by $\mathbf{s}_{j+1} = (1/\beta_j) t_{j+1}$. The action of $\mathcal{B}$ on $\mathbf{s}_{j+1}$ is calculated, and the next Lanczos step can be started (end of Lanczos step).

$n_\mathrm{lancz}$ Lanczos steps yield a tridiagonal matrix with diagonal $\alpha_1, \alpha_2, \ldots, \alpha_{n_\mathrm{lancz}}$ and sub-diagonal (respectively supra-diagonal) $\beta_1, \beta_2, \ldots, \beta_{n_\mathrm{lancz}-1}$. This matrix is diagonalized using a QR algorithm [145]. The eigenvectors of the generalized eigenvalue problem are obtained as a linear combination of the Lanczos vectors, with the coefficients of the linear combination given by the coefficients of the matrix that diagonalizes the tridiagonal matrix.

Using exact arithmetics, this would be the complete Lanczos algorithm. However, in a numerical implementation, the finite precision of the operations leads to rounding errors. The main effect of these rounding errors lies in the loss of the orthogonality of the Lanczos vectors [159]. Thus, we explicitly reorthogonalize the vectors after each Lanczos step (defined above):

$$\mathbf{s}'_j = \mathbf{s}_j - \sum_{i=1}^{j-1} \gamma_i \mathbf{s}_i, \text{ with } \gamma_i = \mathbf{s}_i \cdot \mathcal{B} \cdot \mathbf{s}_j. \tag{3.30}$$

In this way the new vectors $\mathbf{s}'_j$ are orthogonal by construction, even with finite precision of the operations.

Finally, since the number of Lanczos steps is much smaller than the dimension of the matrices, obviously not all eigenvalues are converged. Performing only $n_{\mathrm{lancz}}$ Lanczos steps is equivalent to setting $\beta_{n_{\mathrm{lancz}}} = 0$, therefore it cannot be assumed that eigenvectors with a finite overlap with the last (the $n$-th) Lanczos vector are converged. Thus the convergence of eigenvectors and associated eigenvectors is tested with the requirement that the overlap of the converged eigenvectors with the last row of $\mathbf{S}$, i.e. with $\mathbf{s}_{n_{\mathrm{lancz}}}$, should vanish.

### 3.2.4 Performance of the parallel code

Of course, the first goal of a computer program for the numerical simulation of a physical process is the stable production of reliable, converged results. However, if the size of the problem increases, and the use of so called 'supercomputers' (a fancy term for the 'fastest and most powerful general-purpose scientific computing systems available at any given time' [152]) is needed, an almost equally important requirement is to use the computing facilities in a most efficient way.

The speed of a computer is characterized, e.g., by the peak performance of the CPU (central processing unit), which is measured by the number of floating point operations carried out per second (FLOPS=$10^{-6}$ MFLOPS=$10^{-9}$ GFLOPS). Thus, the performance of a parallel code can be measured in the number of MFLOPS achieved per processing element ('single processing element performance'). In addition, a well performing code should also be scalable, as already mentioned before. In our context, the scalability of the code requires that the solution of a larger problem – which requires a bigger number of processing elements due to the larger size of the matrices – should achieve a similar single processing element performance as a smaller problem does. As already mentioned above, for a good single processing element performance of our code we made use of BLAS where it was possible.(4) Furthermore, the code is written such that the communication overhead is reduced.

To achieve an optimal single processing element performance, the block-size $n_{\mathrm{sizg}}$ can be optimized for the BLAS routines. The optimal choice strongly depends on the specific computer that is employed, in particular on the available cache. While we experienced a quite good performance for $n_{\mathrm{sizg}} \simeq 20$ on the CRAY T3E, we observed a better performance for larger block-size on the HITACHI SR8000-F1. For realistic problem sizes, however, we only tested the range $n_{\mathrm{sizg}} = 28, \dots, 64$, yet we expect an even better performance for larger values of $n_{\mathrm{sizg}}$. However, following (3.12) and (3.13), the block-size $n_{\mathrm{sizg}}$ is determined by the total dimension $n_{\mathrm{tot}}$ of the matrices, and the accessible memory per processing element $M$ according to

$$n_{\mathrm{sizg}} = \frac{M}{n_{\mathrm{r}} \cdot n_{\mathrm{tot}}}. \tag{3.31}$$

---

(4) With much effort eventually a better performance than those of BLAS can be achieved, especially, if basic vector or vector-matrix operations (i.e. BLAS-1 or BLAS-2) are used. However, in general the use of BLAS is preferable, especially, if matrix-matrix operations (BLAS3) are used [160].

Thus, for a large problem size, the block-size decreases and also the single processing element performance decreases. To overcome this problem, and achieve a satisfactory performance even for a large $n_{\text{tot}} \gtrsim 500000$, we did (on the HITACHI SR8000-F1) not employ eight processing elements per node but a smaller number, and could thus enlarge $M$.

Table 14 summarizes the performance of our code for various problem sizes (under production conditions):

| $n_{\text{tot}}$ | 1010016 | 669264 | 617484 | 471912 | 279072 | 279072 | 279072 |
|---|---|---|---|---|---|---|---|
| $n_{\text{larg}}$ | 6306 | 6832 | 6622 | 7936 | 4862 | 4862 | 4862 |
| $n_{\text{lancz}}$ | 210 | 200 | 200 | 210 | 350 | 230 | 100 |
| $n_{\text{sizg}}$ | 28 | 33 | 35 | 42 | 64 | 64 | 64 |
| $\#\text{nodes}$ | 20 | 15 | 15 | 12 | 5 | 5 | 5 |
| $n_{\text{procs}}$ | 114 | 104 | 104 | 96 | 40 | 40 | 40 |
| $n_{\text{procs}}/\text{node}$ | 5.7 | 6.9 | 6.9 | 8 | 8 | 8 | 8 |
| MFLOPS/p.e. | 290 | 305 | 334 | 409 | 408 | 442 | 495 |
| GFLOPS tot. | 33 | 32 | 35 | 39 | 16 | 18 | 20 |
| rel. perf. | 14 | 18 | 19 | 27 | 27 | 30 | 33 |

Table 14: Performance of the code for variable problem size. The size of the problem is specified by the first two lines. The first four and the sixth column display examples with a similar number of Lanczos iterations ($n_{\text{lancz}}$ which is given in the third line). The matrices used for the examples shown in the fifth, the sixth, and the seventh column are the same, only the number of Lanczos iterations varies in the three examples. The fifth and the sixth line show the number of employed nodes and the number of employed processing elements, respectively. For $n_{\text{tot}} > 500000$, we did not employ all processing elements of a node (the average number of processing elements per node is shown in line seven), so that $n_{\text{sizg}}$ (fourth line) does not get too small (to maintain good BLAS performance). The eighth line shows the single processing element (p.e.) performance in MFLOPS, and the ninth line the total performance of the code in GFLOPS, the ratio of this value and of the possible peak performance (peak performance per node times the number of nodes that are employed, given in line six) is shown in the tenth line.

For problems with $n_{\text{tot}} < 500000$, where the block-size $n_{\text{sizg}}$ is consequently relatively large, we achieve a quite good single processing element performance, together with a good effective performance of the code (the expected performance of the HITACHI SR8000-F1 measured with the LRZ-benchmarks is approximately 33% of the peak performance compared to 12% in the most unfavorable case [147]). In those cases we also achieve a good scalability, as can be seen from the comparison of lines six and eight of table 14 (for the examples shown in columns four and six). As mentioned above, for larger $n_{\text{tot}}$ we employed less than eight processing elements per node. While this increases the single processing element performance (using a smaller $n_{\mathrm{sizg}}$ would decrease the single processing element performance in the examples shown in the first four columns even more), a too small number of processing elements per node can reduce the efficiency of the code (since in this case some of the processing elements are 'idle', i.e. they don't do anything during the run of the code and cannot be used by other users of the computer). To specify the efficiency of our code, we display the 'relative performance' given by the ratio of the possible peak performance to the effective performance of the code in the last line of table 14.

For large $n_{\mathrm{tot}}$ we expect an improvement of the relative performance by using the special features of the HITACHI SR8000-F1, i.e., the hybrid architecture. In this case, $n_{\mathrm{sizg}}$ can be increased (as $M$ in (3.31) is given by $6.5\ \mathrm{GByte}$ instead of $6.5\ \mathrm{GByte}$ divided by the number of employed processing elements per node), and hence the efficiency of the BLAS will be also increased. The necessary modification of our code will be accomplished in the near future.

Finally, from the comparison of the examples shown in the fifth, sixth, and seventh columns, we see that an increase of the number of Lanczos vectors decreases the efficiency of the code. Thus, it is preferable to employ only a few hundred Lanczos iterations and perform several diagonalizations, instead of employing a very large number (several thousand) of Lanczos iterations in one single diagonalization.

## 3.3 Application

Our theoretical/numerical apparatus outlined above – the theoretically exact description of microwave driven Rydberg states, together with its numerical implementation – can now be applied to a real physical example. Before the matrices are filled according to (2.50) and (2.52), and before the generalized eigenvalue problem is solved, we have to specify the shift $E_0$ as defined in (3.1). We define $E_0$ by the region of the quasi-energy spectrum we are interested in, which is usually chosen close to the field free limit of the atomic initial states that are expected to show a noticeable ionization probability at the given field parameters (amplitude and frequency).

Typically the states in one Floquet zone of a given generalized parity $\Pi$ are not obtained with a single shift $E_0$ and a large number of Lanczos steps, but it is preferable to divide the Floquet zone in $10-30$ pieces, and to employ only a smaller number (approximately $150-400$) of Lanczos steps per shift. As we have seen in section 3.2.4 such a procedure leads to a more efficient code than using several thousand Lanczos steps. Secondly, the spectrum of driven Rydberg states consists of resonances embedded in the continuum, but to represent the initial atomic states we are interested in, we only need the resonance states [34]. Yet, with an increase of the number of Lanczos steps the number of continuum states we find increases faster than the number of resonances, since there are many continuum states next to each resonance, and the Lanczos algorithm starts to find those eigenvalues which are closest to a given shift. Therefore, we choose a sufficiently dense grid of shifts

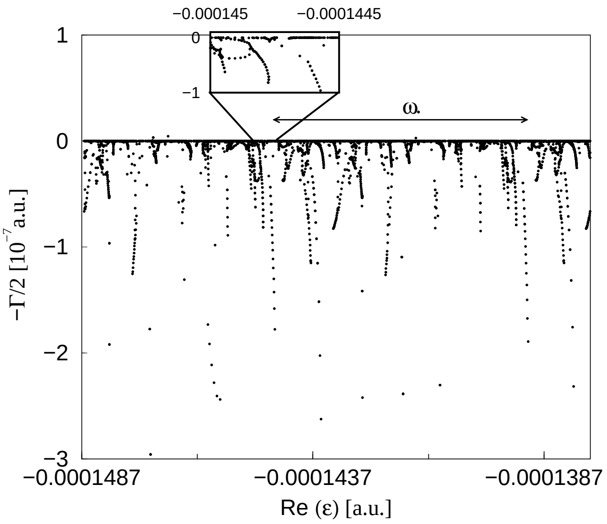

Figure 3.2: Plot of the complex eigenvalues $E_j - \mathrm{i}\Gamma_j/2$ of the complex rotated Hamiltonian of microwave driven lithium atoms exposed to a field with $F = 2.3 \cdot 10^{-9}$ a.u. and $\omega = 36 \cdot 2\pi$ GHz $= 5.47 \cdot 10^{-6}$ a.u.. The continua are rotated in the lower complex plane, ideally by an angle $-2\Theta$ starting from the branching points $-0.00014454$ a.u., and $-0.00013907$ a.u. (defined by the effective threshold $-1/(2(n_{\mathrm{sup}}\alpha))$, with $\alpha = 70$ and $n_{\mathrm{sup}} = 155$, shifted by $-17\omega$ respectively $-18\omega$). This is approximately true only close to the real energy axis, and only near the branching point, as displayed in the inset (the branching point is situated approximately in the middle of the inset, the energy range displayed in the inset is approximately $\omega/10$). Although there exist plenty of continuum states that are not fully converged, the relevant states that contribute to the ionization probability (through a non-vanishing overlap) of the initial state are converged, and exhibit ionization rates of the order $10^{-9}, \ldots, 10^{-13}$. In the plot they appear as black dots close to the (real) energy axis.

in the Floquet zone we are interested in. This provides for a better performance of our code, and a smaller number of continuum states is obtained.

A typical example for the spectrum generated this way is shown in figure 3.2, where we display the complex quasi-energies of lithium atoms exposed to a microwave field of frequency $\omega/2\pi = 36$ GHz, and field amplitude $F = 2.3 \cdot 10^{-9}$ a.u. We display two Floquet zones of width $\omega$, in the subspace with parity $\Pi = +1$ centered around the field-free state $|n_0 = 59, \ell_0 = m_0 = 0\rangle$. As explained in section 2.1.3, theoretically the continuum states are rotated by $2\Theta$ (where $\Theta = 0.06$ in the calculations leading to figure 3.2) around the branching points. The latter are given by the effective threshold (2.46), shifted by integer multiples of $\omega$. In the case of figure 3.2, this corresponds to the branching points at $E_{\mathrm{bp1}} = -0.00013907$ a.u. and $E_{\mathrm{bp2}} = -0.00014454$ a.u. The latter one is located approximately in the middle of the energy range shown in the inset of figure 3.2.

A deeper investigation of figure 3.2 indicates that there are many states with ionization rates $|\Gamma/2| > 5 \cdot 10^{-8}$ a.u., most of which represent continuum states. However, these states are not situated on parallel half lines starting at $E_{\rm bp1}$ or $E_{\rm bp2}$, but they are lying on (not necessarily straight) lines distributed over the Floquet zone. Only close to the real axis and close to the branching points are the continuum states approximately localized along parallel lines, but even here we cannot identify a single half line starting at the branching point, but rather several of them, as displayed in the inset of figure 3.2. A similar behavior was already described in studies on microwave driven atomic hydrogen in a moderately excited energy range $n_0 \simeq 23$ [33], where this apparent splitting of the continua was attributed to the lifting of the continuum angular momentum degeneracy, induced by the finite basis size employed in numerical calculations.(5) This discrepancy between mathematical theory [161, 102] and numerical experiment as far as the continuous part of the spectrum is concerned leads us immediately to the question of the accuracy of the numerical results, i.e. to the question which numerical eigenstates can be considered as converged.

The theory of complex dilation only ensures that the Green's function that involves a sum over all states (resonances and continua), and therefore also the time evolution operator (2.17) is converged [162]. Thus, we can, in principle, only be sure that the ionization probability (2.58) corresponds to a (converged) physical quantity, while single atom-field eigenstates do not represent any physically meaningful quantity. However, as long as a resonance is relatively isolated, and their width $\Gamma$ is not too large, such a state dominates the time evolution operator, and $\varepsilon = E - \mathrm{i}\Gamma/2$ can be identified with the quasienergy and corresponding inverse life-time of a single atom-field eigenstate. Single continuum eigenstates or resonances that are strongly coupled to the continuum, on the other hand, cannot be represented by single complex eigenvalues of the complex dilated Hamiltonian, but their representation requires the sum over all eigenstates of $\mathcal{H}_\Theta$ [163, 164, 64, 162].

In order to make reasonable statements about the convergence of the obtained results it is crucial to do the relevant tests. In our situation, the following criteria have to be fulfilled by converged results:

- $-\Gamma_j < 0$: The imaginary parts of the complex rotated quasi-energies have to be negative.
- $\mathrm{Re}(w_j) = \mathrm{Re}\langle n_0, \ell_0, m = 0|R(-\Theta)|\varepsilon_j^\Theta\rangle^2 \geq 0$: In the complex dilated eigenvalue problem $w_j$ is actually the square and not the modulus square of the projection $\langle n_0, \ell_0, m = 0|R(-\Theta)|\varepsilon_j^\Theta\rangle$. Therefore – in contrast to the un-dilated case – a priori nothing ensures the positivity of $w_j$ nor of $\mathrm{Re}(w_j)$. However, as the weight of a given initial state projected on some

---

(5) Note that in one-dimensional calculations on microwave driven atomic hydrogen, on the other hand, also for the location of the continua good agreement with the mathematical theory was found in [33].

atom-field eigenstate has to be a real, positive number in a converged situation, $\mathrm{Re}(w_j) \geq 0$ has to be fulfilled.

- $\mathrm{Im}\langle n_0, \ell_0, m = 0|R(-\Theta)|\varepsilon_j^{\Theta}\rangle^2 = 0$: The same argument (for $w_j$ being a real, positive number) leads to the requirement that the imaginary parts of the weights have to vanish.

- $P_{\mathrm{ion}}(t = 0) = \sum_j \langle n_0, \ell_0, m = 0|R(-\Theta)|\varepsilon_j^{\Theta}\rangle^2 = 1 + \mathrm{i} \cdot 0$: As the atom-field eigenstates form a complete basis set, the sum over the weights of all atom-field eigenstates in a Floquet zone, summed over both generalized parities must add up to one. This includes the requirement that we have chosen a sufficiently dense grid of shifts $E_0$ and a sufficiently large number of Lanczos iterations per diagonalization at each shift, in order to represent the atomic initial state in the Floquet basis.

- $(E_j^{\Pi} - \mathrm{i}\Gamma_j/2) + \omega = E_j^{-\Pi} - \mathrm{i}\Gamma_j/2$: A typical problem of non-converged results is that the periodicity of the Floquet spectrum does not even hold locally. We experienced this criterion being stronger for the imaginary part of the spectrum. While a too small basis set may still abide the periodicity of the real parts $E_j$ of the quasi-energies, in such non-converged situations the width $\Gamma_j$ of the atom-field eigenstate $\varepsilon_j = E_j - \mathrm{i}\Gamma_j/2$ (in the subspace with parity $\Pi$) typically differs by more than one order of magnitude from the width of the same state dressed by one photon, i.e., from the width $\tilde{\Gamma}_j$ of the state $E_j + \omega - \mathrm{i}\tilde{\Gamma}_j/2$ (which now belongs to the subspace with parity $-\Pi$).

- Finally, the results, i.e., the complex quasi-energies and the weights of the desired initial states, have to be stable under variation of the parameters which determine, e.g., the basis size, the rotation angle $\Theta$,etc.

### 3.3.1 The parameters

In this section we will elucidate the choice of the numerical parameters(6) we employed for our numerical experiment. We start with the basis size that is needed. This is determined by the following parameters:

1. $n_{\mathrm{sup}}$: The number of Sturmian functions $|S^{(\alpha)}_{n,\ell,m}\rangle$ for the expansion of the Floquet-states according to (2.45). As explained in section 2.4, $n_{\mathrm{sup}}$ is related to the effective cutoff $n^{\mathrm{eff}}_{\mathrm{max}}$ by $n^{\mathrm{eff}}_{\mathrm{max}} = \sqrt{n_{\mathrm{sup}} \cdot \alpha}$. In state-of-the-art experiments the effective threshold varies between $n^{\mathrm{eff}}_{\mathrm{max}} \simeq 90$ [20], $n^{\mathrm{eff}}_{\mathrm{max}} \simeq 135$ [42], and $n^{\mathrm{eff}}_{\mathrm{max}} \simeq 280$ [49]. To obtain converged results even for initial states $n_0 = 70 \ldots, 80$, we need an effective threshold $n^{\mathrm{eff}}_{\mathrm{max}} > 100$, and in

---

(6) Here we want to emphasize that our approach includes no free, adjustable parameters. The only parameters we have to choose are tested with the requirement of a stable, converged result, but not employed as free parameters which typically have the job to 'scale' 'numerical' results to experimental data.

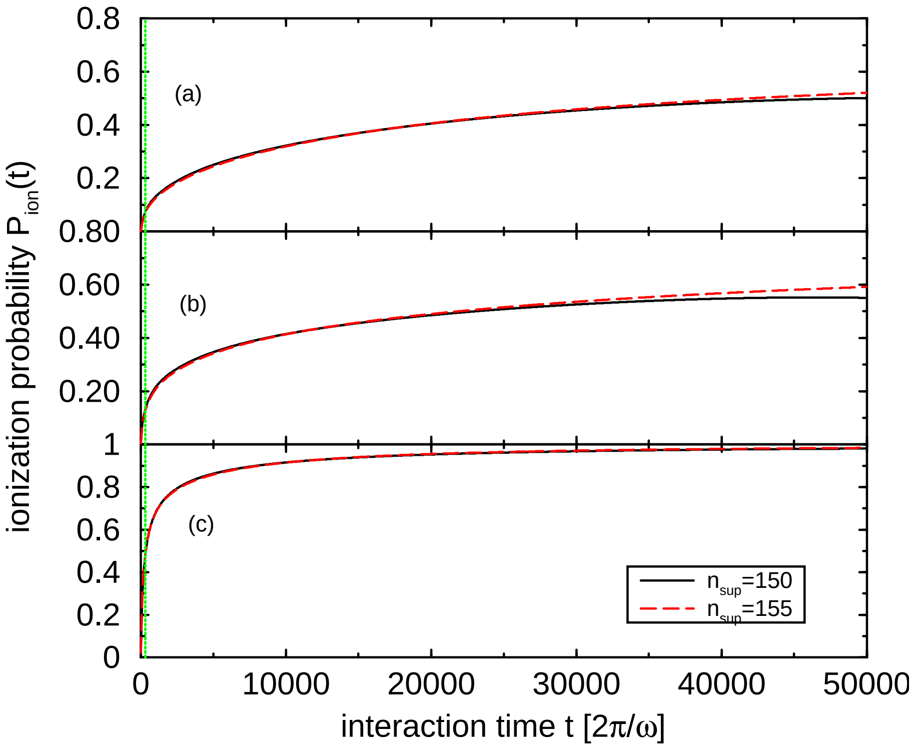

Figure 3.3: Convergence test for variable basis size $n_{\text{sup}}$. The effective cutoff is kept constant $n_{\max}^{\text{eff}} \simeq 104$, by setting either $n_{\text{sup}} = 155$ and $\alpha = 70$ (dashed line), or $n_{\text{sup}} = 150$ and $\alpha = 72.3$ (full line). Displayed is the ionization probability of three different (lithium) initial states $|n_0 = 50, \ell_0 = m_0 = 0\rangle$ (a), $|n_0 = 60, \ell_0 = m_0 = 0\rangle$ (b), and $|n_0 = 66, \ell_0 = m_0 = 0\rangle$ (c), exposed to a field with $F = 3.1 \cdot 10^{-9}$ a.u. and $\omega/2\pi = 36$ GHz, as a function of the interaction time. The vertical dotted line appearing close to $t = 0$ denotes the interaction time $t = 327 \cdot 2\pi/\omega$, a typical experimental interaction time [20] we will employ in our numerical experiments.

practice we employed an effective cutoff $n_{\rm max}^{\rm eff} = 104.2$. This was obtained by fixing $n_{\rm sup} = 155$ and $\alpha = 70.0$ for lithium atoms, and $n_{\rm sup} = 190$ and $\alpha = 57.1$ for rubidium atoms, for which a larger basis size is needed, due to the existence of more non-vanishing quantum defects for the heavier elements (see table 2.3.1). Only in the simulations on rubidium atoms with the parameters of [42], in which a smaller frequency ($\omega/2\pi = 8.87$ GHz) is employed, and hence the condition $\omega \cdot n_0^3 = 1$ requires a larger $n_0 \simeq 91$ (in contrast to $\omega \cdot n_0^3 = 1$ for $\omega/2\pi = 36$ GHz [20] and $n_0 = 57$), we used a slightly larger cutoff $n_{\rm max}^{\rm eff} \simeq 110$ (employing $\alpha = 69.1$ and $n_{\rm sup} = 175$). In figure 3.3 we show the effect of obtaining the same $n_{\rm max}^{\rm eff}$ with slightly different parameters $n_{\rm sup}$ and $\alpha$. Here we display the ionization probability of three different initial states $|n_0 = 50, \ell_0 = m_0 = 0\rangle$ (a), $|n_0 = 60, 0, \ell_0 = m_0 = 0\rangle$ (b), and $|n_0 = 66, \ell_0 = m_0 = 0\rangle$ (c), as a function of the interaction time for the choice $n_{\rm sup} = 150$ and $\alpha = 72.3$ (full line), and the combination $n_{\rm sup} = 155$ and $\alpha = 70$ (dashed line). The results are quite stable under this variation – even for an interaction time of $t = 50000 \cdot 2\pi/\omega$ the relative difference in the ionization probability is smaller than 7% which is in the range of experimental accuracy [86]. For typical interaction times we will be interested in, i.e. $t \simeq 100, \ldots, 1000 \cdot 2\pi/\omega$, the relative error is even smaller than 3%.

2. The number of photons $k$ taken into account in the Fourier expansion (2.10) of the Floquet states. The minimum and the maximum number of photons play a different physical role - it is therefore useful to investigate them both separately:

   (a) $k_{\rm min}$: The results are quite stable under variation of the minimum number of photons employed as a cutoff in the expansion (2.10). Here, the choice $k_{\rm min} \simeq -10$ is typically enough to obtain converged results, as can be seen in figure 3.4, which reproduces a typical situation. Even in the lower plot – which is a magnification of the region close to the real axis in the upper plot – we can detect only a small difference between the results obtained with $k_{\rm min} = -6$ and with $k_{\rm min} < -6$. The choice of $k_{\rm min}$ is mainly governed by the states that we want to describe: for instance, if the shift $E_0$ is set to $E_0 \simeq -0.0003470$ a.u. (close to the field-free energy $E = -0.0003471$ a.u. of the state $|n_0 = 38, \ell_0 = 1, m_0 = 0\rangle$) – which is the case in figure 3.4 – a choice $k_{\rm min} \simeq -8$ makes it impossible to characterize Floquet states emanating from field free states with principal quantum number $n_0 = 35$, since the gap between $E_0$ and $-1/(2 \cdot 35^2)$ is larger than $11 \cdot \omega$. In order to describe these states correctly, the choice $k_{\rm min} \simeq -13, \ldots, -16$ would be appropriate.

   (b) $k_{\rm max}$: The situation is completely different for the maximum cutoff in the sum (2.10). The maximum number of photons which dress the atomic states determines the coupling to the continuum. Obviously,

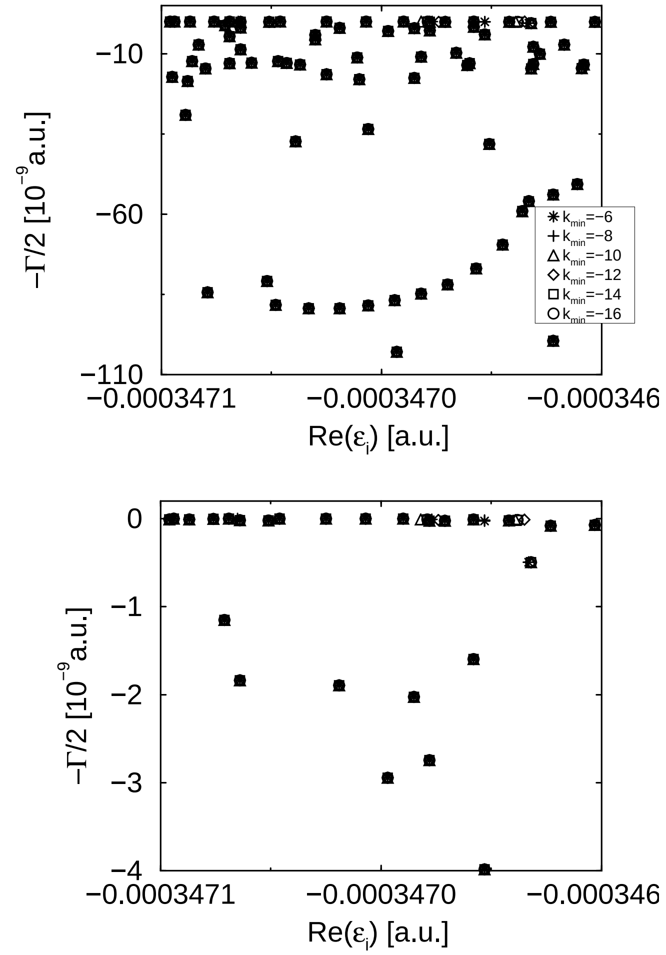

Figure 3.4: Convergence test in $k_{\min}$: Complex energies $\varepsilon_j$ of microwave driven lithium atoms with angular momentum projection $m = 0$, at field amplitude $F = 5.5 \cdot 10^{-9}$ a.u., and frequency $\omega = 5.47 \cdot 10^{-6}$ a.u. (i.e. $\omega/2\pi = 36$ GHz), in the energy range around the field-free state $|n_0 = 38, \ell_0 = 1, m_0 = 0\rangle$. Different symbols correspond to the different values of $k_{\min}$ which is the minimum cutoff value of the photon number employed in the sum (2.10). The lower plot is a magnification of the upper, in the region close to the real axis, the symbols are chosen the same as in the upper plot. Obviously, the results are quite stable under variation of $k_{\min}$. Converged results are achieved already for $k_{\min} \simeq -10$. The other parameters are chosen as $k_{\max} = 74$, $\ell_{\max} = 73$, $\Theta = 0.06$.

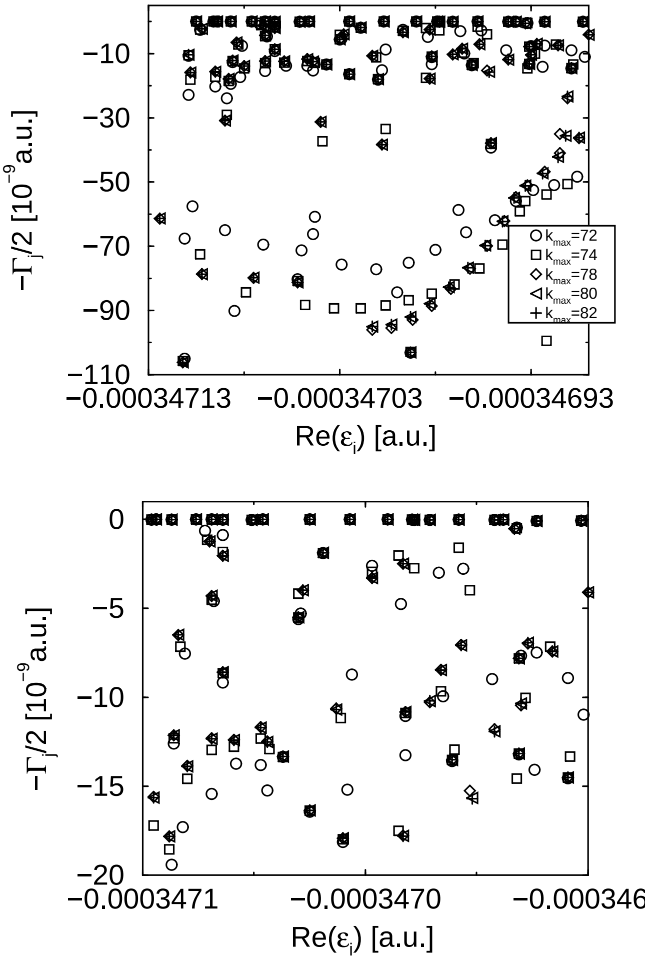

Figure 3.5: Convergence test in $k_{\max}$: For the same situation as in figure 3.4, the cutoff value for the photons that describe the coupling to the continuum is tested. Again, different symbols denote different values of $k_{\max}$. The same values and corresponding symbols are used in the lower plot that is a magnification of the upper, in the region close to the real axis. It can be seen that for converged results at least $k_{\max} = 78$ photons are needed. (The other parameters are chosen as: $k_{\min} = -18$, $\ell_{\max} = 73$, and $\Theta = 0.06$.)

it has to suffice to reach the effective continuum $k_{\rm max} \geq N_{\rm min}$ with $N_{\rm min} = |E_0 + 1/(2n_{\rm sup} \cdot \alpha)|/\omega$. In studies on the microwave ionization of atomic hydrogen with principal quantum numbers $n \simeq 23$ [34] it was found that this minimum number $N_{\rm min}$ is close to the number of photons needed to obtain converged results, i.e., $k_{\rm max} \simeq N_{\rm min} + 2$ was employed. Yet, the situation gets more complicated in our case, but this is only indirectly related to the use of alkali atoms instead of atomic hydrogen: In fact, it is not the non-hydrogenic core that produces the need of a larger photon number, but the use of length gauge instead of velocity gauge which was employed in [34]. It is known from the study of multi-photon processes that the velocity gauge leads to a faster convergence than the length gauge [93, 92], but due to the partition of configuration space our approach requires the use of the length gauge (see section 2.3). A typical situation is displayed in fig. 3.5, where we have plotted the complex energies in a given range with varying photon numbers $k_{\rm max}$. Here the minimum number of photons to reach the effective continuum is given by $N_{\rm min} \simeq 55$, while the minimum number needed to obtain converged results is $k_{\rm max} \simeq 78$. This gives a rough estimate for $k_{\rm max}$ that was valid as a rule-of-thumb for our situation, namely: $k_{\rm max} \simeq 1.5 \cdot N_{\rm min}, \ldots, 2 \cdot N_{\rm min}$. Note, however, that our results on atomic hydrogen presented further down have been obtained in the velocity gauge (see also section 2.1), and there a smaller photon number $k_{\rm max}$ could be used.

3. $\ell_{\rm max}$: The last parameter that determines the dimension of the matrices is the maximum number of angular momenta in the expansion of the atom-field eigenfunctions in the Sturmian basis (2.45). Of course, $\ell_{\rm max} = n_{\rm sup} - 1$ would always lead to converged results, given that the other parameters are chosen properly. Yet, especially in the situation where the multi-photon process is of high order (and hence a large number $k_{\rm max}$ of photons is needed) it is vital to truncate the basis – which determines the memory needed to store the matrices – as much as possible without loss of convergence. A first guess for the choice of $\ell_{\rm max}$ could be $\ell_{\rm max} = n^{\rm eff}_{\rm max}$, but it turned out that this value is not necessarily enough. A situation where a larger number of angular momenta is needed occurs when a large photon number $k_{\rm max} > n^{\rm eff}_{\rm max}$ is needed for the convergence. In this case it is possible to access states with angular momentum $\ell > n^{\rm eff}_{\rm max}$ – that already belong to the effective continuum – via a multi-photon transition of the order $k_{\rm max}$. The fact that the high angular momentum states in the effective continuum are needed to achieve converged results is a consequence of the fact that not only the bound state dynamics, but also the interaction with the continuum is important to describe microwave driven Rydberg states correctly. Consequently, an appropriate choice for the maximum angular momentum is $\ell_{\rm max} \geq \ell_0 + k_{\rm max} \pm j$, where $\ell_0$ is the angular momentum of the initial atomic state that shall be described, and $j$ is a

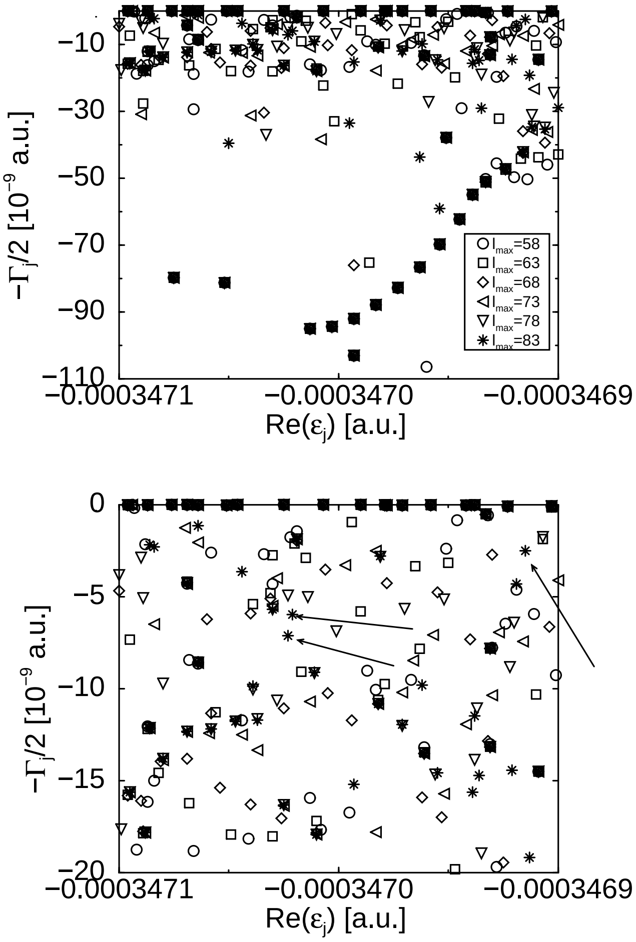

Figure 3.6: In the same situation as shown in figure 3.5 and 3.4 the maximum angular momentum $\ell_{\max}$ used for the representation of the atom-field eigenstates is tested. Here the situation is a little bit more complicated: As can be seen, convergence of *all* states is not achieved, even for $\ell_{\max} = 83$. However, it is sufficient that the eigenvalues with a non-vanishing overlap with the initial state are converged. As apparent from the lower plot, the isolated stars marked by arrows are not converged. These states, however, have an overlap $w_j < 10^{-5}$ with the states we are interested in, i.e. with the initial states $|n_0, \ell_0, m_0 = 0\rangle$ with $n_0 = 35, \ldots, 54$ and $\ell_0 = 0, 1$. The non-converged states are high angular momentum states (and therefore high $n_0$-states), that experience an extremely high field amplitude. Consequently, these states could only be converged with a larger basis size, in particular not only a larger $l_{\max}$ but also a larger number of photons would be required. (The other parameters are $k_{\max} = 80$, $k_{\min} = -18$, and $\Theta = 0.06$.)

small number ($j = 1, \ldots, 5$).
In figure 3.6 the situation is illustrated, again with a typical plot of a region of complex energies obtained for different values of $\ell_{\max}$ (as in the two previous figures the lower plot is a magnification of the region close to the real energy axis in the upper plot). As a matter of fact, pictures like this are a little bit misleading without any additional information:
Apart from the states that are converged with the chosen maximum angular momentum $\ell_{\max}$, there are some states that are still not converged even with the largest value $\ell_{\max}$. In the lower part of figure 3.6 this is the case, e.g., for the isolated stars marked by arrows. Clearly, these states are not converged even for the choice $\ell_{\max} = 83$. These states are emanating from high angular momentum states – and therefore from high $n_0$ states – that experience an extremely large field, and hence the convergence of these states requires a larger photon number. However, they exhibit only vanishing overlap with those initial states we are here interested in. More precisely, these states have an overlap $w_j < 10^{-5}$ with the initial states $|n_0, \ell_0, m_0 = 0\rangle$ with $n_0 = 35, \ldots, 54$ and $\ell_0 = 0, 1$.

So far, we gave account of the parameters $n_{\text{sup}}, k_{\min}, k_{\max}, \ell_{\max}$, which determine the basis size, this is the dimension $n_{\text{tot}}$ of the matrices that have to be diagonalized. However, the required memory to store the matrix $\mathbf{A}$ is not yet completely determined, since the effective bandwidth of $\mathbf{A}$ can still be minimized by choosing an intelligent hierarchy of the quantum numbers $k$, $\ell$, and $n$ for the ordering of the matrices: Due to the selection rules (2.54) and (2.53), even the banded part of the matrix $\mathbf{A}$ is far from being fully occupied. To obtain matrices with the smallest possible bandwidth $n_{\text{larg}}$, it is preferable to choose the quantum number with the smallest range as the outmost and the one with the largest range as the innermost. This leads to the following rule-of-the-thumb: If the total number of photons $k_{\max} + |k_{\min}| + 1$ is less than the maximum angular momentum $\ell_{\max}$, it is reasonable to order the matrices according to $\ell \to k \to n$ (i.e. the outermost quantum number is $\ell$, the next $k$, the innermost $n$). If the number of photons exceeds the maximum angular momentum, the ordering $k \to \ell \to n$ leads to a smaller bandwidth $n_{\text{larg}}$.

Besides the parameters which determine the size of the matrices, there are some additional parameters that fix the basis set without influencing the size of the matrices. They are given by:

1. $\alpha$: The Sturmian scaling parameter in the definition (2.45) was already mentioned above, in the discussion of the effective threshold $n_{\text{sup}}^{\text{eff}}$. Varying $\alpha$ leads to a change of the effective threshold $n_{\text{sup}}^{\text{eff}}$, and may change the photon order of the ionization process. Given that the other parameters are chosen properly (and especially that the effective threshold is not too low in energy), this influences the widths of the atom-field eigenstates only a little bit. More precisely, modeling a situation where the multi-photon process is changed by one order may lead to a (slight) shift of the ionization rates of some eigenstates $\varepsilon_j$, and hence to a small change of the ionization probability at a given

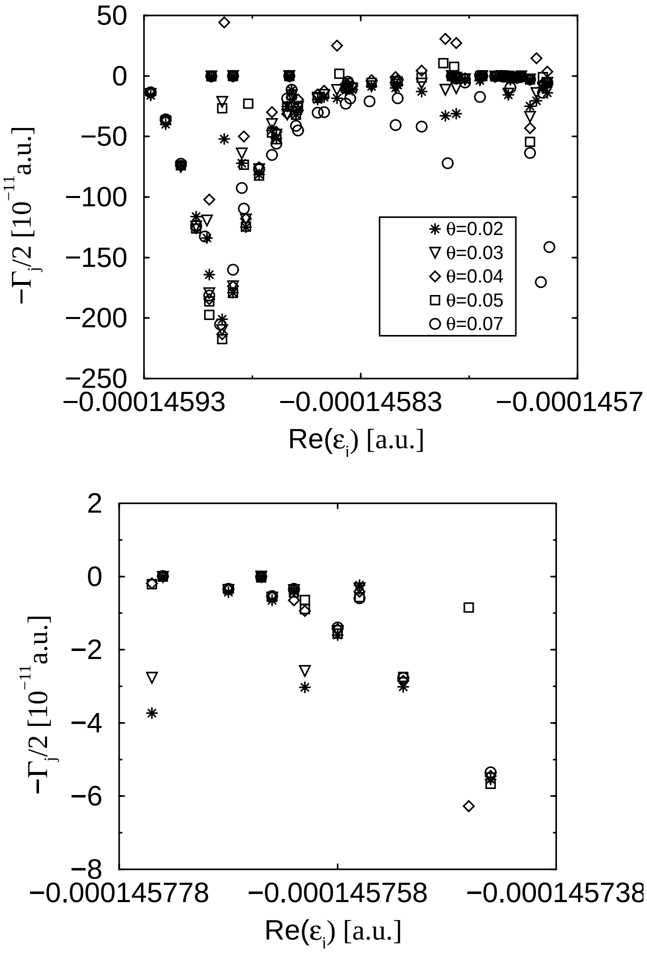

Figure 3.7: Convergence test in $\Theta$: At a field amplitude $F = 2.7 \cdot 10^{-9}$ a.u. and frequency $\omega = 5.47 \cdot 10^{-6}$ a.u., the rotation angle $\Theta$ is tested. As already observed in figure 3.6, it is not possible to obtain convergence of all Floquet states. Again it is sufficient that the states with a non-vanishing overlap with the initial states are converged, what is achieved for $0.02 < \Theta < 0.07$. (The other parameters are chosen as $k_{\max} = 34$, $k_{\min} = -24$, $l_{\max} = 82$, the energy range is chosen close to the field free energy $E = -0.0001456$ of the lithium state $|n_0 = 59, \ell_0 = m_0 = 0\rangle$.)

interaction time. However, such behavior is also observed in laboratory experiments [20], under variation of the effective threshold, and is not an indication of un-converged results, but simply the physical consequence of changing the order of the multi-photon process. Apart from that, the numerical results are quite stable under variation of $\alpha$, at fixed order of the multi-photon process.

2. $\Theta$: According to the theory of complex scaling (see section 2.1.3), the eigenvectors and eigenvalues of the resonances should be independent of $\Theta$, as long as $\Theta$ is large enough to uncover the resonances. As already seen in figure 3.2, a numerical implementation leads to a more complicated situation [165]. Resonances which are too close to continuum states may 'interact' with the latter and slightly shift with respect to their converged position [165, 33]. Too large rotation angles $\Theta > 0.1$ lead to a shift of eigenvalues close to the branching points above the real energy axis, and thus to non-converged results. Too small rotation angles $\Theta < 0.01$, on the other hand, cannot uncover all resonances. We observed stability of the results for $\Theta = 0.02, \ldots, 0.07$. However, it is not possible to obtain convergence of *all* states in a Floquet zone, but at least the states with a non-vanishing overlap with the low-angular momentum initial states can be converged with this choice. An example for the convergence with respect to $\Theta$ is shown in fig 3.7, for this situation a rotation angle $\Theta = 0.04$ was supposed to be an adequate choice.

3. $r_0$: In contrast to simulations of low-lying alkali Rydberg states $n_0 \lesssim 20$ [108], higher excited states (with $n_0 \gtrsim 30$) are very stable under variation of the radius $r_0$ where the inner and the outer region are matched (see section 2.3). The reason for this stability is that the probability for the highly excited electron to be close ($r \simeq 10$ a.u.) to the atomic core is very small. Obviously, this probability increases for states with lower $n_0$. In our calculations we observed stability for $r_0 \simeq 10, \ldots, 20$, for principal quantum numbers $n_0 > 28$. For $n_0 \simeq 20$, smaller matching radii $r_0 \simeq 4$ lead to stable results.

Before proceeding to the real physical problem and presenting the results of our numerical experiment in the second part of this work, we finally want to give account of the quality of the approximation of the linear dependence of the surface term (ALEDST) that was described in section 2.3.3. Without this approximation, the generalized eigenvalue problem (2.47) is only valid for a surface term evaluated *exactly* at the energy $E + k\omega$, and thus reliable results can only be achieved employing a self consistent approach. The production of converged results with the help of a self consistent method needs at least two iterations (two diagonalizations of the generalized eigenvalue problem, where the surface term (2.42) for the matrix in the second iteration is evaluated at the eigenvalue obtained with the previous diagonalization), and as a result only one single atom-field eigenstate is converged, while the error of the other states increases with the distance (in energy) from the converged result.

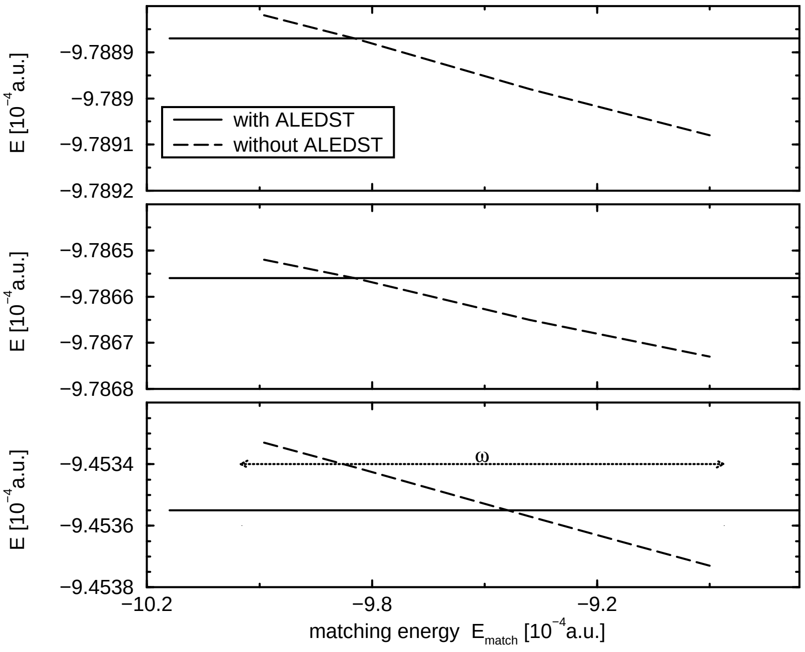

Figure 3.8: Assessment of the quality of ALEDST: Displayed are the field free results for the lithium Rydberg states $|n_0 = 23, \ell_0 = m = 0\rangle$ (upper plot), $|n_0 = 24, \ell_0 = 1, m = 0\rangle$ shifted by $\omega = -1.07171794 \cdot 10^{-4}$ a.u. (middle plot), and $|n_0 = 23, \ell_0 = 2, m = 0\rangle$ (lower plot). The full lines show the results obtained with the surface term calculated according to (2.44) (i.e. with the ALEDST), while the dashed lines show the results obtained with the surface term evaluated according to (2.42), but using a fixed (real) matching energy $E_{\text{match}}$. The results obtained with (2.44) are essentially independent of the matching energy over the whole Floquet zone (displayed by the size of $\omega$ in the lower plot), while the results obtained without this approximation depend strongly on the choice of the matching energy. In the latter case, the results only agree for $E_{\text{match}} = E_j$, with $E_j$ exactly the real part of the quasi-energy of the requested eigenvalue.

For the description of highly excited states, i.e., in the regime of a high density of states, it is crucial to obtain more than one single converged result with a single diagonalization of the generalized eigenvalue problem, since a large number of atom-field eigenstates is needed to represent the field-free initial states. This can be achieved with the ALEDST which we outlined in section 2.3.3.

A typical situation is shown in figure 3.8, where we plotted the (real parts of) three different field free (lithium) eigenvalues $|n_0 = 23, \ell_0 = m_0 = 0\rangle$, $|n_0 = 23, \ell_0 = 2, m_0 = 0\rangle$, and $|n_0 = 24, \ell_0 = 1, m_0 = 0\rangle$ obtained with and without the ALEDST, as a function of the matching energy that was employed.(7) If neither the ALEDST nor the self consistent approach are employed, but the surface term is calculated according to (2.42) with a given matching energy $E_{\mathrm{match}}$, the obtained results (dashed line) depend strongly on the choice of $E_{\mathrm{match}}$. They are only exact if $E_{\mathrm{match}} = E_j = \varepsilon_j + \mathrm{i}\Gamma/2$, where $\varepsilon_j$ is the desired eigenvalue. In contrast, if the ALEDST is employed, the results (solid line) are essentially independent of the matching energy and hence they are located along a horizontal line. In all three examples shown in figure 3.8, the relative error of the (real part of the) results is by three orders of magnitude smaller when the ALEDST is employed as compared to the calculation according to (2.42) (but without employing a self-consistent, iterative procedure). Note that the difference becomes even more significant for the imaginary parts: While we observe a similar stability for the widths $\Gamma_j$ as for the real part of the energy $E_j$ if the ALEDST is employed, the widths fluctuate strongly without this approximation and take negative values as well as positive values.

In the present Floquet problem, the situation seems to be much more complicated than in the case of alkali atoms in static fields [122]. For the static field case it was reported that even without the ALEDST up to hundred converged results could be obtained with a single diagonalization, while we can obtain only a single converged eigenvalue with one diagonalization without employing the linear dependence of the surface term. However, with the use of the ALEDST, we obtain several hundred converged results that are independent of the energy at which they are evaluated.

---

(7) Note that for (field-free and atom-field) eigenstates emanating from states with larger $n_0$ the difference between the results obtained with the ALEDST and without the ALEDST (and without a self-consistent approach) becomes smaller than in the situation displayed in figure 3.8. In such situations, calculations without the ALEDST lead to better results than for low energies around $n \simeq 20$. However, also for higher energies we employed the ALEDST to ensure the convergence of a large number of eigenstates.

# Part II

# The Results

In this second part of this thesis, we shall present and discuss the results of our numerical experiments on microwave driven Rydberg states of hydrogen and alkali atoms. Given the theoretical/numerical apparatus described above, this is the first time that computational physics meets experiment in this intricate and highly complex physical situation. No single approximation on the dimensionality of the problem, on the excitation of the initial atomic state nor on the parameters that characterize the periodic external drive are needed. As a matter of fact, we shall see that in some respect computational physics actually *beats* experiment, since, in our virtual laboratory, experimental conditions can be realized which – though perfectly realistic – are virtually unaccessible for the traditional experimentalist. More precisely, our apparatus allows to perform the same (numerical) experiment on different atomic species, using precisely the same laboratory parameters.

In chapter 4, we start out with the fundamental building block of the experimental analysis of microwave ionization processes, the ionization yield. Its dependence on the driving field amplitude, on the atomic initial state, and on the atom-field interaction time is investigated, and analyzed in terms of the underlying spectral structure, as well as in terms of the population distribution over the bound space part of the spectrum, in terms of the Shannon width.

The following two chapters present the central physical results of this work: In chapter 5, the ionization thresholds of driven alkali and hydrogen atoms are analyzed over a broad range of atomic initial states under *precisely* identical experimental conditions. This comparison elucidates the similarities of alkali and hydrogen Rydberg states, as well as the experimentally observed considerable differences in the ionization dynamics of these systems, that remained hitherto unexplained, for more than one decade. We shall identify three different regimes in the ionization dynamics of driven, singly excited non-hydrogenic Rydberg states, and identify the relevant frequency scales separating these regimes. This ultimately allows to establish scaling rules for the ionization dynamics of driven alkali atoms.

Chapter 6 addresses a complementary aspect of our system: The external field induces a strong coupling of atomic bound and continuum states, leading to ionization on a finite time scale. This highly non-perturbative ionization process can be seen as a probe of the complex bound state dynamics. Hence, microwave-driven Rydberg states represent a typical, complex quantum system which exhibits decay. In chapter 6 we study the decay of the survival probability of the atomic bound state population, and find an algebraic decay as familiar for quantum systems with a classically mixed regular-chaotic counterpart. However, our observations also suggest important qualitative amendments to some predictions based on the study of simple toy models.

Finally, chapter 7 summarizes our results and briefly outlines some open questions.

# Chapter 4

# Microwave Ionization of lithium Rydberg atoms

## 4.1 Fixed field amplitude – various initial states

To provide for a comprehensive understanding of the ionization dynamics of microwave driven alkali Rydberg states, we perform a numerical experiment which employs exactly the parameters of the Stony Brook experiments on atomic hydrogen [20]. Since the latter are by now rather well understood, the direct comparison of alkali and hydrogen results will immediately reflect the additional effects induced by a non-hydrogenic atomic core.

We chose to model the Stony Brook experiment, since it arguably covers the widest range of scaled frequencies, such that the regime of classically chaotic ionization ($\omega_0 < 1$), as well as the regime of dynamical localization ($\omega_0 > 1$) are explored (see section 1.1.1). Following the (classical) scaling rules for atomic hydrogen (2.19) and (2.20), in these experiments the scaled frequency is varied by fixing the laboratory frequency and varying the principal quantum number of the initial atomic states, at fixed interaction time $t \simeq 327 \cdot 2\pi/\omega$. Since our method allows to project the atom-field eigenstates obtained with a fixed field amplitude and frequency on various atomic initial states, a procedure like this is more convenient than fixing the initial state and varying the laboratory frequency. The latter approach was employed in the experiments of the Pittsburgh group [21], which also scanned a wide scaled frequency range and obtained similar results as those of Stony Brook, by exposing eight different atomic initial states to a microwave field of variable frequency $\omega/2\pi$ from $12.4$ GHz to $18$ GHz. Furthermore, in the Pittsburgh experiment, a weak static electric field was added to the microwave field to enforce a quasi one-dimensional motion of the electronic density (by populating extremal parabolic states which are a coherent superposition of different angular momentum states).

To study the influence of the atomic core on the ionization process, we start out with lithium instead of atomic hydrogen. Yet, in contrast to many experiments on lithium atoms of the Virginia group [49, 50, 48], that were performed on initial states

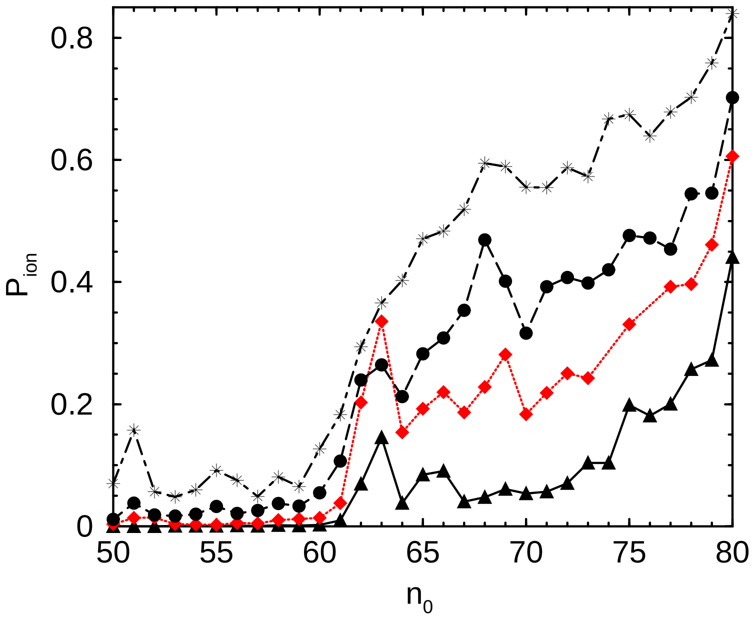

Figure 4.1: Ionization probability of lithium atoms prepared in initial states with angular momentum $\ell_0 = 0$, angular momentum projection $m_0 = 0$, and principal quantum numbers in the range $n_0 = 50, \ldots, 80$. The atoms are exposed to four different field amplitudes $F = 2.0 \cdot 10^{-9}$ a.u. (black triangles), $F = 2.3 \cdot 10^{-9}$ a.u. (red diamonds), $F = 2.7 \cdot 10^{-9}$ a.u. (black circles), and $F = 3.1 \cdot 10^{-9}$ a.u. (stars). The frequency and the atom-field interaction time are kept constant at $\omega/(2\pi) = 36$ GHz and $t = 327 \cdot 2\pi/\omega$, respectively, typical experimental values as they were employed in [20]. The local maxima at $n_0 = 63$ and $n_0 = 68$ are caused by avoided crossings in the Floquet spectrum, that induce a local enhancement of the ionization rates.

with angular momenta $\ell = 1$ or $\ell = 2$, to minimize the effect of the multi-particle core, the influence of the atomic core is precisely our interest. For this purpose, it is natural to choose initial states with angular momentum $\ell = 0$, i.e. states that exhibit the largest quantum defects $\delta_\ell$. More precisely, in our calculation we expose lithium atoms, initially prepared in states $|n_0, \ell_0 = m_0 = 0\rangle$, to a linearly polarized microwave field of frequency $\omega/2\pi = 36$ GHz, at atom-field interaction times indicated above, what precisely matches the situation of the Stony Brook experiment.

Figure 4.1 displays our first (physical) result, the ionization probability as a function of the principal quantum number $n_0$ of the initial atomic state, at four different field amplitudes $F = 2.0 \cdot 10^{-9}$ a.u., $F = 2.3 \cdot 10^{-9}$ a.u., $F = 2.7 \cdot 10^{-9}$ a.u., and $F = 3.1 \cdot 10^{-9}$ a.u. As the external field with fixed (laboratory) amplitude $F$, measured in units of the Coulomb field between electron and atomic core (in other words, the 'scaled' field amplitude $F_0$[1] ), increases with increasing quantum number $n_0$ (scanning $n_0$ from 50 to 80 is equivalent to scanning the 'scaled' field amplitude (2.20) from $n_0^4 \cdot F = 0.0125$ to $n_0^4 \cdot F = 0.08192$, at fixed $F = 2 \cdot 10^{-9}$ a.u.), in all four curves there is an increase of the ionization probability with $n_0$. Besides that, all four curves show a typical threshold behavior: below some quantum number $n_{\mathrm{threshold}}$ (e.g. $n_{\mathrm{threshold}} = 60$ at $F = 2.7 \cdot 10^{-9}$a.u.) the ionization probability remains relatively small and flat. This is the perturbative regime, where the field which is experienced by the electron does not induce appreciable ionization (i.e., where $F$ is small as compared to the Coulomb field $\sim n_0^{-4}$). For $n_0 > n_{\mathrm{threshold}}$, the ionization probability starts to increase rapidly, hereafter the field is strong enough to induce a strong coupling of a large number of atomic bound (and continuum) states. Said differently, beyond the perturbative regime the external field (which has cylindrical symmetry) destroys the spherical symmetry of the unperturbed initial atomic state, leading to a large ionization probability.

Besides the threshold behavior of the four curves, we observe local structures on top of the global trend, e.g. the local maxima at $n_0 = 63$ (at $F = 2.0 \cdot 10^{-9}$ a.u., $F = 2.3 \cdot 10^{-9}$ a.u., and $F = 2.7 \cdot 10^{-9}$ a.u.). Such local enhancement of the ionization probability of a given initial state is caused by the complicated structure of the Floquet spectrum: Near-degeneracies between two (or more) atom-field eigenstates at a given field amplitude reflect multi-photon resonances between atomic bound states. These enhance the coupling to the atomic continuum and thus the observed total ionization rate [38]. The situation is illustrated in figure 4.2 where we display the ionization probability of the ($\ell_0 = m_0 = 0$) state $n_0 = 63$ as a function of the field amplitude (in (a)), together with the evolution of the quasi-energies (real parts in (b),(c), imaginary parts in (d)) as a function of the field amplitude: there is an avoided crossing between two atom-field eigenstates close to $F \simeq 2.3 \cdot 10^{-9}$ a.u. (in (c)). The projection of the initial state $|n_0 = 63, m_0 = \ell_0 = 0\rangle$ on the near-degenerate Floquet states (displayed in (e)) is larger than the projection of the $\ell_0 = 0$ states with principal quantum number $n_0 = 62$ and $n_0 = 64$, and thus the initial state $|n_0 = 63, m_0 = \ell_0 = 0\rangle$ exhibits an enhanced ionization probability at this field amplitude. The effect reaches its maximum at $F = 2.3 \cdot 10^{-9}$ a.u., leading to an even larger ionization probability of the $n_0 = 63$ state than at $F = 2.7 \cdot 10^{-9}$ a.u. The same phenomenon, i.e. a local maximum in $P_{\mathrm{ion}}$ caused by a multi-photon resonance, appears close to $n_0 = 68$ (in figure 4.1), and also, below threshold, at $n_0 = 51$ for $F = 3.1 \cdot 10^{-9}$ a.u. We will return to the role of avoided crossings in the Floquet spectrum, and to the discussion of figure 4.2 in the next section.

Let us also mention here that a similar behavior as the one of the ionization yield as a function of the principal quantum number $n_0$ (i.e. a threshold behavior of the

---

[1] As noted in section 2.2, the scaling rules (2.19) and (2.20) are a priori only applicable for the driven two-body Coulomb problem. However, to give an estimate of the order of magnitude, we will use the notion of scaled variables also for the dynamics of alkali atoms. To emphasize that the use of scaling rules is a priori not justified we will use the notion 'scaled' variables for alkali atoms in quotation marks.

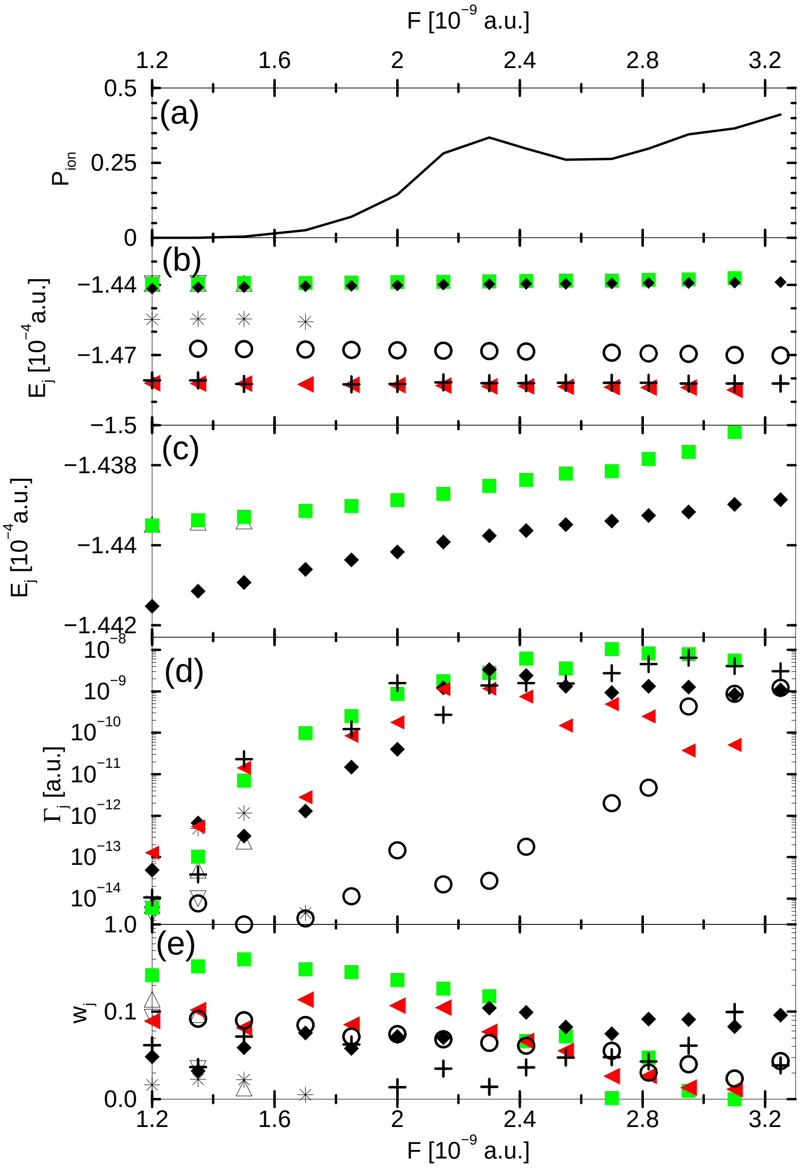

Figure 4.2: Spectral structure underlying the ionization yield of the state $|n_0 = 63, \ell_0 = m_0 = 0\rangle$ (compare figures 4.1 and 4.3), which is shown in (a). In (b) we plot the level dynamics of the real part of the quasi-energies in a single Floquet zone, and a detail of the Floquet zone in (c), where we recognize the avoided crossing between the state indicated by green squares and the one represented by black diamonds. This anticrossing is responsible for the maximum of $P_{\rm ion}$ in (a), at precisely the same field amplitude: (d) displays the dynamics of the corresponding ionization rates, and (e) the associated overlaps of the atom-field eigenstates with the initial state $|n_0 = 63, \ell_0 = m_0 = 0\rangle$. The avoided crossing in (c) also induces the steep rise of the widths and a (local) maximum of these widths at $F = 2.3 \cdot 10^{-9}$ a.u. as observed in (d). To keep the complexity of the present plots at a reasonable level, we only display the quasienergies, widths, and weights of those states having an overlap larger than $2\%$ with the atomic initial state.

global trend, together with the appearance of local extrema) was also reported in the discussion of laboratory experiments on the microwave ionization of atomic hydrogen [31]. There, local minima of the ionization probability were observed close to $\omega_0 = 1$, $\omega_0 = 1/2$, and $\omega_0 = 1/3$, and attributed to quantum signatures of local stability islands in classical phase space, i.e. manifestations of resonances between the external driving frequency and the characteristic frequencies of the unperturbed classical Kepler motion. Due to the lack of a uniquely defined classical one-particle potential for alkali atoms, a similar explanation for the local structure in figure 4.1 cannot be adopted here. However, as we will see in chapter 5, in the region where we observe most of the local structures, i.e. for $n_0 = 59, \ldots, 80$, the alkali dynamics mimics the one of hydrogen. Nonetheless, since the single-valued ionization yield $P_{\rm ion}$ is a quantity which averages over all the details of the atomic excitation process (see equation (2.58)), similar ionization yields do not suffice to postulate a classical analog of the alkali excitation and ionization process, and we therefore refrain from a purely classical interpretation of the above results.

## 4.2 Fixed initial states – changing the field amplitude

After changing the ’scaled’ field amplitude by varying the principal quantum number $n_0$ at fixed field amplitude, we will now do the reverse, and vary $F$ for constant $n_0$ as it is typically also done in laboratory experiments. In figure 4.3 we plotted the ionization probability of five initial states ($n_0 = 61$, $n_0 = 63$, $n_0 = 65$, $n_0 = 67$, $n_0 = 69$, $\ell_0 = m_0 = 0$) as a function of the field amplitude $F$. Much alike the previous section, we observe a threshold behavior for each $n_0$-value. Below a certain threshold amplitude, the Coulomb field largely dominates the external drive, and the dynamics is dominated by the symmetry of the pure atom, i.e. the situation can be treated in a perturbative way and, consequently, the ionization probability does not increase appreciably. Above the threshold field, we observe a steep increase of $P_{\rm ion}$, caused by non-perturbative couplings, involving multi-photon processes of different order [34]. The threshold field also defines the ionization border, below which ionization is negligible. This ionization border is traditionally defined as that field amplitude which causes an ionization probability of ten percent (the so-called ’10% ionization threshold’), at given interaction time.

In the discussion of figure 4.1 we recognized that the state $|n_0 = 63, \ell_0 = m_0 = 0\rangle$ is less stable at a driving field amplitude $F = 2.3 \cdot 10^{-9}$ a.u. than at the stronger field $F = 2.7 \cdot 10^{-9}$ a.u. This pronounced local maximum in figure 4.1 also manifests in figure 4.3. Here we see it as a shoulder in the ionization signal of $|n_0 = 63, \ell_0 = m_0 = 0\rangle$, which exceeds all the other curves shown in the plot, up to $F \simeq 2.4 \cdot 10^{-9}$ a.u. As a matter of fact, this curve can be understood as a vertical cut through $n_0 = 63$ in figure 4.1. The large overlap of $|n_0 = 63, \ell_0 = m_0 = 0\rangle$ with the anticrossing states in figure 4.2 causes the enhancement of $P_{\rm ion}(n_0 = 63)$ locally in $n_0$ in figure 4.1, and locally in $F$ in figure 4.2 and 4.3. The local maximum of $P_{\rm ion}(n_0 = 63)$ at $F \simeq 2.3 \cdot 10^{-9}$ a.u. (in figure 4.3 and 4.2 (a)) precisely corresponds

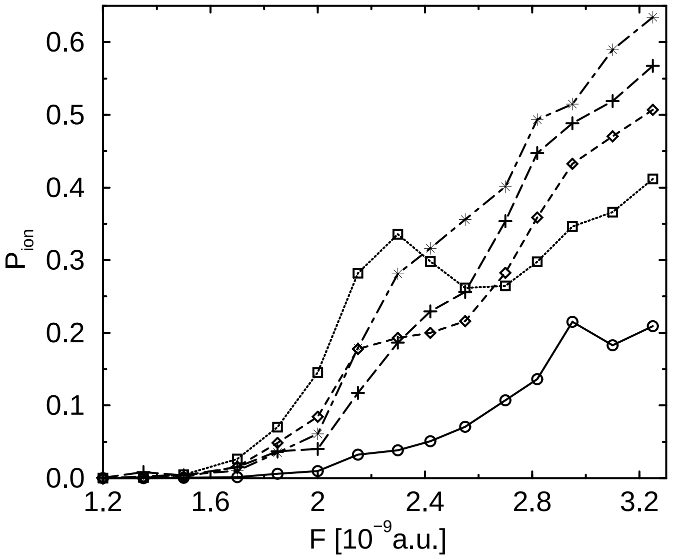

Figure 4.3: Ionization probability of five different initial states $|n_0, \ell_0 = m_0 = 0\rangle$ with $n_0 = 61$ (circles), $n_0 = 63$ (squares), $n_0 = 65$ (diamonds), $n_0 = 67$ (crosses), $n_0 = 69$ (stars) as a function of the field amplitude $F$ (interaction time and frequency as in figure 4.1). Above threshold, there exist local structures like the local maxima for $n_0 = 63$ and $n_0 = 61$. The broad shoulder in the ionization yield of $n_0 = 63$ is caused by avoided crossings in the Floquet spectrum, which were already identified in figures 4.1 and 4.2.

to the closest approach of the anticrossing states in figure 4.2 (c), as well as to a local maximum in their ionization rates (figure 4.2 (d)), and of their relative weights (figure 4.2 (e)) in the representation of the atomic initial state.

Besides the broad shoulder of the ionization signal of $n_0 = 63$ in figure 4.2 (a) and 4.3, all atomic initial states exhibit a rather steep increase of the ionization signal as a function of $F$. This is paralleled by a dramatic increase of the number of Floquet states which generate the dynamics (i.e. which have a non-negligible overlap with the initial atomic state, see equation (2.58)). Indeed, the Shannon width (2.61) – which measures the number of states that contribute appreciably to the representation of the initial state – increases from $W = 46$ at $F = 2 \cdot 10^{-9}$ a.u. to $W = 118$ at $F = 2.42 \cdot 10^{-9}$ a.u., for $n_0 = 63$, and similarly for the other quantum numbers represented in figure 4.3, see section 4.2.2. This observation correlates with the usual picture of the ionization process in the regime of dynamical localization: an increased localization length, which can be measured by the Shannon width, induces an enhanced ionization yield, at fixed atomic initial state $n_0$.

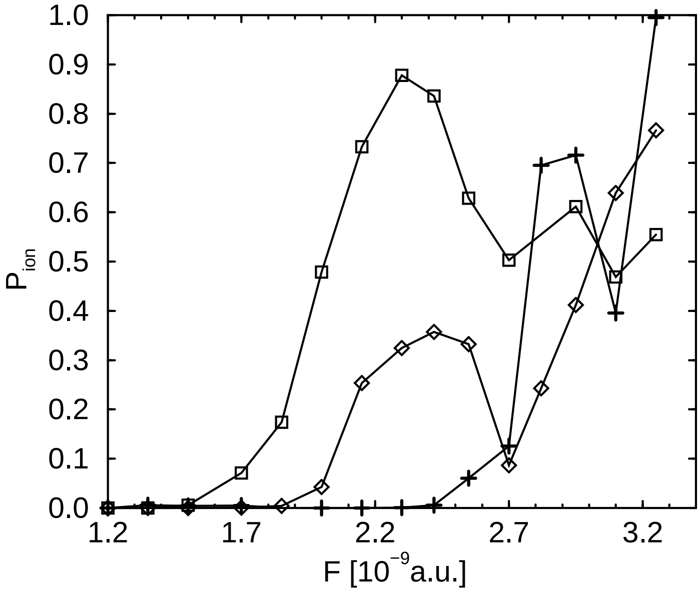

Figure 4.4: Ionization probability of the ($\ell_0 = m_0 = 0$) initial states $n_0 = 63$ (squares), $n_0 = 65$ (diamonds), and $n_0 = 67$ (crosses) obtained in the single Floquet state approximation (interaction time and frequency as in figure 4.1). As only one single Floquet state is populated, the enhancement of the ionization rates at avoided crossings plays a more important role than in the ionization probability evaluated in the sudden approximation. Thus the SFSA yields show more local maxima than the ionization signals plotted in figure 4.3. Note that the ionization probability of the state $|n_0 = 63, \ell_0 = m_0 = 0\rangle$ exactly follows the run of the widths of those eigenstates in figure 4.2 (d) which exhibit the largest weights in the representation of the atomic initial state.

### 4.2.1 Comparison with the single Floquet state approximation

We have seen in the preceding sections that the ionization yield $P_{\text{ion}}$ can be strongly affected by local structures in the Floquet spectrum, locally in some parameter like $F$ or $n_0$. Depending on the actual switching of the microwave pulse, the sudden approximation (2.58) providing us with figures 4.1 and 4.3 may not be the closest description of the actual situation in the laboratory, notably for experiments which switch the microwave rather slowly. To estimate the possible influence of the switching stage of the atom-field interaction on the local as well as on the global dependence of the ionization yield on $F$, it is therefore useful to compare the predictions of the single Floquet state approximation (SFSA, (2.59) to our above results. Doing so, we always use the Floquet state with the largest overlap with the field-free atomic initial state (at given $F$) as input for equation (2.59) [137].

Figure 4.4 displays the SFSA-results obtained with the same parameters as those in figure 4.3 for the ($\ell_0 = m_0 = 0$) atomic initial states $n_0 = 63,\ 65,\ 67$. The ionization curves of the $n_0 = 63$, and the $n_0 = 65$ states resemble those obtained with the sudden approximation for a weak driving field $F \lesssim 2.1 \cdot 10^{-9}$ a.u. ($n_0 = 65$) and $F \lesssim 1.9 \cdot 10^{-9}$ a.u. ($n_0 = 63$). For larger field amplitudes, the results obtained with the two different approaches deviate. This can be easily understood from the plot of the avoided crossing in figure 4.2: At $F \simeq 2 \cdot 10^{-9}$ a.u., the continuation of the atomic initial state (i.e. the Floquet state marked by squares in figure 4.2, which has the largest overlap with $|n_0 = 63, \ell_0 = m_0 = 0\rangle$ up to $F \simeq 2.3 \cdot 10^{-9}$ a.u.) undergoes an avoided crossing with another Floquet state (marked by diamonds), and thus the ionization probability increases in both approaches, the SFSA and the sudden approximation, and both curves exhibit a local maximum at $F \simeq 2.3 \cdot 10^{-9}$ a.u.. However, as the state marked by squares in figure 4.2 has an overlap of less than $25\%$ with the atomic initial state, in the sudden approximation the single avoided crossings are by far less important than they are in the SFSA and the sudden approximation leads to a smoother curve and to a less pronounced maximum.

The same scenario leads to the pronounced structure in the ionization yield of the $n_0 = 65$ and $n_0 = 67$ states (i.e. the maxima around $F = 2.5 \cdot 10^{-9}$ a.u. and $F = 2.9 \cdot 10^{-9}$ a.u.), which are smoothed out in the sudden approximation.

As we see in figure 4.2 (e), and in the similarity of the obtained ionization curves for weak driving field, the SFSA is only a useful approximation as long as there is one single Floquet state having a large overlap with the atomic initial state (this explains the large discrepancy between the two approaches for the state $n_0 = 67$, where even at $F = 1.2 \cdot 10^{-9}$ a.u. the largest overlap of a single Floquet state with the field-free initial state is only approximately 14 %), and as long as the adiabatic continuation of the initial state is relatively isolated in the spectrum. The second condition implies that the continuation of the initial state does not undergo avoided crossings. There, the atom-field eigenstates get strongly mixed, what is accounted for by the contribution of both states to the representation of the initial atomic state in the sudden approximation. In the SFSA on the other hand, the identification of the state which represents the continuation of the field free eigenstate becomes ambiguous: For a reasonable application of the SFSA, one has to decide whether the diabatic continuation (in this case the avoided crossing is crossed) or the adiabatic continuation (when the avoided crossing is really avoided) is populated after the anticrossing. Therefore the time scale $\tau$ defined by the avoided crossing, which is roughly given by the inverse energy splitting [137], has to be compared with the time needed to pass the avoided crossing. If the change of $F$ is much slower than $\tau$, i.e. for $\tau << (1/F)\mathrm{d}F/\mathrm{d}t$, the electronic population follows the adiabatic continuation, whereas the diabatic continuation is the appropriate choice in the opposite case. In the intermediate situation, however, both states are populated and the SFSA breaks down [137].

Since the spectrum of microwave driven Rydberg states exhibits abundant avoided crossings of variable size, in general, an atomic initial state is represented by multiple atom-field eigenstates. Thus, summing over multiple atom-field eigenstates as it is done in the sudden approximation typically provides for a better description of the experimental situation than the SFSA. This is in particular true for the latest generation of the Virginia experiments on lithium atoms [49], that employ a switching time of only three field-cycles. But also in the experiments in Stony Brook [20, 31] and in Munich [42, 9], that employ switching times of approximately 50 field-cycles, more than just one single atom-field eigenstate are populated at field amplitudes strong enough to induce appreciable ionization. This manifests, e.g., in the experimentally observed transition from a mono-exponential time dependence of the ionization probability to an algebraic time dependence for an increasing field strength in the Munich experiments [86]. Such a non-exponential time dependence, however, is only possible if the initial atomic state is represented by a large number of atom-field eigenstates as suggested by (2.58) rather than by only one single atom-field eigenstate as suggested by (2.59). We will study the temporal dependence of the ionization probability of microwave driven Rydberg states in more detail in chapter 6, where we will also refer to assumptions concerning the temporal decay of complex quantum systems made by other research groups.

While not only the set-up of the recent Virginia experiments [49], but also the Munich and presumably the Stony Brook set-ups provide for the population of multiple atom-field eigenstates, the finite switching time can induce the prefered population of a reduced number of atom-field eigenstates (as compared to the sudden approximation), possibly with specific stability properties [166, 167]. Thus, the experimentally observed ionization probability may locally in $F$ or $n_0$ significantly differ from the results obtained with the sudden approximation which, however, globally will provide for a good description of the experiments. Due to these pulse induced effects, we will also observe local deviations of the numerically obtained 10% ionization threshold from experimental data in chapter 5, but we expect an excellent agreement of our results to results obtained with a very fast switching of the field as it is approximately possible, e.g., in the Virginia experiments.

### 4.2.2 Shannon width

In the previous sections we recognized that the abundance of avoided crossings in the Floquet spectrum expresses the coupling of the atomic initial state to a large number of atom-field eigenstates. To quantify the number of Floquet states contributing to the representation of the initial state, we introduced the Shannon width $W(n_0, F, \omega)$ (2.61) in section 2.5.2, and we already used this quantity in section 4.2, in our discussion of the threshold behavior of the ionization yields in figure 4.3. In figure 4.5 we display $W(n_0, F, \omega)$ as a function of the field amplitude $F$ for the initial atomic states we studied in figure 4.3.

The width function $W(n_0, F, \omega)$ shows a similar dependence on the field amplitude as we observed it for the ionization probability: The stronger the external perturbation, the more Floquet states are needed to represent the initial state. Much as for the ionization probability, the slope of $W(n_0, F, \omega)$ is not constant and it also exhibits a threshold behavior. Since a weak driving field does not induce a strong perturbation of the initial atomic state, the state is represented by only a small num-

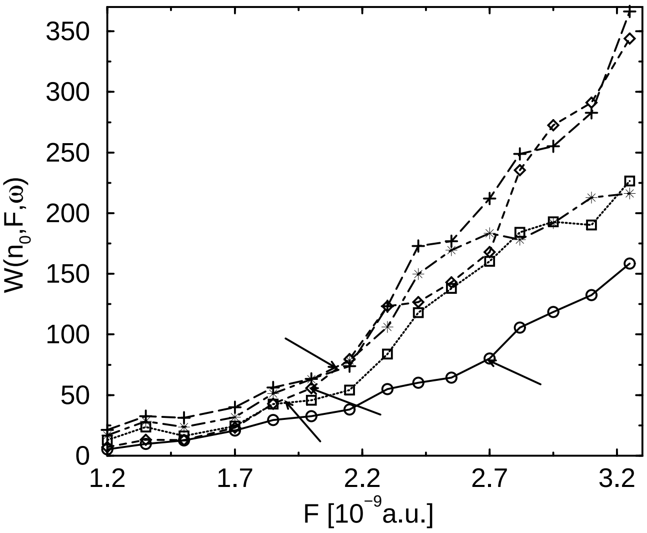

Figure 4.5: Shannon width $W(n_0, F, \omega)$ (2.61) of the $\ell_0 = m_0 = 0$ initial states $n_0 = 61$ (circles), $n_0 = 63$ (squares), $n_0 = 65$ (diamonds), $n_0 = 67$ (crosses), and $n_0 = 69$ (stars), as a function of the field amplitude $F$. The frequency of the driving field is chosen as in figure 4.1. The arrows mark the field amplitude of the 10% ionization threshold (at $t = 327 \cdot 2\pi/\omega$) of (from left to right) $n_0 = 63$, $n_0 = 65$, $n_0 = 67$ (which agrees with the threshold of $n_0 = 69$), and $n_0 = 61$. These thresholds coincide roughly with the positions where the slope of the Shannon $W$ changes from a weaker to a steeper slope.

ber of Floquet-states, associated with a small ionization probability. Above a critical field, the external perturbation is strong enough to destroy the atomic symmetry properties, and consequently, the atomic initial state is distributed over a large number of atom-field eigenstates. As already noted above, this is generally the case when the continuation of the initial state – which is relatively isolated in the quasienergy spectrum for weaker field amplitudes – undergoes several avoided crossings, and thus, its character (i.e. its symmetry properties) changes. Starting from this threshold value of $F$, $W(n_0, F, \omega)$ increases faster than it does for weaker fields, in accordance with the steep increase of $P_{\mathrm{ion}}$ above threshold. However, the width function does not show the pronounced maximum we observed for $n_0 = 63$, and which we attributed to the avoided crossing. At this maximum the ionization rates of two single atom-field eigenstates that dominate the representation of the initial state get strongly enhanced, and the weights of these two atom-field eigenstates when projected on the initial state decrease after the avoided crossing as we observed in figure 4.2. Thus, the Shannon width – which is calculated of the weights $w_j$ rather than of the ionization rates $\Gamma_j$ – does not show a maximum like the ionization probability, but it increases at the avoided crossing.

Since the change of the Shannon width reminds us of the $F$-dependence of the ionization probability, we compare the values of $W(n_0, F, \omega)$ at the 10% ionization threshold fields in table 4.2.2 for different values of $n_0$:

| $n_0$ | $F_{10\%}$ [a.u.] | $W(n_0, F_{10\%}, \omega)$ |
|---|---|---|
| 61 | $2.7 \cdot 10^{-9}$ | 77 |
| 63 | $1.9 \cdot 10^{-9}$ | 37 |
| 65 | $2.0 \cdot 10^{-9}$ | 63 |
| 67 | $2.1 \cdot 10^{-9}$ | 85 |
| 69 | $2.1 \cdot 10^{-9}$ | 69 |

Table 4.2.2: Shannon width $W(n_0, F, \omega)$ at the $10\%$ threshold $F_{10\%}(t = 327{\cdot}2\pi/\omega)$ for the initial states $|n_0, \ell_0 = m_0 = 0\rangle$, with the same $n_0$ values as employed in figures 4.3 and 4.5.

The table shows that for different initial states, $W(n_0, F_{10\%}, \omega)$ varies by more than a factor two, although the ionization probability of all five states (with principal quantum numbers that differ by only 10%) reaches the same value at the given driving fields. Here, some of the eigenstates over which the field-free eigenstate spreads below threshold exhibit large ionization rates (as it is the case with the anticrossing states for $n_0 = 63$) and hence a smaller value of $W$ is sufficient to induce 10% ionization (compare $W = 37$ for $n_0 = 63$ vs. $W = 63, \ldots, 85$ for $n_0 = 61, 65, 67, 69$ at threshold). However, it is close to threshold where the Shannon width increases dramatically. Consequently, the threshold fields $F_{10\%}(t = 327 \cdot 2\pi/\omega)$ roughly agree with the fields where the slope of $W(n_0, F, \omega)$ changes from a weak to a steeper increase, as can be observed in figure 4.5.

## 4.3 Time dependence of the ionization signal

We have seen that, for fixed interaction time $t$, local structures in the ionization yield (vs. $F$ or $n_0$) are caused by avoided crossings in the Floquet spectrum, eventually amended by a pulse-induced redistribution of the weights $w_j$ of the various Floquet states which contribute to the ionization signal. Whereas the avoided crossings induce local enhancements of the ionization rates of the interacting states, pulse induced redistributions of the $w_j$ determine the path of the wave function across the crossing and hence the dependence of the total ionization yield on the control parameter $F$, through $P_{\rm ion} = 1 - \sum_j w_j \exp(-\Gamma_j t)$. By virtue of this last equation (or (2.58), where the $w_j$ are given by the overlaps of the field-free initial state with all atom-field eigenstates), however, it is clear that local structures of $P_{\rm ion}$ will also depend on the interaction time $t$, since both, $\Gamma_j$ and $w_j$ depend on $F$, and $w_j$ additionally depends on $n_0$ (for a given microwave pulse). Therefore, the yield will

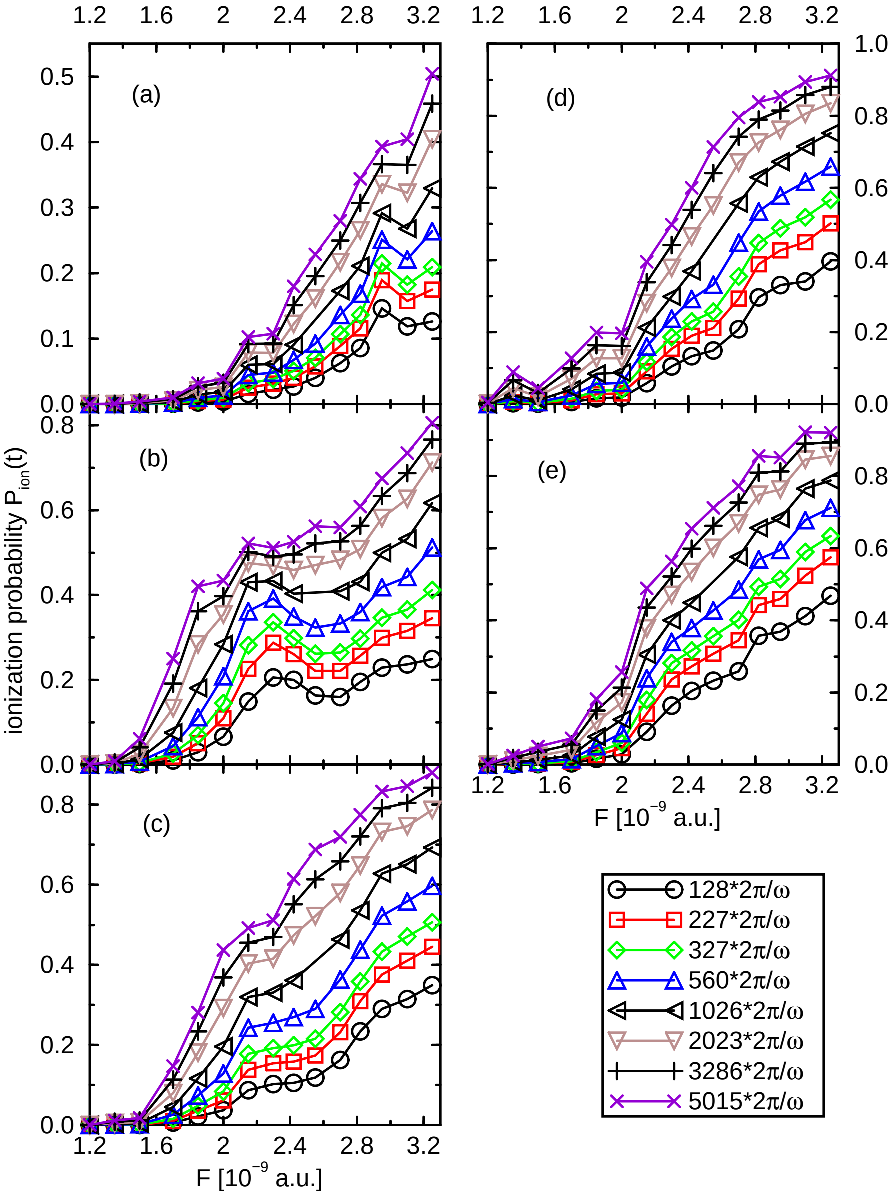

Figure 4.6: Ionization yield $P_{\rm ion}(t)$ vs. field amplitude $F$, for different interaction times (as given in the legend) for the ($\ell_0 = m_0 = 0$) initial states $n_0 = 61$ (a), $n_0 = 63$ (b), $n_0 = 65$ (c), $n_0 = 67$ (d), and $n_0 = 69$ (e). An increase of the interaction time leads to an overall increase of the slope of the ionization signal. Furthermore, local structures emerge and/or disappear, induced by avoided crossings in the Floquet spectrum (see figure 4.2), at specific vales of $F$.

increase in time with locally (in $F$ or $n_0$) distinct rates, causing changes in the local structures of the ionization signal, on time scales which reflect the distribution of the $\Gamma_j$ over several orders of magnitude.

As an example, figure 4.6 shows the time evolution of the ionization signals of figure 4.3, for $t = 128 \cdot 2\pi/\omega, \ldots, 5015 \cdot 2\pi/\omega$. Changing the interaction time by a factor 39 obviously does not change the global trend of the five ionization curves, apart from a global increase of the slope.

However, closer inspection of figure 4.6 reveals a change in the local structure of the ionization signals. The pronounced local maximum in the yield of the $n_0 = 63$ state, around $F = 2.3 \cdot 10^{-9}$ a.u. at $t = 327 \cdot 2\pi/\omega$, flattens out for longer interaction times. This is caused by a faster decay of the $n_0 = 63$ state at $F \simeq 2.6 \cdot 10^{-9}$ a.u. than at $F \simeq 2.3 \cdot 10^{-9}$ a.u. The faster decay at $F \simeq 2.6 \cdot 10^{-9}$ a.u. seems to contradict the observation we made in the discussion of figure 4.2, i.e. the fact that the ionization rate of the Floquet state with the largest contribution to the $n_0 = 63$ state reaches a maximum ($\Gamma_j \simeq 4 \cdot 10^{-9}$ a.u.) at $F \simeq 2.3 \cdot 10^{-9}$ a.u. However, for long interaction times the two anticrossing states already decayed (e.g., $\exp(-\Gamma_j \cdot t) \simeq 9 \cdot 10^{-3}$ for $\Gamma_j \simeq 4 \cdot 10^{-9}$ a.u. and $t = 1026 \cdot 2\pi/\omega$), and their contribution to the representation of the initial state $n_0 = 63$ become less important. On long time scales, more stable states (with $\Gamma_j < 10^{-9}$ a.u.) dominate the decay of $n_0 = 63$, and the ionization probability increases slower than on short time scales.

While the maximum in the $n_0 = 63$ curve flattens out with increasing interaction time, the opposite behavior is observed for the $n_0 = 67$ state at $F = 1.35 \cdot 10^{-9}$a.u. (figure 4.6 (d)). Here, interaction times $t > 500 \cdot 2\pi/\omega$ lead to the emergence of a subthreshold peak at $F = 1.35 \cdot 10^{-9}$ a.u.

This variation of the local structure in the ionization signal due to a change of the interaction time was recently experimentally observed in the study of ($\ell_0 = m_0 = 1$ states of) lithium atoms by the Virginia group [49]. There (see figure 3(a) of reference [49]), a similar situation occurred as we observe it in the temporal evolution of the ionization curve for the $n_0 = 61$ state at $F \simeq 2.2 \cdot 10^{-9}$ a.u., and for $n_0 = 67$ at $F \simeq 1.8 \cdot 10^{-9}$ a.u.: at short atom-field interaction times (in the Virginia experiment at $t \leq 115 \cdot 2\pi/\omega$, in our results at $t \lesssim 600 \cdot 2\pi/\omega$) the ionization yield is essentially flat below threshold. For large interaction times (in the Virginia experiment $t = 1150 \cdot 2\pi/\omega$, in our simulation $t > 2000 \cdot 2\pi/\omega$) an additional 'shoulder'-like structure appears.

To finish this chapter, let us come back to the ionization probability as a function of $n_0$, for a fixed field amplitude, what we studied already in section 4.1.

In figure 4.7, where we display the time evolution of $P_{\text{ion}}$ vs. $n_0$ (for $F = 2.3 \cdot 10^{-9}$ a.u.), we see that the distinct time evolution of different atomic initial states (at a given field amplitude) induces a change in the local structures much as we observed it in the temporal evolution of $P_{\text{ion}}$ vs. $F$. While, e.g., the local maximum at $n_0 = 66$, that is only hardly identified for $t = 128 \cdot 2\pi/\omega$, gets more pronounced for longer interaction times, the local minimum at $n_0 = 70$, for instance, gets less pronounced for increasing interaction times. Whereas in these two examples only

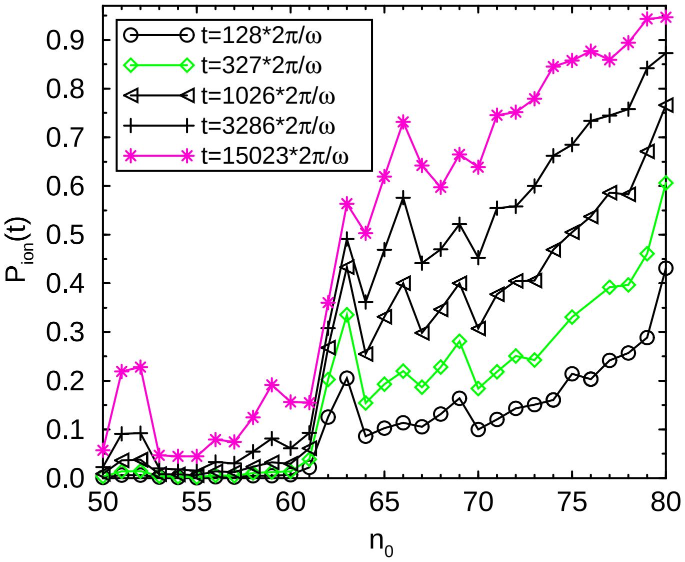

Figure 4.7: Temporal evolution of the ionization probability as a function of the principal quantum number $n_0$ ($\ell_0 = m_0 = 0$), at fixed field amplitude $F = 2.3 \cdot 10^{-9}$ a.u.. The distinct time evolution of different initial states leads to an enhancement of some of the local structures already observed in figure 4.1 (e.g., the pronounced local maximum at $n_0 = 63$), and occasionally to the emergence of new local structures, as the local maximum at $n_0 = 66$

the difference between the ionization probability at the local extremum ($n_0 = 66$ respectively $n_0 = 70$) and the preceding local extremum ($n_0 = 64$ respectively $n_0 = 69$) changes with increasing interaction time, we observe a different behavior at the minimum at $n_0 = 67$ (at, e.g., $t = 1026 \cdot 2\pi/\omega$): The minimum gets more pronounced from $t = 128 \cdot 2\pi/\omega$ to $t = 3286 \cdot 2\pi/\omega$, but at $t = 15023 \cdot 2\pi/\omega$ the minimum is no more located at $n_0 = 67$, but rather at $n_0 = 68$. This means that for each local structure there is a certain time scale when it appears most pronounced. Once again, as for the change of the local structures of $P_{\text{ion}}$ vs. $F$ under variation of the interaction time, this can be understood from the ionization probability as a weighted sum over the exponentials $\exp(-\Gamma_j t)$. Different widths $\Gamma_j$ play a dominant role on different time scales $t$, and the impact of these widths on the ionization probability of a given initial state is determined by the weight $w_j$ which differs for different states $|n_0, \ell_0, m_0\rangle$. Thus, we observe a distinct time evolution of $P_{\text{ion}}$ for different initial conditions (i.e. $n_0$ or $F$).

Studying the time dependence of $P_{\text{ion}}$ vs. $F$ (figure 4.6) and $P_{\text{ion}}$ vs. $n_0$ (figure 4.1), we observe that also the 10% ionization threshold changes with $t$. While this change (induced by local structures of $P_{\text{ion}}$ vs. $n_0$ or $F$) is in some cases only a small change to lower field amplitudes or principal quantum numbers, the emergence of subthreshold peaks (e.g., at $F \simeq 1.3 \cdot 10^{-9}$ a.u. in figure 4.6 d) may induce rather pronounced changes of the ionization threshold. Accordingly, we will also observe time-dependent changes in the dependence of the threshold on the 'scaled' frequency (see the succeeding chapter). Such changes were observed in the recent experiment of the Virginia group [49], after earlier theoretical predictions [33, 38]. These (theoretical and experimental) observations, as well as our observations of the change of $P_{\rm ion}$ (vs. $F$, or vs $n_0$) with the change of $t$, already show that (2.58) creates a complicated time dependence of $P_{\rm ion}(t)$ involving multiple time scales, which differs for different initial conditions (set by $F$ and $n_0$). As already mentioned, an algebraic time dependence (for a sufficiently strong driving field) was already observed, both in laboratory and in numerical experiments [86], and is nowadays intensely discussed [79, 80, 84, 82, 83, 78]. In chapter 6 we will study this aspect in more detail.

# Chapter 5

# (Scaled) Frequency dependence of the ionization threshold

We now come to the central result of this thesis, the first numerically exact description of the ionization threshold of highly excited Rydberg states, covering essentially the complete parameter space of typical laboratory experiments, without any adjustable parameters. Since a large part of the experimental data as well as essentially all theoretical model treatments so far dealt with atomic hydrogen, and given the well-defined classical analogy for the driven two-body Coulomb problem, we will therefore first compare our ab initio results on hydrogen to experimental data. Afterwards, we will enter the discussion of the ionization dynamics of alkali Rydberg states, which bears some unexpected surprises, as we will see in the sequel of this chapter.

## 5.1 Atomic hydrogen

Numerical experiments on the ionization dynamics of atomic hydrogen in a broad range of the scaled frequency were already performed in [33, 34, 38, 32]. However, at that time, neither the available supercomputers were powerful enough nor was there, more importantly, the necessary expertise on large scale parallel computing. Consequently, these calculations were done either using a one-dimensional approximation of the real atom [38], or by employing the scaling rules (2.19) and (2.20), to 'rescale' results obtained in three-dimensional calculations on initial states around $n_0 \simeq 20$ to typical experimental quantum numbers $n_0 \simeq 60$ [32, 34]. Here, we need not resort to any approximations any more, and can use precisely the experimental parameters of [20], i.e. a microwave frequency $\omega/2\pi = 36$ GHz, and principal quantum numbers of the initial state in the range $n_0 = 46, \ldots, 78$, defining a multiphoton process of the order $44, \ldots, 15$.

As already mentioned in the previous chapter, for our calculations we chose the experimental parameters of the Stony Brook group [20] instead of the parameters of the Pittsburgh experiment [21], since fixing the laboratory frequency $\omega$ and

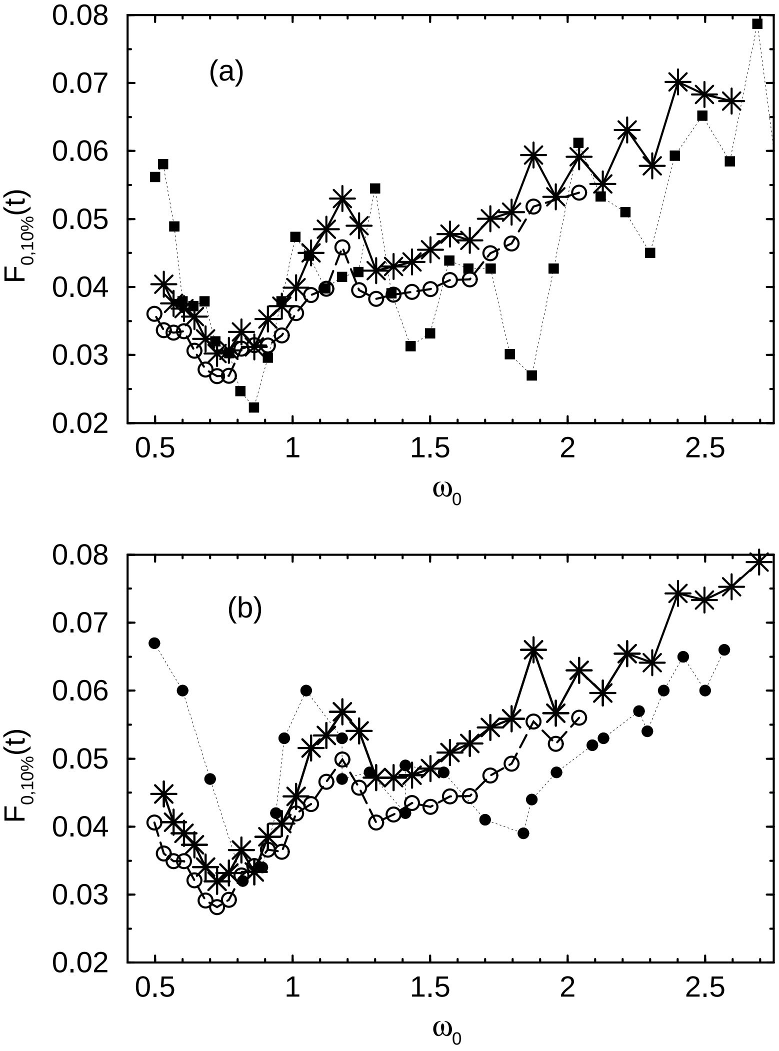

Figure 5.1: Scaled ionization threshold $F_{0,10\%}(t)$ vs. scaled frequency $\omega_0$ of microwave driven atomic hydrogen: Three-dimensional numerical results obtained at frequency $\omega/2\pi = 36$ GHz for the initial states $\ell_0 = m_0 = 0$ (stars) and $\ell_0 = 1,\ m_0 = 0$ (open circles), with an atom-field interaction time $t = 327 \cdot 2\pi/\omega$ (a), and $t = 128 \cdot 2\pi/\omega$ (b). The laboratory results (squares, [20]) shown in (a) were obtained at exactly the same frequency $\omega/2\pi = 36$ GHz and atom-field interaction time, but the atomic initial state was a microcannonical mixture of different $m_0$ and $\ell_0$ states on the $n_0$ energy shell. The experimental results shown in (b) (filled circles, [21]) were obtained at frequencies in the range $\omega/2\pi = 12.4, \ldots, 18$ GHz, and with interaction times $t = 93, \ldots, 135\ \cdot 2\pi/\omega$. Furthermore, in the laboratory experiment [21] a quasi one-dimensional extremal parabolic state was chosen as the initial state.

changing $n_0$ is more convenient for our numerical set-up than changing both $\omega$ and $n_0$, as it was done in [21]. However, as we want to compare the ionization thresholds of atomic hydrogen with the thresholds of low angular momentum alkali states later on, we employ a well-defined initial state $|n_0, \ell_0, m_0 = 0\rangle$ with $\ell_0 = 0$ and $\ell_0 = 1$ also for our hydrogen calculations. This is in contrast to the experimental set-up [20, 31] where the initial state was a microcannonical mixture of $m$ and $\ell$ states in the $n_0$-energy shell. As noted already in the previous chapter, in the Pittsburgh experiments [21], on the other hand, well-defined atomic initial states (i.e. extremal parabolic states, a superposition of different $\ell_0$ states) were populated by superimposing a weak static electric field on the microwave.

In figure 5.1 we display our numerical results for the scaled 10% ionization threshold $F_{0,10\%}$ as a function of the scaled frequency $\omega_0$, together with the laboratory results of the groups in Stony Brook (a), and Pittsburgh (b), respectively. Precisely as in both laboratories, an atom-field interaction time $t = 327 \cdot 2\pi/\omega$ $(= 9.1\,\mathrm{ns})$ was employed in (a), while a shorter pulse $t = 128 \cdot 2\pi/\omega$ was used in (b).(1) The ionization thresholds were extracted from ionization signals as depicted in figure 4.3, for each value of $n_0$. In contrast to our Floquet approach that implies a flat pulse (with constant field amplitude $F$) of duration $t$, in both laboratory set-ups a finite switching time of the field, given by approximately $50$ field-cycles in [20], and determined by a half-sine pulse in [21] was used.

The overall agreement of the numerical data with the experimental results of both groups is very satisfactory. The scaled threshold follows the theory outlined in section 1.1.1 (see figure 1.1). We only briefly summarize the major observations here:

- For low scaled frequencies $\omega_0 \lesssim 0.8, \ldots, 0.86$, the quantum dynamics follows the classical prediction, and the scaled ionization threshold $F_{0,10\%}(\omega_0)$ decreases with increasing frequency.
- For larger scaled frequencies $\omega_0 \gtrsim 0.86, \ldots, 0.8$, the classically chaotic ionization is suppressed by quantum mechanical interference processes – known as dynamical localization [24] – and $F_{0,10\%}(t)$ increases with $\omega_0$.
- On top of the global behavior of $F_{0,10\%}(t)$, there are local structures, notably a maximum near $\omega_0 \simeq 1.2$, and – less pronounced – close to $\omega_0 \simeq 1.9$. These are signatures of the classical stability islands induced by resonant driving of the atom, i.e., at $\omega_0 = 1, 2, 3$ (the exact position of these maxima, however, varies a little bit, as can be seen in the figure, from $\omega_0 \simeq 1.05$ in the Pittsburgh experiment to $\omega_0 \simeq 1.0, \ldots, 1.3$ in the Stony Brook experiment [20, 33]).

Apart from the overall agreement of the numerical and the experimental results, there are also some deviations between both data sets. Firstly, the laboratory results of both experiments show globally slightly lower thresholds as compared to our numerical results, for frequencies $\omega_0 \gtrsim 1.3$ (in (a), respectively for $\omega_0 \gtrsim 1.5$ in (b)). This can be attributed to the difference in the initial states chosen in our numerical and in the laboratory experiments. Already from the comparison of the numerical results for $\ell_0 = 0$ and $\ell_0 = 1$, it is apparent that the exact value of the ionization threshold depends on the choice of the angular momentum of the initial state. The comparison of the numerical results shows that the $\ell_0 = 0$ states are more stable than the $\ell_0 = 1$ states for all scaled frequencies $\omega_0 = 0.5, \ldots, 2$. Such behavior – i.e. an increase of the stability for decreasing angular momentum – was observed already before in calculations on moderately excited hydrogen atoms [33] where a weak dependence of $F_{0,10\%}$ on the angular momentum was found with a minimum at intermediate angular momenta. Thus, we expect an even better global agreement between results of our numerical and the laboratory experiment, if precisely the same initial atomic state is populated. However, even with the population of the identical initial state, our numerical data may still slightly deviate from the laboratory results locally, since we employ a sudden switching of the microwave field, in contrast to the finite switching time of the laboratory experiments. As already noted in the preceding chapter, a finite switching time may provide for the contribution of only a reduced number of atom-field eigenstates to the ionization probability as compared to the sudden approximation. This changes also the local structures in the ionization probability, and hence also the local structures in $F_{0,10\%}$ vs. $\omega_0$. The pronounced local minimum at $\omega_0 \simeq 1.4$ in the Stony Brook experiment (see figure 5.1 (a)), for instance, can most probably be attributed to such a pulse-induced effect [33].

---

(1) In the laboratory set-up [21] the interaction time actually varied between $93$ and $135$ field cycles, as the frequency was varied $\omega/2\pi = 12.4, \ldots, 18$ GHz and the laboratory interaction time $t = 7.5\,\mathrm{ns}$ was kept constant.

## 5.2 Alkali atoms

### 5.2.1 Lithium vs. hydrogen – three frequency regimes in the ionization dynamics

To understand the influence of a non-hydrogenic core on the ionization dynamics of periodically driven Rydberg states, we start out with lithium atoms exposed to a microwave field. Frequency $\omega$, principal quantum number of the initial state $n_0$, and the interaction time $t$ remain fixed by the values employed in [20] and in our numerical treatment of atomic hydrogen above. The angular momentum of the initial states was chosen as in our hydrogen calculations, $\ell_0 = 0$ and $\ell_0 = 1$ (with $m = 0$).

In figure 5.2.1 we display the results, the 'scaled' 10% ionization threshold as a function of the 'scaled' frequency of our numerical experiment on lithium $|n_0, \ell_0 = m_0 = 0\rangle$ states together with experimental (a) and our numerical (b) results obtained on atomic hydrogen (in figure 5.2.1 (b) we also display our $\ell_0 = 1$ results for lithium and hydrogen). Since the (laboratory) hydrogen experiments performed with $\omega/2\pi = 36$ GHz [20] only considered principal quantum numbers $n_0 = 45, \ldots 80$, we additionally reproduce laboratory results obtained on atomic hydrogen with $\omega/2\pi = 9.92$ GHz and $n_0 = 32, \ldots, 90$, which cover the regime of low scaled frequencies $\omega_0 = 0.05, \ldots, 1.1$.

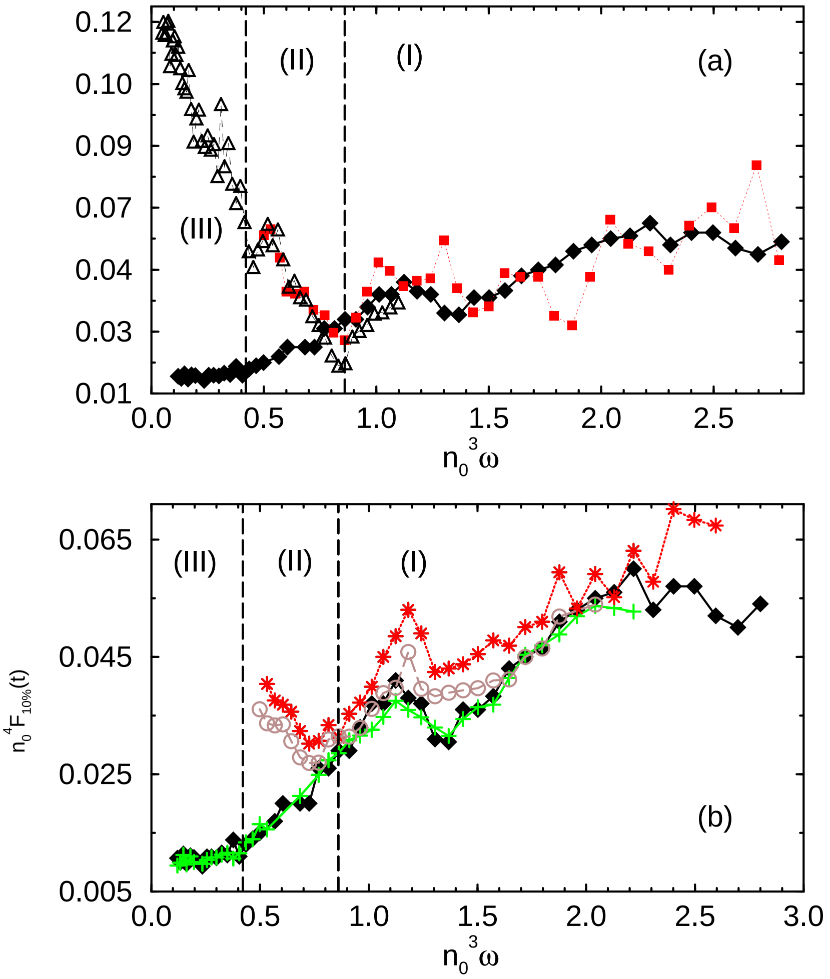

Figure 5.2: Calculated 'scaled' threshold fields $n_0^4 \cdot F_{10\%}$ of lithium atoms ($\ell_0 = m_0 = 0$ states: filled diamonds, and $\ell_0 = 1,\ m_0 = 0$ states: crosses) together with experimentally measured scaled thresholds of atomic hydrogen (squares, [20], and open triangles, [31]) in (a), and with numerically observed hydrogen thresholds (stars, $\ell_0 = m_0 = 0$ states, and open circles, $\ell_0 = 1,\ m_0 = 0$ states) in (b). The parameters for the calculations on lithium, for the experiment [20] and for the calculations on atomic hydrogen are exactly the same, i.e., $\omega/2\pi = 36$ GHz and $t = 9.1$ ns $= 327 \cdot 2\pi/\omega$. Since the experiment [20] only covers the frequency regime $\omega_0 > 0.5$, we also display the experimentally measured thresholds of [31] (in (a), open triangles) that were obtained with $\omega/2\pi = 9.95$ GHz, and $n_0 = 32, \ldots, 90$ (corresponding to $\omega_0 = 0.05, \ldots, 1.1$)

Since the only difference between the $\omega/2\pi = 36$ GHz laboratory and numerical experiment on hydrogen, on the one hand, and the lithium calculations, on the other hand, is the quantum defect, we can present both the hydrogen and the lithium results in terms of scaled variables as defined in section 2.2. Therefore, such a plot allows for the unambiguous identification of the core-induced differences and the similarities in the ionization dynamics of non-hydrogenic Rydberg states as compared to the driven two-body Coulomb problem realized by atomic hydrogen.

A comparison of the (numerical and laboratory) hydrogen to the lithium results clearly suggests a separation of the dynamics in three regimes:

(I) In regime (I), $n_0^3 \cdot \omega > 0.86$ (as suggested by a comparison of our numerical lithium data and the laboratory [20] hydrogen thresholds, respectively $n_0^3 \cdot \omega > 0.8$ as suggested by a comparison of our numerical thresholds of lithium and hydrogen), the 'scaled' threshold of lithium follows the global trend of the hydrogenic curve. In particular, the scaled thresholds of both species exhibit local maxima at $n_0^3 \cdot \omega \simeq 1, \ldots, 1.3$ and $n_0^3 \cdot \omega \simeq 2, \ldots, 2.2$.

(II) For 'scaled' frequencies $0.4 \lesssim n_0^3 \cdot \omega < 0.8, \ldots, 0.86$ (regime (II)) there is a dramatic difference between the hydrogen and the lithium data: whereas the hydrogen curve follows the classical ionization threshold and increases with decreasing $n_0^3 \cdot \omega$, it decreases in the case of lithium.

(III) The 'scaled' lithium threshold is essentially $n_0^3 \cdot \omega$-independent in regime (III), i.e., for $n_0^3 \cdot \omega \lesssim 0.4$, while the hydrogen threshold follows the classical behavior. This leads to up to 13 times larger scaled (laboratory) thresholds for hydrogen as compared to lithium.

The distinct dependence of lithium and hydrogen thresholds on the 'scaled' frequency in these three regimes can be explained by inspection of the level structure of unperturbed lithium and hydrogen atoms, as sketched in figure 5.3:

#### 5.2.1.1 Regime (I): $n_0^3 \cdot \omega > 0.8$

In regime (I) – for $n_0^3 \cdot \omega > 0.8, \ldots, 0.86$ – the external frequency exceeds or is comparable to the splitting between adjacent unperturbed hydrogen energy levels, which coincides with the splitting $\Delta_{\mathrm{Hyd}}$ between the unperturbed hydrogenic part (i.e. the high angular momentum states, with vanishing quantum defects) of adjacent lithium manifolds. Here, the external field can efficiently mix hydrogenic (emanating from unperturbed levels with $\ell_0 > 1$) and non-hydrogenic (emanating from low angular momentum states) energy levels, and the hydrogenic character of the ionization process prevails.

Both, hydrogen and lithium atoms evince dynamical localization, i.e. the suppression of a diffusive ionization due to quantum interference effects in this regime. The emergence of dynamical localization manifests in the overall increase of the 'scaled' ionization threshold with increasing 'scaled' frequency [24, 21].

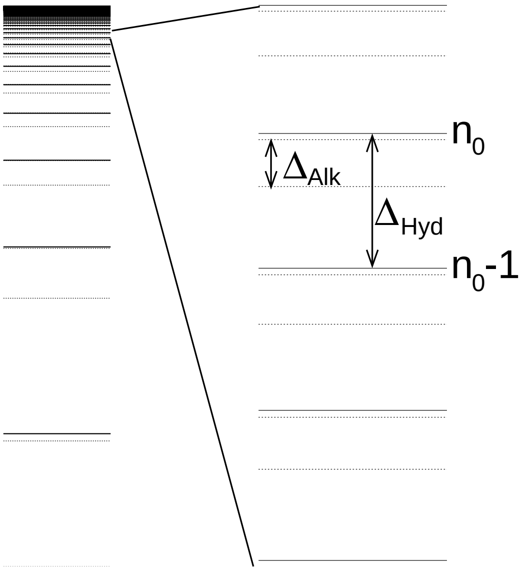

Figure 5.3: Hydrogenic (full lines) and non-hydrogenic (dotted lines) energy levels of the unperturbed lithium atom, with a detail of the Rydberg progression on the right. In alkali atoms, the angular momentum degeneracy of the hydrogen spectrum is lifted by the multi-electron core. The latter induces non-vanishing quantum defects $\delta_\ell$ [113] of the low angular momentum states, which lead to the apparent energy shift of the non-hydrogenic with respect to the hydrogenic eigenstates. The relevant frequency scales for the ionization process, which define the intervals (I), (II), and (III) in figure 5.2.1, are $\Delta_{\mathrm{Hyd}}(n_0)$, the spacing of adjacent hydrogenic manifolds, and $\Delta_{\mathrm{Alk}}(n_0)$, the energy splitting corresponding to the first dipole-allowed upward transition leaving the non-hydrogenic initial state of the atom.

On top of the global increase of the 'scaled' ionization threshold we can detect local maxima of the 'scaled' lithium threshold, similar to those already observed in the numerical and laboratory thresholds of hydrogen. However, the absolute values of the lithium ionization threshold at the maxima deviate a little bit from that of the (numerically obtained) hydrogen threshold, e.g. $n_0^4 \cdot F_{10\%} \simeq 0.041$ (lithium $\ell = 0$ states) vs. $n_0^4 \cdot F_{10\%} \simeq 0.05$ (hydrogen $\ell = 0$ states) at the principle resonance, but in both cases the maximum is similarly pronounced as the difference between the local maximum and the succeeding minimum – $n_0^4 \cdot F_{10\%} \simeq 0.0305$ (lithium $\ell = 0$ states) vs. $n_0^4 \cdot F_{10\%} \simeq 0.042$ (hydrogen $\ell = 0$ states) – coincides. For atomic hydrogen, these maxima are caused by a resonance between the external frequency and the Rydberg electron's Kepler frequency which coincides with the local energy spacing in the hydrogenic Rydberg progression. Such non-linear resonances generate regular islands in the classical (mixed regular-chaotic) phase space of the periodically driven (classical) hydrogen atom and induce also a local stability of the quantum-mechanical atom. Thus, these stable regions in the dynamics of the driven hydrogen atom are a direct consequence of the classical phase space structure of the driven two-body Coulomb problem. The appearance of these maxima in the lithium threshold indicates that these non-linear resonances provide for a local stability even in the alkali dynamics, where the Coulomb symmetry is broken already in the unperturbed alkali atom (which manifests in the fact that the Runge-Lenz vector [168] – which is the additional constant of motion for the Coulomb problem, describing the position of the unperturbed Kepler ellipse – is no more conserved in the presence of a non-Coulombic potential). In both atomic species – atomic hydrogen and lithium – the relevant frequency scale is given by the splitting between the hydrogenic part of the $n_0$ and the $n_0 + 1$ manifolds. The possibility to drive this frequency (quasi-) resonantly dominates both the alkali and the hydrogen dynamics. Thus, in this regime the ionization dynamics of driven alkali atoms is well-described by the dynamics of driven atomic hydrogen. More precisely, here, the transition to chaotic transport in the classical dynamics of atomic hydrogen governs also the $n_0^3 \cdot \omega$ dependence of alkali states, despite their manifestly non-classical character, due to the scattering of the Rydberg electron off the multi-particle core [58, 169].

The dominance of the hydrogenic phase space structure for frequencies $n_0^3 \cdot \omega > 0.86$ agrees with earlier studies on moderately excited microwave driven alkali atoms. In these studies [170, 108] a prominent structure in the spectrum of driven hydrogen atoms, which is directly related to the symmetry properties of the Coulomb system [106], was found also in the lithium spectrum (note that these studies were performed below the ionization threshold, i.e., in the regime where it is still appropriate to speak of the symmetry properties of the atom, which are not yet destroyed by the external field.) Despite the presence of the non-hydrogenic core – which causes a detachment of the states emanating from the low-angular momentum states (with a non-vanishing quantum defect) from the hydrogenic part of the manifold – both, the ionization rates and (the real parts of) the quasi-energies, emanating from the hydrogenic part of the alkali manifold agree well with those of the driven hydrogen atom. The core induces only a small shift of the real parts of the quasi-energies relative to the energies of the driven hydrogen atom.

#### 5.2.1.2 Regime (II): $\Delta_{\mathrm{Hyd}} < \omega < \Delta_{\mathrm{Alk}}$

In regime (II) the situation changes significantly. This regime corresponds to the frequency window $\Delta_{\mathrm{Hyd}} < \omega < \Delta_{\mathrm{Alk}}$, i.e., here the external frequency is smaller than the splitting between adjacent unperturbed hydrogenic energy levels $\Delta_{\mathrm{Hyd}}$, while it is larger than the next possible dipole transition $\Delta_{\mathrm{Alk}}$ leaving the initial atomic state. This frequency cannot drive a one-photon transition between the unperturbed hydrogen levels, while it can strongly couple the non-hydrogenic alkali initial state to the hydrogenic manifold. Thus, an efficient mixing of non-hydrogenic and hydrogenic energy levels is still possible, for the ionization dynamics of alkali atoms there is no qualitative change with respect to regime (I), and $n_0^4 \cdot F_{10\%}$ increases with increasing $n_0^3 \cdot \omega$.

In contrast to the quantum dynamics following the classical predictions in the case of hydrogen, the alkali threshold shows the signature of dynamical localization, as in regime (I), without, however, any classical counterpart.

#### 5.2.1.3 Regime (III): $\omega < \Delta_{\mathrm{Alk}}$

Finally, for frequencies $\omega < \Delta_{\mathrm{Alk}}$, i.e., in regime (III) where the frequency is smaller than the next dipole allowed transition leaving the initial atomic state, even the alkali spectrum does not offer any possible one-photon dipole transition that can be driven efficiently. Thus, only higher order processes can activate the transport of the electronic population to higher energies. In figure 5.2.1, the transition from high to low 'scaled' frequencies is reflected by a transition from a decreasing to an essentially $n_0^3 \cdot \omega$-independent 'scaled' threshold, when the frequency falls below $n_0^3 \cdot \omega \simeq 0.4$ . The 'scaled' frequency $n_0^3 \cdot \omega \simeq 0.4$ corresponds to $n_0 = 42$, where the external frequency equals $1.13$ times the splitting between the unperturbed $\ell_0 = 0$ and the $\ell_0 = 1$ state. For $n_0 = 41$, the frequency $\omega$ equals $1.05$ times the $\ell_0 = 0$ – $\ell_0 = 1$ splitting, while for $n_0 < 41$ the splitting between the unperturbed $\ell_0 = 0$ and the $\ell_0 = 1$ states exceeds the external frequency, and here a one-photon transition is impossible.

The transition from frequencies $\omega$ which are small compared to $\Delta_{\mathrm{alk}}$ to high 'scaled' frequencies, i.e. the transition from the low 'scaled' frequency regime (III) to the high 'scaled' frequency regimes of dynamical localization (II) and (I), can be extracted most clearly from the 'unscaled' representation in figure 5.4. It becomes clear from this plot that the apparent $n_0^3 \cdot \omega$ independence of the 'scaled' threshold in regime (III) as suggested in figure 5.2.1 is really a feature of the representation of the data in 'scaled' units, while in laboratory units the threshold indeed does depend on the principal quantum number $n_0$. In the low 'scaled' frequency regime, i.e. for principal quantum numbers $n_0 \leq 42$, there is a steep decrease of the laboratory value of the threshold amplitude with increasing $n_0$. This decrease changes abruptly at $n_0 = 42$ to a weaker fall-off of $F_{10\%}$ with $n_0$. For larger $n_0$, the overall slope of the 'unscaled' alkali threshold does not change much, and finally, for $n_0 \geq 55$, also the (numerical and laboratory) hydrogen thresholds follow the alkali threshold, in agreement with the observations for regime (I) depicted above.

With the 'unscaled' representation of the data, we can now draw a connection between the different approaches for the understanding of the microwave ionization of alkali atoms as they were sketched in section 1.1.2. For this purpose we plotted also the functions $(3.7n_0^5)^{-1}$, $(3n_0^5)^{-1}$ and $(90n_0^4)^{-1}$ in figure 5.4. While the function $(90n_0^4)^{-1}$ is drawn as an approximate fit to our data (for $n_0 = 28, \ldots, 42$), the functions $(3.7n_0^5)^{-1}$ [53, 46] and $(3n_0^5)^{-1}$ [171, 47, 111] are the ionization thresholds proposed by the Virginia group as sketched in section 1.1.2.2. Since the difference between $(90n_0^4)^{-1}$ and $(3n_0^5)^{-1}$ is only small for $n_0 \simeq 30$, it is unclear whether our results can be approximated by the Virginia thresholds, but it is consistent with figure 5.4 that a $n_0^{-5}$ dependence is the limiting curve for the lithium thresholds in this regime. Hence, we can now verify the assumption of an $n_0^{-5}$ dependence of the alkali ionization thresholds, as proposed by the Virginia group. However, it is clear

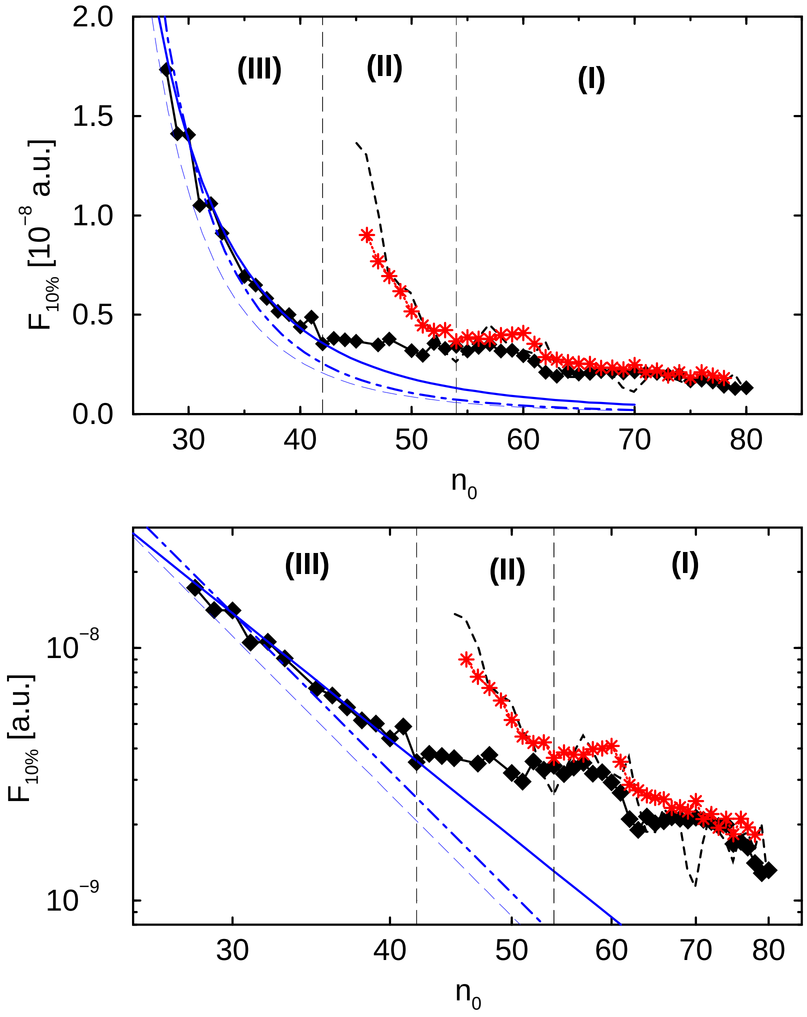

Figure 5.4: 'Unscaled' representation of the data shown in figure 5.2.1, on a linear (above) and on a double-logarithmic plot (below). For large principal quantum numbers $n_0 > 54$, the ionization threshold of lithium (filled diamonds) roughly coincides with the hydrogen thresholds (stars: numerical results, and dashed line: experimental results [20]). These quantum numbers determine regime (I) in figure 5.2.1, regime (II) is defined by quantum numbers $n_0 = 42, \ldots, 54$. Quantum numbers $n_0 < 42$ determine the low 'scaled' frequency regime (III). Here the threshold follows a trend between $1/(3.7 \cdot n_0^5)$ (thin dashed line) and $1/(90 \cdot n_0^4)$ (full line). The dash-dotted line follows a law $1/(3 \cdot n_0^5)$. Both $n_0^{-5}$ curves determine the ionization threshold proposed by the Virginia group [53, 46, 171, 111].

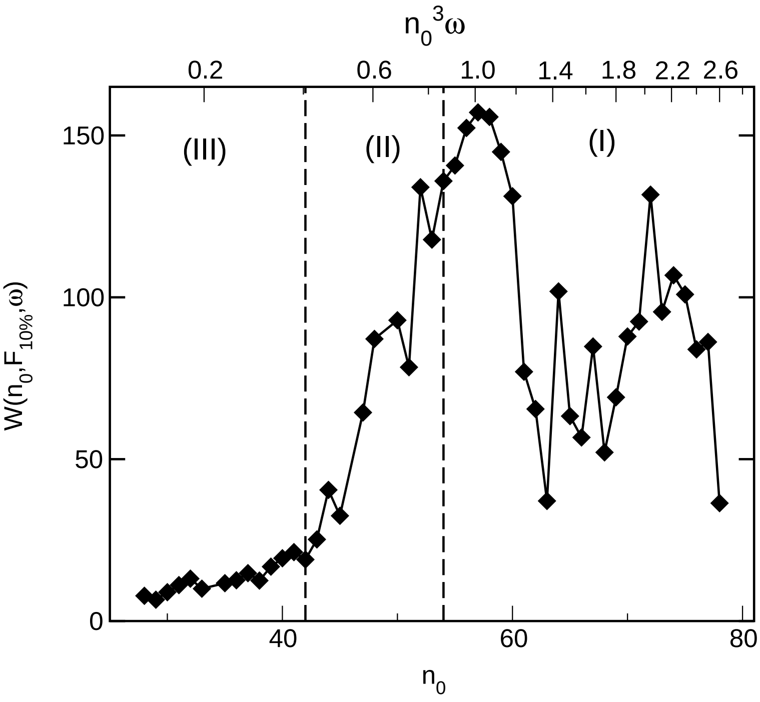

Figure 5.5: Shannon width of microwave driven lithium atoms, prepared in the initial states $|n_0, \ell_0 = m_0 = 0\rangle$, evaluated at $F_{10\%}(t = 327 \cdot 2\pi/\omega)$, for $\omega/2\pi = 36$ GHz. The width function $W$ is plotted as a function of the principal quantum number of the atomic initial state $n_0$ (lower abscissa) and of the 'scaled' frequency $n_0^3 \cdot \omega$ (abscissa on top). The frequency is chosen as in 5.2.1.

that such a dependence is only true in regime (III), i.e. for frequencies $\omega$ smaller than the energy splitting between the atomic initial state and the next state accessible via a dipole transition, while for larger $n_0$ the atom shows the signature of dynamical localization as observed by the Munich group.

### 5.2.2 The Shannon width

Before presenting the results of our numerical experiment on rubidium atoms, we want to give account for another means to discriminate the dynamics in the low 'scaled' frequency regime (III) from the dynamics in the regimes (II) and (I) of dynamical localization. Following the considerations about the onset of the ionization process – i.e. the Virginia proposal (see section 1.1.2.2) leading to a $n_0^{-5}$ dependence in regime (III), vs. ionization in the presence of dynamical localization in regimes (II) and (I) – the number of Floquet states involved in the dynamics should differ qualitatively in the different regimes. In regime (III), higher order multi-photon resonances induce a transport of the electronic population via some Landau-Zener transitions to higher lying quasi-energy states, which ionize at a much weaker field amplitude (as can be seen in figure 5.4). In this regime there is only a small number of possible paths leading to ionization, and hence only a few states are involved in the ionization process. In the regimes (II) and (I) on the other hand, the external frequency can couple many atomic bound and continuum states quasi resonantly and hence the electronic density spreads over many Floquet states. Thus, we expect less states participating in the ionization process in regime (III) than in the regimes (I) and (II). As a measure for the number of states partaking in the ionization process, and to quantify the difference between 'few' and 'many' states more precisely, we calculated the Shannon width (2.61) at the 10%-ionization threshold for each initial state. The result is shown in figure 5.5.

Although the ionization probability after $327$ field cycles is the same for all states, the Shannon width varies strongly. In particular, we see a significant difference between regime (III) and the regimes (II) and (I) of dynamical localization. As explained above, in regime (III), the splitting between adjacent unperturbed (alkali) energy levels $\Delta_{\rm alk}$ is larger than the photon energy $\omega$, what prevents an efficient coupling of many states, and the initial state extends over only a small number of atom-field eigenstates.(2)

The transition from the low 'scaled' frequency regime to regime (II) is visible as a steep increase of the Shannon width as soon as the frequency exceeds $\Delta_{\rm Alk}$, i.e. exactly for $n_0 > 42$. It further exhibits local maxima around $n_0^3 \cdot \omega = 1$ and $n_0^3 \cdot \omega = 2$, where the frequency is in resonance with the splitting between adjacent hydrogen-like manifolds.

Although the Shannon width is in principle basis dependent, similar plots as figure 5.5 are also feasible in laboratory experiments that allow for measuring the final state distribution of the electronic population over the bound states. This can be done, for instance, in the recent experiments of the Virginia group [49]. These experiments should not only measure a difference in the slope of $n_0^4 \cdot F_{10\%}$ as a function of $n_0^3 \cdot \omega$ in the low (regime (III)) and the high (regime (II) and (I)) 'scaled' frequency regimes, but also a qualitative difference in the number of states over which the electronic density spreads after the interaction time $t$ at the field amplitude inducing ten percent ionization probability. Hence, a marked transition between the different regimes (i.e. from (III) to (II)) can immediately be measured not only by means of the ionization probability, but also by the final state distribution in state-of-the-art experiments.

### 5.2.3 Rubidium

Understanding the difference between the hydrogen and the lithium thresholds, we will now address the question whether the behavior of lithium atoms under external driving is generic for singly excited Rydberg atoms. The specific feature of lithium atoms is the presence of only one single large quantum defect for $\ell = 0$, while already the splitting between the $\ell = 1$ and the $\ell > 1$ states can be neglected compared to the splitting induced by an external field that produces an ionization probability of a few per cent. Moving downwards in the periodic table of the elements to the heavier alkali atoms, the number of non-vanishing quantum defects is increasing: In sodium atoms, the $\ell = 0$ and $\ell = 1$ quantum defects have to be considered as non-vanishing, whereas in potassium and rubidium there are already three ($\ell = 0,\ \ell = 1,\ \ell = 2$) non-vanishing quantum defects (see table 2.3.1). To study the influence of multiple quantum defects, we shall now employ rubidium ($m_0 = 0$) atoms, for which the signature of dynamical localization was already observed experimentally, with, however, strongly enhanced ionization rates as compared to atomic hydrogen [42, 9, 172].

---

(2) Note that although in regime (III) only a small number – between 8 and 25 – of atom-field eigenstates contribute to the representation of the initial state, this does not imply that this is a perturbative regime, since in this regime the minimum number of photons to reach the effective continuum varies from 44 to 112, what makes a perturbative description at least questionable, and practically impossible.

For rubidium we performed two sets of numerical experiments: For the sake of comparison with the numerical (lithium and hydrogen) results presented above, in the first set we employed exactly the same parameters as already used for hydrogen and lithium, i.e. a laboratory frequency $\omega/2\pi = 36$ GHz, with principal quantum numbers $n_0 = 38, \ldots, 66$. In addition, we performed a simulation with the laboratory parameters used in the experiments on microwave driven rubidium atoms [42], more precisely with the frequency $\omega/2\pi = 8.87$ GHz, and principal quantum numbers in the range $n = 59, \ldots, 80$. The atom-field interaction time in both “experiments” (i.e. the $36$ GHz and the $8.87$ GHZ simulation) was set to $t = 327 \cdot 2\pi/\omega$,$^{(3)}$ and the angular momentum of the initial state was chosen as $\ell_0 = 0$ and $\ell_0 = 1$, respectively.

In figure 5.6 we display the results of both numerical experiments, the 'scaled' ionization threshold $n_0^4 \cdot F_{10\%}(t)$ as a function of the 'scaled' frequency $n_0^3 \cdot \omega$. The upper plot compares the data of all our numerical experiments performed at frequency $\omega/2\pi = 36$ GHz: the ($\ell_0 = 0$) thresholds of hydrogen and lithium atoms, together with thresholds of $\ell_0 = 0$ and $\ell_0 = 1$ states of rubidium. In the lower plot, we compare the results of both rubidium simulations, at $\omega/2\pi = 36$ GHz and at $\omega/2\pi = 8.87$ GHz, respectively, covering essentially the same interval of 'scaled' frequencies.

On a first glance, the lithium and the rubidium curves in the upper plot look quite similar, i.e. also rubidium shows the separation in the three frequency regimes we are already familiar with:

(I) For frequencies $n_0^3 \cdot \omega > 0.8 \ldots 0.86$ – in regime (I), which is only partially covered by our numerical experiment on rubidium in the $\omega/2\pi = 36$ GHz,

---

(3) This is in contrast to the laboratory experiments on rubidium [42, 9] where an atom-field interaction time $t = 5\ \mu$s was employed. However, such an interaction time corresponds to $t = 2 \cdot 10^{11}$ a.u., and, hence, to obtain reliable results for the ionization threshold, the error of the widths $\Gamma_j$ has to be smaller than $\sim 10^{-14}$ a.u., what is beyond the accuracy of our numerical results (limited by finite precision arithmetics). To achieve such accuracy employing a higher precision in the code (i.e. a higher precision than double precision) would eventually help, however, this would also require much larger memory (which is a critical resource).

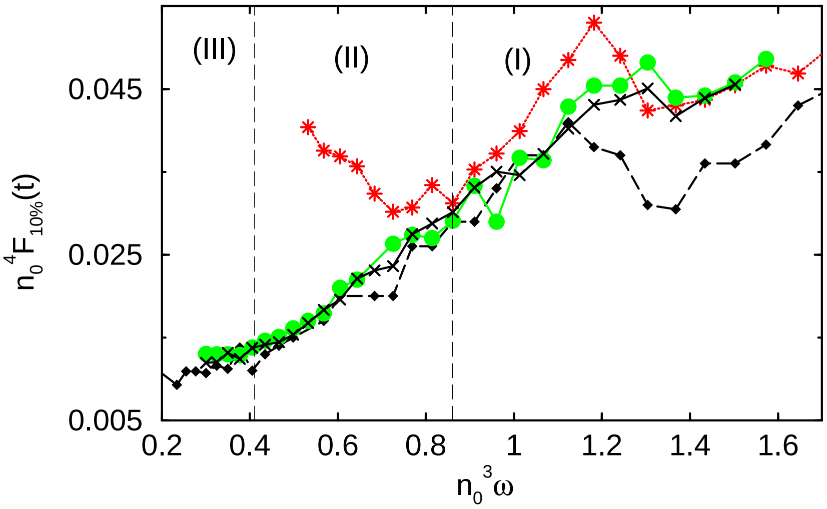

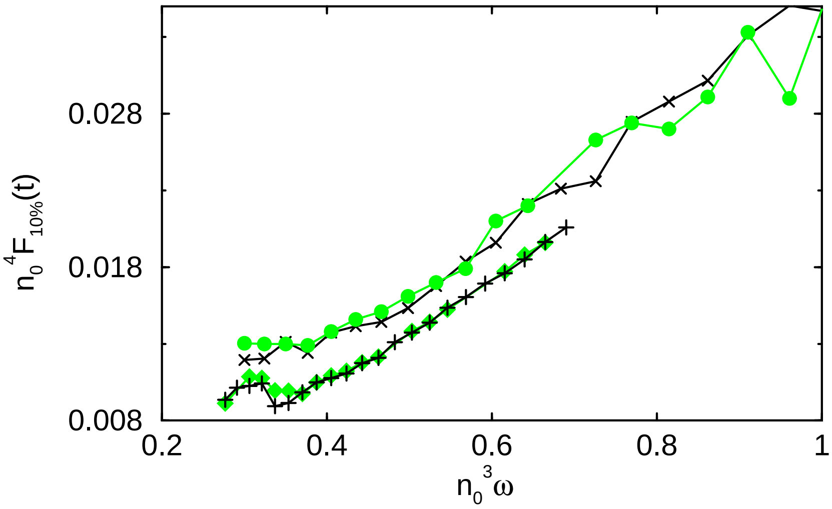

Figure 5.6: Upper plot: 'Scaled' ionization threshold vs. 'scaled' frequency for rubidium atoms initially prepared in the states $|n_0, \ell_0 = m_0 = 0\rangle$ (filled green circles), and $|n_0, \ell_0 = 1, m_0 = 0\rangle$ (black x) together with the results for initial states $|n_0, \ell_0 = 0, m_0 = 0\rangle$ of lithium (filled black diamonds) and of hydrogen (stars). Principal quantum numbers, frequency and interaction time are the same in all simulations, i.e. $\omega/2\pi = 36$ GHz, and $t = 327 \cdot 2\pi/\omega$. Lower plot: 'Scaled' ionization threshold vs. 'scaled' frequency of rubidium atoms, obtained with the same parameters as in the upper plot (filled circles: $|n_0, \ell_0 = m_0 = 0\rangle$; x: $|n_0, \ell_0 = 1, m_0 = 0\rangle$), compared to results for $\omega/2\pi = 8.87$ GHz, $n_0 = 59, \ldots, 80$, and $t = 327 \cdot 2\pi/\omega$. Also for the lower frequency, results for $\ell_0 = 0$ (filled green diamonds) and for $\ell_0 = 1$ (black crosses) are shown.

and which is not at all covered in the $\omega/2\pi = 8.87$ GHz simulation – the 'scaled' rubidium threshold follows the lithium and the hydrogen results, both qualitatively and quantitatively. In particular, we can also observe a local maximum close to the principal non-linear resonance in the classical phase space of the driven Coulomb system, more precisely at $n_0^3 \cdot \omega \simeq 1.3$, corresponding to $n_0 = 62$. In contrast to the lithium and the hydrogen data, however, this maximum is less pronounced in the case of rubidium. We attribute this to the difference in the level structure of unperturbed rubidium and lithium (or hydrogen) atoms due to the additional non-vanishing quantum defects. These anticrossings in the spectrum of the driven atom that induce the local minimum at $n_0^3 \cdot \omega \simeq 1.3$ become less important in the representation of the $\ell_0 = 0, 1$ initial states of rubidium atoms and we do only observe a less pronounced maximum in the 'scaled' rubidium threshold as compared to lithium or hydrogen.

(II) In regime (II) ($0.4 \lesssim n_0^3 \cdot \omega < 0.86$), the agreement between lithium and rubidium thresholds is qualitatively and quantitatively perfect for $\omega/2\pi = 36$ GHz (displayed in a), while there is a small deviation between the lithium ($\omega/2\pi = 36$ GHz) and the rubidium ($\omega/2\pi = 8.87$ GHz) data displayed in (b), i.e. the $8.87$ GHz results show slightly lower thresholds. However, this does not imply that the hydrogenic scaling rules are not applicable in this regime. On the contrary, the perfect qualitative agreement of the $8.87$ GHz and the $36$ GHz data strongly supports the validity of the scaling rules for alkali atoms. Note that even for atomic hydrogen – where the scaling rules are applicable [31] – a similar deviation can be observed when laboratory results for $n_0 \simeq 60$ are compared with numerical results for $n_0 \simeq 23$ [34, 33]. This can be understood already from the statistical theory of dynamical localization [24], which introduces a 'scaled' delocalization border that depends not only on the 'scaled' frequency, but also on the principal quantum number $n_0$ [33], as it was already noted in section 1.1.1. Thus the delocalization border decreases for increasing $n_0$ (and fixed 'scaled' frequency), and therefore also the 'scaled' ionization threshold decreases for increasing $n_0$ in the regime of dynamical localization. Note that such effect can be attributed to the finite size of Planck's constant $\hbar$, as already mentioned earlier (see footnote on page 5).

(III) Finally, for low 'scaled' frequencies – in regime (III) – the 'scaled' threshold is nearly flat, i.e. essentially independent of the 'scaled' frequency. Again, the $\omega/2\pi = 36$ GHz rubidium data agree well with the lithium results. The $\omega/2\pi = 8.87$ GHz data, however, show the transition from (III) to (II) at a slightly lower 'scaled' frequency ($n_0^3 \cdot \omega \simeq 0.37$ vs. $n_0^3 \cdot \omega \simeq 0.42$), and – as in regime (II) – exhibit slightly lower thresholds than the $36$ GHz data.

Yet, a closer look to the transition from the low 'scaled' frequency (III) to the high 'scaled' frequency regime (II), together with the attempt to interpret the transition from regime (III) to regime (II), reveals some differences between the rubidium and the lithium thresholds.

#### 5.2.3.1 Modifications of the transition from frequency regime (II) to (III) in the presence of multiple quantum defects

For a better identification of the different transitions between the frequency regimes (II) and (III), we present the data of figure 5.6 in 'unscaled' units (ionization threshold vs. principal quantum number of the initial state) in figure 5.7. Again, the upper plot displays the $\omega/2\pi = 36$ GHz data for hydrogen, lithium, and rubidium $\ell_0 = 0$ states, and for rubidium $\ell_0 = 1$ states. The lower plot displays the $\omega/2\pi = 8.87$ GHz results for the rubidium $\ell_0 = 0$ and $\ell_0 = 1$ states.

As already observed in the last section, microwave driven lithium atoms show a relatively clear transition from regime (III) to (II) at $n_0 \simeq 42$, from a dependence between $n_0^{-4}$ to $n_0^{-5}$ for $n_0$ below $42$, to a manifestly smaller slope for $n_0 > 42$. For the $\ell_0 = 0$ and $\ell_0 = 1$ states of rubidium, on the other hand, we can also observe a dependence between $n_0^{-4}$ and $n_0^{-5}$ for low $n_0$. However, there is no abrupt change to a smaller slope at a precise value of $n_0$, but rather a smooth transition to regime (II) between $n_0 \simeq 40$ and $n_0 \simeq 46$. The same scenario is also observed in the $8.87$ GHz rubidium data, where the $\ell_0 = 0$ and $\ell_0 = 1$ thresholds start to deviate from the approximate $n_0^{-4}$ or $n_0^{-5}$ dependence already at $n_0 \simeq 65$, but – much as the 36 GHz data – exhibit a rather smooth transition to a lithium-like $n_0$ dependence in regime (II), which is not reached before approximately $n_0 = 70$. This is in slight disaccord with the rules which we formulated in the discussion of our lithium results for the transition from regime (III) to (II), according to which the slope of the $36$ GHz threshold should change at $n_0 = 47$, corresponding to $E_{n_0=47,\ell_0=1} - E_{n_0=47,\ell_0=0} \simeq 2\pi \cdot 36$ GHz (while the transition in the $8.87$ GHz data is expected at $n_0 = 74$, corresponding to $E_{n_0=74,\ell_0=1} - E_{n_0=74,\ell_0=0} \simeq 2\pi \cdot 8.87$ GHz).

To understand the apparent deviation of the $n_0$-dependence of the rubidium thresholds with respect to the lithium behavior, we define the function

$$D_{\mathrm{atom}}^{\ell\to\ell+1}(n) = \frac{\frac{-1}{2\left(n'-\delta_{\ell+1,\mathrm{atom}}\right)^2} - \frac{-1}{2\left(n-\delta_{\ell,\mathrm{atom}}\right)^2}}{\omega}, \tag{5.1}$$
$$\text{with atom} = \mathrm{Li},\ \mathrm{Na},\ \mathrm{K},\ \mathrm{Rb},\ \text{and } n' = n \text{ or } n-1.$$

It is clear that $D_{\mathrm{atom}}^{\ell\to\ell+1}(n)$ expresses the energy difference between the unperturbed $\ell$ state and the closest unperturbed $\ell+1$ state (which potentially has the principal quantum number $n-1$, e.g. for the $\ell = 1 \to 2$ transition in rubidium, since the integer parts of the relevant quantum defects may differ by unity in the cases considered here, see table 2.3.1) normalized by the frequency $\omega$. In figure 5.8 we display the function (5.1) as a function of $n_0$ for lithium (a) and rubidium ((b) and (c)). Following the (lithium) rules for the transition from (III) to (II), $D^{\ell_0\to\ell_0+1} = 1$ should indicate the quantum number $n_0$ where the transition from regime (III) to (II) occurs. Comparison of figures 5.8(a) and 5.2.1 shows that this prediction fits well for

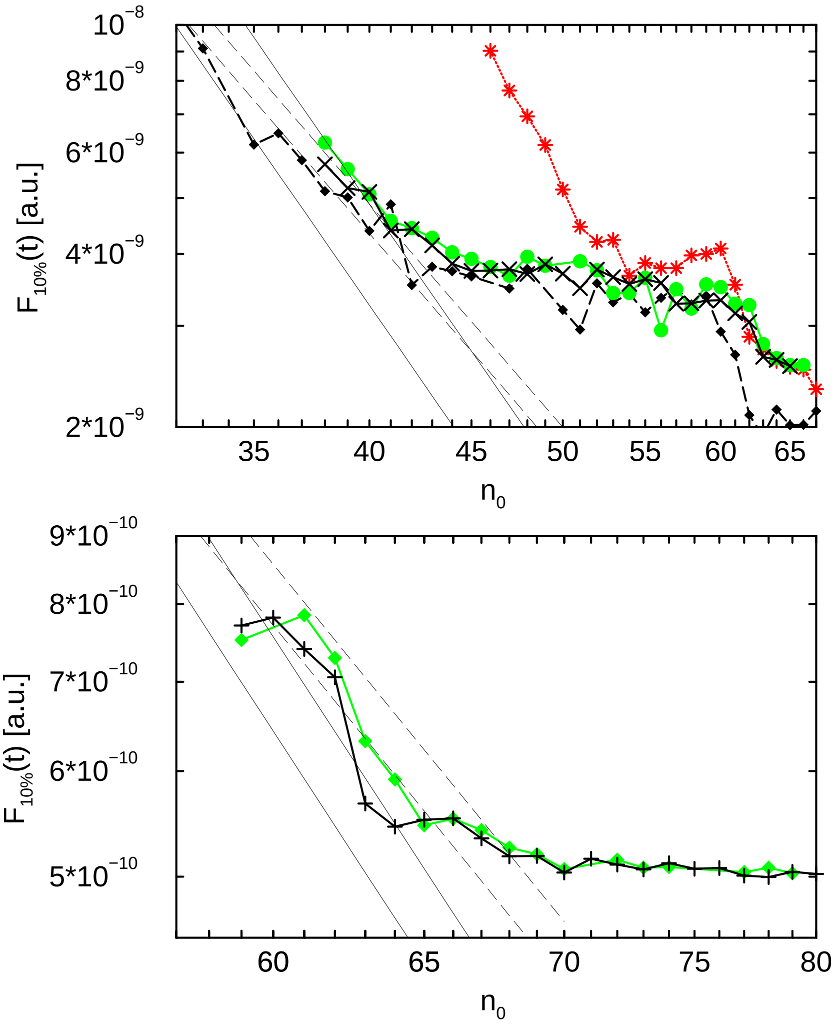

Figure 5.7: 'Unscaled' representation of the 10% ionization thresholds of figure 5.6. In the upper plot, the results on hydrogen (stars), lithium (small filled black diamonds), and rubidium $|n_0, \ell_0 = m_0 = 0\rangle$ states (filled green circles), as well as on rubidium $|n_0, \ell_0 = 1, m_0 = 0\rangle$ states (black x) are shown. All these results were obtained for $\omega/2\pi = 36$ GHz. In the lower plot, we display results on rubidium $|n_0, \ell_0 = m_0 = 0\rangle$ (filled green diamonds) and $|n_0, \ell_0 = 1, m_0 = 0\rangle$ states (black crosses) obtained for $\omega/2\pi = 8.87$ GHz. In both plots the full (dashed) lines have a slope $\sim n_0^{-5}$ ($\sim n_0^{-4}$).

lithium, since $D_{\mathrm{Li}}^{0\to 1} = 1$ between $n_0 = 40$ and $n_0 = 41$ (in agreement with the transition occurring at this quantum numbers in figure 5.2.1).

For rubidium, however, the situation changes significantly, as we learn from figure 5.8 (b) and (c), where we plotted $D_{\mathrm{Rb}}^{\ell_0\to \ell_0+1}$ for the transitions $\ell_0 = 0 \to 1$, $\ell_0 = 1 \to 2$, and $\ell_0 = 2 \to 3$ (for $\omega/2\pi = 36$ GHz (b), and $\omega/2\pi = 8.87$ GHz (c)). In (b) $D_{\mathrm{Rb}}^{0\to 1}$ intersects the function $D = 1$ close to $n_0 = 47$, giving rise to the assumption that in rubidium (initial angular momentum $\ell_0 = 0$) the transition from (III) to (II) should take place at $n_0 \simeq 47$. However, it is the transition $\ell_0 = 1 \to 2$ that plays the important role, since $D_{\mathrm{Rb}}^{1\to 2} = 1$ between $n_0 = 40$ and $n_0 = 41$. At this quantum number we observe a deviation from the lithium-like trend in regime (III), i.e. this value defines the quantum number where the smooth transition to regime (II) starts. This indicates that the possibility to drive the transition $\ell_0 = 1 \to 2$ resonantly is already sufficient to change the character of the ionization process, even for the initial state $|n_0, \ell_0 = 0, m_0 = 0\rangle$, which a priori remains unaffected by this coupling. The reason for this deviation from the lithium rules is that the external field is strong enough to couple low angular momentum states already below threshold, thus leading to the importance of $D_{\mathrm{Rb}}^{1\to 2}$. $D_{\mathrm{Rb}}^{0\to 1}$ plays another role: it approximates the quantum number where the smooth transition from regime (III) to regime (II) is completed. In the specific case of the upper plot in figure 5.7, this is the quantum number $n_0 \simeq 46$, for which we observe a lithium-like trend of the rubidium threshold (in agreement with $D_{\mathrm{Rb}}^{0\to 1} = 1$ at $n_0 \simeq 47$). Since the low-angular momentum states are efficiently coupled already below threshold, the same arguments are valid for atomic initial states with $\ell_0 = 1$. Again, $D_{\mathrm{Rb}}^{1\to 2} = 1$ marks the quantum number where the transition between regimes (III) and (II) starts, and $D_{\mathrm{Rb}}^{1\to 0} = 1$ gives the quantum number which define the upper edge of the transition region.

We observe the same situation for the $8.87$ GHz data in figure 5.8(c). Here, the transition from low to high 'scaled' frequencies approximately starts at $n_0 = 65$, in rough agreement with $D_{\mathrm{Rb}}^{1\to 2} = 1$ at $n_0 \simeq 63$, while the transition is completed at $n_0 \simeq 70$, again in rough agreement with $D_{\mathrm{Rb}}^{0\to 1} = 1$ at $n_0 \simeq 74$.

## 5.3 Does the alkali ionization dynamics obey scaling rules?

In section 2.2, we noted that there are a priori no scaling rules for the dynamics of driven alkali atoms, as the size of the atomic core introduces a finite length scale. Only now, with the results of our numerical experiments on lithium, rubidium, and on hydrogen atoms, we can *a posteriori* assert that there are indeed scaling rules for the dynamics of periodically driven singly excited Rydberg atoms. These scaling rules, however, differ from the semi-empirical scaling rules proposed by the Munich group that were mentioned in the introduction. The picture suggested by our data is the following:

1. Regime (I): By virtue of (2.19) and (2.20), all alkali and hydrogen thresholds are mapped on each other, for frequencies $n_0^3 \cdot \omega \gtrsim 0.86$. Classical

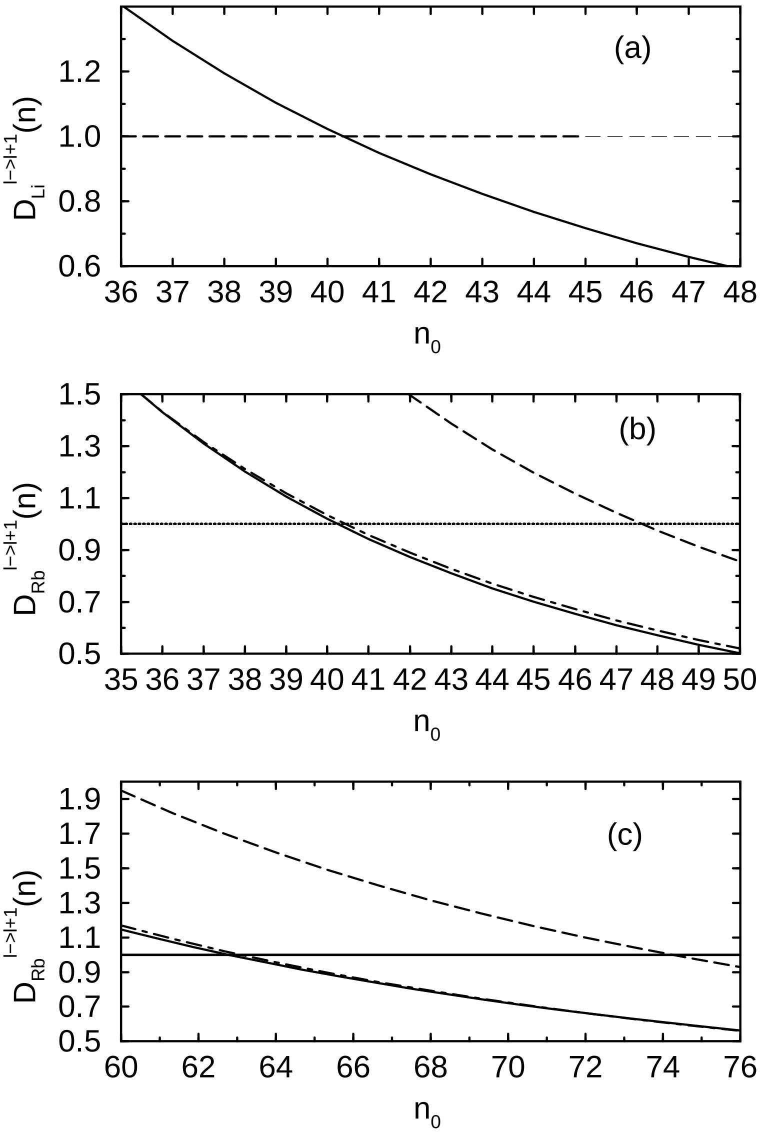

Figure 5.8: Splitting of adjacent, unperturbed, non-hydrogenic alkali energy levels as defined by (5.1), normalized to the driving frequencies $\omega = 2\pi \cdot 36$ GHz (in (a) and (b)) and by $\omega = 2\pi \cdot 8.87$ GHz (in (c)). In (a) we display $D_{\rm Li}^{0\to1}(n_0)$, in (b) the functions $D_{\rm Rb}^{0\to1}(n_0)$ (dashed line), $D_{\rm Rb}^{1\to2}(n_0)$ (solid line), and $D_{\rm Rb}^{2\to3}(n_0)$ (dash-dotted line). The implicit equation $D_{\rm Li}^{0\to1}(n_0) = 1$ indicates the quantum number $n_0$ where the transition from frequency regime (III) to (II) in the ionization threshold (compare figure 5.2.1) takes place. In (b) and (c), $D_{\rm Rb}^{0\to1}(n_0) = 1$ and $D_{\rm Rb}^{1\to2}(n_0) = 1$ define the range of quantum numbers $n_0$ where the smooth transition from (II) to (III) occurs (see figure 5.7).

stability islands of the driven two-body Coulomb problem even prevail in the alkali ionization dynamics, at $n_0^3 \cdot \omega \simeq 1.1, \ldots, 1.3$ (lithium, rubidium), and at $n_0^3 \cdot \omega \simeq 2.2$ (lithium). Consequently, the scaling property of the alkali thresholds in this frequency regime expresses the dominant role of the classical phase space structure of the hydrogen problem [108], eventually amended by core-induced scattering [173] between invariant tori of the Coulomb dynamics. The latter, however, can hardly be detected in the ionization yield or threshold which both are rather insensitive to details of the atomic excitation and ionization dynamics.

2. Regime (II): Whereas, in 'scaled' units defined by (2.19) and (2.20), all alkali thresholds coincide in this frequency window, there is a dramatic difference with respect to the scaled hydrogen thresholds, which nonetheless abide the same scaling rules. Since the latter results directly reflect the classical phase space structure, it obviously follows that the alkali thresholds do no longer mimic any characteristics of the classical Coulomb dynamics but rather are a pure consequence of the alkali quantum spectrum.
   Scaling prevails since, notwithstanding, every sufficiently strong field with frequency larger than the relevant alkali energy splitting $\Delta_{\text{alk}}$ will induce strong atomic excitation, irrespective of the element-specific unperturbed level structure. Normalization of $\omega$ by $n_0^{-3}$ additionally eliminates the local density of states.

3. Regime (III): Only for frequencies which are smaller than the element-specific $\Delta_{\text{alk}}$ does the scaling break down for non-hydrogenic alkali states. This is natural, since the value $\Delta_{\text{alk}}$ directly reflects the finite size of the atomic core (see our discussion in chapter 2.3), and defines the – element-specific – value of $n_0^3 \cdot \omega$ which separates regimes (III) and (II).

In the following section we shall discuss the laboratory results of the Virginia and of the Munich group in the context of our scaling rules formulated above. This sheds new light on many laboratory results which so far have not been explained satisfactorily. As we will see, the laboratory results are fully consistent with our own findings.

## 5.4 Laboratory experiments

We shall now compare the results of our numerical experiments with those obtained in the laboratory, on rubidium [42, 9], lithium [48], and sodium [47]. As mentioned in the introduction, experiments on microwave driven non-hydrogenic states (where transitions to states with non-vanishing quantum defects are possible) of alkali atoms provoked the following observations and working hypotheses:

E1 Alkali atoms show enhanced ionization rates as compared to hydrogen [53, 47, 48, 42, 9].

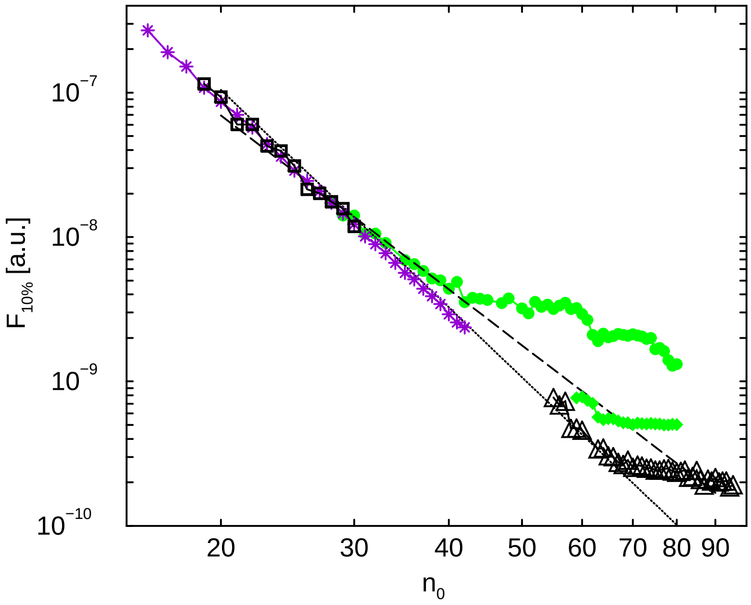

Figure 5.9: 'Unscaled' representation of (laboratory) experimental results on microwave driven lithium (open squares [48]), sodium (stars [47], and rubidium (triangles [42]), together with our numerical data on lithium (filled green circles) and on rubidium (filled green diamonds). The different experiments were performed at different frequencies and interaction times $t$: Li (experiment): $\omega/2\pi = 15$ GHz, $t = 15000 \cdot 2\pi/\omega$; Na (exp.): $\omega/2\pi = 8$ GHz, $t = 4000 \cdot 2\pi/\omega$; Li (numerics): $\omega/2\pi = 36$ GHz, $t = 327 \cdot 2\pi/\omega$; Rb (num. and exp.): $\omega/2\pi = 8.87$ GHz, $t = 327 \cdot 2\pi/\omega$ (numerics), and $t = 44335 \cdot 2\pi/\omega$ (laboratory). The full (dashed) line has a slope $n_0^{-5}$ ($n_0^{-4}$).

E2 The ionization dynamics of alkali atoms differs quantitatively and qualitatively from the hydrogen dynamics [53, 47, 48].

E3 Employing semi-empirical scaling rules (which consists in normalizing the driving field frequency with respect to the next energy gaining dipole transition leaving the initial state) the scaled alkali ionization thresholds show qualitatively the same behavior as the scaled hydrogen thresholds [42, 9].

On the basis of the insight we have gained with our numerical experiments on the ionization dynamics of microwave driven Rydberg states, we can now reformulate these statements. In particular, we can clarify the apparent contradiction between E2 and E3 above – and corroborate our predictions (based on numerical experiments) by means of experimentally measured ionization thresholds.

For this purpose, we display experimental results for the 10% thresholds of microwave driven lithium [48], sodium [47], and rubidium [42] atoms as a function of the principal quantum number $n_0$, together with our numerical results on lithium ($\omega/2\pi = 36$ GHz) and the numerical $8.87$ GHz data on rubidium in figure 5.9. To understand the similarities and differences between the different results shown in that figure, we shall now discuss the results of the different experimental groups in detail.

### 5.4.1 The Virginia experiments on lithium and sodium

The experiments on lithium [48] and sodium [47] were performed at rather low frequencies $\omega_{\rm Li}/2\pi = 15$ GHz (for lithium), and $\omega_{\rm Na}/2\pi = 8$ GHz (for sodium), and for relatively low-lying Rydberg states ($n_{\rm Li} = 19, \ldots, 30$, and $n_{\rm Na} = 16, \ldots, 42$, respectively). By virtue of (5.1), these frequencies correspond to a transition from regime (III) to regime (II) at $n_0 \simeq 54$ (lithium) and at $n_0 \simeq 52$ (sodium). Hence, both experiments were performed solely in regime (III), far below the transition to the regime of dynamical localization, and in figure 5.9 the experimental lithium and sodium thresholds cover only the low frequency regime. Thus, it is clear that, on the one hand, lower thresholds than those of atomic hydrogen (which follows the classical predictions in this regime) were measured (E1), and, on the other hand , a qualitatively distinct behavior of the lithium and sodium ionization dynamics from that of atomic hydrogen was observed (E2).

As discussed in [48, 47], and as evident from figure 5.9, the thresholds of both experiments exhibit a dependence $F_{10\%} \simeq (3n_0^5)^{-1}$, which was also the limiting curve of our lithium and rubidium results for low quantum numbers (see section 5.2.1 and 5.2.3). The choice of the parameters in [48, 47] also explains why the data obtained in these experiments follow the $n_0^{-5}$ behavior much more neatly than our numerical data (as apparent from figure 5.9): the reason is that these experiments were performed much closer to the limit of quasistatic fields, i.e. the employed quantum numbers correspond to $n_0^3 \cdot \omega_{\rm Li} = 0.016, \ldots, 0.06$, and $n_0^3 \cdot \omega_{\rm Na} = 0.005, \ldots, 0.09$, respectively, while our numerical experiment was performed at $n_0^3 \cdot \omega > 0.12$.

### 5.4.2 The Munich experiments on rubidium

While the experiments on rubidium [42, 9] were also performed at a rather low frequency $\omega_{\rm Rb}/2\pi = 8.87$ GHz, they employ higher Rydberg states than the Virginia group, i.e. states in the range $n = 55, \ldots, 93$, corresponding to $n_0^3 \cdot \omega_{\rm Rb} = 0.22, \ldots, 1.16$. This low ('scaled') frequency interval was also covered by our numerical $8.87$ GHz experiments on rubidium which were performed using precisely the same parameters, apart from a shorter atom-field interaction time $t = 327 \cdot 2\pi/\omega$ as compared to the laboratory value $t = 44335 \cdot 2\pi/\omega$. Consequently, the results of the rubidium experiments show the same features as we already observed in our simulation: For low principal quantum numbers, $n_0 < 65$, the laboratory thresholds show a dependence close to $n_0^{-5}$. However, as in our numerical results, this law remains an approximation, since relatively large quantum numbers $n_0$ and hence, larger 'scaled' frequencies than in the Virginia experiments were employed.

Since rubidium atoms exhibit multiple non-vanishing quantum defects, the transition from regime (III) – with $F_{10\%} \sim n_0^{-5}$ – to regime (II) – where the decrease of $F_{10\%}$ with $n_0$ is slower – does not occur abruptly. On the contrary, the laboratory experiments observe a smooth transition between $n_0 \simeq 65$ and $n_0 \simeq 70$, i.e., exactly in the range where we observe the transition in our simulation. However, the absolute values of laboratory and numerical thresholds do not agree, what we attribute to the difference in the atom-field interaction time (as noted earlier, the extremely long laboratory interaction time $t = 5\ \mu\mathrm{s} = 44335 \cdot 2\pi/\omega$ cannot be simulated for $\omega/2\pi = 8.87$ GHz, within our numerical set-up with finite precision arithmetics)

In figure 5.10 we display the laboratory results on rubidium [42], together with our numerical (rubidium) thresholds and the (numerical and laboratory) results on atomic hydrogen [20], in 'scaled' variables. This comparison clearly demonstrates that these early experimental results [42, 9] already provided strong evidence in favor of our prediction of a separation of the alkali ionization dynamics in three different frequency regimes, with:

(I) the hydrogenic regime (I) of dynamical localization, where the ionization dynamic follows the ionization process of atomic hydrogen;

(II) the non-hydrogenic regime (II) of dynamical localization, where the scaled threshold for microwave driven alkali atoms increases with increasing scaled frequency, while it decreases for atomic hydrogen;

(III) and finally regime (III), where the 'scaled' alkali threshold only weakly depends on the 'scaled' frequency, or slightly increases with decreasing $n_0^3 \cdot \omega$.

The immediate interpretation of these (laboratory) data [9, 42] was based on the hypothesis that the (element-specific) characteristic level splitting between the non-hydrogenic alkali initial states and the adjacent Rydberg level (see equation (5.1)) was the relevant frequency scale in the alkali ionization process, and that the hydrogen level splitting (associated with the classical Kepler frequency) did not retain any relevance for the physical process at hand. Consequently, it was only natural to redefine $\omega_0$ by normalizing the driving field frequency with respect to the alkali transition (see E3 above) rather than to $n_0^{-3}$. Obviously, this very initial hypothesis precludes the distinction between regimes (I) and (II) identified by our numerical data, and could not provide any satisfactory explanation of the apparent quantitative differences between alkali and hydrogenic thresholds. Given the manifestly distinct interaction times in rubidium and hydrogen experiments and the resulting (though, as we shall see, secondary) temporal decrease of the threshold field, it was probably hopeless to develop a consistent picture of the ionization process which put all available experimental data on common grounds. With the correct scaling rules for microwave driven alkali atoms (i.e. the same scaling rules as for atomic hydrogen) we

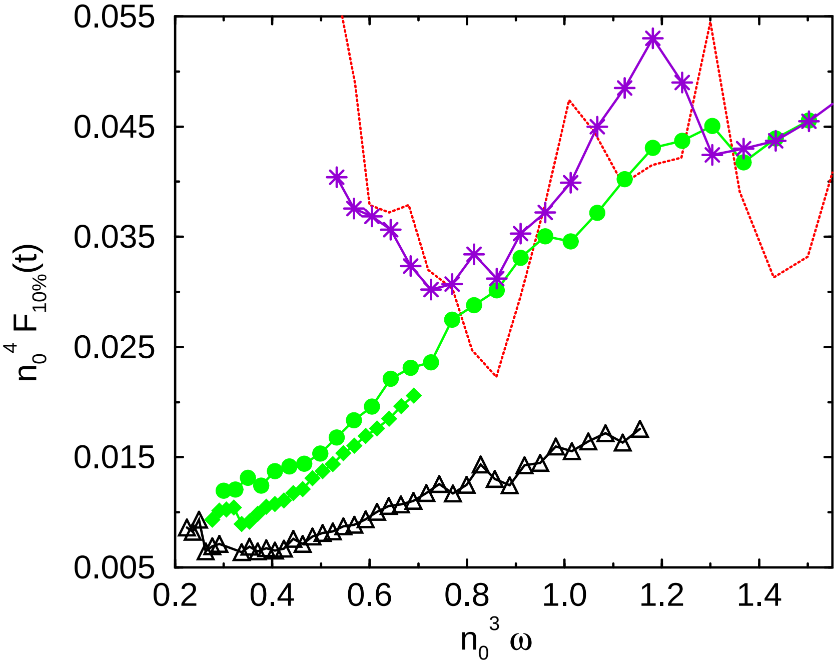

Figure 5.10: 'Scaled' representation of the experimental (triangles) [42] and numerical (diamonds) rubidium ionization thresholds of figure 5.9, at $\omega/2\pi = 8.87$ GHz, as a function of the 'scaled' frequency $n_0^3 \cdot \omega$. For comparison, the $\omega/2\pi = 36$ GHz numerical results on rubidium (filled circles) and on atomic hydrogen (stars), as well as the laboratory results on atomic hydrogen [20] (dotted line, also for $\omega/2\pi = 36$ GHz) are shown. In the (laboratory) experiments on rubidium, the atoms were exposed to atom-field interaction times approximately 130 times longer ($t = 5\ \mu$s) than in numerical simulations on rubidium, or in the (laboratory and numerical) experiments on hydrogen.

see that the principal reason for the different (laboratory) thresholds of hydrogen and rubidium atoms is the fact that the rubidium data were obtained mainly in regimes (III) and (II), where the ionization dynamics is qualitatively and quantitatively distinct from that of driven hydrogen atoms. The difference in the interaction time only causes a weaker slope of $n_0^4 \cdot F_{10\%}(t)$ as a function of the 'scaled' frequency, and a deviation of the (laboratory) rubidium results (obtained with $t = 44000 \cdot 2\pi/\omega$) by less than a factor 2.7 (3.3) from the laboratory (numerical) hydrogen results (obtained with $t = 327 \cdot 2\pi/\omega$) in regime (I), and by less than a factor 2.1 from our numerical $\omega/2\pi = 8.87$ GHz data (also obtained with $t = 327 \cdot 2\pi/\omega$).

Yet our novel understanding of the microwave ionization process sheds new light on another puzzling experimental observation of the Munich group. In the experiment [9], rubidium atoms with principal quantum numbers $n_0 = 55, \ldots, 99$

were exposed to a microwave field with frequency $\omega/2\pi = 12.6$ GHz. The experimentally measured 'scaled' ionization threshold showed a local maximum close to $n_0 = 89$ (see figure 5 (b) in reference [9]). According to the incorrect 'scaling' rules, this maximum was attributed to a 'scaled' frequency $\omega/(\Delta(E(n_0, \ell = 1), E(n_0 - 1, \ell = 2))) \simeq 4$. However, since the results did not show any local maxima for lower frequencies (in particular there were no extrema at 'scaled' frequencies $\omega_0 \simeq 1$, $\omega_0 \simeq 2$, or $\omega_0 \simeq 3$) the origin of the mysterious maximum at $\omega_0 \simeq 4$ seemed to be inexplicable. Now, understanding how to scale the alkali dynamics, we can elucidate the origin of the maximum. Employing the hydrogenic scaling rules (2.19) the quantum number $n = 89$ corresponds to the 'scaled' frequency $n_0^3 \cdot \omega \simeq 1.3$. Hence, the prominent structure of this experiment can be attributed to the principal non-linear resonance in the classical phase space of the driven two-body Coulomb system. Precisely as already observed in figure 5.2.1 at $n_0^3 \cdot \omega \simeq 1.1$ for lithium, and in figure 5.6 at $n_0^3 \cdot \omega \simeq 1.3$ for rubidium ($\omega/2\pi = 36$ GHz), this remnant of the regular island in the classically chaotic phase space of periodically driven atomic hydrogen, prevails in the presence of a non-hydrogenic core. However, in the experimental results, the maximum appeared much more pronounced than in our simulation on rubidium atoms. This can most probably be attributed to the finite switching time of the experiment (approximately 70 microwave oscillations), in contrast to the sudden switching of the field assumed in our simulation.

Let us finish this section by noting that the existence of the maximum at the 'scaled' frequency $n_0^3 \cdot \omega \simeq 1.3$ in the experimentally measured rubidium thresholds is a further evidence for the validity of the scaling rules in regimes (II) and (I).

## 5.5 Time dependence of the 10% ionization threshold

### 5.5.1 Time dependence of $n_0^4 \cdot F_{10\%}(t)$ vs. $n_0^3 \cdot \omega$

In a comparison of our numerical (8.87 GHz) ionization threshold values for the microwave ionization of rubidium Rydberg states with the results obtained in the laboratory [9], we observe a discrepancy by a factor of approximately $1.6 \ldots 2.1$, together with a smaller slope of $n_0^4 \cdot F_{10\%}(t)$ as a function of $n_0^3 \cdot \omega$, in the laboratory results. As both (the laboratory and the numerical) experiments were performed with exactly the same frequency and the same quantum numbers of the initial states, we attribute this difference to the different interaction times, which were approximately 135 times longer in the laboratory than in the numerical experiment.

To study the time dependence of the 10% ionization threshold in more detail, we plotted the scaled threshold of microwave driven lithium atoms ($\omega/2\pi = 36$ GHz) as a function of the scaled frequency in figure 5.11, for different interaction times ranging from $t = 128 \cdot 2\pi/\omega$ to $t = 12795 \cdot 2\pi/\omega$. The result resembles the observations we made in the comparison of the numerical and the laboratory rubidium results:

Albeit we varied the interaction time by a factor 100, the ionization thresholds only differ by a factor $1.2 \ldots 1.7$. The global structure of $n_0^4 \cdot F_{10\%}$ vs. $n_0^3 \cdot \omega$ is not

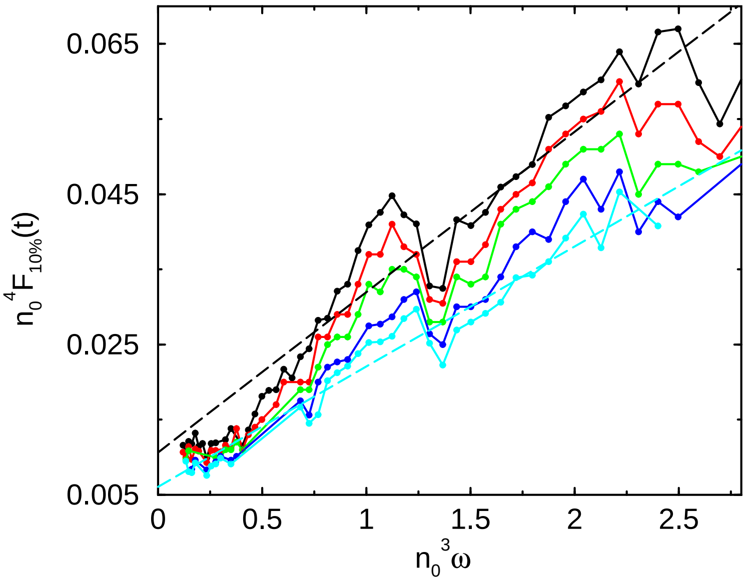

Figure 5.11: 'Scaled' ionization threshold as a function of the 'scaled' frequency, for lithium atoms and different atom-field interaction times $t$. The parameters are the same as in figure 5.2.1, except for the interaction time, which was varied from (read the curves in the plot from above) $t = 128 \cdot 2\pi/\omega$, over $t = 327 \cdot 2\pi/\omega$ (the time used in figure 5.2.1) , $t = 1025 \cdot 2\pi/\omega$, and $t = 3718 \cdot 2\pi/\omega$, to $t = 12795 \cdot 2\pi/\omega$. Quite obviously, a longer interaction time induces a smaller slope of $n_0^4 \cdot F_{10\%}(t)$ as already observed in recent experiments [49].

affected by the different interaction times, the main effect of the longer interaction time is a smaller slope in regimes (I) and (II), and lower thresholds in regime (III). Some of the local structures in the curve, however, do change with a variation of the interaction time, much as we already observed in the temporal evolution of the ionization yield $P_{\rm ion}$ vs. $n_0$ (or $P_{\rm ion}$ vs. $F$) in section 4.3. The most prominent among these changes in figure 5.11 is the change of the position of the local maximum close to the principal resonance, from $n_0^3 \cdot \omega \simeq 1.12$ for $t = 128 \cdot 2\pi/\omega$ to $n_0^3 \cdot \omega \simeq 1.24$ for $t = 12795 \cdot 2\pi/\omega$. As noted in section 4.3, the reason for such changes in the local structures lies in the complicated sum that defines the ionization probability, which provides for an interplay of various Floquet states with different weights $w_j$ and widths $\Gamma_j$ on different time scales. This leads to a distinct time evolution of the ionization yield of different initial states (see section 4.3), and also to a distinct evolution of their ionization thresholds.

As expected, the situation does not change significantly if we perform the numerical experiment using rubidium atoms instead of lithium atoms (but leaving the other parameters constant). For the sake of completeness, we display the analogue to figure 5.11 in figure 5.12, the 'scaled' 10% threshold for rubidium atoms as a

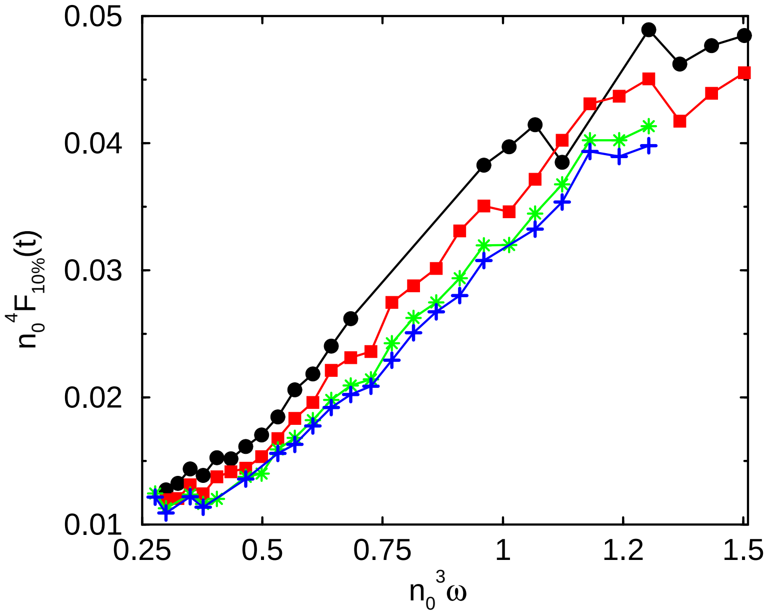

Figure 5.12: Same as in figure 5.11, but for rubidium atoms exposed to a microwave field of frequency $\omega/2\pi = 36$ GHz. Here the interaction time is varied from $t = 128 \cdot 2\pi/\omega$ (for some values of $n_0^3 \cdot \omega$, the threshold is missing in the plot), over $t = 327 \cdot 2\pi/\omega$, and $t = 759 \cdot 2\pi/\omega$, to $t = 1029 \cdot 2\pi/\omega$.

function of the 'scaled' frequency, for different interaction times. Again we observe a decrease of the slope of $n_0^4 \cdot F_{10\%}$ with increasing atom-field interaction time $t$, and a by far less pronounced change of $n_0^4 \cdot F_{10\%}$ in regime (III), where the 'scaled' threshold is essentially independent of the 'scaled' frequency.

As a matter of fact, very similar results on the time dependence of $n_0^4 \cdot F_{10\%}$ vs. $n_0^3 \cdot \omega$ as observed in our simulations were already experimentally observed in a recent experiment of the Virginia group [49] (which we already mentioned several times). There, hydrogen-like ($m = 1$) states of lithium were exposed to a microwave field ('scaled' frequency $0.2, \ldots, 1.4$) with three interaction times $t = 5 \cdot 2\pi/\omega$, $t = 110 \cdot 2\pi/\omega$, and $t = 1100 \cdot 2\pi/\omega$. Very much alike our results, the experimental dependence of $n_0^4 \cdot F_{10\%}$ on $n_0 \cdot n_0^3\omega$ did not significantly change with time, with the exception of the slope of the experimental graph – which also decreases with increasing interaction time – and changes of some local structures of the ionization signal.

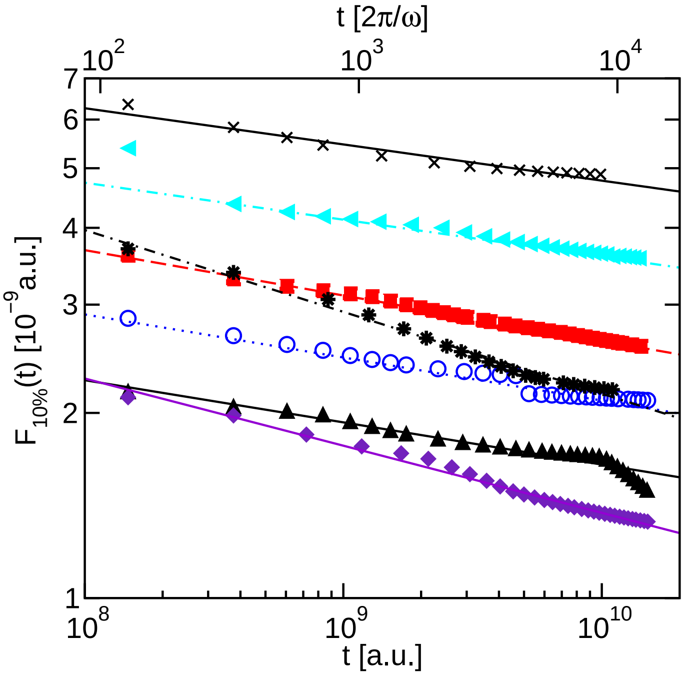

Figure 5.13: Time dependence of the 10% ionization threshold for lithium atoms, prepared in $|n_0, \ell_0 = m_0 = 0\rangle$ states with $n_0 = 37$ (x), $n_0 = 40$ (blue triangles), $n_0 = 53$ (red squares), $n_0 = 59$ (stars), $n_0 = 61$ (blue circles), $n_0 = 69$ (black triangles), and $n_0 = 73$ (diamonds).

### 5.5.2 Algebraic time dependence of the ionization threshold

So far, the time dependence of the ionization threshold of microwave driven Rydberg states has rarely been investigated in the laboratory. Apart from the Virginia experiment mentioned above, a systematic study of the temporal change of $F_{10\%}(t)$ for a few atomic initial states was only performed in an experiment [42] on rubidium atoms, and in numerical simulations on moderately excited ($n_0 = 23$) atomic hydrogen [38]. In the experiment [42], atomic initial states $|n_0, \ell_0 = 1, m_0 = 0\rangle$ with $n_0 = 75, 84, 85, 95$ were exposed to a microwave field of frequency $\omega/2\pi = 8.87$ GHz, and the interaction time was varied from $t = 270 \cdot 2\pi/\omega$ to $t = 89000 \cdot 2\pi/\omega$. The results showed an algebraic dependence $F_{10\%}(t) \simeq t^{-\gamma}$, with $\gamma = 0.13 \pm 0.04 \ldots 0.27 \pm 0.04$, depending on the initial state. Also the numerical studies on atomic hydrogen [38] showed an algebraic dependence of $F_{10\%}(t)$, with $\gamma \simeq 0.07$.

In a first attempt to explain these experimental results, a simplified model system based on the standard map [174] (where the interaction of the bound spectrum with the continuum was omitted) attributed the algebraic dependence of $F_{10\%}(t)$ as measured in [42] to the presence of (uncontrolled) noise in the experimental set-up.

With our exact numerical treatment of a purely coherent driving of the atom we can now ponder this assertion, by studying the time dependence of the ionization threshold in the absence of noise. For this purpose, we display in figure 5.13 the 10% ionization threshold as a function of the interaction time, for seven initial states of lithium, exposed to a $\omega/2\pi = 36$ GHz field. In all seven cases we observe an approximative algebraic dependence $F_{10\%}(t) \sim t^{-\gamma}$, over the whole range of the interaction time, with the following exponents $\gamma$:

| $n_0$ | 37 | 40 | 53 | 59 | 61 | 69 | 73 |
|---|---|---|---|---|---|---|---|
| $\gamma$ | 0.059 | 0.06 | 0.074 | 0.133 | 0.07 | 0.069 | 0.11 |

Additionally for the states with $n_0 = 61$ and $n_0 = 69$ we observe a change of $\gamma$ at a specific value of the interaction time. After $t \simeq 5 \cdot 10^9$ a.u. ($t \simeq 10^{10}$ a.u.) the decay of the state $|n_0 = 61, \ell_0 = m_0 = 0\rangle$ ( $|n_0 = 69, \ell_0 = m_0 = 0\rangle$) changes to a slower (faster) algebraic decay with $\gamma \simeq 0.0134$ ($\gamma \simeq 0.3$). While these results for $\gamma$ are in perfect agreement with the numerical studies on hydrogen [38], they slightly deviate from the experimentally measured values of [42]. Since we experienced similar results for $\gamma$ in studies on microwave driven rubidium atoms (with the same frequency $\omega/2\pi = 36$ GHz different from the frequency $\omega/2\pi = 8.87$ GHz used in the experiment [42]), we do not assume that the larger value of $\gamma$ is a result of the additional quantum defects of rubidium as compared to lithium.

A possible reason for a larger $\gamma$ might be the initial conditions chosen in [42], i.e. the lower frequency and the larger principal quantum numbers of the initial atomic states. Employing higher $n_0$ but the same 'scaled' frequency may result in a difference in the time dependence of the ionization threshold (since a higher $n_0$ causes a different distribution of the weights $w_j$). However, such distinct time evolution for different $n_0$ need not be caused by the use of alkali atoms instead of atomic hydrogen. We rather attribute it to the fact that the semiclassical limit consists in taking $\hbar \to 0$ (i.e. $n_0 \to \infty$) *and* $t \to \infty$ which, in general, do not commute [105]. Therefore, it is not surprising that the time evolution of the ionization threshold changes when proceeding to higher excited states.

We expect an even better agreement of our numerical values $\gamma$ with the laboratory values, if we would employ the frequency $8.87$ GHz also in the numerical experiment (which is – as already noted before – computationally only feasible with a larger memory). Furthermore, the finite switching time of the laboratory set-up might also provide for different values of $\gamma$, as compared to the flat pulse model of our calculations.

Given the qualitatively good agreement of the time dependence of our numerically obtained ionization threshold with the laboratory threshold [42] (as well as with the numerical studies in [38]), we can conclude that the aforementioned assumption of [174] is wrong. More precisely, we can confirm that an algebraic time dependence of the ionization threshold – as it was measured in [42] – is not caused by the presence of noise in the experimental set-up, but by the field-induced interaction of the atomic bound states with the continuum (which was omitted in [174]).

# Chapter 6

# Time dependence of the ionization yield

In the previous chapter we studied the ten percent ionization threshold as a measure for the onset of the ionization process. Studying the time dependence of the threshold we recognized that a change of the interaction time plays only a secondary role for the onset of ionization (see figure 5.11). This manifests in a weak algebraic decay $F_{10\%} \sim t^{-\gamma}$ with an exponent $\gamma = 0.06, \ldots, 0.13$ (see figure 5.13). Also in chapter 4.2 did we already vary the interaction time by a factor 40 (respectively 117) and observed a change in the local structure of the ionization probability $P_{\rm ion}(t)$ as a function of the field amplitude $F$ (respectively $n_0$) displayed in figure 4.6 (figure 4.7), albeit the global trend of $P_{\rm ion}(t)$ vs. $F$ ($n_0$) did not change much. There, we attributed this change to the complicated weighted sum defining the ionization probability given by (2.58).

In the present chapter, we shall study the temporal decay of our system in more detail, i.e., also for situations that lead to a larger ionization probability than studied up to now. This discussion will make direct contact with a vivid ongoing debate (which motivated this chapter), while it is intimately connected with our investigations above. However, whereas the various aspects of dynamical localization in real atomic systems enjoy renewed interest only recently [49, 108, 175, 176] – possibly since rigorous theoretical treatments beyond one-dimensional model systems, including predictions of interesting novel phenomena have become available only during the last couple of years – there is a considerable activity concentrating on the temporal decay of chaotic quantum systems in a broad community ranging from chemical physics [177] to mesoscopic [75], optical [178] and nuclear [179] physics. Once again, a large part of these studies is devoted to simple model systems which often suggest universal laws. As we shall see, realistic physical systems such as strongly driven atoms tend to be too complex to feature universality.

## 6.1 Algebraic decay of the survival probability

It is known that in classical systems which exhibit completely chaotic dynamics the probability that a trajectory remains inside a given phase space region decays quite fast, namely exponentially as $P_{\rm surv}^{\rm class}(t) \sim {\rm e}^{-\alpha t}$ [68, 177]. Typical Hamiltonian systems, however, are neither completely chaotic nor completely integrable, but they exhibit a mixed phase space structure where regular and chaotic regions coexist [18, 180, 30, 31]. In such situations the hierarchical structure of phase space causes a particle's trajectory to be trapped inside a given phase space region much longer, leading to a slower decay than in the fully chaotic case. As already mentioned in the introduction, in this case the probability to stay inside such a region decays algebraically $P_{\rm surv}^{\rm class}(t) \sim t^{-z}$ [69, 70, 71, 72].

Here, we are interested in the implications of such a (classically chaotic) phase space structure on the quantum mechanical survival probability, or, differently said, on the time dependence of the survival probability of a decaying, open quantum system that exhibits complex dynamics (with or without a classical (-ly chaotic) counterpart). As we have seen in the preceding chapters of this thesis, an example of such a system is provided by strongly driven alkali Rydberg states.

Due to its importance in the following discussion, we remind the reader of the definition of the survival probability (2.57), and rewrite its definition here, in a slightly modified form:

$$P_{\rm surv}(t) = \sum_j w_j \exp(-\Gamma_j t). \tag{6.1}$$

The $w_j$ now define the weight of the atom-field eigenstate with the quasi-energy $\varepsilon_j$ (and the corresponding width $\Gamma_j$), when projected on the given atomic initial state. With increasing number of non-vanishing weights $w_j$, together with a broader distribution of the widths $\Gamma_j$ – in other words with increasing strength of the perturbation induced by the microwave field – the sum (6.1) generates a complicated time dependence of the survival probability. If the distribution of the widths $\Gamma_j$ is sufficiently dense, the sum in (6.1) can be transformed into an integral, leading to

$$P_{\rm surv}(t) \simeq \int_0^\infty w(\Gamma) \exp(-\Gamma t) {\rm d}\Gamma. \tag{6.2}$$

Starting from an equation like (6.2), several groups derived different proposals for the decay of a complex quantum system. To deduce the explicit functional form of the decay law from (6.2), one needs to know the distribution of the weights $w_j$ and of the widths $\Gamma_j$ of the resonances, which possibly should be condensed in a function $w(\Gamma)$. In derivations of decay laws $P_{\rm surv}(t) \sim t^{-z}$ with constant decay exponents $z$, it is typically assumed that the widths are proportional to the weights, i.e., $w_j \sim \Gamma_j$ [82, 78, 81]. Furthermore, a certain distribution of the resonances has to be assumed [82, 81] to solve the integral in (6.2).

Decay exponents larger than one were obtained by employing general expressions describing the distribution of resonance widths for open chaotic systems. With the help of the Porter-Thomas distribution [181] for a system with one decay channel the exponent $z = 3/2$ [82] was found. Recently, a distribution of the widths $\Gamma$ for systems with multiple decay channels was derived in [182]. Employing this distribution the decay law $\sim t^{-M}$ [183] (with $M$ counting the number of decay channels) was found. In [183] this $t^{-M}$ law was tested by simulating a Bloch particle in the presence of static and time-periodic forces. This realistic physical system (i.e. a Bloch particle) showed an algebraic decay, the decay exponent, however, deviates from the theoretical predictions, what remained unexplained in [183].

For systems exhibiting Anderson localization, on the other hand, the distribution of the resonance widths [184, 185] differs from the distribution used in the above derivation of $z = 3/2$ or $z = M$ quoted above. Thus, the emergence of Anderson (or dynamical) localization obviously also has implications on the time dependence of the survival probability, and we cannot assume that the decay exponents $z = 3/2$ or $z = M$ are valid for our system.

For highly excited atomic systems with a completely chaotic classical counterpart, in [83] a smaller decay exponent was found, by using general scaling rules for Rydberg state matrix elements. Employing such rules, it is expected that $\Gamma_n \sim w_n \sim n^{-3}$ holds. With this relations a decay $t^{-2/3}$ is obtained, what was also observed in (classical) simulations on doubly excited helium atoms [83].

Arguing that the widths are distributed according to $1/\Gamma$ [81] one obtains a decay exponent $z = -1$. The same value is derived with the argument that the relation $\Gamma_n \sim w_n \sim \exp(-2n/\ell_{\text{loc}})/D$ (with $D$ the classical diffusion constant of chaotic transport, and $\ell_{\text{loc}} \simeq D/2$ the localization length) holds [78]. The decay $\sim t^{-1}$ obtained by these groups is advertised to be a universal law for systems with a mixed regular-chaotic classical counterpart that exhibit localization, as realized by periodically driven Rydberg atoms. Accordingly, it was tested on the quantum version of the standard map [78, 81], and on a refined version of this map ('quantum Kepler map') describing a simplified model of microwave driven atomic hydrogen [85], as well as on a one-dimensional model of microwave-driven hydrogen atoms [85] (employing absorbing boundary conditions), and found to describe the temporal decay with $z = 1$ perfectly well, in the employed parameter range.(1)

However, the larger part of the studies on the survival probability (or on similar functions like the dwell time distribution [84]) were either performed using simplified model systems, or the property that the system is an open system is rather crudely modeled by the use of absorbing boundary conditions [85, 78, 81], instead of treating the continuum coupling through some sort of 'leads' rigorously. The system we are studying, on the contrary, directly reproduces experimentally accessible situations (where an algebraic decay was already found [86]). Furthermore, employing complex dilation together with the Sturmian basis, the continuum coupling is treated exactly in our theoretical/numerical approach.

---

(1)Note that also calculations on a three-dimensional model of microwave driven hydrogen atoms are reported in [85]. However, the three-dimensional results are only compared with the one-dimensional results for short time scales $t < 2 \cdot 10^3 \cdot 2\pi/\omega$ (where the one-dimensional and the three-dimensional results roughly agreed), while the algebraic decay (of the quantum Kepler map and the one-dimensional model) is observed for $30 \cdot 2\pi/\omega \ldots 10^6 \cdot 2\pi/\omega$. Thus, the results of [85] do provide no evidence, that also the three-dimensional atom follows the $t^{-1}$ dependence for long times, i.e. for $t > 2 \cdot 10^3 \cdot 2\pi/\omega$.

With our set-up we can easily change the atomic species, and hence 'switch' our system from a system with a classical counterpart (i.e., periodically driven hydrogen atoms employing vanishing quantum defects for all angular momenta) to a pure quantum system as it is given by alkali atoms due to the scattering of the the electron off a non-hydrogenic atomic core [58]. Hence, our approach is ideally suited to study the decay of the survival probability of an open quantum system exhibiting complex dynamics (with or without a classical, possibly chaotic counterpart) and thus, to test the existence of possibly universal algebraic decay laws.

In the following section, we shall start our investigation of the time evolution of the survival probability on lithium atoms. Afterwards, we will also deal with rubidium and atomic hydrogen.

## 6.2 Microwave driven Rydberg states as an open quantum system

### 6.2.1 Lithium

Before dealing with parameters that lead to an algebraic decay of the survival probability, in the following section we present results for a weak driving field, where no algebraic decay is found.

#### 6.2.1.1 Mono-exponential decay for weak driving

If the amplitude of the field is small, and the system close to the perturbative regime, the main contribution to the sum in (6.1) stems from the adiabatic continuation of the unperturbed atomic initial state. There the survival probability is essentially given by a mono-exponential function of the interaction time.(2) This situation is displayed in figure 6.1, where the survival probability is plotted for lithium atoms initially prepared in the state $|n_0 = 54, \ell_0 = m_0 = 0\rangle$, exposed to a microwave field of amplitude $F = 1.5 \cdot 10^{-9}$ a.u. The 'scaled' field amplitude experienced by the Rydberg electron, $n_0^4 \cdot F = 0.013$, is still rather small, compared to the 'scaled' ionization threshold $F_{0,10\%}(t = 327 \cdot 2\pi/\omega) \simeq 0.029$ (see figure 5.2.1) for the given initial state. Accordingly, even at the largest interaction time displayed in figure 6.1, the field induces an ionization probability of only $13\%$. Here, the field amplitude is too small to couple the initial atomic state efficiently to other bound

---

(2) Of course, this mono-exponential decay is not at all related to the exponential decay of classical systems exhibiting a completely chaotic phase space. On the contrary, in this case the exponential decay can be addressed to the representation of the initial state by (nearly) one single atom-field eigenstate, as the quantum mechanical implication of the symmetries of the unperturbed system being (almost completely) conserved.

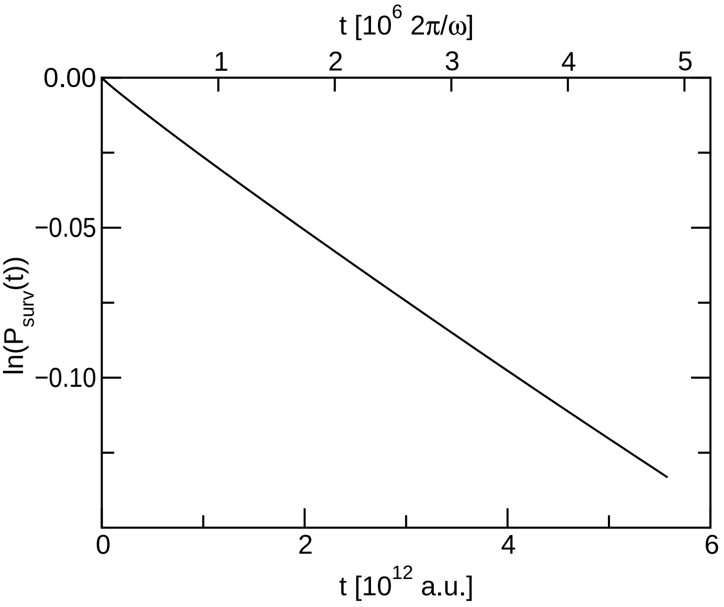

Figure 6.1: Time dependence of the survival probability of lithium $|n_0 = 54, \ell_0 = m_0 = 0\rangle$ states exposed to a microwave field of amplitude $F = 1.5 \cdot 10^{-9}$ a.u. and frequency $\omega/2\pi = 36$ GHz ($n_0^4 \cdot F = 0.013$, $n_0^3 \cdot \omega = 0.861$). The external field doesn't induce a large ionization probability (even for interaction times $t = 5 \cdot 10^{12}$ a.u. $\simeq 4.3 \cdot 10^6 \cdot 2\pi/\omega$ the ionization probability only amounts to 13%), and the survival probability is close to a mono-exponential function of the interaction time $t$.

or continuum states. This becomes clear in the upper plot of figure 6.2, where we plotted the weights $w_j$ of the atom-field eigenstates when projected on the initial atomic state, and the corresponding widths $\Gamma_j$. There are only eight eigenstates with a weight $w_j > 1\%$, which are enough to assemble a weight of 86% (in agreement with a relatively small Shannon width $W = 12.4$ for the given situation). Below the ionization threshold, it is precisely the contribution of only few eigenstates (that exhibit ionization rates $\Gamma_j \lesssim 5 \cdot 10^{-14}$) to the survival probability, that leads to an exponential decay, on the time-scale $t < 5.5 \cdot 10^{12}$ a.u. $(\simeq 5 \cdot 10^6 \cdot 2\pi/\omega)$ shown in figure 6.1.

#### 6.2.1.2 Regime (I) and (II): Algebraic decay of $P_{\rm surv}(t)$ for stronger fields

The situation changes significantly if the representation of the field-free initial state needs a large number of atom-field eigenstates. Such a situation is shown in the lower plot of figure 6.2, that shows the weights $w_j$ and the widths $\Gamma_j$ of lithium atoms initially prepared in the state $|n_0 = 80, \ell_0 = m_0 = 0\rangle$, exposed to a microwave field of amplitude $F = 3.1 \cdot 10^{-9}$ a.u. In contrast to the previous case,

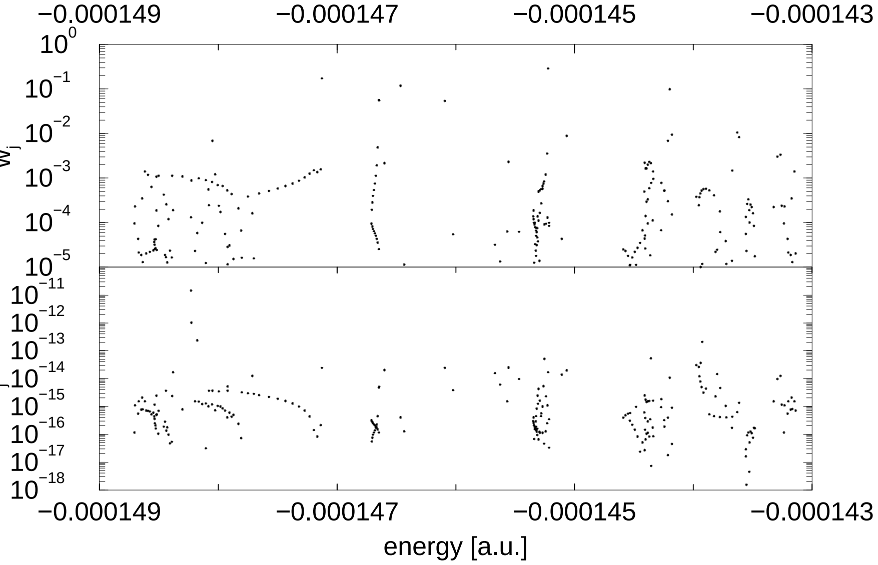

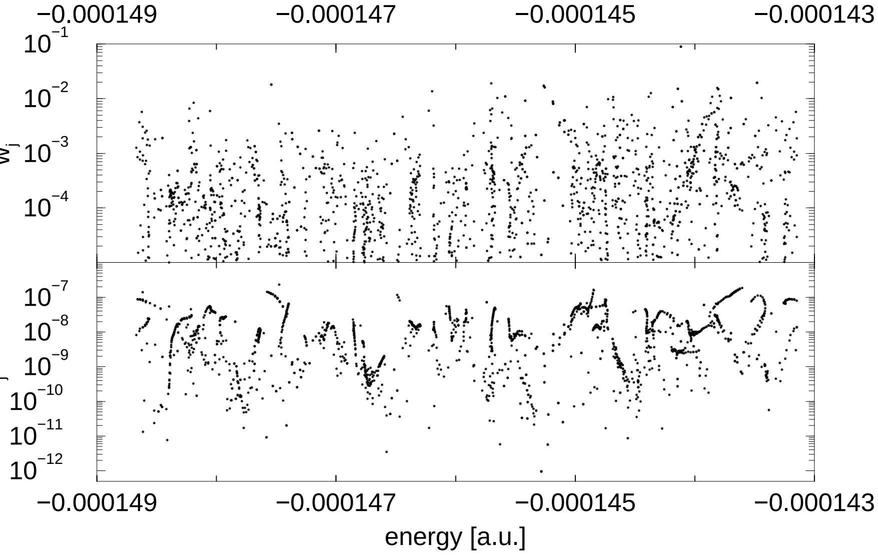

Figure 6.2: Ionization rates $\Gamma_j$ and corresponding weights $w_j$ of the atom-field eigenstates $\varepsilon_j$ when projected on the initial state $|n_0 = 54, \ell_0 = m_0 = 0\rangle$ (upper plot), and $|n_0 = 80, \ell_0 = m_0 = 0\rangle$ (lower plot), in a Floquet zone of width $\omega$ (only the states with a weight $w_j > 10^{-5}$ are shown). Microwave field amplitudes $F = 1.5 \cdot 10^{-9}$ a.u. ($n_0^4 \cdot F \simeq 0.013$, upper plot), and $F = 3.1 \cdot 10^{-9}$ a.u. ($n_0^4 \cdot F \simeq 0.127$, lower plot), at frequency $\omega/2\pi = 36$ GHz ($n_0^3 \cdot \omega \simeq 0.86$, and $2.8$, respectively). These are the raw data which generate the time dependence of the survival probability depicted in figures 6.1 and 6.3 (black dash-dotted curve), respectively.

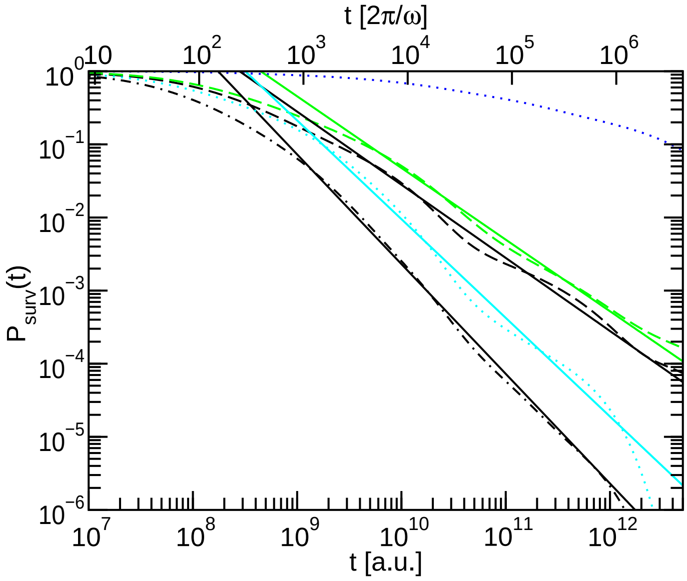

Figure 6.3: Time dependence of the survival probability of microwave driven lithium atoms, for five different initial states exposed to the same field of amplitude $F = 3.1 \cdot 10^{-9}$ a.u. and frequency $\omega/2\pi = 36$ GHz. Clearly, this amplitude causes a more complicated time dependence of the survival probability (for all five initial conditions) than the one observed in figure 6.1. The dark blue dotted curve shows the decay of $|n_0 = 50, \ell_0 = m_0 = 0\rangle$ ($n_0^4 \cdot F = 0.019$, $n_0^3 \cdot \omega = 0.68$, close to the 10% threshold $n_0^4 \cdot F_{10\%}(t = 327 \cdot 2\pi/\omega) = 0.02$, see figure 5.2.1) which is neither exponential nor algebraic. In the other four cases (all with initial states $|n_0, \ell_0 = m_0 = 0\rangle$) an algebraic decay $P_{\rm surv} \sim t^{-z}$ can be observed over several decades of the interaction time $t$: the green dashed line ($z \simeq 0.98$) represents the initial state $n_0 = 68$ ($n_0^4 \cdot F = 0.07$, $n_0^3 \cdot \omega = 1.72$, $n_0^4 \cdot F_{10\%}(t = 327 \cdot 2\pi/\omega) = 0.047$), the black dashed line ($z \simeq 1$) shows the initial state $n_0 = 74$ ($n_0^4 \cdot F = 0.09$, $n_0^3 \cdot \omega = 2.22$, $n_0^4 \cdot F_{10\%}(t = 327 \cdot 2\pi/\omega) = 0.06$), the light blue dotted line ($z \simeq 1.4$) shows the initial state $n_0 = 78$ ($n_0^4 \cdot F = 0.11$, $n_0^3 \cdot \omega = 2.6$, $n_0^4 \cdot F_{10\%}(t = 327 \cdot 2\pi/\omega) = 0.052$), and the black dash-dotted line ($z \simeq 1.5$) presents the initial state $n_0 = 80$ ($n_0^4 \cdot F = 0.127$, $n_0^3 \cdot \omega = 2.8$, $n_0^4 \cdot F_{10\%}(t = 327 \cdot 2\pi/\omega) = 0.054$). Comparison of the 'scaled' field amplitudes with the 'scaled' ionization thresholds shows that, apart from the initial state $n_0 = 50$, all curves are obtained in the 'delocalized' regime, i.e., at field amplitudes above the ionization threshold.

here not only a larger number of atom-field eigenstates is needed to represent the field-free initial atomic state, but also the weights and the widths show a broad distribution over approximately four orders of magnitude. While in the above (nearly perturbative) case the Shannon width of the initial state was given by $W = 12.4$, in this case there are 19 atom-field eigenstates with a weight $w_j > 1\%$ that sum up to only 30%. In addition, there are many states with a smaller weight $w_j$ leading to a large Shannon width $W = 285$. Thus, the 'scaled' field amplitude $n_0^4 \cdot F = 0.127$ (compared to $n_0^4 \cdot F_{10\%}(t = 327 \cdot 2\pi/\omega) = 0.054$, see figure 5.2.1) is clearly large enough to induce an efficient coupling of a large number of bound or continuum states to the initial atomic state. And indeed, this leads to an algebraic decay of the survival probability, displayed in figure 6.3. As already observed in numerical experiments on atomic hydrogen and in laboratory experiments on rubidium atoms [86], the survival probability starts to decay neither exponentially nor algebraically, and after approximately $t = 10^9$ a.u. ($\simeq 870 \cdot 2\pi/\omega$) we observe an algebraic decay according to $P_{\text{surv}} \sim t^{-1.5}$. The decay follows this dependence over three decades of the interaction time, i.e. up to $t \simeq 10^{12}$ a.u. $\simeq 870000 \cdot 2\pi/\omega$. For longer times, the atom-field eigenstates with widths $\Gamma_j \gtrsim 10^{-11}$ already decayed, and the sum (2.57) is dominated by only a few states with even smaller widths $\Gamma_j$ which contribute significantly (i.e. with a weight $w_j > 10^{-5}$) to the representation of the initial state under external driving. This is in agreement with figure 6.2, which shows seven states with $\Gamma_j < 10^{-11}$ a.u. as the states which contribute to $|n_0 = 80, \ell_0 = m_0 = 0\rangle$ with the smallest width $\Gamma_j$.

In figure 6.3 we furthermore display survival probabilities of ($\ell_0 = m_0 = 0$) initial states with principal quantum numbers $n_0 = 78, 74, 68$, and $50$, exposed to the same microwave field with amplitude $F = 3.1 \cdot 10^{-9}$ a.u. As for the case $n_0 = 80$, the initial states $n_0 = 78$ (Shannon width $W = 313$), $n_0 = 74$ ($W = 283$) and $n_0 = 68$ ($W = 277$) exhibit algebraic decay after approximately $t \simeq 10^9 \ldots 3 \cdot 10^9$ a.u., over approximately three decades of the interaction time $t$. The decay exponents are close to $z = 1$ in the cases $n_0 = 68$ ($z \simeq 0.98$) and $n_0 = 74$ ($z \simeq 1$), whilst larger for $n_0 = 78$ ($z \simeq 1.4$). For the initial state $n_0 = 50$ ($W = 88$), on the other hand, the field does not induce a clear algebraic decay. At least on time scales $t < 5 \cdot 10^{12}$ a.u., only a decay which is neither exponential nor algebraic can be observed.

From our inspection of the survival probability, in particular of the states with $n_0 = 78$ and $n_0 = 74$ in figure 6.3, the emergence of an algebraic decay becomes clear. On different time scales, different atom-field eigenstates with different weights and widths dominate the ionization process described by (6.1). This leads to bumps in the survival probability vs. time in this double-logarithmic plot. If several bumps succeed on successive time scales (or in other words, if the weights $w_j$ and widths $\Gamma_j$ are uniformly distributed over several orders of magnitude as in the lower plot of figure 6.2), this leads to an approximate algebraic decay over several decades of the interaction time [86].(3)

---

(3) Note that for a clean algebraic decay it is crucial that the widths are not only distributed over

The time dependence of the survival probability we observed in figure 6.3 – i.e. an algebraic decay for $F > F_{10\%}$ but with various decay exponents $z = 1 \ldots 1.5$ – seems to be in contradiction with the predictions $z = 2/3$ made in [83] and $z = 1$ made in [78, 85]. In [83] it was argued that (classical) electrons are excited into extremely highly excited Kepler orbits, whose excursion times are longer than the microwave pulse duration. If the external perturbation (field amplitude) is strong enough that the classical dynamics of the system (i.e. the classical dynamics of the initially populated electronic trajectory) is fully chaotic, it is the population of such highly excited states that prevents the system from fast decay and leads to the decay $\sim t^{-2/3}$. Consequently, such decay can only be expected if the set-up allows for the population or detection of extremely high lying Rydberg states, i.e., Rydberg states whose (unperturbed) Kepler period exceeds or is of the order of the microwave pulse length. For interaction times $t \simeq 10^3 \cdot 2\pi/\omega$ (this is roughly the time when the algebraic decay of the curves in figure 6.3 starts) this would require the population of states $n_0 \simeq 1000$ (see the scaling rules (2.18)). However, our approach to describe microwave driven Rydberg states introduces an effective continuum threshold $n^{\text{eff}}_{\text{max}} \simeq 104$ (due to finite memory), as explained in section 2.4. The chosen cutoff is sufficient to represent experimental results (see chapter 5), which are obtained at not too long interaction times, but (as well as state-of-the-art laboratory experiments that introduce effective continuum thresholds $n^{\text{eff}}_{\text{max}} \simeq 90$ [20]. . . $280$ [176, 49]) inappropriate to describe such extremely highly excited states. Thus, our present set-up is not suitable to check the predictions of [83] for the long-time behavior.

The prediction of [78, 85], on the other hand, does not require the population of such extremely high lying Rydberg states. Following [78, 85], the decay $P_{\text{surv}} \sim 1/t$ should be reached after the Heisenberg time, up to which the quantum system follows the classical analog. The definition of the Heisenberg time – which is usually given by the inverse of the mean level spacing – is somehow unclear for microwave driven alkali states, as the quasi-energy spectrum consists in principle of resonances embedded in the continuum. But assuming that the mean level spacing $\Delta_{\text{mean}}$ is given by the width of a Floquet zone (into which all the spectrum is folded) divided by the number of states that contribute to the dynamics of a given initial state (measured by the Shannon width), we obtain the following approximative expression for the mean level spacing:

$$\Delta_{\text{mean}} \simeq \frac{\omega}{W(F, n_0, \omega)}. \tag{6.3}$$

For the states displayed in figure 6.3, this leads to a Heisenberg time between $t_{\text{H}} \simeq 5.7 \cdot 10^7$ a.u. and $t_{\text{H}} \simeq 1.6 \cdot 10^7$ a.u. Thus the Heisenberg time should definitely be reached at the largest times $t = 5 \cdot 10^{12}$ a.u. displayed in figure 6.3 (which corresponds to an energy splitting of $2 \cdot 10^{-13}$ a.u. ($\simeq \omega/2.5 \cdot 10^7$)). Another requirement for the appearance of the decay rate $z = 1$ is that the field parameters

---

several orders of magnitude, but that, furthermore, the widths are sufficiently dense. This is needed for the transition from the sum (6.1) to the integral (6.2).

are chosen in the delocalized regime [24, 85] (where the field is strong enough to ionize the atom that exhibits dynamical localization, see section 1.1.1). Employing both, the estimate for the localization border introduced in [24] or the numerically obtained ionization border at $t = 327 \cdot 2\pi/\omega$ (see section 5.2.1), apart from the initial state $n_0 = 50$, all states in figure 6.3 are in the delocalized regime, and hence all the prerequisites for the appearance of the 'universal' decay $\sim t^{-1}$ are fulfilled for the states $n_0 = 68, 74, 78,$ and $80$. Yet, only the examples closer to the localized regime, i.e., the states $n_0 = 68$ ($n_0^3 \cdot F \simeq 0.07$ vs. $n_0^3 \cdot F_{10\%} \simeq 0.047$) and $n_0 = 74$ ($n_0^3 \cdot F \simeq 0.09$ vs. $n_0^3 \cdot F_{10\%} \simeq 0.06$), show the predicted decay rate, while according to [85] the $1/t$ decay should hold better in the strongly delocalized regime, i.e. for $n_0 = 78$ ($n_0^3 \cdot F \simeq 0.11$ vs. $n_0^3 \cdot F_{10\%} \simeq 0.052$) and $n_0 = 80$ ($n_0^3 \cdot F \simeq 0.127$ vs. $n_0^3 \cdot F_{10\%} \simeq 0.054$), where we observe $z = 1.4$ and $z = 1.5$, respectively.

The reason for the failure of the prediction of a universal decay with $z = 1$ lies in the intricate dynamics that leads to the decay of a real atomic system, which is only inadequately described by simple maps like the quantum standard map or the quantum kicked rotor, or by models of real atoms which employ absorbing boundary conditions, as the fundament of the predictions in [81, 78, 85]. To emphasize this statement, we checked the assumption that the weights $w_j$ are proportional to the ionization rates $\Gamma_j$, which is an essential input for the derivation of $z = -1$ [81, 78]. According to [81], this proportionality should be valid for atom-field eigenstates with $\Gamma_j < \Delta_{\mathrm{mean}}$. For these states it is assumed that the relation between the widths $\Gamma_j$ and the weights $w_j$ can be described by first order perturbation theory (according to Fermi's golden rule), yielding $\Gamma_j \sim w_j$. In our situation, however, the initial atomic state is coupled to a large number of bound and continuum states, and there are many paths leading to the ionization of the electron. More precisely, each atom-field eigenstate with ionization rate $\Gamma_j$ reflects a coherent sum over multi-photon processes of different order. Thus, in this highly non-perturbative situation, we cannot expect that the proportionality of the widths and the weights still holds. The breakdown of the proportionality is illustrated conspicuously in figure 6.8, where we plot the weights on the initial state $|n_0 = 80, \ell_0 = m_0 = 0\rangle$ as a function of the corresponding ionization rates for a field amplitude $F = 3.1 \cdot 10^{-9}$ a.u. (with the resulting temporal decay displayed in figure 6.3). From this figure it becomes clear that in our case a proportionality of widths and weights does not hold, not even approximately. On the contrary, we observe a broad distribution of the weights $w_j$ over some orders of magnitude, with the corresponding widths spread over the range $5 \cdot 10^{-11} < \Gamma_j < 2 \cdot 10^{-7}$, while the mean level spacing can be approximated by $\Delta_{\mathrm{mean}} \simeq 1.8 \cdot 10^{-8}$ a.u., i.e. $\Gamma_j << \Delta_{\mathrm{mean}}$ for the larger part of the eigenvalues. This is in contrast to the quantum standard map, for which a large number of states exists with $\Gamma_j > \Delta_{\mathrm{mean}}$ (see figure 3.11 in [81]), and hence the perturbative description of the states with $\Gamma_j < \Delta_{\mathrm{mean}}$ might provide correct results [81]. However, as apparent from figure 6.3 this proportionality is not a generic situation and therefore, it cannot be expected that the decay law $t^{-1}$ – which is based on the mentioned perturbative assumption – defines a universal law.

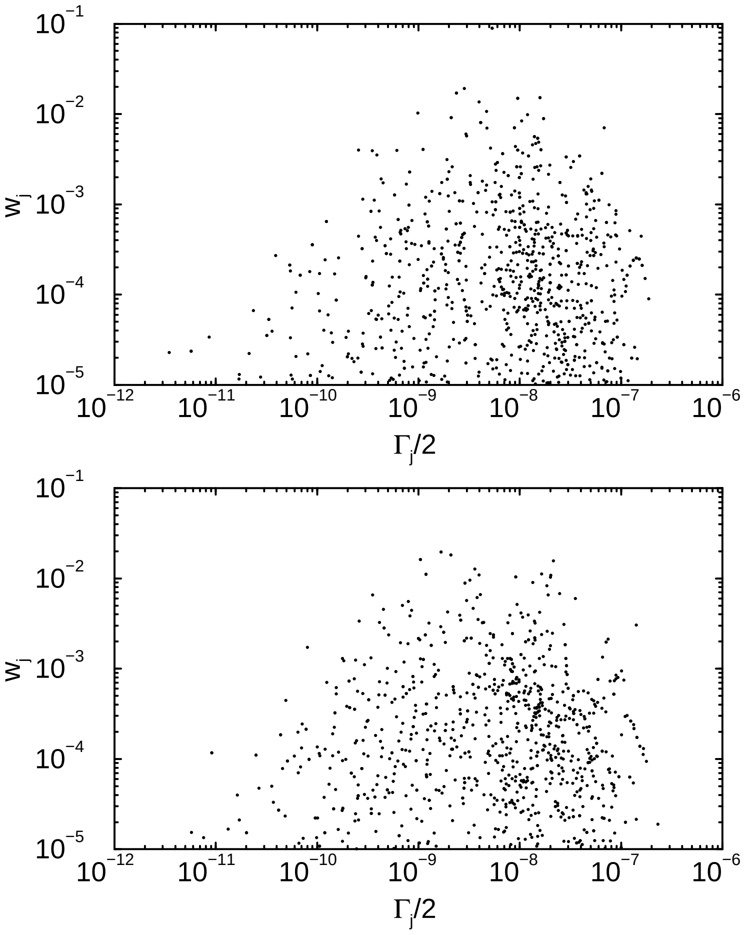

Figure 6.4: Weights $w_j$ vs. associated widths $\Gamma_j$ of the atom-field eigenstates which contribute to the decay of the atomic initial state $|n_0 = 80, \ell_0 = m_0 = 0\rangle$ exposed to a field of amplitude $F = 3.1 \cdot 10^{-9}$ a.u. (see figure 6.3). The upper plot displays $w_j$ and $\Gamma_j$ in the subspace $\Pi = +1$, the lower plot in the subspace $\Pi = -1$. Both plots show the states in a Floquet zone of width $\omega = 36 \cdot 2\pi$ GHz, only those states with $w_j > 10^{-5}$ are displayed. In contrast to the assumption made in [78, 81], the widths are obviously not proportional to the corresponding weights. On the contrary, the widths $\Gamma_j$ are widely spread for all weights $w_j$, as a consequence of the highly non-perturbative continuum coupling induced by the driving field.

#### 6.2.1.3 Increasing decay exponent for increasing field amplitude

As we have seen now that microwave driven Rydberg states decay algebraically in a certain parameter range (i.e. for sufficiently strong external fields), but without a universal decay law, the next topic to study is of course the change of the decay exponent. For an exemplary study of $z$, we consider again a field amplitude $F = 3.1 \cdot 10^{-9}$ a.u., with different principal quantum numbers of the atomic initial states $|n_0, \ell_0 = m_0 = 0\rangle$ exposed to the field. The survival probability as a function of the atom-field interaction time is displayed in figure 6.5, 6.6 and 6.7, for $n_0 = 62 \ldots 83$. The corresponding decay exponents are collected in table 6.2.1.3.

| $n_0$ | $n_0^4 \cdot F$ | $n_0^3 \cdot \omega$ | $z$ | $W(F, n_0, \omega)$ | $n_0^4 \cdot F_{10\%}$ |
|---|---|---|---|---|---|
| 62 | 0.046 | 1.30 | 0.48 (0.196) | 135 | 0.031 |
| 63 | 0.049 | 1.37 | 0.324 | 190 | 0.0305 |
| 64 | 0.052 | 1.43 | 0.45 | 239 | 0.036 |
| 65 | 0.055 | 1.50 | 0.33 (0.657) | 291 | 0.036 |
| 66 | 0.059 | 1.57 | 0.75 | 240 | 0.0383 |
| 67 | 0.062 | 1.65 | 0.82 | 283 | 0.043 |
| 68 | 0.066 | 1.72 | 0.98 | 277 | 0.045 |
| 69 | 0.070 | 1.80 | 0.916 | 212 | 0.0465 |
| 70 | 0.074 | 1.88 | 0.65 | 281 | 0.051 |
| 71 | 0.079 | 1.96 | 0.964 | 227 | 0.053 |
| 72 | 0.083 | 2.04 | 0.994 | 299 | 0.055 |
| 73 | 0.088 | 2.13 | 0.967 | 268 | 0.056 |
| 74 | 0.093 | 2.22 | 1.0 | 283 | 0.06 |
| 75 | 0.098 | 2.31 | 1.04 | 306 | 0.053 |
| 76 | 0.103 | 2.40 | 1.074 | 351 | 0.057 |
| 77 | 0.109 | 2.50 | 1.132 | 318 | 0.057 |
| 78 | 0.115 | 2.60 | 1.35 | 313 | 0.052 |
| 79 | 0.121 | 2.70 | 1.698 | 270 | 0.050 |
| 80 | 0.127 | 2.80 | 1.459 | 285 | 0.054 |
| 81 | 0.133 | 2.91 | 1.578 | 285 | 0.052 |
| 82 | 0.140 | 3.02 | 2.4(1.361) | 259 | 0.068 |
| 83 | 0.147 | 3.13 | 2.5(1.327) | 278 | 0.058 |

Table 6.2.1.3: Decay exponents $z$ (fourth column) extracted from figures 6.5, 6.6 and 6.7 for initial atomic states $|n_0, \ell_0 = m_0 = 0\rangle$ exposed to a field of amplitude $F = 3.1 \cdot 10^{-9}$ a.u. In columns two and three we also show the 'scaled' field amplitude and frequency experienced by the respective initial states. The fifth column displays the Shannon width (2.61) of the atomic initial state in the Floquet basis, and the last column displays the 'scaled' ionization threshold at $t = 327 \cdot 2\pi/\omega$ (see figure 5.2.1). By comparison of columns two and five it is apparent that all the examples are in the delocalized regime, i.e. the 'scaled' field amplitude is larger than the 'scaled' ionization threshold.

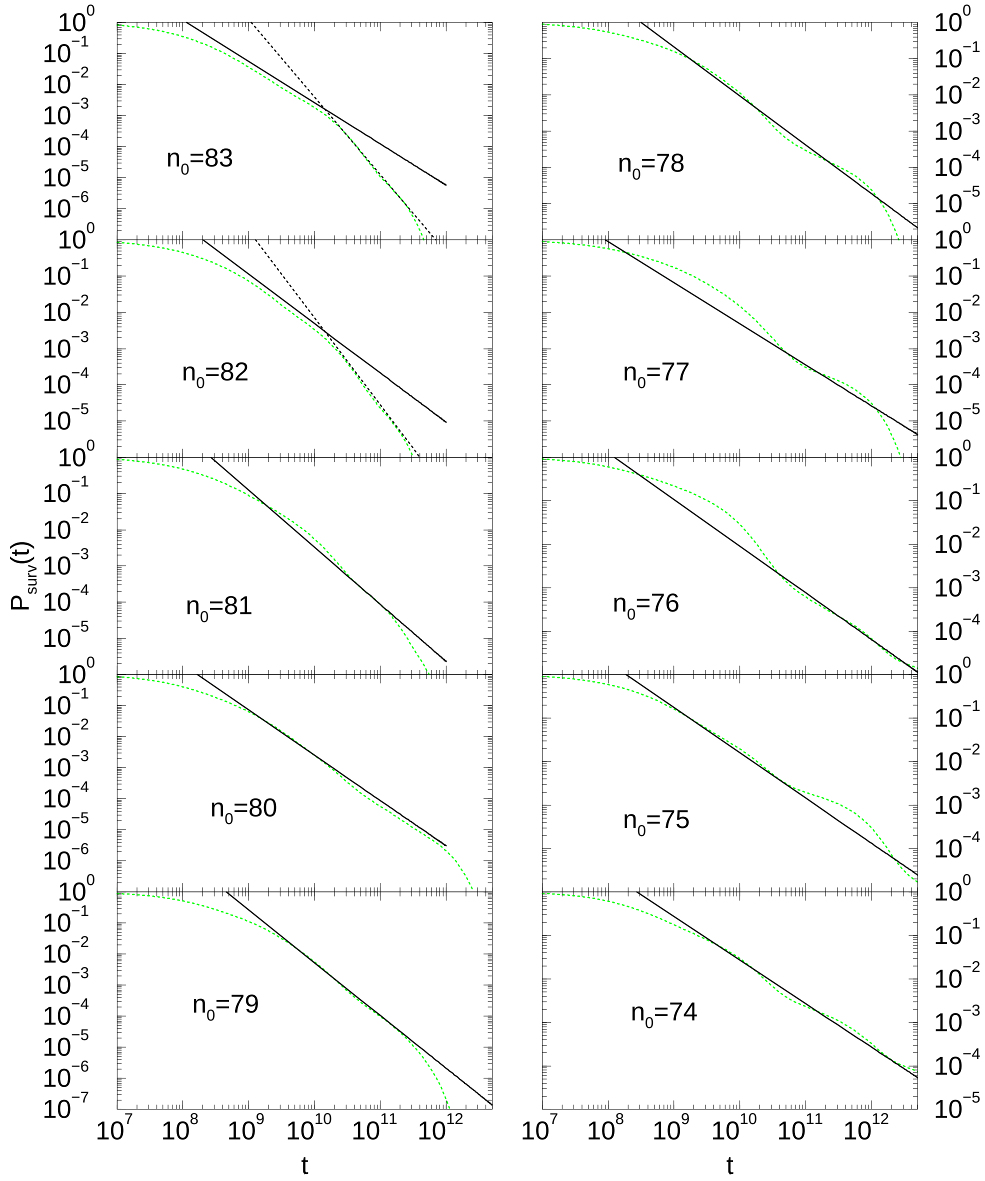

Figure 6.5: Survival probability of lithium atoms exposed to a microwave field of amplitude $F = 3.1 \cdot 10^{-9}$ a.u., and frequency $\omega/2\pi = 36$ GHz for several atomic initial states $|n_0, \ell_0 = m_0 = 0\rangle$ (with $n_0$ given in the plots). In all cases an algebraic decay over more than one decade of the interaction time can be extracted. The decay exponents $z$ are summarized in table 6.2.1.3.

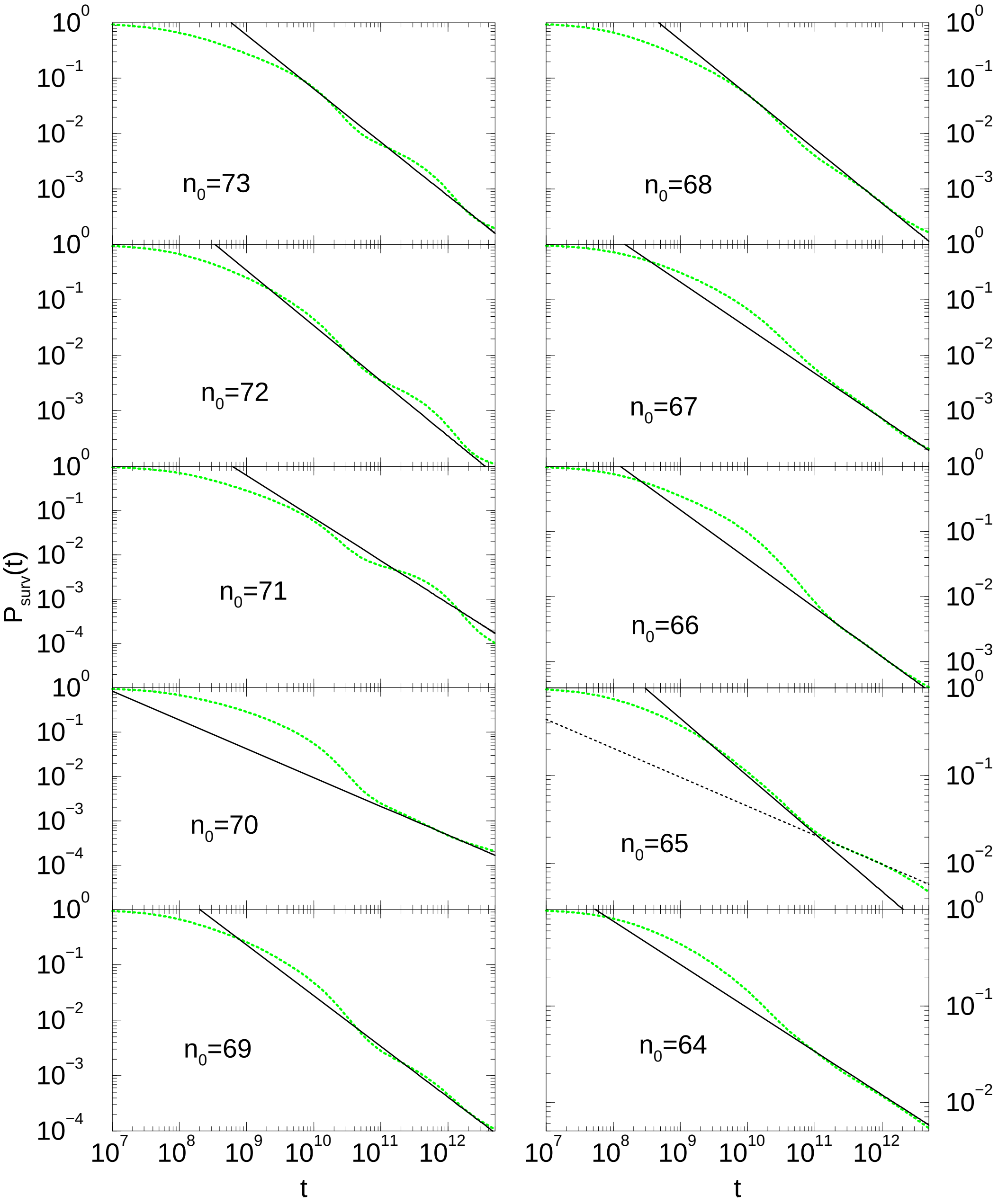

Figure 6.6: Same as in figure 6.5, but for different $n_0$ values.

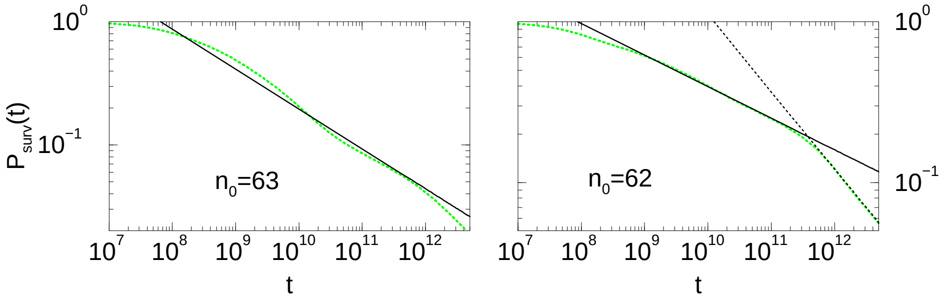

Figure 6.7: Same as in figure 6.5 and figure 6.6, but for different $n_0$ values.

In all cases we observe an algebraic decay over more than one decade of the interaction time. For $n_0 = 62, 65, 82, 83$ we observe different decay exponents on different time scales, both are displayed in table 6.2.1.3, the exponent that is valid on shorter time scales is shown in brackets. Such change of different decay exponents valid on different time scales was already observed in [87], where it was attributed to the electron being trapped in the vicinity of distinct hierarchical phase space structures on different time scales.

In total, we observe an increase of the decay exponent from small values $z \simeq 0.2$, to large exponents $z \simeq 2.5$, with increasing quantum number, i.e. with increasing 'scaled' field amplitude and frequency (note that all examples are in the delocalized regime, i.e. $n_0^4 \cdot F > n_0^4 \cdot F_{10\%}(t = 327 \cdot 2\pi/\omega)$ while according to the delocalization border introduced in [24] – which only gives a rough estimate of the real atomic dynamics – only the examples with $n_0 \geq 70$ are in the delocalized regime). The increase of the decay exponent from $z \simeq 0.2$ to $z \simeq 1$ is accompanied by a non-monotonous increase of the Shannon width which fluctuates between $W = 259$ and $W = 351$ in the situations leading to $z > 1$. However, also $z$ exhibits a locally non-monotonous dependence on $n_0$, e.g., for $n_0 = 78, 79, 80$. We attribute this behavior to particular structures in the Floquet spectrum which are selected via the overlaps $w_j$ with the specific atomic initial state. However, a detailed analysis of this phenomenon remains to be accomplished.

#### 6.2.1.4 Algebraic decay in regime (III)?

So far we studied the time dependence of the survival probability in the frequency regimes (II) ($n = 50$) and (I) ($n = 62, \ldots, 83$), where the external frequency is sufficiently large to couple a large number of atomic bound and continuum states, and where the atoms exhibit dynamical localization.

In the following, we will also show examples of the time dependence of the survival probability in regime (III). In figure 5.5, it was seen that the number of eigenstates which are coupled efficiently to the atomic initial state – measured by the Shannon width of a given atomic initial state – is noticeably smaller in this regime, although the same ionization probability ($P_{\text{ion}} = 10\%$ for all field amplitudes in figure 5.5) is induced. This also leads to a qualitative change of the time dependence

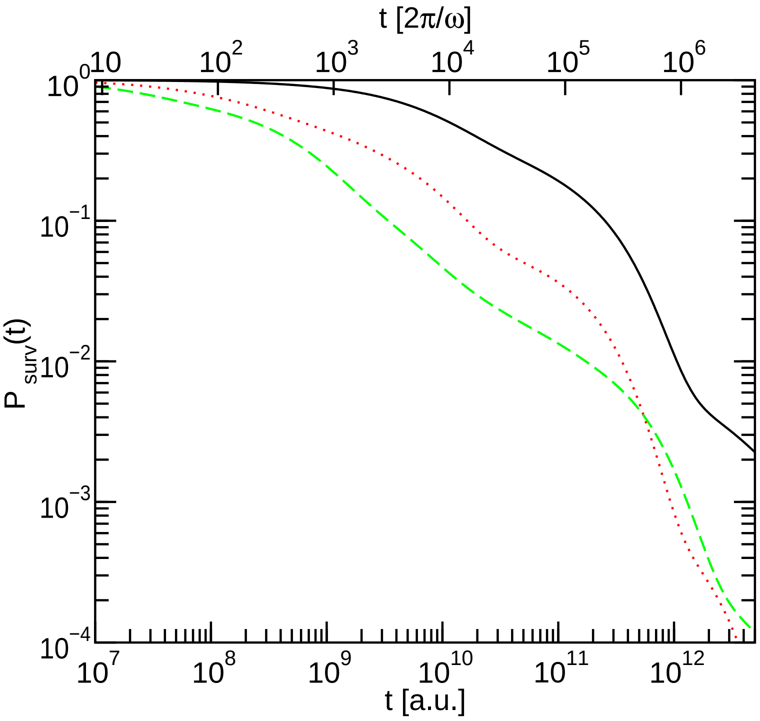

Figure 6.8: Lithium atoms prepared in the state $|n_0 = 37, \ell_0 = m_0 = 0\rangle$, driven by a field of amplitude $F = 5.5 \cdot 10^{-9}$ a.u. (solid line, $n_0^4 \cdot F = 0.01$, Shannon width $W = 13$), $F = 8.5 \cdot 10^{-9}$ a.u. (dotted line, $n_0^4 \cdot F = 0.016$, $W = 35$), and $F = 1.3 \cdot 10^{-8}$ a.u. (dashed line, $n_0^4 \cdot F = 0.024$, $W = 101$). Although both 'scaled' field amplitudes $0.016$ and $0.024$ are larger than the 'scaled' ionization threshold $n_0^4 \cdot F_{10\%}(327 \cdot 2\pi/\omega) = 0.0109$ (see figure 5.2.1), only for the largest field amplitude an approximate algebraic decay over more than two decades can be observed. The 'scaled' frequency $n_0^3 \cdot \omega = 0.28$ (with $\omega/2\pi = 36$ GHz the 'unscaled' frequency) of the three examples corresponds to regime (III).

of $P_{\rm surv}(t)$. Figure 6.8 shows the situation for lithium atoms prepared in the states $|n_0 = 37, \ell_0 = m_0 = 0\rangle$. The figure displays the survival probability of the given initial state exposed to a field of variable amplitude $F = 5.5 \cdot 10^{-9}$ a.u., $F = 8.5 \cdot 10^{-9}$ a.u., and $F = 1.3 \cdot 10^{-8}$ a.u., respectively. All the curves in figure 6.8 display a similar behavior of the survival probability: The interplay of different weights $w_j$ and widths $\Gamma_j$ leads to bumps in the survival probability in this double logarithmic plot, but only for the strongest field this leads to an approximately algebraic decay over roughly three decades of the interaction time. This is a clear manifestation of the difference to the high 'scaled' frequency regimes (I) and (II): For an algebraic decay in the regimes of dynamical localization (i.e. in regime (I) and (II)) it is sufficient that the parameters are in the delocalized regime, and in figure 6.7 and 6.6

we observed an algebraic decay over more than two decades for $n_0^4 \cdot F \geq 1.4 \cdot n_0^4 \cdot F_{10\%}(t = 327 \cdot 2\pi/\omega)$ (see columns two and five in table 6.2.1.3). In regime (III), larger 'scaled' field amplitudes are needed to induce an algebraic decay (e.g., at $F = 8.5 \cdot 10^{-9}$ a.u. – for $n_0^4 \cdot F \simeq 1.5 \cdot n_0^4 \cdot F_{10\%}$ – no clear algebraic decay can be observed), i.e. here the field is strong enough to induce appreciable ionization, but – due to the absence of atomic transitions that can be driven (quasi-) resonantly with the given frequency – it cannot induce a strong mixing of a large number of atomic states (see also figure 5.5). Consequently, we do observe an algebraic decay over more than two orders of magnitude only for considerably larger 'scaled' field amplitudes as compared to the ionization threshold (e.g. $n_0^4 \cdot F \geq 2.2 \cdot n_0^4 \cdot F_{10\%}(t = 327 \cdot 2\pi/\omega)$ at $F = 1.3 \cdot 10^{-8}$ a.u.), that are strong enough to couple the initial state to many bound or continuum states, i.e. when the external field induces a large Shannon width of the initial state (compare $W(F = 8.5 \cdot 10^{-9}\ \text{a.u.}) = 35$ to $W(F = 1.3 \cdot 10^{-8}\ \text{a.u.}) = 101$).

### 6.2.2 Rubidium

We report now some typical results for the time dependence of the survival probability of microwave driven rubidium atoms. In figure 6.9 we display the survival probability of $|n_0 = 50, \ell_0 = 1, m_0 = 0\rangle$ and $|n_0 = 55, \ell_0 = 1, m_0 = 0\rangle$ exposed to microwave fields, with the parameters and the decay exponents displayed in table 6.2.2.

| $n_0$ | $n_0^4 \cdot F$ | $n_0^3 \cdot \omega$ | $z$ | $W(F, n_0, \omega)$ | $n_0^4 \cdot F_{10\%}(t = 327 \cdot 2\pi/\omega)$ |
|---|---|---|---|---|---|
| 50 | 0.025 | 0.68 | 0.25 | 134 | 0.023 |
| 50 | 0.034 | 0.68 | 0.9 | 257 | 0.023 |
| 55 | 0.064 | 0.91 | 1.27 | 601 | 0.033 |

Table 6.2.2: Decay exponents $z$ (fourth column) extracted from figure 6.9 of rubidium $|n_0, \ell_0 = 1, m_0 = 0\rangle$ states. All three examples are in the delocalized regime (compare column two and six), and exhibit an algebraic decay with increasing exponent $z$ for increasing 'scaled' field amplitudes. Much as in the case of lithium we observe an increase of the Shannon width (fifth column) with increasing field strength, with $W > 100$ in all three examples. The extremely large Shannon width $W = 601$ for $n_0 = 55$ can be attributed to the fact that here ($n_0^3 \cdot \omega = 0.91$) the atom is driven nearly resonantly (where we already observed a maximum of the Shannon width at the ionization threshold in figure 5.5) and to the large field amplitude $F \simeq 2 \cdot F_{10\%}(t = 327 \cdot 2\pi/\omega)$.

Much as in the case of lithium, all three examples – which are all in the delocalized regime, i.e., $F > F_{10\%}$ (since the examples are chosen in regime (II), the localization border of [24] – approximately valid for hydrogen atoms, and hence only valid in the alkali regime (I) – cannot be applied) – exhibit an algebraic decay. As in the above for lithium, in all three examples a large number of atom-field eigenstates

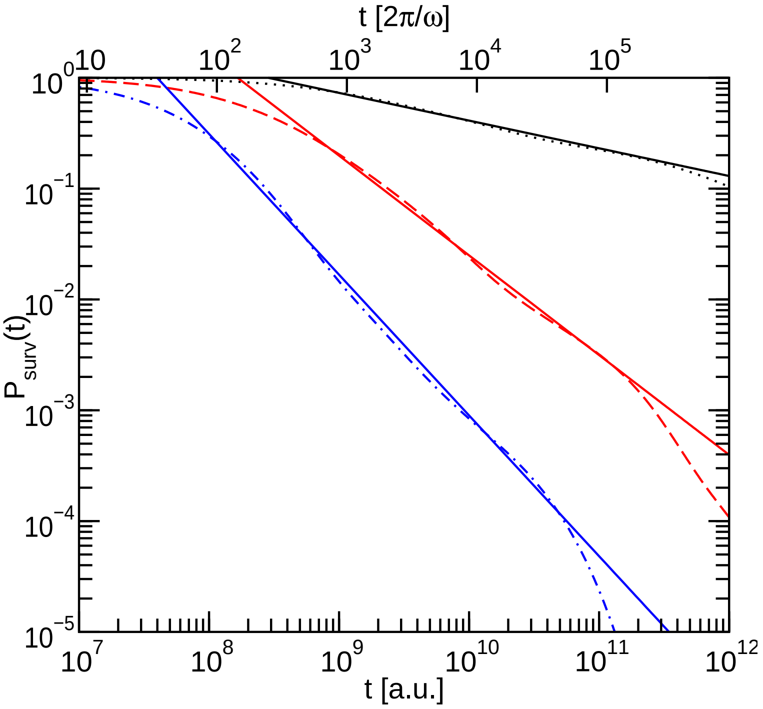

Figure 6.9: Survival probability $P_{\rm surv}(t)$ of rubidium Rydberg states $|n_0, \ell_0 = 1, m_0 = 0\rangle$ for $n_0 = 50$ (dotted line: $F = 4 \cdot 10^{-9}$ a.u.; dashed line: $F = 5.5 \cdot 10^{-9}$ a.u.), and $n_0 = 55$ (dash-dotted line: $F = 7 \cdot 10^{-9}$ a.u.), respectively, at $\omega/2\pi = 36$ GHz. We observe a clear algebraic decay $P_{\rm surv} \sim t^{-z}$. The decay exponents $z$, as well as the 'scaled' field parameters are displayed in table 6.2.2.

contribute to the sum defining the survival probability ($W > 100$) and we observe an algebraic decay. Again, no universal decay law $t^{-1}$ can be observed, but a systematically increasing decay exponent with increasing 'scaled' field amplitude. Let us note here, that – in agreement with our results presented above – for microwave driven rubidium atoms (frequency $\omega/2\pi = 8.87$ GHz, initial state $n_0 = 84$, i.e. 'scaled frequency $n_0^3 \cdot \omega \simeq 0.8$) an algebraic decay with $z \simeq 0.44 \pm 0.02$ (i.e. $z \neq 1$) was already found experimentally [86]. The exact modeling of the experimental situation, however, would require a larger memory (as already mentioned before), hence, so far we cannot provide for a quantitative comparison with the experimental results.

### 6.2.3 Atomic hydrogen

For the sake of completeness, we also provide results on the 'simplest' atom under periodic driving, i.e. on microwave driven atomic hydrogen. As already mentioned, in [85] the prediction of a 'universal' decay law was tested on a one-dimensional

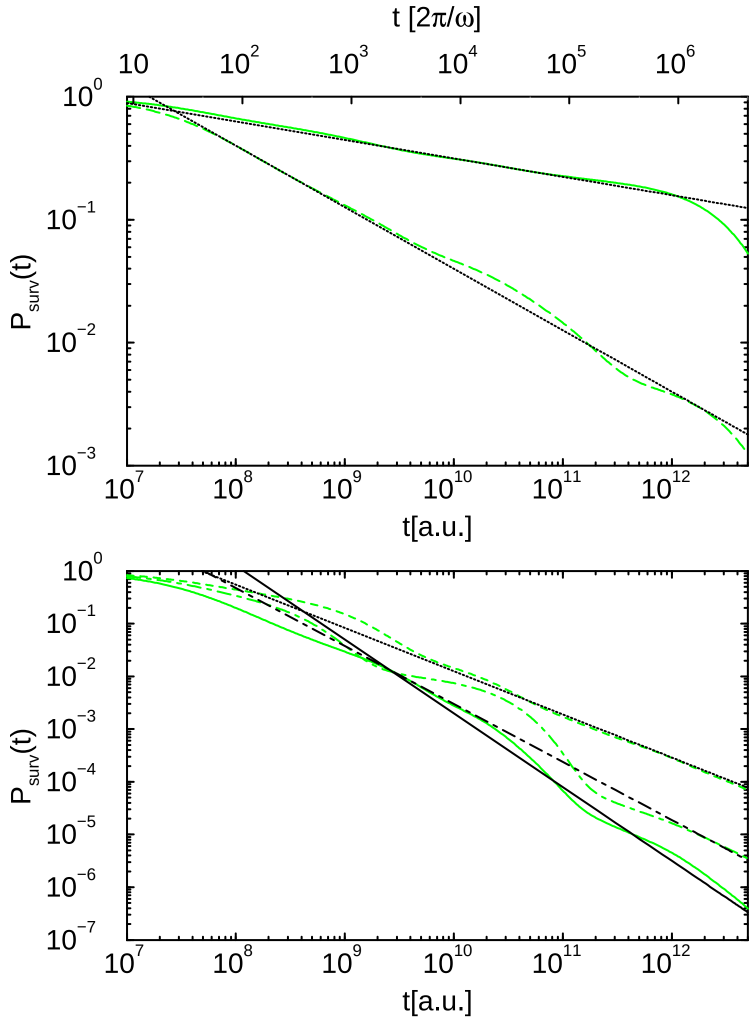

Figure 6.10: Survival probability of hydrogen $|n_0, \ell_0 = m_0 = 0\rangle$ states exposed to a microwave field of amplitude $F = 6 \cdot 10^{-9}$ a.u. Upper plot: green solid line: $n_0 = 61$; green dashed line: $n_0 = 63$. Both curves follow a dependence $t^{-z}$, the decay exponents $z$ as well as the scaled field parameters $F_0$ and $\omega_0$ are collected in table 6.2.3. Lower plot: green dashed line: $n_0 = 65$; green dash-dotted line: $n_0 = 69$; green solid line: $n_0 = 71$. Much as in the upper plot all three initial states exhibit an algebraic decay, with the decay exponents and the scaled field parameters given in table 6.2.3.

model of microwave driven hydrogen atoms, and on the quantum Kepler map that should approximate the dynamics of driven hydrogen atoms [24]. Furthermore, such a decay was also predicted for driven, non-hydrogenic Rydberg states [85]. In the previous sections, however, we saw that the latter prediction fails. Here, we will investigate the validity of the $t^{-1}$ law for atomic hydrogen.

For this purpose, we exposed hydrogen $(\ell_0 = m_0 = 0)$ states, with $n_0$ in the range $61 \ldots 71$, to a microwave field of amplitude $F = 6 \cdot 10^{-9}$ a.u. (again the frequency is chosen as $\omega/2\pi = 36$ GHz). The survival probability of the various initial states is displayed in figure 6.10. Again, we observe an algebraic decay over several decades of the interaction time for all initial states. The resulting decay exponents are collected in table 6.2.3:

| $n_0$ | $n_0^4 \cdot F$ | $n_0^3 \cdot \omega$ | $z$ | $W(F, n_0, \omega)$ | $n_0^4 \cdot F_{10\%}$ |
|---|---|---|---|---|---|
| 61 | 0.08 | 1.24 | 0.15 | 155 | 0.049 |
| 63 | 0.09 | 1.37 | 0.52 | 201 | 0.043 |
| 65 | 0.11 | 1.50 | 0.82 | 171 | 0.045 |
| 69 | 0.14 | 1.80 | 1.1 | 208 | 0.051 |
| 71 | 0.15 | 1.96 | 1.4 | 187 | 0.053 |

Table 6.2.3: Decay exponents $z$ extracted from figure 6.10, for hydrogen $\ell_0 = m_0 = 0$ states. Comparison of the scaled field amplitude (second column) to the scaled ionization threshold at $t = 327 \cdot 2\pi/\omega$ (sixth column, see figure 5.1) shows that all cases corresponds to the delocalized regime (note that the examples are also in the delocalized regime according to the the qualitative localization border introduced in [24]). Again the Shannon width (fifth column) exceeds $W = 100$ in all five examples.

As apparent from figure 6.10 and table 6.2.3, microwave driven hydrogen atoms show essentially the same decay as we observed it for lithium and rubidium atoms in section 6.2.1, and 6.2.2, respectively: The atoms (exposed to a field with parameters chosen in the delocalized regime) exhibit an algebraic decay $t^{-z}$ with increasing decay exponent $z$ – from $z \simeq 0.15$ to $z \simeq 1.4$ – for increasing scaled field amplitude. Thus, we observed (qualitatively) exactly the same decay of lithium, rubidium, and hydrogen atoms under periodic driving, i.e. all three atomic species experience an algebraic decay for sufficiently large driving fields (that cause a coupling of a large number of atom-field eigenstates), but they do not obey any universal decay law.

## 6.3 Outlook

In this chapter we provided the first exact theoretical/numerical results on the survival probability of real-existing three-dimensional atomic systems with principal quantum numbers $n_0 = 37, \ldots, 83$. As already observed in numerical studies on moderately excited atomic hydrogen ($n_0 = 23$) in the localized regime [86] as well as in laboratory experiments on rubidium in the localized and the delocalized regime [86],(4) we identify an algebraic decay of the survival probability for sufficiently large 'scaled' field amplitudes. 'Sufficiently large' requires that the field is larger than the ionization threshold in regimes (I) and (II), while it has to be considerably larger in the low 'scaled' frequency regime (III). In other words it has to be large enough to induce a strong coupling of many ($W \gtrsim 100$) states. In contrast to predictions based on the study of simplified model systems using absorbing boundary conditions to model the decay [85, 78, 81], we found strong numerical evidence that there is no universal decay law, at least we did not observe universal decay for microwave driven Rydberg states. On the contrary, in our studies on lithium, rubidium and hydrogen atoms we observed a global (but locally non-monotonous) increase of the decay exponent with increasing perturbation strength. Furthermore, occasionally there is a transition between different decay exponents for different time scales, as already observed in [87].

A crucial point to deduce the universal decay law $t^{-1}$ in [78, 81] was the assumption that the weights $w_j$ of some atomic initial state when projected on the atom-field eigenstates are proportional to the corresponding widths $\Gamma_j$. In our system, however, we do not even observe an approximate proportionality of the $w_j$ and the $\Gamma_j$, but a broad distribution of the weights and widths. Hence, we can conclude that the assumed proportionality does not at all represent a generic situation.

Since our system exhibits a high density of states, and we model a coherent coupling of the bound states to the continuum, we expect the results obtained in this chapter to be more general and to be also valid for other systems. More precisely, we believe that the prediction of a universal decay law does neither hold for other quantum systems with a high density of states that exhibit a strong coupling of many bound and continuum states. Typically such systems will not show the proportionality $w_j \sim \Gamma_j$, and we expect an (eventually non-monotonous) increasing decay exponent with increasing perturbation strength as a general rule.

In agreement with our results obtained on alkali and on hydrogen atoms, such behavior is not restricted to the traditional field of quantum chaos, but can be obseved for quantum (-chaotic) systems with a mixed regular-chaotic classical counterpart (like atomic hydrogen), as well as for pure quantum systems (like alkali atoms).

---

(4) Note that these experiments were performed partially in regime (II), and hence the (hydrogenic) localization border introduced in [24] cannot be employed. However, for typical interaction times $t \simeq 300 \cdot 2\pi/\omega$ the ionization probability of the example showing an algebraic decay exceeds 10% (see figure 3 (b) in [86]), and hence we can assume that the parameters correspond to the delocalized regime.

# Chapter 7

# Summary and perspectives

## 7.1 Summary

In this thesis we performed an exact numerical experiment on the microwave ionization of Rydberg states of alkali atoms and atomic hydrogen. Our experimental apparatus combines sophisticated numerical methods with state-of-the-art (parallel) computing techniques, and allows for an exact description of the field induced coupling of the atomic bound states to the atomic continuum. In our fully three-dimensional simulations of the periodically time-dependent problem, we employed parameters (microwave frequency, field amplitude, principal quantum numbers of the atomic initial states, and atom-field interaction time) as they are used in typical laboratory experiments. In this parameter regime, we have to deal with a high density of states – scaling as $n_0^5$ – and therefore the availability of large-scale parallel computing facilities – together with an efficient parallel implementation of our code – is essential for our calculations. Yet, our numerical experiment bears some advantages as compared to laboratory experiments: In contrast to laboratory set-ups, we can easily keep all parameters constant and perform precisely the same experiment with different atomic species. Furthermore, our approach models a purely coherent driving of the atom, without any external noise.

Performing our numerical experiments over a broad range of parameters, we could identify three frequency regimes in the ionization dynamics of periodically driven alkali atoms and specify the relevant frequency scales that separate these regimes. In regime (I) – where the external frequency is larger than or comparable to the level splitting of unperturbed hydrogenic energy levels, the alkali dynamics mimics the hydrogen dynamics, both, qualitatively and quantitatively. Here also the alkali dynamics is dominated by the hydrogenic phase space structure, and both, alkali and hydrogen atoms exhibit dynamical localization (i.e., the quantum mechanical suppression of classically diffusive ionization). Furthermore, both atomic species experience enhanced stability against ionization at initial conditions corresponding to stable (elliptic) islands in the classically mixed regular-chaotic phase space of the driven two-body Kepler problem, realized by microwave driven atomic hydrogen. For smaller frequencies, the alkali and hydrogen ionization dynamics differs dramatically, and we enter regime (II), where alkali atoms show the signature of dynamical localization, whilst atomic hydrogen ionizes classically. In this frequency window we can thus observe the emergence of dynamical localization in a pure quantum system, without a classical analogue. Finally, for small frequencies (regime (III)) also alkali atoms do no longer experience dynamical localization, the alkali thresholds follow the behavior as proposed and intensively studied in laboratory experiments by the Virginia group. The difference in the ionization dynamics of alkali and hydrogen atoms in regimes (II) and (III) leads to up to 13 times lower ionization thresholds of alkali atoms in this regime.

With this novel insight in the ionization dynamics of periodically driven singly excited multi-electron Rydberg atoms, we could reinterpret the available data of laboratory experiments of the Munich and the Virginia experiments. Comparison of the frequency used in these experiments with the internal atomic frequencies (determined by the hydrogenic level splitting and the element-specific quantum defects) shows that so far all laboratory experiments on alkali atoms were performed mainly in (the non-hydrogenic) regimes (III) and (II). Consequently, these experiments showed considerable discrepancies in the ionization thresholds of alkali and hydrogen atoms (up to one order of magnitude), hitherto inexplicable. Our identification of the above frequency regimes does not only explain these experimentally measured differences and provides for the missing link between the ionization scenarios suggested by the Virginia and the Munich group, but also suggests frequency scales where (future) laboratory experiments should measure essentially the same ionization thresholds for alkali as compared to hydrogen atoms.

By performing our numerical experiment on hydrogen, lithium, and rubidium atoms, we furthermore could answer the question whether the dynamics of driven alkali atoms obeys any scaling rules. In contrast to atomic hydrogen, the multi-particle atomic core of alkali atoms introduces a finite length scale, and hence scaling of the alkali dynamics is *a priori* not justified. With our experiments on different atomic species, we can now, *a posteriori* substantiate the existence of scaling laws also for the alkali dynamics. Our results evince that in the regimes of dynamical localization (i.e. regime (I) and (II)) it is indeed the splitting of unperturbed hydrogenic energy levels (which coincides with the classical Kepler frequency of the unperturbed hydrogen atom) that dominates the dynamics (although in regime (II) the alkali and the hydrogen excitation process differ qualitatively and quantitatively). Hence, in these regimes it is appropriate to use the hydrogenic scaling rules also for the alkali dynamics. Employing these rules, it is possible to map the 'scaled' alkali ionization thresholds as a function of the 'scaled' frequency of different atomic (alkali) species on top of each other. The transition to regime (III), however, occurs at an element-specific quantum number, and thus the scaling rules break down. This is in agreement with the fact that in this regime it is no longer the hydrogenic energy splitting, but the splitting between (unperturbed) low-angular momentum alkali states that dominates the dynamics.

Apart from the identification of the frequency dependence of the ionization dynamics of driven Rydberg atoms, our system is an ideal candidate for the study of the temporal decay of open, complex systems. Whilst this is a subject of vivid ongoing discussion in literature, many contributions to this subject, however, are based on the study of simplifying models of real existing systems, or model systems for which an experimental verification is not straightforward. Our system, on the contrary, has the advantage that it exhibits sufficiently complex dynamics due to its highly non-linear level structure, is a decaying system, and can be studied in laboratory experiments and now – with the apparatus described in this thesis – also in numerical experiments. As predicted for complex quantum system by various groups, and as already experimentally observed for driven rubidium atoms [86], for sufficiently large field amplitude we observed an algebraic decay $\sim t^{-z}$ of the survival probability of the microwave driven atom. In contrast to the assumption of a universal decay law following $t^{-1}$ proposed by [78, 85, 81], however, we found an increasing decay exponent with increasing 'scaled' field amplitude. Thus we provided strong numerical evidence that there is no such universal decay law at least for complex atomic decay processes. Moreover, since our system bears many aspects of typical time-dependent quantum systems (like scattering the electron off the atomic core [58], dynamical localization, coherent coupling to multiply degenerate continua via multiphoton transition amplitudes of variable order) we expect the increase of the decay exponent for increasing perturbation to be a general phenomenon for the decay of open, complex quantum systems.

## 7.2 Perspectives

One of the main results of this thesis is the identification of the three frequency regimes in the ionization dynamics of microwave driven alkali atoms, and hence the elucidation of the experimentally observed dramatic differences in the ionization thresholds of periodically driven alkali and hydrogen atoms in regime (III) and (II). These differences are obviously caused by the existence of a multi-particle core which induces non-hydrogenic modifications of the driven alkali spectrum as compared to that of driven hydrogen atoms. Such additional structures in the spectrum allow an efficient transport of the electronic population from the initial atomic state towards the atomic continuum at field parameters (frequency and amplitude) where such transport is not possible for atomic hydrogen. To discern these non-hydrogenic structures in the spectrum of the driven atom it is necessary to undertake a detailed analysis of the complex energy spectrum of the system. A possible and worthwhile attempt in this direction is the study of the photoexcitation or photoionization cross sections which can also be measured experimentally by probing the energy spectrum with an additional weak probe field ('Floquet spectroscopy') [186, 187, 188]. In similar studies (i.e. in studies on the photoabsorption cross section) on non-hydrogenic atoms exposed to external static electric and/or magnetic fields [189, 59, 190] it was found that non-hydrogenic structures in the spectrum can be attributed to the scattering or diffraction of the Rydberg electron at the atomic core. Thus, the core acts as a point-like scatterer for the electronic wave-function [58]. In analogy to the time-independent problem, we expect considerable differences in the photoionization spectrum of microwave driven alkali and hydrogen atoms in the non-hydrogenic frequency regimes (II) and (III). In regime (I), however, where our studies showed that the alkali ionization dynamics follows the hydrogenic dynamics, we expect no significant differences in the alkali and the hydrogen spectrum. Since the classical phase space of the driven hydrogen atom is (mixed regular-) chaotic in regime (I), such findings would agree with studies on billiard systems with and without point-like interactions. There, no deviations between the spectral statistics with and without a point-scatterer were found for chaotic billiards [191, 192], whereas for integrable billiards the spectral statistics do change with the existence of a point-scatterer [193, 194, 195]. While in studies on time-independent problems (billiards, Rydberg atoms in static fields) the existence of a point scatterer only changes the spectral statistics, in our problem the non-hydrogenic core also causes the atom to be less stable against ionization than without a scatterer (as we observed it in regime (II) and (III)). Thus, it would be worthwhile to perform a (laboratory or numerical) experiment that measures both, the photoionization cross section and the ionization probability of periodically driven Rydberg states. Such an experiment should not only show the differences in the ionization thresholds between alkali and hydrogen atoms in regimes (II) and (III) (that we identified in this thesis), but also a difference in the spectral statistics of both atomic species in these frequency regimes. To our knowledge, such studies would provide for the first case where a difference in a robust, experimentally accessible quantity – the ionization probability (which averages over the entire spectrum) – can be traced back to the difference in the spectral statistics induced by core-scattered or diffractive orbits. Furthermore, these studies would be the first studies on modifications of the spectral statistics caused by a point-like interaction in an explicitly time-dependent system.

Another worthwhile program that should be accomplished in future studies concerns the decay of our system. In solid state physics it is well known that Anderson localization causes fluctuations in the conductance across disordered solids. Recently, a suitable generalization of conductance for driven atomic systems was undertaken, and atomic conduction fluctuations were observed in one-dimensional calculations on microwave-driven atomic hydrogen [66, 67, 196]. With our apparatus, it is now possible to extend such studies to three-dimensional microwave driven hydrogen atoms, to verify that such fluctuations are no artefact of the one-dimensional model of the atom. Moreover, such fluctuations should also appear in microwave driven alkali atoms in regime (I), and also in regime (II), where we observe the signatures of dynamical localization for alkali atoms, without a classical analogue. In contrast to our studies on the decay of the survival probability, such studies require a statistical analysis of the ’atomic conductance’ as a function of some parameter [196]. For such a statistical analysis a large number of atomic samples (specified by the field amplitude, frequency, and principal quantum number) has to be probed. Therefore a larger amount of computation time is needed. Yet, in the near future, with the ongoing increasing availability of supercomputing facilities also for civil purposes these studies become feasible.

Finally, our work proves that nowadays the exact treatment of complex dynamical systems – without the application of (over-) simplified models, and without the use of adjustable parameters – is indeed possible. In addition, we did not only show that this kind of program is possible, but moreover our results show that a such a numerical ’tour-de-force’ is crucial for the comprehensive understanding of highly non-perturbative situations at high spectral densities.

# Bibliography

[1] A. Einstein, *Über einen die Erzeugung und Verwandlung des Lichtes betreffenden heuristischen Gesichtspunkt*, Ann. Phys. **17**, 132 (1905).

[2] C. C. Tannoudji, *Nobel Lecture: Manipulating atoms with photons*, Rev. Mod. Phys. **70**, 707 (1998).

[3] S. Chu, *Nobel Lecture: The manipulation of neutral particles*, Rev. Mod. Phys. **70**, 685 (1998).

[4] W. D. Phillips, *Nobel Lecture: Laser cooling and trapping of neutral atoms*, Rev. Mod. Phys. **70**, 721 (1998).

[5] T. W. Hänsch and H. Walther, *Laser spectroscopy and quantum optics*, Rev. Mod. Phys. **71**, S242 (1999).

[6] D. J. Tannor and S. A. Rice, *Control of selectivity of chemical reaction via control of wave packet evolution*, J. Chem. Phys. **83**, 5013 (1985).

[7] P. Brumer and M. Shapiro, *Control of unimolecular reactions using coherent light*, Chem. Phys. Lett. **126**, 541 (1986).

[8] J. E. Bayfield and P. M. Koch, *Multiphoton Ionization of Highly Excited Hydrogen Atoms*, Phys. Rev. Lett. **33**, 258 (1974).

[9] O. Benson, A. Buchleitner, G. Raithel, M. Arndt, R. N. Mantegna, and H. Walther, *From coherent to noise–induced microwave ionization of Rydberg atoms*, Phys. Rev. A **51**, 4862 (1995).

[10] J. E. Bayfield, L. D. Gardner, and P. M. Koch, *Observation of Resonances in the Microwave-Stimulated Multiphoton Excitation and Ionization of Highly Excited Hydrogen Atoms*, Phys. Rev. Lett. **39**, 76 (1977).

[11] J. G. Leopold and I. C. Percival, *Microwave Ionization and Excitation of Rydberg Atoms*, Phys. Rev. Lett. **41**, 944 (1978).

[12] N. B. Delone, B. A. Zon, and V. P. Krainov, *Diffusion mechanism of ionization of highly excited atoms in an alternating electromagnet field*, Sov. Phys. JETP **48**, 2 (1978).

[13] B. V. Chirikov, *A universal instability of many-dimensional oscillator systems*, Phys. Rep. **52**, 263 (1979).

[14] B. I. Meerson, E. A. Oks, and P. V. Sasorov, *Stochastic instability of an oscillator and the ionization of highly-excited atoms under the action of electromagnetic radiation*, JETP Lett. **29**, 72 (1979).

[15] N. B. Delone, B. P. Krainov, and D. L. Shepelyansky, *Highly excited atoms in the electromagnetic field*, Sov. Phs. Usp. **26**, 551 (1983).

[16] R. Bümel and U. Smilansky, *Quantum Mechanical Suppression of Classical Stochasticity in the Dynamics of Periodically Perturbed Surface-State-Electrons*, Phys. Rev. Lett. **52**, 137 (1984).

[17] H. P. Breuer and M. Holthaus, *Adiabatic processes in the ionization of highly excited hydrogen atoms*, Z. Phys. D **11**, 1 (1989).

[18] R. V. Jensen, S. M. Susskind, and M. M. Sanders, *Chaotic Ionization of Highly Excited Hydrogen Atoms: Comparison of Classical and Quantum Theory with Experiment*, Phys. Rep. **201**, 1 (1991).

[19] K. A. H. v. Leeuwen, G. v. Oppen, S. Renwick, J. B. Bowlin, P. M. Koch, R. V. Jensen, O. Rath, D. Richards, and J. G. Leopold, *Microwave Ionization of Hydrogen Atoms: Experiment versus Classical Dynamics*, Phys. Rev. Lett. **55**, 2231 (1985).

[20] E. J. Galvez, B. E. Sauer, L. Moormann, P. M. Koch, and D. Richards, *Microwave Ionization of H Atoms: Breakdown of Classical Dynamics for High Frequencies*, Phys. Rev. Lett. **61**, 2011 (1988).

[21] J. E. Bayfield, G. Casati, I. Guarneri, and D. W. Sokol, *Localization of Chaotic Diffusion for Hydrogen Atoms in Microwave Fields*, Phys. Rev. Lett. **63**, 364 (1989).

[22] V. Gontis and B. Kaulakys, *Stochastic dynamics of hydrogenic atoms in the microwave field: modelling by maps and quantum description*, J. Phys. B **20**, 5051 (1987).

[23] G. Casati, I. Guarneri, and D. L. Shepelyansky, *Exponential photonic localization for the hydrogen atom in a monochromatic field*, Phys. Rev. A **36**, 3501 (1987).

[24] G. Casati, Chirikov, I. Guarneri, and D. Shepelyansky, *Hydrogen Atom in Monocromatic Field: Chaos and Dynamical Photonic Localization*, I.E.E.E., Journal of Quantum Electronics **24**, 1420 (1988).

[25] P. W. Anderson, *Absence of Diffusion in Certain Random Lattices*, Phys. Rev. **109**, 1492 (1958).

[26] S. Fishman, D. R. Grempel, and R. E. Prange, *Chaos, Quantum Recurrences, and Anderson Localization*, Phys. Rev. Lett. **49**, 509 (1982).

[27] P. A. Lee and T. V. Ramakrishnan, *Disordered electronic systems*, Rev. Mod. Phys. **57**, 287 (1985).

[28] L. D. Landau and E. M. Lifschitz, *Mechanik*, Vol. I of *Lehrbuch der theoretischen Physik*, 2 ed. (Akademie Verlag, Berlin, 1964).

[29] I. C. Percival, *Planetary Atoms*, Proc. R. Soc. London A **353**, 289 (1977).

[30] D. Delande and A. Buchleitner, in *Advances in atomic, molecular, and optical physics*, edited by B. Bederson (Academic Press, New York, 1994), Vol. 34, p. 85.

[31] P. M. Koch and K. A. H. van Leeuwen, *The importance of resonances in microwave "ionization" of excited hydrogen atoms*, Phys. Rep. **255**, 289 (1996).

[32] A. Buchleitner and D. Delande, *Dynamical Localization in More Than One Dimension*, Phys. Rev. Lett. **70**, 33 (1993).

[33] A. Buchleitner, *Atomes de Rydberg en champ microondes: régularité et chaos*, Thèse de Doctorat (Université Pierre et Marie Curie), Paris (1993).

[34] A. Buchleitner, D. Delande, and J. C. Gay, *Microwave ionization of 3-d hydrogen atoms in a realistic numerical experiment*, J. Opt. Soc. Am. B **12**, 505 (1995).

[35] B. I. Meerson, E. A. Oks, and P. V. Sasorov, *A highly excited atom in a field of intense resonant electromagnetic radiation: I. Classical motion*, J. Phys. B **15**, 3599 (1982).

[36] G. P. Berman and G. M. Zaslavsky, *Theory of quantum nonlinear resonance*, Phys. Lett. A **61**, 295 (1977).

[37] G. M. Zaslavsky, *Stochasticity in quantum systems*, Phys. Rep. **80**, 157 (1981).

[38] A. Buchleitner and D. Delande, *Spectral Aspects of the Microwave Ionization of Atomic Rydberg States*, Chaos, Solitons & Fractals **5**, 1125 (1995).

[39] J. Zakrzewski, D. Delande, J. C. Gay, and K. Rzazewski, *Ionization of highly excited hydrogen-atoms by a circularly polarized microwave field*, Phys. Rev. A **47**, R2468 (1993).

[40] W. v. d. Water, K. A. H. v. Leeuwen, S. Yoakum, E. J. Galvez, L. Moorman, T. Bergeman, B. E. Sauer, and P. M. Koch, *Microwave Multiphoton Excitation of Helium Rydberg Atoms: The Analogy with Atomic Collisions*, Phys. Rev. Lett. **63**, 762 (1989).

[41] W. v. d. Water, S. Yoakum, T. v. Leeuven, B. E. Sauer, L. Moorman, E. J. Galvez, D. R. Mariani, and P. M. Koch, *Microwave multiphoton ionization and excitation of helium Rydberg atoms*, Phys. Rev. A **42**, 572 (1990).

[42] M. Arndt, A. Buchleitner, R. N. Mantegna, and H. Walther, *Experimental Study of Quantum and Classical Limits in Microwave Ionization of Rubidium Rydberg Atoms*, Phys. Rev. Lett. **67**, 2435 (1991).

[43] A. Buchleitner, L. Sirko, and H. Walther, *Rubidium Rydberg Atoms in Bichromatic Microwave Fields*, Europhys. Lett. **16**, 1 (1991).

[44] R. Blümel, A. Buchleitner, R. Graham, L. Sirko, U. Smilansky, and H. Walther, *Dynamical localization in the microwave interaction of Rydberg atoms: The influence of noise*, Phys. Rev. A **44**, 4521 (1991).

[45] J. M. Hettema, P. Fu, and T. F. Gallagher, *Microwave ionization rates of Na Stark states*, Phys. Rev. A **41**, 6555 (1990).

[46] P. Pillet, H. B. van Linden van den Heuvell, W. W. Smith, R. Kachru, and T. F. Gallagher, *Microwave Ionization of Na Rydberg atoms*, Phys. Rev. A **30**, 280 (1984).

[47] H. B. van Linden van den Heuvell and T. F. Gallagher, *Ionization of Na atoms by 8-GHz electric fields*, Phys. Rev. A **32**, 1495 (1985).

[48] C. R. Mahon, J. L. Dexter, P. Pillet, and T. F. Gallagher, *Ionization of sodium and lithium Rydberg atoms by 10-MHz to 15-GHz electric fields*, Phys. Rev. A **44**, 1859 (1991).

[49] M. W. Noel, M. W. Griffith, and T. F. Gallagher, *Classical subharmonic resonances in microwave ionization of lithium Rydberg atoms*, Phys. Rev. A **62**, 063401 (2000).

[50] T. F. Gallagher, C. R. Mahon, P. Pillet, P. Fu, and J. B. Newman, *Microwave ionization of hydrogenlike Li and Na*, Phys. Rev. A **39**, 4545 (1989).

[51] M. Seng, U. Eichmann, V. Lange, T. F. Gallagher, and W. Sandner, *Microwave ionization of Rydberg states of the barium ion*, Eur. Phys. J. D **3**, 21 (1998).

[52] B. E. Sauer, S. Yoakum, L. Moorman, P. M. Koch, D. Richards, and P. A. Dando, *Dynamic Tunneling Ionization of Excited Hydrogen Atoms: A Precise Experiment versus Theories*, Phys. Rev. Lett. **68**, 468 (1992).

[53] P. Pillet, W. W. Smith, R. Kachru, N. H. Tran, and T. F. Gallagher, *Microwave Ionization of Na Rydberg Levels*, Phys. Rev. Lett. **50**, 1042 (1983).

[54] M. L. Zimmerman, M. G. Littman, M. M. Kash, and D. Kleppner, *Stark structure of the Rydberg states of alkali-metal atoms*, Phys. Rev. A **20**, 2251 (1979).

[55] D. Banks and J. G. Leopold, *Ionisation of highly excited atoms by electric fields II. Classical theory of the Stark effect*, J. Phys. B **11**, 2833 (1979).

[56] H. Friedrich, *Theoretische Atomphysik* (Springer, Berlin, 1990).

[57] R. C. Stoneman, D. S. Thomson, and T. F. Gallagher, *Microwave multiphoton transitrions between Rydberg states of potassium*, Phys. Rev. A **37**, 1527 (1988).

[58] T. Jonckheere, B. Grémaud, and D. Delande, *Spectral Properties of Nonhydrogenic Atoms in Weak External Fields*, Phys. Rev. Lett. **81**, 2442 (1998).

[59] P. A. Dando, T. S. Monteiro, D. Delande, and K. T. Taylor, *Beyond Periodic Orbits: An Example in Nonhydrogenic Atoms*, Phys. Rev. Lett. **74**, 1099 (1995).

[60] G. Benenti, G. Casati, and D. Shepelyansky, *Chaotic enhancement in microwave ionization of Rydberg atoms*, Eur. Phys. J. D **5**, 311 (1999).

[61] J. Rao, B. Li, and K. T. Taylor, *A new Floquet-based method for calculation of multiphoton transition probabilities of non-hyrogenic atoms in strong microwave fields*, J. Phys. B **32**, L145 (1999).

[62] T. Ericson, *Fluctuations of nuclear cross sections in the "continuum"region*, Phys. Rev. Lett. **5**, 430 (1960).

[63] R. Blümel and U. Smilansky, *Classical Irregular Scattering and Its Quantum-Mechanical Implications*, Phys. Rev. Lett. **60**, 477 (1988).

[64] J. Main and G. Wunner, *Ericson Fluctuations in the Chaotic Ionization of Hydrogen Atoms in Crossed Magnetic and Electric Fields*, Phys. Rev. Lett. **69**, 586 (1992).

[65] H. A. Weidenmüller, *Ericson fluctuations versus conductance fluctuations*, Nucl. Phys. **A518**, 1 (1990).

[66] A. Buchleitner, I. Guarneri, and J. Zakrzewski, *Conductance Fluctuations of Rydberg States in Microwave Fields*, Europhys. Lett. **44**, 162 (1998).

[67] S. M. Wimberger, *Der Leitwert von Atomen*, Diploma thesis (Ludwig-Maximilians-Universität), München (2000).

[68] C. F. F. Karney, *Long-time Correlations in the Stochastic Regime*, Physica D **8**, 360 (1983).

[69] R. S. MacKay, J. D. Meiss, and I. C. Percival, *Stochasticity and Transport in Hamiltonian Systems*, Phys. Rev. Lett. **52**, 697 (1984).

[70] R. S. MacKay, J. D. Meiss, and I. C. Percival, *Transport in Hamiltonian systems*, Physica **13D**, 55 (1984).

[71] J. D. Meiss and E. Ott, *Markov-Tree Model of Intrinsic Transport in Hamiltonian Systems*, Phys. Rev. Lett. **55**, 2741 (1985).

[72] J. D. Meiss and E. Ott, *Markov tree model of transport in area-preserving maps*, Physica D **20**, 387 (1986).

[73] B. V. Chirikov and D. L. Shepelyansky, *Correlation Properties of Dynamical Chaos in Hamiltonian Systems*, Physica D **13**, 395 (1984).

[74] B. V. Chirikov and D. L. Shepelyansky, *Asymptotic Statistics of Poincaré Recurrences in Hamiltonian Systems with Divided Phase Space*, Phys. Rev. Lett. **82**, 528 (1999).

[75] B. Huckestein, R. Ketzmerick, and H. Lewenkopf, *Quantum transport through ballistic cavities: soft vs. hard quantum chaos*, Phys. Rev. Lett. **84**, 5504 (2000).

[76] R. Ketzmerick, L. Hufnagel, F. Steinbach, and M. Weiss, *New Class of Eigenstates in Generic Hamiltonian Systems*, Phys. Rev. Lett. **85**, 1214 (2000).

[77] M. Weiss, L. Hufnagel, and R. Ketzmerick, *Do Chaotic Trajectories Care About Self-Similarity?*, (2001), arXiv:nonlin.CD/0106021.

[78] G. Casati, G. Maspero, and D. L. Shepelyansky, *Quantum Poincaré Recurrences*, Phys. Rev. Lett. **82**, 524 (1999).

[79] H. Alt, H.-D. Gräf, H. L. Harney, R. Hofferbert, H. Rehfeld, A. Richter, and P. Schardt, *Decay of classical chaotic systems: The case of the Bunimovich stadium*, Phys. Rev. E **53**, 2217 (1996).

[80] R. Ketzmerick, *Fractal conductance fluctuations in generic chaotic cavities*, Phys. Rev. B **54**, 10841 (1996).

[81] M. Weiß, *Quantenmechanik zwischen Regularität und Chaos: Vom gemischten Phasenraum zu ungeordneten Systemen*, PhD thesis (Georg-August-Universität), Göttingen (2000).

[82] F.-M. Dittes, H. L. Harney, and A. Müller, *Nonexponential decay of a stochastic one-channel system*, Phys. Rev. A **45**, 701 (1992).

[83] P. Schlagheck and A. Buchleitner, *Algebraic decay of the survival probability in chaotic helium*, Phys. Rev. A **63**, 024701 (2001).

[84] M. Henseler, T. Dittrich, and K. Richter, *Signatures of chaos and tunneling in AC-driven quantum scattering*, Europhys. Lett. **49**, 289 (2000).

[85] G. Benenti, G. Casati, G. Maspero, and D. L. Shepelyansky, *Quantum Poincaré Recurrences for a Hydrogen Atom in a Microwave Field*, Phys. Rev. Lett. **84**, 4088 (2000).

[86] A. Buchleitner, D. Delande, J. Zakrzewski, R. N. Mantegna, M. Arndt, and H. Walther, *Multiple Time Scales in the Microwave Ionization of Rydberg Atoms*, Phys. Rev. Lett. **75**, 3818 (1995).

[87] Y.-C. Lai, C. Greborgi, R. Blümel, and M. Ding, *Algebraic decay and phase-space metamorphoses in microwave ionization of hydrogen Rydberg atoms*, Phys. Rev. A **45**, 8284 (1992).

[88] G. Tanner, K. Richter, and J. M. Rost, *The theory of two-electron atoms: between ground state and complete fragmentation*, Rev. Mod. Phys. **72**, 498 (2000).

[89] P. Lambropoulos, P. Maragakis, and J. Zhang, *Two-electron atoms in strong fields*, Phys. Rep. **305**, 203 (1998).

[90] H. A. Bethe and E. E. Salpeter, *Quantum Mechanics of One- and Two-Electron Atoms* (Plenum Publishing Corporation, New York, 1977).

[91] C. Cohen-Tannoudji, J. Dupont-Roc, and G. Grynberg, *Photons and Atoms* (John Wiley & Sons, New York, 1989).

[92] R. Shakeshaft, *Multiphoton ionization of an atom; the choice of gauge*, Z. Phys. D **8**, 47 (1988).

[93] E. Cormier and P. Lambropoulos, *Optimal gauge and gauge invariance in non-perturbative time-dependent calculation of above threshold ionization*, J. Phys. B **29**, 1667 (1996).

[94] M. G. Floquet, *Équations différentielles linéaires à coefficients périodiques*, Annales de l'École Normale Supérieure **12**, 47 (1883).

[95] J. H. Shirley, *Solution of the Schrödinger Equation with a Hamiltonian Periodic in Time*, Phys. Rev. **138**, B979 (1965).

[96] Y. B. Zeldovich, *The quasienergy of a quantum-mechanical system subjected to a periodic action*, JETP (Soviet Physics) **24**, 1006 (1967).

[97] C. Kittel and C. Y. Fong, *Quantentheorie der Festkörper*, 3 ed. (Oldenbourg, München, 1989).

[98] D. Delande and J. Zakrzewski, *Spontaneous emission of nondispersive Rydberg wave packets*, Phys. Rev. A **58**, 466 (1998).

[99] K. Yajima, *Resonances for the AC-Stark Effect*, Comm. Math. Phys. **87**, 331 (1982).

[100] S. Graffi, V. Grecchi, and H. J. Silverstone, *Resonances and convergence of perturbation theory for N-body atomic systems in external AC-electric field*, Ann. Inst. Henri Poincaré **42**, 215 (1985).

[101] M. L. Goldberger and K. M. Watson, *Scattering Theory* (John Wiley & Sons, New York, 1964).

[102] M. Reed and B. Simon, *Analysis of Operators*, *Methods of Modern Mathematical Physics* (Academic Press, San Diego, 1980).

[103] Y. K. Ho, *The Method of Complex Coordinate Rotation and its Applications to Atomic Collision Processes*, Phys. Rep. **99**, 2 (1983).

[104] L. D. Landau and E. M. Lifschitz, *Quantenmechanik*, Vol. III of *Lehrbuch der theoretischen Physik*, 9 ed. (Akademie Verlag, Berlin, 1979).

[105] M. Berry, in *Chaos and Quantum Physics*, Vol. LII of *Les Houches Lectures*, edited by M. J. Giannoni, A. Voros, and J. Zinn-Justin (North–Holland, Amsterdam, 1989), p. 669.

[106] A. Buchleitner and D. Delande, *Secular motion of three-dimensional Rydberg states in a microwave field*, Phys. Rev. A **55**, R1585 (1997).

[107] A. Buchleitner, K. Sacha, D. Delande, and J. Zakrzewski, *Quasiclassical dynamics of resonantly driven Rydberg states*, Eur. Phys. J. D **5**, 145 (1999).

[108] A. Krug and A. Buchleitner, *Residual symmetries in the spectrum of periodically driven alkali Rydberg states*, Europhys. Lett. **49**, 176 (2000).

[109] H. Stöcker, *Taschenbuch der Physik*, 2 ed. (Harry Deutsch, Frankfurt a. Main, 1994).

[110] M. J. Seaton, *Quantum defect theory*, Rep. Prog. Phys. **46**, 167 (1983).

[111] T. F. Gallagher, *Rydberg Atoms*, 1 ed. (Cambridge University Press, Cambridge, 1994).

[112] J.-P. Connerade, *Highly Excited Atoms* (Cambridge University Press, Cambridge, 1998).

[113] C. J. Lorenzen and K. Niemax, *Quantum Defects of the* $n^2P_{1/2,3/2}$ *Levels in* $^{39}$*KI and* $^{85}$*RbI*, Physica Scripta **27**, 300 (1983).

[114] D. Meschede, *Centimeter–wave spectroscopy of highly excited rubidium atoms*, J. Opt. Soc. Am. B **4**, 423 (1987).

[115] M. J. Seaton, *The Quantum Defect Method*, Mon. Not. R. Astr. Soc. **118**, 504 (1958).

[116] M. Abramowitz and I. E. Stegun, *Handbook of Mathematical Functions*, Vol. 55 of *Applied Mathematics Series* (National Bureau of Standards, New York, 1964).

[117] M. J. Seaton, *Coulomb Functions Analytic in the Energy*, Comp. Phys. Comm **25**, 87 (1982).

[118] M. J. Seaton, *Quantum defect theory XI. Clarification of some aspects of the theory*, J. Phys. B **11**, 4067 (1978).

[119] M. J. Seaton, *Quantum defect theory VII. Analysis of resonance structures*, J. Phys. B **2**, 5 (1968).

[120] M. H. Halley, D. Delande, and K. T. Taylor, *The combination of R-matrix and complex coordinate methods: application to resonances in the diamagnetic Rydberg spectrum of Li*, J. Phys. B **25**, L525 (1992).

[121] M. H. Halley, D. Delande, and K. T. Taylor, *The combination of R–matrix and complex coordinate methods: application to the diamagnetic Rydberg spectra of Ba and Sr*, J. Phys. B **26**, 1775 (1993).

[122] M. H. Halley, *Diamagnetism in non–hydrogenic Rydberg–atoms*, PhD thesis (University of London), London (1993).

[123] C. Bloch, *Une Formulation Unifiée de la Théorie des Réactions Nucléaires*, Nucl. Phys. **4**, 503 (1951).

[124] B. I. Schneider, *Direct calculation of resonance energies and widths using an R–matrix approach*, Phys. Rev. A **24**, 1 (1981).

[125] P. G. Burke, A. Hibbert, and W. D. Robb, *Electron scattering by complex atoms*, J. Phys. B **4**, 153 (1971).

[126] P. G. Burke, in *Atomic Physics 10, Proceedings of the 10th International Conference on Atomic Physics*, edited by N. Narumi and I. Shimamura (North Holland, Amsterdam, 1987), p. 243.

[127] P. F. O'Mahony and K. T. Taylor, *Quadratic Zeeman Effect for Nonhydrogenic Systems: Application to the Sr and Ba Atoms*, Phys. Rev. Lett. **57**, 2931 (1986).

[128] C. W. Clark and K. T. Taylor, *The quadratic Zeeman effect in hydrogen Rydberg series: application of the Sturmian functions*, J. Phys. B **15**, 1175 (1982).

[129] D. Delande and J. C. Gay, *The hydrogen atom in a magnetic field. Spectrum from the Coulomb dynamical group*, J. Phys. B **19**, L173 (1986).

[130] D. Delande, in *Chaos and Quantum Physics*, Vol. LII of *Les Houches Lectures*, edited by M. J. Giannoni, A. Voros, and J. Zinn-Justin (North–Holland, Amsterdam, 1989), p. 669.

[131] A. Messiah, *Quantenmechanik* (W. de Gruyter, Berlin, Mew York, 1976), Vol. I.

[132] G. B. Arfken and H. J. Weber, *Mathematical Methods For Physicists* (Academic Press, San Diego, 1995).

[133] J. J. Sakurai, *Modern Quantum Mechanics* (Addison Wesley, Reading, Massachusetts, 1994).

[134] D. Delande, *Atomes de Rydberg en champs statiques intenses*, Thèse d'Etat (Université Pierre et Marie Curie), Paris (1988).

[135] M. W. Noel, L. Ko, and T. F. Gallagher, *Microwave Ionization of an Atomic Electron Wave Packet*, Phys. Rev. Lett. **87**, 043001 (2001).

[136] A. Messiah, *Quantenmechanik* (W. de Gruyter, Berlin, 1990), Vol. II.

[137] J. Zakrzewski and D. Delande, *Stabilization in circularly polarized light: Floquet–adiabatic versus exact treatment*, J. Phys. B **28**, L667 (1995).

[138] R. M. Potvliege and R. Shakeshaft, *Time-independent theory of multiphoton ionization of an atom by an intense field*, Phys. Rev. A **38**, 4597 (1988).

[139] R. Bümel and U. Smilansky, *Microwave Ionization of Highly Excited Hydrogen Atoms*, Z. Phys. D **6**, 83 (1987).

[140] C. E. Shannon, *A Mathematical Theory of Communication*, The Bell System Technical Journal **27**, 379 (1948).

[141] K. Hornberger, *Strahlungszerfall nichtdispergierender Wellenpakete*, Diploma thesis (Ludwig-Maximilians-Universität), München (1997).

[142] K. Hornberger and A. Buchleitner, to be published.

[143] C. Lanczos, *An iteration method for the solution of the eigenvalue problem of linear differential and integral operators*, J. Res. Nat. Bur. Standards, Sect. B **45**, 225 (1950).

[144] T. Ericsson and A. Ruhe, *The Spectral Transformation Lanczos Method for the Numerical Solution of Sparse Generalised Symmetric Eigenvalue Problems*, Math. Comput. **35**, 1251 (1980).

[145] G. H. Golub and C. F. v. Loan, *Matrix Computations*, 3 ed. (The John Hopkins University Press, Baltimore, Maryland, 1996).

[146] http://www.rzg.mpg.de/rzg/hpc.html.

[147] Hardware Description of the HITACHI SR8000-F1, http://www.lrz-muenchen.de/services/compute/hlrb/hardware-en/.

[148] http://www.mpi-forum.org/docs/docs.html.

[149] M. Snir, S. Otto, S. Huss-Lederman, D. W. Walker, and J. J. Dongarra, *MPI: The Complete Reference* (MIT Press, Cambridge, 1995).

[150] D. Walker and J. J. Dongarra, *MPI: A Standard Message Passing Interface*, Supercomputer **12**, 56 (1996).

[151] R. Hempel and D. W. Walker, *The Emergence of the MPI Message Passing Standard for Parallel Computing*, Computer Standards and Interfaces **21**, 51 (1999), also available at http://www.epm.ornl.gov/∼walker/papers/compstandards99.ps.

[152] J. J. Dongarra, I. S. Duff, D. C. Sorensen, and H. A. v. d. Vorst, *Solving Linear Systems on Vector and Shared Memory Computers* (SIAM, Philadelphia, 1991).

[153] U. Rüde, Technik des Wissenschaftlichen Rechnens, Vorlesungsskript, TU München, WS94/95.

[154] G. Amdahl, in *Proceedings of the AFIPS Computing Conference* (AFIPS Press, Reston, Va., 1967), Vol. 30, pp. 483–485.

[155] J. L. Gustafson, *Reevaluating Amdahl's Law*, Commun. ACM **31**, 532 (1988).

[156] D. Delande, K. Taylor, and A. Buchleitner, unpublished.

[157] J. J. Dongarra, J. D. Croz, and S. Hammarling, *An Extended Set of FORTRAN Basic Linear Algebra Subprograms*, ACM Trans. Math. Softw. **14**, 1 (1988).

[158] J. J. Dongarra, *A Set of Level 3 Basic Linear Algebra Subprograms*, ACM Trans. Math. Softw. **16**, 1 (1990).

[159] B. N. Parlett and D. S. Scott, *The Lanczos Algorithm With Selective Orthogonalization*, Mat. Comp. **33**, 217 (1979).

[160] M. Brehm, R. Bader, H. Heller, and F. Wagner, Optimization, (Pseudo-) Vectorization, and Parallelization on the Hitachi SR8000-F1, Supplement to the Hitachi SR8000 Tuning Manual, http://www.lrz-muenchen.de/services/compute/hlrb/optvecpar, 2000.

[161] B. Simon, *Resonances and Complex Scaling: A Rigorous Overview*, Int. J. Quantum Chem. **XIV**, 529 (1978).

[162] A. Buchleitner, B. Grémaud, and D. Delande, *Wavefunctions of atomic resonances*, J. Phys. B **27**, 2663 (1994).

[163] T. N. Rescigno and V. McKoy, *Rigorous method for computing photoabsorption cross sections from a basis set expansion*, Phys. Rev. A **12**, 522 (1975).

[164] D. Delande, A. Bommier, and J.-C. Gay, *Positive–Energy Spectrum of the Hydrogen Atom in a Magnetic Field*, Phys. Rev. Lett. **66**, 141 (1991).

[165] O. E. Alon and N. Moiseyev, *Balslev-Combes theorem within the framework of the finite-matrix approximation*, Phys. Rev. A **46**, 3807 (1992).

[166] A. Buchleitner, J. Zakrzewski, and D. Delande, *A Wave Packets Can Be a Stationary State*, Europhys. Lett. **32**, 107 (1995).

[167] J. Zakrzewski and D. Delande, *How to build experimentally a non-spreading wavepacket*, J. Phys. B **30**, L87 (1997).

[168] W. Lenz, *Über den Bewegungsverlauf und die Quantenzustände der gestörten Keplerbewegung*, Z. Phys. **24**, 197 (1924).

[169] K. Karremans, A. Kips, W. Vassen, and W. Hogervorst, *Effects of core scattering on level statistics in helium atoms in scaled external fields*, Phys. Rev. A **60**, R2649 (1999).

[170] A. Krug, *Mikrowellenionisaion von Alkaliatomen in einem realistischen numerischen Experiment*, Diploma thesis (Ludwig-Maximilians-Universität), München (1999).

[171] H. B. van Linden van den Heuvell, R. Kachru, N. H. Tran, and T. F. Gallagher, *Excitation Spectrum of Na Rydberg States in a Strong Microwave Field: A Connection Between Two Points of View*, Phys. Rev. Lett. **53**, 1901 (1984).

[172] O. Benson, G. Raithel, and H. Walther, in *Quantum Chaos between order and disorder*, edited by G. Casati and B. Chirikov (Cambridge University Presss, Cambridge, 1995), pp. 247–267.

[173] W. Jans, T. S. Monteiro, W. Schweitzer, and P. A. Dando, *Phase-space distributions and spectral properties for nonhydrogenic atoms in magnetic fields*, J. Phys. A **26**, 3187 (1993).

[174] S. Fishman and D. Shepelyansky, *Manifestation of Localization in Noise-Induced Ionization and Dissociation*, Europhys. Lett. **16**, 643 (1991).

[175] A. Krug and A. Buchleitner, *Chaotic Ionization of Nonhydrogenic Alkali Rydberg States*, Phys. Rev. Lett. **86**, 3538 (2001).

[176] M. W. Noel, M. W. Griffith, and T. F. Gallagher, *Population Trapping in Extremely Highly Excited States in Microwave Ionization*, Phys. Rev. Lett. **83**, 1747 (1999).

[177] P. Brumer and M. Shapiro, *Chaos and Reaction Dynamics*, Adv. Chem. Phys. **70**, 365 (1988).

[178] O. A. Starykh, P. R. J. Jaquod, E. E. Narimanov, and A. D. Stone, *Signature of dynamical localization in the resonance width distribution of wave-chaotic dielectric cavities*, Phys. Rev. E **62**, 2078 (2000).

[179] S. Drozdz, J. Okolowicz, M. Ploszajczak, and I. Rotter, *Statistical aspects of nuclear coupling to continuum*, Phys. Rev. C **6202**, 4313 (2000).

[180] C. F. Hillermeier, R. Bümel, and U. Smilansky, *Ionization of H Rydberg atoms: Fractals and power-law decay*, Phys. Rev. A **45**, 3486 (1992).

[181] C. E. Porter and R. G. Thomas, *Fluctuations of Nuclear Reactions Widths*, Phys. Rev. **104**, 483 (1956).

[182] Y. V. Fyodorov and H.-J. Sommers, *Statistics of resonance poles, phase shifts and time delays in quantum chaotic scattering: Random matrix approach for systems with broken time-reversal invariance*, J. Math. Phys. **38**, 1918 (1996).

[183] M. Glück, A. R. Kolovsky, and H. J. Korsch, *About universality of lifetime statistics in quantum chaotic scattering*, Physica E **9**, 478 (2001).

[184] M. Terraneo and I. Guarneri, *Distribution of resonance widths in localized tight-binding models*, Eur. Phys. J. B **18**, 303 (2000).

[185] M. Titov and Y. V. Fyodorov, *Time-delay correlations and resonances in one-dimensional disordered systems*, Phys. Rev. B **61**, R2444 (2000).

[186] Y. Zhang, M. Ciocca, L.-W. He, C. E. Burkhardt, and J. J. Leventhal, *Floquet spectroscopy of hydrogenic states: Classical and quantal descriptions*, Phys. Rev. A **50**, 4608 (1994).

[187] J. W. Pang, D. Neuhauser, and N. Moiseyev, *Photoabsorption probability for a system governed by a time-dependent Hamiltonian through the* $(t, t')$ *formalism*, J. Chem. Phys. **106**, 6839 (1997).

[188] A. Buchleitner, J. Zakrzewski, and D. Delande, in *Multiphoton Processes 1996*, Vol. 154 of *Institute of Physics Conference Series*, edited by P. Lambropoulos and H. Walther (Institute of Physics, Bristol and Philadelphia, 1997), p. 19.

[189] B. Hüpper, J. Main, and G. Wunner, *Photoabsorption of Nonhydrogenic Rydberg Atoms in a Magnetic Field: Effects of Core-Scattered Classical Orbits*, Phys. Rev. Lett. **76**, 2650 (1995).

[190] P. A. Dando, T. S. Monteiro, and S. M. Owen, *Periodic Orbit Theory for Rydberg Atoms in External Fields*, Phys. Rev. Lett. **80**, 2797 (1998).

[191] M. Sieber, *Spectral statistics of systems with a point interaction*, J. Phys. A **33**, 6263 (2000).

[192] E. Bogomolny, P. Leboeuf, and C.Schmit, *Spectral Statistics of Systems with a Pointlike Scatterer*, Phys. Rev. Lett. **85**, 2486 (2000).

[193] P. Seba, *Wave Chaos in Singular Quantum Billiard*, Phys. Rev. Lett. **64**, 1855 (1990).

[194] T. Shigehara and T. Checon, *Spectral properties of three-dimensional quantum billiards with a pointlike scatterer*, Phys. Rev. E **55**, 6832 (1997).

[195] O. Legrand, F. Mortessagne, and R. L. Weaver, *Semiclassical analysis of spectral correlations in regular billiards with point scatterers*, Phys. Rev. E **55**, 7741 (1997).

[196] S. Wimberger and A. Buchleitner, *Signatures of Anderson localization in the ionization rates of periodically driven Rydberg states*, J. Phys. A (2001), in print.

Fini, c’est fini, ça va finir, ça va peut-être finir.
Les grains s’ajoutent aux grains, un à un, et un jour,
soudain, c’est un tas, un petit tas, l’impossible tas.

S. Beckett, *Fin de partie*

*This work was carried out under the guidance of Andreas Buchleitner. I am very grateful to Andreas, who encouraged and supported me in the past years, it was a pleasure to work with him. With him, I enjoyed many fruitful discussions about physics and also about the 'rest of the world'.*

*I am also grateful to the Garching and Dresden crew, especially to Amalia Apalategui-Rebollo, Angelika Hofmann, Andreas Kemp, Lukas Kurtz, Giovanna Morigi, Jens Schneider, Christoph Skornia, and to Ivo Häring, Klaus Hornberger, Javier Madronero, Florian Mintert, Cord Mueller, Peter Schlagheck, Tobias Schneider, Christian Siedschlag, Juan-Diego Urbina, Thomas Wellens and Sandro Wimberger. They created a stimulating and open-minded atmosphere where it was fun to work in.*

*Thanks also to Dominique Delande for the possibility to stay some weeks in Paris, and for interesting discussions. Thanks also to Thibaut Jonckheere in Paris, hopefully we can continue our point-scatterer-project.*

*This work was carried out at the Max-Planck-Institut für Quantenoptik and at the Max-Planck-Institut für Physik komplexer Systeme. Thanks to Peter Lambropoulos for the possibility to work in the theory group at the MPQ. Furthermore, I want to thank the scientific and the 'non-scientific' staff at the both institutes for creating a friendly environment.*

*Obviously computers did play a crucial role for this work. Thus I want to thank Reinhard Volk and Hubert Scherrer for administrating the computer network in Garching and Dresden which is – I guess – not always an easy job. The largest part of the calculations in this work, however, could not be performed on the local computers but only on the CRAY T3E of the Rechenzentrum Garching of the Max-Planck-Gesellschaft, and on the Hitachi SR8000-F1 of the Leibniz-Rechenzentrum of the Bayrische Akademie der Wissenschaften. Thanks to the MPG and the Bayrische Akademie der Wissenschaften for computing time. A special 'thank you' to the LRZ-team for the excellent support on the HITACHI.*

*Last but not least I want to thank my family (my parents, and Steffi, Harry and Helena) and especially to Rita, who 'has to' live together with a physicist, and encouraged me whenever it was needed.*

# Curriculum Vitae

Andreas Krug
geboren am 27. August 1970 in München
Familienstand: ledig (verheiratet ab dem 15.9.2001 mit Rita Neiteler)

**1977-1981:** Grundschule Bad Tölz.

**1981-1990:** Gymnasium Bad Tölz.

**1990:** Abitur.

**1990-1992:** Zivildienst, Wohnheim für Geistig Behinderte Erwachsene der Lebenshilfe Bad Tölz.

**1992-1993:** Studium Maschinenbau, Rheinisch–Westfälische Technische Hochschule Aachen.

**1993-1995:** Studium der Physik und Mathematik, Rheinisch–Westfälische Technische Hochschule Aachen.

**1995-1999:** Studium der Physik, Ludwig-Maximilians-Universität München.

**1999:** Hauptdiplom Physik.

**seit 3/1999:** Doktorand am Max-Planck-Institut für Physik komplexer Systeme Dresden und am Max-Planck-Institut für Quantenoptik Garching.